Adaptive Beamforming for Medical Ultrasound Imaging

Holfort, Iben Kraglund

Publication date:
2010

Document Version
Publisher's PDF, also known as Version of record

Technical University
of Denmark

Adaptive Beamforming for Medical Ultrasound Imaging

Iben Kraglund Holfort

November 2009

DTU Electrical Engineering
Department of Electrical Engineering

Technical University of Denmark
Department of Electrical Engineering
Center for Fast Ultrasound Imaging
DK-2800 Kgs. Lyngby
Denmark

Submitted in partial fulfillment of the requirements for the degree of Doctor of Philosophy at the Technical University of Denmark.

Preface

This dissertation has been submitted to the Technical University of Denmark in partial fulfillment of the requirements for the degree of Doctor of Philosophy.

The content of this dissertation is based on work carried out from December 1st, 2006 to November 30th, 2009 at the Center for Fast Ultrasound Imaging, Department of Electrical Engineering, Technical University of Denmark.

During this period, I have had the privilege to collaborate with a selection of exceptional researchers; home and abroad. I have had the opportunity to travel the world; participation in conferences has allowed me to travel to four different continents. And finally, I have been teaching students in signal processing and medical imaging courses, and co-supervised student projects. Out of the many experiences I have had during the last three years, these are the ones that I will definitely miss the most.

It is my hope that you will enjoy reading this dissertation, and that there will be someone to pick up the baton and continue the relay of this very interesting area of research.

Iben Kraglund Holfort
Kgs. Lyngby, November 2009

Acknowledgments

First of all, I would like to thank my supervisor, Professor Jørgen Arendt Jensen, for giving my the opportunity to dive into the very exciting fields of medical ultrasound imaging and adaptive beamforming.

My co-supervisor, Fredrik Gran, who gave me the best start possible, before he ventured out into the industrial world. He has continued to inspire me and has provided valuable input throughout my project period.

Professor Sverre Holm, Andreas Austeng, Johan-Fredrik Synnevåg, Ann Blomberg, Are Jensen, Angelique Berthelot, and the rest of the Digital Signal Processing and Image Analysis Group at the Department of Informatics, University of Oslo, Norway. They have all been very kind to welcome me into their group, providing a friendly atmosphere, and giving me very valuable input during my visits.

The two MDs, Kristoffer Lindskov Hansen and Mads Møller Pedersen, for their several discussions, ideas and help carrying out in-vivo measurements.

Current and former colleagues for numerous discussions, inputs, talks and pleasant travels; these include Henrik Andresen, Svetoslav Nikolov, Jacob Kortbek, Jesper Udesen, Niels Oddershede, Borislav Tomov, Lasse Henze, David Bæk, Yigang Du, Martin Hemmsen, Michael Pihl, Gertrud Laura Sørensen, Julie Brinck Jensen and Morten Fischer Rasmussen.

Furthermore, Henrik Laursen and Elna Sørensen for their always very kind help in any computer related or administrative issue.

Last, but definitely not least, I would like to thank my family and friends for supporting me during these three years. Especially my father, who has

managed to make me believe that he has always been sincerely interested in my work. And of course, my husband-*to-be*, Lars, for listening, suggesting, supporting, helping and always being there, when I needed it.

Abstract

This dissertation investigates the application of adaptive beamforming for medical ultrasound imaging. The investigations have been concentrated primarily on the Minimum Variance (MV) beamformer. A broadband implementation of the MV beamformer is described, and simulated data have been used to demonstrate the performance.

The MV beamformer has been applied to different sets of ultrasound imaging sequences; synthetic aperture ultrasound imaging and plane wave ultrasound imaging. And an approach for applying MV optimized apodization weights on both the transmitting and the receiving apertures is suggested. These investigations show that the MV beamformer provides a significantly reduced main-lobe width compared to the conventional delay and sum beamformer.

The effects of near-field propagation and a comparison between a subband and a temporal implementation are considered. And an investigation of the influence of sound speed errors on the adaptive beamformers; MV and the Amplitude and Phase EStimation (APES) beamformer.

Furthermore, the investigations of previously suggested adaptive spectral Doppler techniques are continued by additional in-vivo measurements. These investigations shows that the adaptive spectral Doppler techniques are indeed capable of providing spectrograms with increased resolution and contrast compared to the conventional methods, based on Welch's spectral estimator. The investigation includes measurements of both arterial and venous flow patterns, located at different depths within the human body.

Contents

Nomenclature

c	Speed of sound
$\mathcal{E}\{\cdot\}$	Expectation value
$\mathcal{F}\{\cdot\}$	Fourier transform
j	Imaginary unit, $j = \sqrt{-1}$
w	Scalar value
$\mathbf{w}$	Vector (bold notation)
$\mathbf{W}$	Matrix (bold notation, capital letter)
$\vec{r}$	Euclidean vector
$s(t)$	Signal in time
$S(f), S(\omega)$	Fourier transform of $s(t)$
$\mathrm{Tr}\{\cdot\}$	Trace operator
$*$	Convolution operator
$\|\cdot\|$	Euclidean distance
$\lvert\cdot\rvert$	Modulus
$\{\cdot\}^*$	Complex conjugate
$\{\cdot\}^T$	Matrix transpose (non-conjugate)
$\{\cdot\}^H$	Hermitian transpose (complex conjugate)

Abbreviations

APES	Amplitude and Phase EStimation
BAPES	Blood Spectral Amplitude and Phase EStimation
BPC	Blood Spectral Power Capon
DAS	Delay and Sum
DFT	Discrete Fourier Transform
FWHM	Full Width at Half Maximum
MV	Minimum Variance
PSL	Peak-side-lobe level
PW	Plane Wave
RASMUS	Remotely Accessible Software configurable Multi-channel Ultrasound Sampling-System
Rx	Receive
SA	Synthetic Aperture
SNR	Signal-to-noise ratio
Tx	Transmit
W.BOX	Welch's method using Boxcar weights
W.HAN	Welch's method using Hanning weights

CHAPTER

ONE

Introduction

For decades, ultrasound imaging has been used for diagnostic purposes. Using ultrasound, the interior structures of the human body can be displayed in real-time and without the use of ionizing radiation. Furthermore, ultrasound imaging benefit from being in-expensive, relatively portable, and it provides very little discomfort for the patient.

Ultrasound examinations are most commonly known from fetal scans during pregnancy. An example of an ultrasound B-mode (or *Brightness*-mode) image is seen in Fig. 1.1. The scan shows a 19-week-old fetus.

An ultrasound scan is carried out by emitting high-frequency acoustic wave fields into the body of the patient. These acoustic waves are in the MHz range and thus, out of the human audible range. Due to changes in the tissue characteristics, the acoustic waves are reflected at different depth within the human body.

The reflected echoes are measured by an array of piezo-electric sensors. By combining these sensor signals using array processing techniques, the distances and intensities of the echoes form the ultrasound B-mode image.

Conventionally, the sensor signals are processed using the so-called Delay and Sum (DAS) beamformer. The principle of the DAS beamformer is to maximize its output by delaying, weighting, and subsequently summing the individual sensor signals.

The DAS beamformer uses predefined apodization weights, which are independent of the input data. As is commonly known, an inherent compromise between the main-lobe width and the side-lobe level exists. Choosing a smoothing apodization function, such as Hanning, the side-lobe level can be

Figure 1.1: Example of an ultrasound B-mode image. The scan shows a 19-week-old fetus.

reduced at the expense of a lateral broadening of the main-lobe.

For decades, data-dependent, adaptive beamformers have been used in other fields of array signal processing, e.g. sonar and radar. Whereas the conventional beamformer is a passive process using data-independent apodization weights, the adaptive beamformer actively updates a set of new apodization weights for each point in the image. These apodization weights are directly dependent on the input data.

One of the widely used methods was originally introduced by Capon in 1969 [1]. The Capon or Minimum Variance (MV) beamformer continuously updates the apodization weights, so that the variance (or power) of the weighted sensor signals is minimized under the constraint that the signal emerging from the point of interest is passed without distortion.

The main objective of the project forming this dissertation is to investigate adaptive beamforming for ultrasound imaging. The investigations have primarily been focused on the MV beamformer.

1.1 State of the Art

Recently, the application of adaptive beamforming to the field of medical ultrasound imaging has become an area of increased interest. The adap-

tive beamformers potentially provide improvements of the image quality, in terms of lateral resolution and contrast.

In 2002, Mann and Walker [2] introduced the linearly constrained adaptive beamformer, also referred to as the Frost beamformer [3]. They applied the method to experimental data of a single point target and a cyst phantom using diagonal loading to ensure a well-conditioned covariance matrix.

Another approach to obtain a well-conditioned covariance matrix is to use spatial averaging, which was introduced to ultrasound data by Sasso and Cohen-Bacrie in 2005 [4]. They apply the MV beamformer on a simulated cyst.

Four different adaptive beamformers were introduced by Viola and Walker in 2005 [5]. One of these was later developed into the high resolution method, TONE (Time-domain Optimized Near-field Estimator) [6,7].

Synnevåg *et al.* [8] applied the MV beamformer to simulated and experimental ultrasound data, and they proposed a robust approach, which less sensitivity towards imperfections of the wave field, such as errors in the sound speed estimate, using diagonal loading.

Wang *et al.* [9] also applied the MV beamformer, and furthermore, the MUSIC (MUltiple SIgnal Classification) approach. They introduce yet another approach to obtain a well-conditioned covariance matrix by averaging over several emissions from different spatial positions.

A semi-adaptive approach with low complexity was suggested by Synnevåg *et al.* in 2008 [10]. Choosing between several sets of predefined apodization weights and combining the resulting images using an MV criterion yields an approach with a reduced computational complexity without matrix inversions.

In 2008 and 2009, Vignon and Burcher provide in-vivo ultrasound images using the MV beamformer. In [11] they have used a measurement sequence with focused beams, and in [12] they use the MV in combination with spatial compounding.

The previous work within this field is characterized by the fact that narrowband methods have been applied directly on broadband ultrasound data. Instead, we have in Paper I-II [13, 14] proposed an approach for near-field, adaptive beamforming of broadband data.

This approach is implemented in the frequency domain, and it provides a

set of adapted, complex apodization weights for each frequency subband. Whereas the conventional method, and the previous implementations of the MV beamformer, provide a single weight value for each sensor. The proposed method continuously updates a set of spatial filters for each sensor signal. This approach was applied to simulated synthetic aperture ultrasound data in Paper I-II [13, 14] and to plane wave emission data in Paper I, III [14, 15].

In Paper V [16], the performance of the MV beamformer for transducers with different physical sizes was investigated. It was seen that an increased resolution can be obtained, when using only a part of the array for the adaptive beamforming algorithm. This was observed, when the physical footprint of the transducer was increased.

The sensitivity towards sound speed errors of the MV and APES (Amplitude and Phase EStimation) beamformers was investigated in Paper VI [17]. The performance of the APES beamformer was further investigated in Paper VII by Blomberg *et al.* [18]. This investigation showed that the APES beamformer provides a more robust amplitude estimate than the MV beamformer.

An approach for utilizing adapted apodization weights on both the receiving and transmitting apertures was suggested in Paper IV [19]. The approach was based on a synthetic aperture ultrasound imaging frame-work and the concept of the method was demonstrated using simulated data. The method provides significantly reduced main-lobe width compared to the conventional DAS beamformer, as well as compared to using adapted weights on the receiving aperture, only.

1.2 Contributions

During my PhD project period I have had the privilege to collaborate with a variety of colleagues; medical doctors, engineers and engineering students in Denmark as well as Norway. This has lead to the following contributions to the research field of ultrasound imaging applications.

Journal Paper(s)

- **I. K. Holfort**, F. Gran and J. A. Jensen, "Broadband Minimum Variance Beamforming for Ultrasound Imaging", *Transactions on Ultrasonics, Ferroelectrics, and Frequency Control*, Vol. 56, No. 2, pp. 314-325, Feb. 2009.

- K. L. Hansen, F. Gran, M. M. Pedersen, **I. K. Holfort**, J. A. Jensen and M. B. Nielsen, "In-vivo Validation of Fast Spectral Velocity Estimation Techniques", *Ultrasonics*, 2009.

Conference Paper(s)

- **I. K. Holfort**, A. Austeng, J.-F. Synnevåg, S. Holm, F. Gran and J. A. Jensen, "Adaptive Receive and Transmit Apodization for Synthetic Aperture Ultrasound Imaging", *Proceedings of the IEEE International Ultrasonics Symposium*, Rome, Italy, Sep. 2009.
- A. E. A. Blomberg, **I. K. Holfort**, A. Austeng, J.-F. Synnevåg, S. Holm and J. A. Jensen, "APES Beamforming Applied to Medical Ultrasound Imaging", *Proceedings of the IEEE International Ultrasonics Symposium*, Rome, Italy, Sep. 2009.
- K. L. Hansen, F. Gran, M. M. Pedersen, **I. K. Holfort**, J. A. Jensen and M. B. Nielsen, "Evaluation Study of Fast Spectral Estimators Using In-vivo Data", *Proceedings of the IEEE International Ultrasonics Symposium*, Rome, Italy, Sep. 2009.
- **I. K. Holfort**, F. Gran and J. A. Jensen, "High Resolution Ultrasound Imaging Using Adaptive Beamforming with Reduced Number of Active Elements", *Proceedings of the International Congress on Ultrasonics*, Santiago, Chile, Jan. 2009.
- **I. K. Holfort**, F. Gran and J. A. Jensen, "Investigation of Sound Speed Errors in Adaptive Beamforming", *Proceedings of the IEEE International Ultrasonics Symposium*, Beijing, China, Nov. 2008, pp. 1080-1083.
- K. L. Hansen, F. Gran, M. M. Pedersen, **I. K. Holfort**, J. A. Jensen and M. B. Nielsen, "In-vivo Validation of Fast Spectral Velocity Estimation Techniques: Preliminary Results", *Proceedings of the IEEE International Ultrasonics Symposium*, Beijing, China, Nov. 2008, pp. 1615-1618.
- G. L. Sørensen, J. B. Jensen, J. Udesen, **I. K. Holfort** and J. A. Jensen, "Pulse Wave Velocity in the Carotid Artery", *Proceedings of the IEEE International Ultrasonics Symposium*, Beijing, China, Nov. 2008, pp. 1386-1389.
- L. Henze, **I. K. Holfort**, J. Kortbek and J. A. Jensen, "Transverse Correlation: An Efficient Transverse Flow Estimator – Initial Results", *Proceedings of the IEEE International Ultrasonics Symposium*, Beijing, China, Nov. 2008, pp. 1619-1622.

- **I. K. Holfort**, F. Gran and J. A. Jensen, "Plane Wave Medical Ultrasound Imaging Using Adaptive Beamforming", *Proceedings of the 5th IEEE Sensor Array and Multichannel Signal Processing Workshop*, Darmstadt, Germany, July 2008, pp. 288-292.
- **I. K. Holfort**, F. Gran and J. A. Jensen, "Minimum Variance Beamforming for High Frame-Rate Ultrasound Imaging", *Proceedings of the IEEE International Ultrasonics Symposium*, New York, NY, USA, Oct. 2007, pp. 1541-1544.
- L. Henze, **I. K. Holfort**, J. Kortbek and J. A. Jensen, "In-vivo Vector Flow Imaging Using Improved Directional Beamforming", *Proceedings of the IEEE International Ultrasonics Symposium*, New York, NY, USA, Oct. 2007, pp. 2438-2441.
- **I. K. Holfort**, J. Kortbek and J. A. Jensen, "In-vivo Vector Velocity Imaging Using Directional Cross-Correlation", *Proceedings of the IEEE International Ultrasonics Symposium*, Vancouver, BC, Canada, Oct. 2006, pp. 2023-2026.

1.3 Structure of the Dissertation

The dissertation is divided into the following chapters.

Chapter 2 provides the theory of beamforming and adaptive beamforming from a far-field perspective using plane wave fields.

Chapter 3 introduces adaptive beamforming to medical ultrasound imaging using broadband spherical wave fields.

Chapter 4 presents the results of the application of the adaptive beamformers to ultrasound imaging. This chapter is based on the results published in one journal paper and six conference papers, and an additional, yet unpublished, investigation.

Chapter 5 presents a selection of spectrograms obtained using adaptive spectral Doppler techniques. The results form the basis of a continuation of an in-vivo study that investigate the performance of two previously suggested spectral Doppler techniques.

Chapter 6 contains summary and conclusions on the results presented in this dissertation. Furthermore, this chapter includes a set of suggestions for future work.

Paper I-VI are the papers that form the basis of the results in Chapter 4.

Appendix A includes a set of additional publications, Paper VII-XIV. Except for Paper VII, these are are not covered in the dissertation.

CHAPTER

TWO

Beamforming

This chapter will introduce the theory of beamforming and adaptive beamforming. The theory in the following sections is based on [20]. The reader is assumed to have a basic understanding of acoustics and the theory of ultrasound imaging. For more on these two topics, please consult [21] and [22], respectively.

2.1 Sensor Arrays

Beamforming is a method to process the output of a sensor array. A sensor array is a collection of sensors located at different spatial positions, and is primarily used to

- Enhance the signal-to-noise ratio compared to that of a single sensor.
- Characterize a signal in time and space, e.g. by determining the number of emitting sources, their locations or signal parameters.
- Track moving sources.

Three very different sets of sensor arrays are shown in Fig. 2.1. These three sets of sensor arrays are all very different in both shape and size. However, they can all be used to sample a signal in time and space.

As Fig. 2.1(a) indicates, our ears can be regarded as a short array of sensors; these can e.g. be used to characterize the direction of a sound that will make one turn his or her head in the direction of the sound. A very large array of

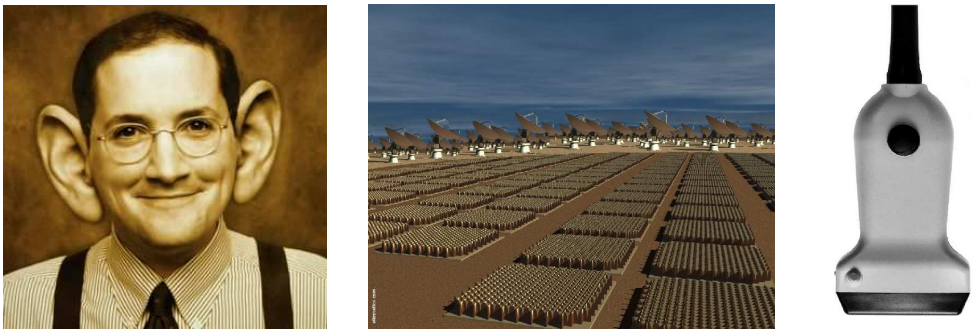

(a) (b) (c)

Figure 2.1: Three very different sets of sensor arrays. (a) Ears. (b) The Square Kilometer Array. From [23]. (c) Ultrasonic transducer.

sensors occupying one square kilometer is shown in Fig. 2.1(b). These telescopes are used for receiving and detecting electromagnetic radiation from objects in outer space. And in Fig. 2.1(c), we see the sensor array that is the primary topic of this dissertation; a linear ultrasonic transducer.

2.2 Signal in Time and Space

Using an arbitrarily shaped array of M sensors, a signal in time and space is sampled at the spatial positions of the sensors, $\mathbf{r}_m = (x_m, y_m, z_m)$, for $m = 0, 1, \ldots, M-1$. For a propagating plane wave field, each of the M sensor signals can be expressed as

$$g_m(t, \mathbf{r}) = a \exp\{j(\omega t - \mathbf{k}^T \mathbf{r}_m)\} , \tag{2.1}$$

where a is an arbitrary amplitude value, $\omega = 2\pi f$ is the angular (temporal) frequency, and $\mathbf{k} = (k_x, k_y, k_z)$ is a spatial frequency also referred to as the wavenumber vector.

For simplicity, the theory in the following is described for a uniformly spaced linear array and a plane wave field. An illustration indicating the geometry of an incoming plane wave onto a uniformly spaced linear array is shown in Fig. 2.2. The array of sensors is illustrated in the top along the x-axis, and the incident angle of the wave is denoted θ.

For a uniformly spaced linear array, $\mathbf{r}_m = (x_m, 0, 0)$, the wave field is only sampled along the dimension of the array, and the wave number vector $\mathbf{k}$ reduces to the scalar, $k_x = -\frac{\omega}{c} \sin(\theta)$, where θ denotes the angle of the incident

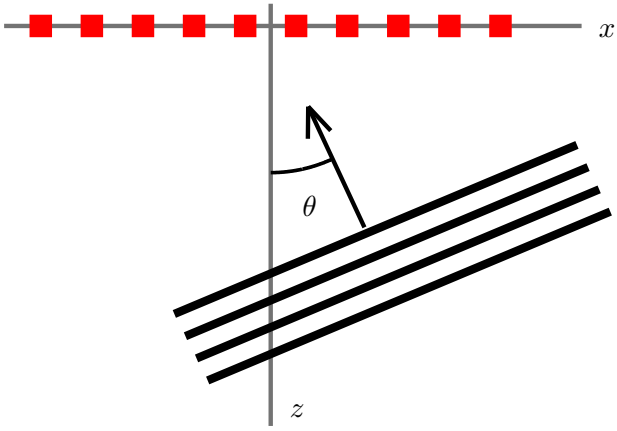

Figure 2.2: Geometry of a uniformly spaced linear array of sensors, placed along the x-axis, with an incoming plane wave, where θ denotes the incident angle.

wave. Thus, the wave field can be expressed as

$$s_m(t) = g_m(t, x_m) = a \exp\{j(\omega t - k_x x_m)\} \,, \tag{2.2}$$

where x denotes the direction along the array. Using the Fourier transform each temporal frequency of (2.2) can be eliminated

$$S_m(\omega) = \int s_m(t) \exp\{-j\omega t\} \, dt \tag{2.3}$$

$$= \int a \exp\{j(\omega t - k_x x_m)\} \exp\{-j\omega t\} \, dt \tag{2.4}$$

$$= a \exp\{-j k_x x_m\} \,, \tag{2.5}$$

which can be recognized as a complex sinusoid oscillating with a spatial frequency of k_x.

The real and imaginary parts of two sampled wave fields are shown in Fig. 2.3(a)-(b) for a uniformly spaced linear array of sensors. The two plane wave fields have incident angles of $\theta = 10^\circ$ and $\theta = 35^\circ$, respectively.

It is seen that these signals resemble sinusoids with frequencies dependent on the incident angle. Thus, if one could determine this frequency, the incoming direction of the plane wave can be found.

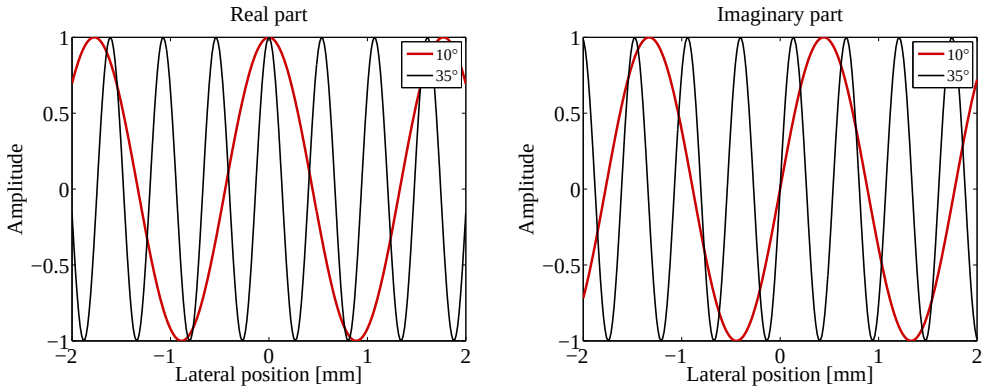

(a) Real part (b) Imaginary part

Figure 2.3: Real and imaginary parts of the spectra of the sensor signals across the array at the center frequency. The plane waves have incident angles of $\{10^\circ, 35^\circ\}$, center frequency $f_0 = 5$ MHz, propagation speed $c = 1540$ m/s, and sampling frequency $f_s = 100$ MHz.

2.3 Beamforming

Beamforming is an approach to estimate the direction of an incoming wave. Steering the wave field at different directions and summing the sensor signals yields maximum output power at the direction of the incoming wave due to in-phase summation. Steering the signal from (2.5), the beamformer output for a single frequency becomes

$$B(\kappa_x, \omega) = \sum_{m=0}^{M-1} S_m(\omega) \exp\{j\kappa_x x_m\} \tag{2.6}$$

$$= \sum_{m=0}^{M-1} a \exp\{-jk_x x_m\} \exp\{j\kappa_x x_m\} \tag{2.7}$$

$$= \sum_{m=0}^{M-1} a \exp\{-j(k_x - \kappa_x) x_m\} \,, \tag{2.8}$$

where κ_x is the x-component of the wave number representing the steering direction. It is seen that (2.6)-(2.8) resembles the expression for the discrete Fourier transform. In fact, beamforming and spectral estimation are analytically equivalent, see e.g. [24]. Obviously, the main difference is that beamforming is in the spatial domain and spectral estimation works in the temporal domain.

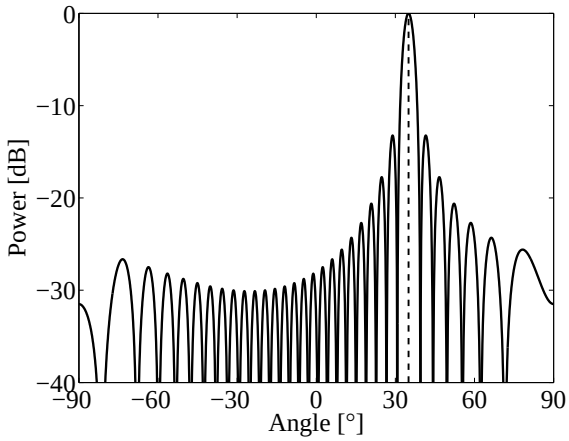

Figure 2.4: Beamformer output for a plane wave incident at $35°$. The vertical dashed line indicates the direction of the incoming wave.

In Fig. 2.4 the beamformer output for an incoming wave incident at $35°$ is shown. It is seen that the beamformer output peaks at the direction of the incoming wave. It has the characteristic sinc-structure and resembles the output of the discrete Fourier transform for a time-limited, monochromatic sinusoid.

2.3.1 Apodization

As known from spectral estimation, introducing a weighting function on the data can reduce the side-lobes of a spectrum at the expense of a broadening of the main-lobe. This is directly equivalent to beamforming, where the introduction of a weighting function across the array is referred to as shading, tapering, weighting, aperture function or the phrase commonly used in ultrasound imaging; apodization.

The Fourier transform relates a complex exponential function in the frequency domain to a phase (or time) shift in the temporal domain. Thus, with the introduction of a weighting function, w_m, (2.6) can be expressed in the temporal domain as

$$b(\kappa_x, t) = \sum_{m=0}^{M-1} w_m^* s_m\big(t + \tau_m(\kappa_x)\big) = \sum_{m=0}^{M-1} w_m^* y_m(t)\,, \tag{2.9}$$

where $s_m(t)$ denotes the received sensor signals, and τ_m is a delay, which is dependent on the steering direction, κ_x. Note that the weighting function,

w_m, can be either fixed or changing with the steering direction, κ_x. The superscript, $\{\cdot\}^*$, denotes the complex conjugate operator, which is introduced here for later notational purposes; and to indicate that the apodization weights can be complex.

By introducing the vectors,

$$\mathbf{w} = \begin{bmatrix} w_0 \\ w_1 \\ \vdots \\ w_{M-1} \end{bmatrix} \text{ and } \mathbf{y} = \begin{bmatrix} y_0(t) \\ y_1(t) \\ \vdots \\ y_{M-1}(t) \end{bmatrix} = \begin{bmatrix} s_0\big(t + \tau_m(\kappa_x)\big) \\ s_1\big(t + \tau_m(\kappa_x)\big) \\ \vdots \\ s_{M-1}\big(t + \tau_m(\kappa_x)\big) \end{bmatrix}, \tag{2.10}$$

the sum in (2.9) can also be written as the inner product of these two vectors. Thus, (2.9) can be rewritten as

$$b(\kappa_x, t) = \mathbf{w}^H \mathbf{y}\,, \tag{2.11}$$

where $\{\cdot\}^H$ denotes the Hermitian transpose. Keep in mind that the Hermitian transpose and the non-conjugate matrix transpose are identical operators for real vectors.

A block diagram illustrating the concept of apodized beamforming is shown in Fig. 2.5(a). The M sensor signals are delayed, weighted and subsequently summed to form the beamformer output. This beamformer is usually referred to as the Delay and Sum (DAS) beamformer.

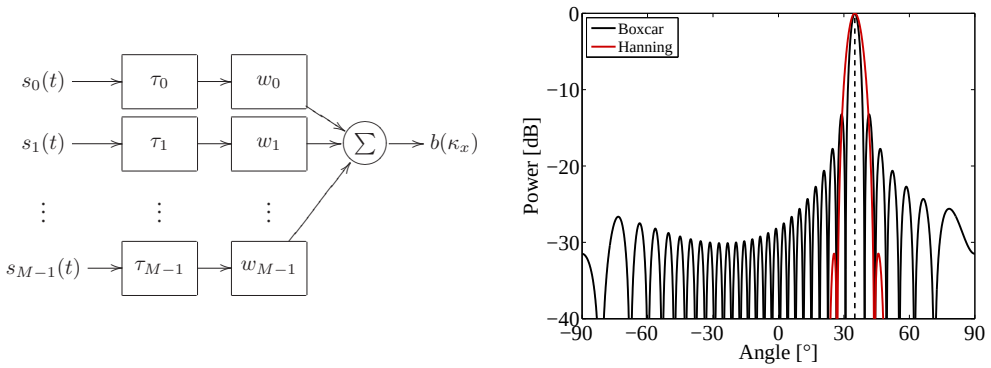

(a) (b)

Figure 2.5: (a) Block diagram of the conventional, delay and sum beamformer. The sensor signals are delayed, weighted, and subsequently summed to form the beamformer output. (b) Beamformer output for a plane wave incident at 35° using Boxcar and Hanning apodization.

An example of an apodized beamformer output is shown in Fig. 2.5(b) for a plane wave incident at $35°$. The beamformer outputs are the responses using Boxcar and Hanning apodization, respectively. As expected, the Hanning apodization provides a reduction of the side-lobes at the expense of a broadening of the main-lobe.

2.4 Adaptive Beamforming

Conventionally, beamforming is carried out using the DAS beamformer (2.9), where the apodization weights are predefined. These weights can either be fixed or changing with steering direction, but either way they are predefined. Adaptive beamformers are methods to automatically find a set of adapted apodization weights that is optimized directly from the measured wave field.

In Fig. 2.6, a block diagram illustrates the principle of an adaptive beamformer. As seen, an adaptive beamformer is simply an extension to the conventional beamformer, where the only difference is the choice of weights. Instead of using predefined weights, the adaptive processor actively updates a set of new apodization weights, which are directly dependent on the delayed sensor signals.

The adaptive processor is the optimization or adaptation process, which changes with the different types of adaptive beamformers. In the following two adaptive beamformers will be described; these are the so-called Mini-

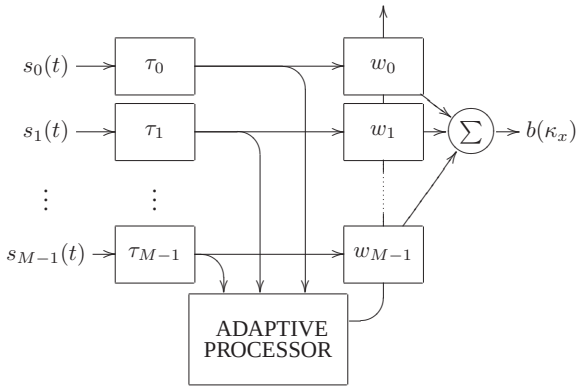

Figure 2.6: Block diagram of an adaptive beamformer. The adaptive processor determines a set of optimized apodization weights from the delayed sensor signals. The optimized weights are applied to the sensor signal, which are subsequently summed to form the beamformer output.

mum Variance (MV) or Capon method and the Amplitude and Phase EStimation (APES) method.

2.4.1 Minimum Variance Beamforming

In beamforming, it is desirable to remove – or at least minimize – the contributions from noise and interfering signals. As the names states, the Minimum Variance (MV) beamformer attempts to reduce the noise contributions by minimizing the variance of the output noise.

However, as the noise terms are inherent in the measured signals, it is not straightforward to minimize the noise, only. Instead, the MV beamformer minimizes the variance of the beamformer output. Assuming zero-mean of the beamformer output, the variance can be expressed as

$$\sigma^2 = \mathcal{E}\left\{|b(\kappa_x,t)|^2\right\} = \mathcal{E}\left\{(\mathbf{w}^H\mathbf{y})^2\right\} = \mathcal{E}\left\{\mathbf{w}^H\mathbf{y}(\mathbf{w}^H\mathbf{y})^H\right\} \tag{2.12}$$

$$= \mathcal{E}\left\{\mathbf{w}^H\mathbf{y}\mathbf{y}^H\mathbf{w}\right\} = \mathbf{w}^H\mathcal{E}\left\{\mathbf{y}\mathbf{y}^H\right\}\mathbf{w} = \mathbf{w}^H\mathbf{R}_y\mathbf{w}\,, \tag{2.13}$$

where $\mathbf{R}_y$ denotes the covariance matrix of the steered sensor signals given by

$$\mathbf{R}_y = \mathcal{E}\left\{\mathbf{y}\mathbf{y}^H\right\}\,. \tag{2.14}$$

Note that $\mathbf{R}_y$ is dependent on the steering direction, but to simplify notation this dependency have been omitted.

It is seen that simply minimizing the variance will provide all-zero weights, and thus a constraint must be introduced to the optimization problem. The constraint in this case is that the signal from the steering direction should be passed without distortion. Thus, the MV beamformer can be expressed mathematically as [1]

$$\begin{array}{l}\min\limits_{\mathbf{w}} \mathbf{w}^H\mathbf{R}_y\mathbf{w} \\ \text{subject to } \mathbf{w}^H\mathbf{e} = 1\end{array}\,, \tag{2.15}$$

where $\mathbf{e}$ is the so-called steering vector, which consists of complex exponential functions that steer the signal in the direction of interest.

The optimization problem in (2.15) can be solved analytically using Lagrange multiplier theory, see e.g. [25]. The cost and the constraint functions are combined into a new function, the Lagrange function, given as

$$\mathcal{L}(\mathbf{w},\nu) = \mathbf{w}^H\mathbf{R}_y\mathbf{w} + \nu(\mathbf{w}^H\mathbf{e} - 1)\,, \tag{2.16}$$

where ν is a scalar value referred to as the Lagrange multiplier. The purpose of ν is to penalize solutions that do not satisfy the constraint. Note that the constraint function has been rearranged as $\mathbf{w}^H\mathbf{e} = 1 \Leftrightarrow \mathbf{w}^H\mathbf{e} - 1 = 0$. Thus, when the constraint is satisfied, the second term in (2.16) will not contribute.

The solution to (2.15) can be found using the first derivatives of (2.16), which can be expressed as

$$\nabla_{\mathbf{w}^H}\mathcal{L}(\mathbf{w}, \nu) = 2\mathbf{R}_y\mathbf{w} + \nu\mathbf{e} = \mathbf{0} \tag{2.17}$$

$$\frac{\partial}{\partial\nu}\mathcal{L}(\mathbf{w}, \nu) = \mathbf{w}^H\mathbf{e} - 1 = 0 \Leftrightarrow \mathbf{w}^H\mathbf{e} = 1\,. \tag{2.18}$$

It is seen that the zero-crossing of the first derivative of $\mathcal{L}(\mathbf{w}, \nu)$ with respect to ν forces the constraint to be satisfied. Solving (2.17) for $\mathbf{w}$ yields

$$\mathbf{w} = -\frac{1}{2}\nu\mathbf{R}_y^{-1}\mathbf{e}\,, \tag{2.19}$$

provided that $\mathbf{R}_y^{-1}$ exists. Using $\mathbf{w}^H\mathbf{e} = 1 \Leftrightarrow \mathbf{e}^H\mathbf{w} = 1$, and multiplying (2.19) by $\mathbf{e}^H$ from the left leads to

$$\mathbf{e}^H\mathbf{w} = -\frac{1}{2}\nu\mathbf{e}^H\mathbf{R}_y^{-1}\mathbf{e} = 1 \Leftrightarrow -\frac{1}{2}\nu = \frac{1}{\mathbf{e}^H\mathbf{R}_y^{-1}\mathbf{e}}\,, \tag{2.20}$$

which inserted into (2.19) yields the closed-form solution to the optimization problem (2.15)

$$\mathbf{w} = \frac{\mathbf{R}_y^{-1}\mathbf{e}}{\mathbf{e}^H\mathbf{R}_y^{-1}\mathbf{e}}\,. \tag{2.21}$$

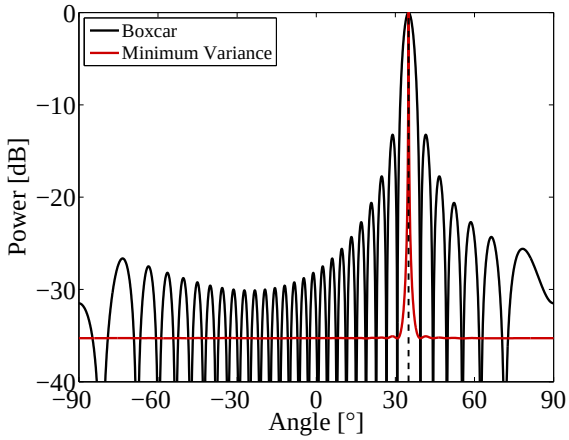

Figure 2.7: Beamformer output for a plane wave incident at $35°$ using Boxcar and Minimum Variance apodization.

An example using a plane wave incident at 35° is shown in Fig. 2.7. The beamformed responses are obtained with Boxcar weights and using the MV beamformer. It is seen that MV provides a significantly reduced main-lobe width and side-lobe level.

2.4.2 Covariance Matrix Estimation

In real applications, the covariance matrix is unknown and must be replaced by the sample covariance matrix, which is estimated from the data. To estimate the sample covariance matrix a number of realizations of data is required. These realizations are obtained by dividing the data from a single acquisition into a number of subgroups. This follows the spatial smoothing approach suggested in e.g. [26].

As illustrated in Fig. 2.8, the spatially smoothed covariance matrix estimate is obtained by dividing the array into P overlapping subarrays of size L. For each subarray, a sub-covariance matrix is estimated, and these are averaged across the array. The covariance matrix estimate can be expressed as

$$\hat{\mathbf{R}}_y = \frac{1}{P} \sum_{p=0}^{P-1} \mathcal{E} \left\{ \mathbf{g}_p \mathbf{g}_p^H \right\} \ , \tag{2.22}$$

where $P = M - L + 1$, and $\mathbf{g}_p$ denotes the pth subarray given by

$$\mathbf{g}_p = \begin{bmatrix} y_p(t) & y_{p+1}(t) & \dots & y_{p+L-1}(t) \end{bmatrix}^T \tag{2.23}$$

for $p = 0, 1, \dots, P-1$. Note that this reduces the dimension of the covariance matrix, and thus the number of weights will be reduced correspondingly. The reduced weight vector, $\widetilde{\mathbf{w}}$, is applied to the data by averaging over the P

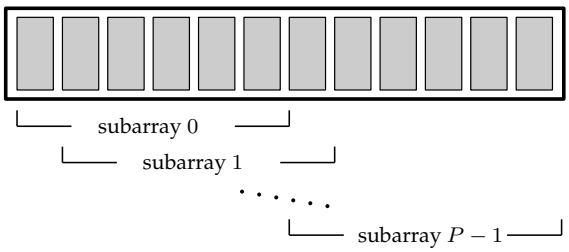

Figure 2.8: Spatial smoothing. The array is divided into P overlapping subarrays, and the covariance matrix is averaged across the array.

subarrays, which is expressed as

$$b(\kappa_x, t) = \tilde{\mathbf{w}}^H \frac{1}{P} \sum_{p=0}^{P-1} \mathbf{g}_p \,. \tag{2.24}$$

Note that the reduced dimension influences the resolution due to the inherent compromise between the width of the array and the achievable resolution [20]. However, the dimension reduction will also reduce the computation load of the matrix inversion in (2.21).

Diagonal Loading

Adaptive beamformers can be sensitive towards imperfections of the measured wave field, such as small errors in the sound speed estimate. A common method to introduce robustness is to use diagonal loading, where a small scalar value is added to the diagonal of the covariance matrix. For more on robust adaptive beamforming methods see e.g. [27]. The diagonal loaded covariance matrix is given as

$$\hat{\mathbf{R}}_\varepsilon = \hat{\mathbf{R}}_y + \varepsilon \mathbf{I} \,, \tag{2.25}$$

where ε is small scalar value, and $\mathbf{I}$ is the $L \times L$ identity matrix. Note that this approach corresponds to adding independent noise on each of the sensor signals.

2.4.3 APES Beamforming

The Amplitude and Phase EStimation (APES) beamformer [24] is based on a optimization formulation equivalent to (2.15) with the closed-form solution (2.21). However, instead of using the sample covariance matrix estimated directly from the measured wave field, the APES covariance matrix is an estimate of the noise covariance matrix.

The APES estimate can be found by replacing the covariance matrix in (2.21) by [24]

$$\hat{\mathbf{Q}} = \hat{\mathbf{R}}_y - \mathcal{E}\left\{\hat{\mathbf{g}}\hat{\mathbf{g}}^H\right\} \,, \tag{2.26}$$

where $\hat{\mathbf{R}}_y$ is the covariance matrix estimate given in (2.22), and $\hat{\mathbf{g}}$ is a vector

averaged in-phase across sub-arrays given by

$$\hat{\mathbf{g}} = \frac{1}{P}\sum_{p=0}^{P-1} \mathbf{g}_p \exp\{jk_x x_p\}\,, \tag{2.27}$$

where $\mathbf{g}_p$ is the pth sub-array vector given in (2.23).

Forward-Backward Averaging

An additional approach to covariance estimation is to use the forward-backward approach [28]. In this context, the estimate in (2.22) is referred to as the forward-only approach. Forward-backward averaging of the covariance matrix can be expressed mathematically as [24]

$$\widetilde{\mathbf{R}}_y = \frac{1}{2}(\hat{\mathbf{R}}_y + \mathbf{J}\hat{\mathbf{R}}_y^T\mathbf{J})\,, \quad \mathbf{J} = \begin{bmatrix} 0 & & 1 \\ & \iddots & \\ 1 & & 0 \end{bmatrix}\,, \tag{2.28}$$

where $\hat{\mathbf{R}}_y$ also can be substituted for $\hat{\mathbf{Q}}$, and $\mathbf{J}$ is the so-called *exchange matrix* with ones along the anti-diagonal. Note that the left and right multiplication of the exchange matrix, $\mathbf{J}$, corresponds to rotating the matrix $\hat{\mathbf{R}}_y^T$ $180°$.

CHAPTER

THREE

Adaptive Beamforming for Ultrasound Imaging

The adaptive beamforming techniques were originally developed for radar imaging systems [20]. Thus, these methods have been developed for narrowband, far-field systems, and they are primarily optimized for discrete point targets. Consequently, when applying adaptive beamformers to ultrasound imaging data, a number of problematic issues arise. The measured ultrasound wave fields are broadband and near-field, and furthermore discrete point targets rarely exist in an ultrasound imaging situation. This chapter will introduce approaches to overcome some of these issues.

3.1 Presteering

Steering the measured wave field at the point of interest will convert the near-field wave into a semi-far-field wave as also described in [29]. The steering is carried out as the delay part of the conventional DAS beamformer. As the steering is carried out prior to the summation and adaptation processes, it will in the following be referred to as *pre*steering.

The concept of presteering is illustrated in Fig. 3.1(a)-(b), which show the responses from three point targets located at $(x, z) = \{(0, 40), (5, 42), (-2, 45)\}$ mm. The responses are simulated for a transducer of $M = 128$ elements using Field II [30, 31]. Fig. 3.1(a) shows the received sensor signals, $s_m(t)$, for $m = 0, 1, \ldots, M-1$. In Fig. 3.1(b), the sensor signals are presteered at the point $\vec{r}_p = (0, 40)$ mm.

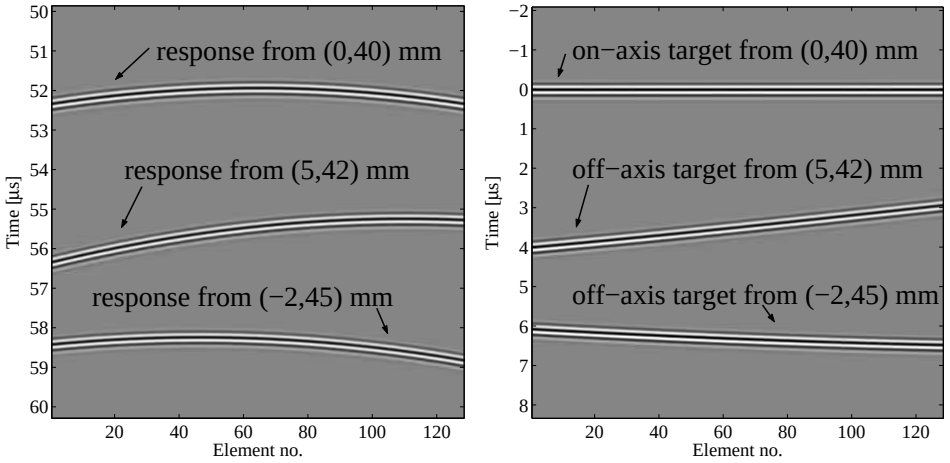

(a) Received signals, $s_m(t)$ (b) Presteered signals, $y_m(t)$

Figure 3.1: (a) The received sensor signals, $s_m(t)$, for $m = 0, 1, \ldots, M-1$. The figure shows the responses from three point targets located at $(x, z) = \{(0, 40), (5, 42), (-2, 45)\}$ mm. (b) Sensor signals presteered at the focus point $\vec{r}_p = (0, 40)$ mm. After presteering, the response from the focus point resembles a plane wave impinging directly onto the array.

Due to the compensation for the delay line across the array, the response from the focus point resembles a plane wave impinging directly onto the array. Thus, the presteered sensor signals will sum in phase, maximizing the DAS beamformer output power at the focus point.

Presteering at the point, $\vec{r}_p = (x_p, z_p)$, is carried out by compensating for the propagation delay profile for this point. The delay is calculated as the propagation path from the transmit element to the focus point and back to the mth receiving element, see illustration in Fig. 3.2. For a transducer array of M elements, the delay is given by

$$\tau_m(\vec{r}_p) = \frac{\|\vec{r}^{\,(Tx)} - \vec{r}_p\| + \|\vec{r}_m^{\,(Rx)} - \vec{r}_p\|}{c} \,, \tag{3.1}$$

for $m = 0, 1, \ldots, M-1$, where c is the speed of sound, and $\vec{r}^{\,(Tx)}$ and $\vec{r}_m^{\,(Rx)}$ are the spatial positions of the transmitting and mth receiving element, respectively.

By compensating for the delay, the mth presteered sensor signal is given by

$$y_m(t) = s_m(t + \tau_m(\vec{r}_p)) \,, \tag{3.2}$$

where $s_m(t)$ is the received waveform on the mth sensor. By definition, the

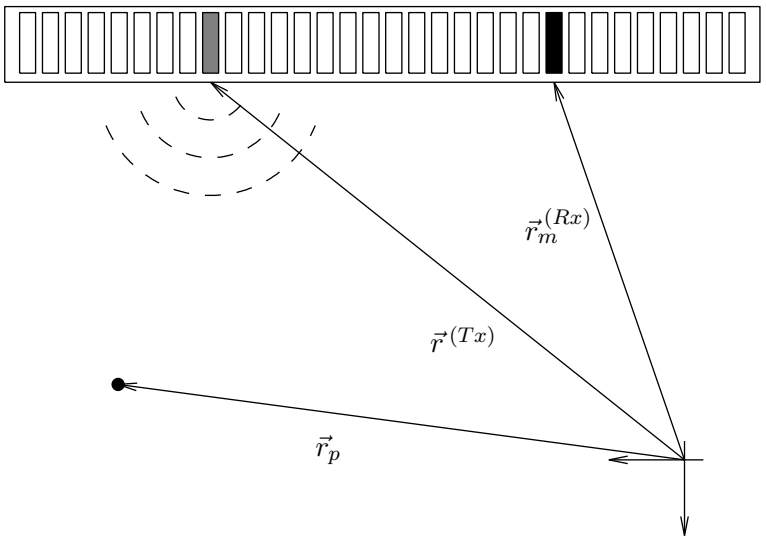

Figure 3.2: Geometry of the propagation path calculation. The figure illustrates the spatial positions of the focus point, $\vec{r}_p$, the transmitting element, $\vec{r}^{(Tx)}$, and the mth receiving element, $\vec{r}_m^{(Rx)}$. From [32].

presteered signals, $y_m(t)$, are dependent on the focus point, $\vec{r}_p$. However, to simplify the notation this dependence is omitted.

In the beamforming process, the presteered sensor signals are weighted and subsequently summed. The amplitude of the beamformer output at $t = 0$, provides the amplitude at the focus point, $\vec{r}_p$, in the resulting beamformed image. Thus, the beamformer output is given by

$$b(\vec{r}_p) = \sum_{m=0}^{M-1} w_m^* y_m(0) = \sum_{m=0}^{M-1} w_m^* s_m(\tau_m(\vec{r}_p)) \,, \tag{3.3}$$

where w_m are the apodization weight on the mth sensor, and $\{\cdot\}^*$ denotes the complex conjugate. Note that the apodization weights can be different for each focus point, but the dependence on $\vec{r}_p$ is here omitted.

3.2 Subband Beamforming

As mentioned previously, adaptive beamforming was originally developed for narrowband applications. However, by dividing the sensor signals into frequency subbands using the short-time, discrete Fourier transform (DFT),

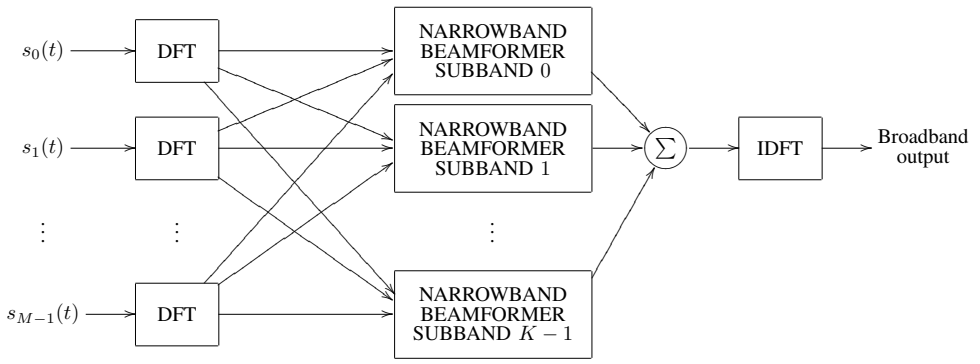

Figure 3.3: Block diagram of a broadband beamformer. Each broadband sensor signal is divided into a set of narrowband signals using the discrete Fourier transform (DFT). Each frequency subband is processed independently by a narrowband beamformer. Subsequently, the processed subband responses are summed to provide the broadband beamformer output.

the adaptive beamformer can be applied to broadband data. This approach was also described in [27].

Each separate subband will satisfy the narrowband condition of the adaptive beamformer. These subbands are processed independently by the beamformer as illustrated in Fig. 3.3. First, the processed subband responses are summed, and then the inverse DFT is used to obtain the beamformed response from the focus point.

For each focus point, the DFT is applied on a segment of the presteered sensor signals. Due to the compensation for the delay line, the response from the focus point will be centered around $t = 0$, as seen in Fig. 3.1(b). The mth segmented, presteered sensor signal is thus given by

$$y_m(t) \text{ for } t \in [-t_d/2; t_d/2] \,, \tag{3.4}$$

where t_d is the time duration of the segment size. To sustain the axial resolution, t_d should not exceed the pulse length, which is given by the convolution of the excitation pulse and the two-way impulse response of the transducer.

For the given focus point, the beamformer output for each frequency subband, ω, is given by

$$B(\omega, \vec{r}_p) = \sum_{m=0}^{M-1} w_m^*(\omega) Y_m(\omega) \,, \tag{3.5}$$

where $Y_m(\omega)$ is the Fourier transform of the mth segmented sensor signal

(3.4). By defining the vectors

$$\mathbf{w}(\omega) = \begin{bmatrix} w_0(\omega) & w_1(\omega) & \cdots & w_{M-1}(\omega) \end{bmatrix}^T \tag{3.6}$$

$$\mathbf{Y}(\omega) = \begin{bmatrix} Y_0(\omega) & Y_1(\omega) & \cdots & Y_{M-1}(\omega) \end{bmatrix}^T , \tag{3.7}$$

the beamformer output (3.5) rewrites into

$$B(\omega, \vec{r}_p) = \mathbf{w}(\omega)^H \mathbf{Y}(\omega) , \tag{3.8}$$

where the superscripts, $\{\cdot\}^T$ and $\{\cdot\}^H$, denote the non-conjugate and the conjugate transpose, respectively. Note that the subband division provides the possibility of weighting both each subband and each point differently.

The subband beamformer output is found by applying the optimized weights to the delayed sensor signals using (3.8). This yields an adaptively weighted spectrum, and the amplitude corresponding to the focus point is found from the inverse Fourier transform of this spectrum and choosing the sample at $t = 0$.

It should be noted that e.g. Synnevåg *et al.* [8] have shown that a direct temporal implementation is also possible. A comparison of the subband and temporal implementation approaches is found in Sec. 4.3.

3.3 Ultrasound Imaging Sequences

Ultrasound imaging can be carried out using very different imaging sequences. The results in Chap. 4 are obtained using three different imaging sequences; a linear array scan, a plane wave emission and a synthetic aperture approach. In the following these three approaches will be introduced.

Linear Array Imaging

A linear array scan, Fig. 3.4(a), is carried out using a linear array transducer, where a small part of the aperture is used for transmitting a narrow beam with a transmitting focus point. In this way, a single line, from the aperture through the focus point, is obtained. Sliding the active part of the aperture across the array, an image consisting of several lines can be created.

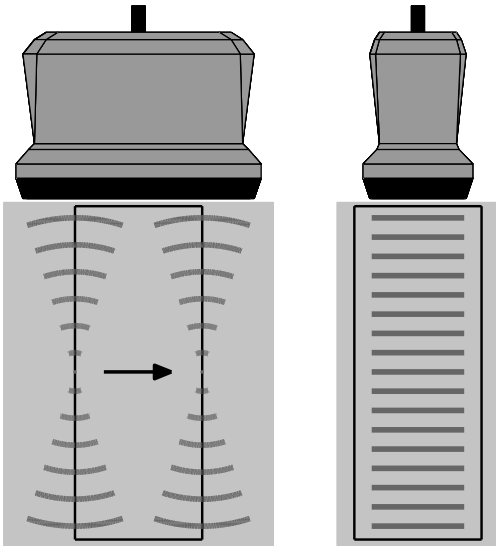

(a) Linear Scan (b) Plane Wave

Figure 3.4: Illustration of scan sequences, the transducer is shown in the top and the image region is indicated by the black lines. (a) A linear scan is carried out by transmitting several focused beams, while sliding the active part of the aperture along the scan plane. (b) Using a plane wave transmission the entire image region is obtained from a single transmission.

Conventionally, these linear array scans are subsequently beamformed with dynamic apodization, where the f-number is kept constant. This will provide images with point spread functions that are rather spatially invariant throughout the depth.

Plane Wave Imaging

A plane wave (PW) emission can be achieved by using all elements as both the transmitting and receiving aperture. In this way, the entire image region can be covered in a single emission, as shown in Fig. 3.4(b).

Note that when using PW, the propagation path from the transmitting element, $\vec{r}^{(Tx)}$, to the current image point, $\vec{r}_p = (x_p, z_p)$, in (3.1) simply becomes the axial distance, z_p, from the array to the image point

$$\|\vec{r}^{(Tx)} - \vec{r}_p\| = z_p \, . \tag{3.9}$$

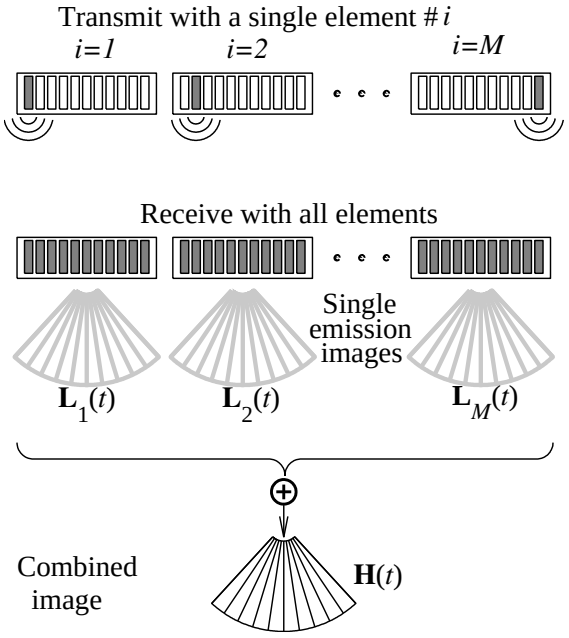

Figure 3.5: Concept of synthetic aperture imaging. A number of images are created from a single emission. These single emission images are averaged to obtain an image with a higher resolution and contrast. From [35].

Synthetic Aperture Imaging

Synthetic aperture (SA) imaging was originally developed for radar imaging [33], where images from several antennas are combined to produce images with a higher resolution. The same principle has been introduced to ultrasound imaging, see e.g. [34].

Fig. 3.5 illustrates the concept of SA imaging. A single transducer element is active, emitting a spherical wave in all directions, covering the entire image region. The active element is then moved along the array, while all elements are used for receiving the backscattered echoes. For each single emission a so-called low-resolution image is created. And by combining these single emission images, an image of high resolution can be obtained.

An emission sequence using only a single transmitting element is not always desirable, as the amount of emitted energy is relatively small. Thus, virtual sources are introduced. As illustrated in Fig. 3.6, a virtual source is placed at a spatial position behind the aperture. A collection of array elements are used for the transmission. Using the proper delay curve, the emitted spherical will

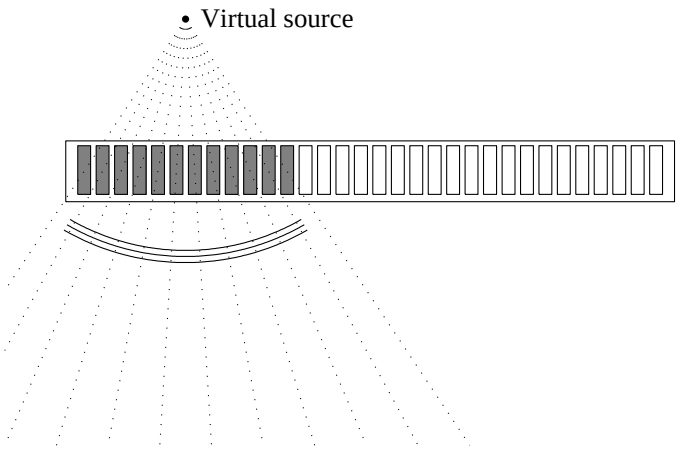

Figure 3.6: Virtual source positioned behind the transducer. A collection of array elements are used for the transmission. Using the proper delay curve, the emitted spherical will seem as if it originated from the spatial position of the virtual source. From [32].

seem as if it originated from the spatial position of the virtual source. This provides an increased amount of emitted energy into the object of interest compared to the single transmitting element approach.

CHAPTER

FOUR

Application to Ultrasound Imaging

This chapter demonstrates the application of adaptive beamforming to ultrasound imaging data. The results in this chapter are segments of the results from the investigations published in Paper I-VII [13–19]. Furthermore, a selection of results from an additional relevant, yet unpublished, investigation is included as well.

4.1 Synthetic Aperture Ultrasound Imaging

The results in this section is a segment of the results that are published as part of Paper I [14] and in Paper II [13]. The purpose of this work is to demonstrate the performance of the MV beamformer on simulated synthetic aperture (SA) ultrasound data.

The data was simulated with Field II [30, 31] using a 7 MHz phased array transducer with $\lambda/2$-spacing and 128 elements. Data is obtained using a single element as the transmitting aperture and all elements as the receiving aperture. A full SA sequence consisting of 128 emissions was simulated by sliding the active transmitting element across the array. Data for 13 point targets and a circular cyst with a radius of 5 mm were simulated.

The MV beamformer is implemented in the frequency domain using the short-time Fourier transform with a segment size corresponding to the length of the excitation pulse convolved with the two-way impulse response of the transducer. A subarray size of $L = \frac{M}{4} = 32$ was used.

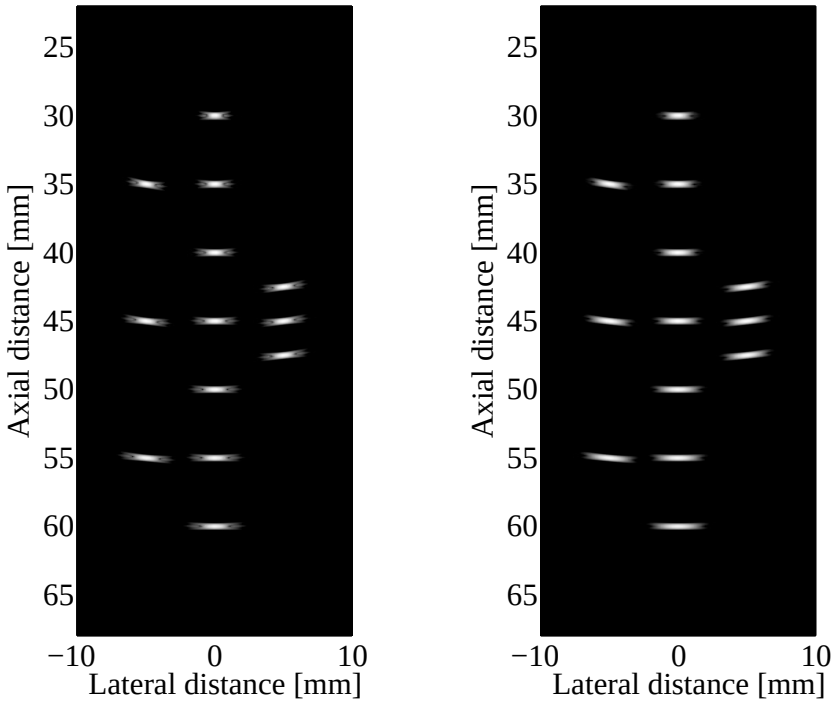

(a) DAS Boxcar (b) DAS Hanning

The performance of MV is compared to DAS using Boxcar and Hanning weights. The performance is quantified by the Full Width at Half Maximum (FWHM) and the peak-side-lobe level (PSL), which is defined as the peak value of the first side-lobe. These values are not included in this section, but can be found in Paper I-II, where it is seen that the FWHM of MV from a single emission response comprise only $\{12.7\%, 8.2\%\}$ of the FWHM from the full DAS sequence using DAS{Boxcar,Hanning}.

The beamformed responses of 13 point targets are shown in Fig. 4.1(a)-(d) with a dynamic range of 50 dB. Fig. 4.1(a)-(b) show the DAS beamformer responses using Boxcar and Hanning apodization weights, respectively. The three responses in Fig. 4.1(a)-(c) are combined images from a full SA sequence. Thus, these have been averaged over 128 emissions. The MV response on the right, Fig. 4.1(d), is the response from a single emission, where a single element (element #64) was used as the transmitting aperture.

The lateral variation of the beamformed responses, Fig. 4.1(a)-(d), are shown in Fig. 4.2(a)-(b) at depths of 40 mm and 45 mm. As expected, it is seen that applying Hanning apodization weights to the DAS beamformer, reduces the side-lobe level at the expense of a lateral broadening of the main-lobe,

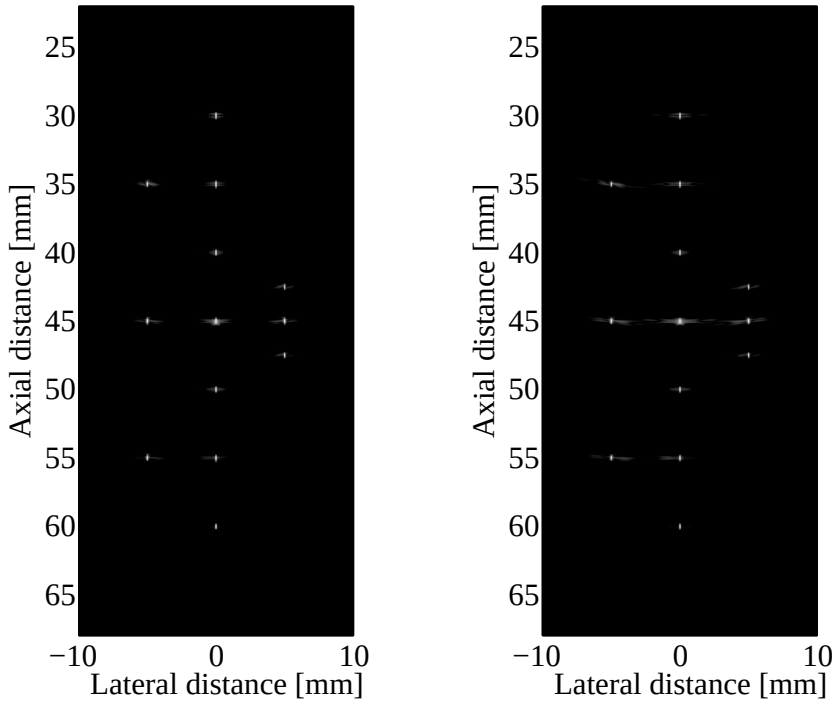

(c) MV (d) MV, single emission

Figure 4.1: Beamformed responses of the 13 point targets using simulated synthetic aperture data. (a)-(c) The images are averaged over 128 emissions from different spatial positions. (a) DAS using Boxcar weights; (b) DAS using Hanning weights; and (c) MV response combined from 128 emissions. (d) MV response from a single element emission (element #64). All images are shown with a dynamic range of 50 dB.

compared to DAS using Boxcar weights.

The MV response does not change significantly in the interval of $[-40; 0]$ dB. The FWHM is calculated at a level of -6 dB and will not change for MV, when averaging over all 128 emissions. This is shown in Fig. 4.3(a), where the FWHM for DAS and MV are shown with respect to the number of emissions.

Furthermore, the ratio of energy above and below -40 dB has been calculated and shown relative to the number of emissions in Fig. 4.3(b). This ratio is a measure of the relative energy within the main-lobe. As it reduces, the relative energy within the main-lobe reduces, which could mean that the width of the main-lobe decreases. It is seen that this ratio reduces with the number of emissions. However, the reduction for MV is not as immense as for DAS. Thus, the MV response does not improve significantly, when averaging over

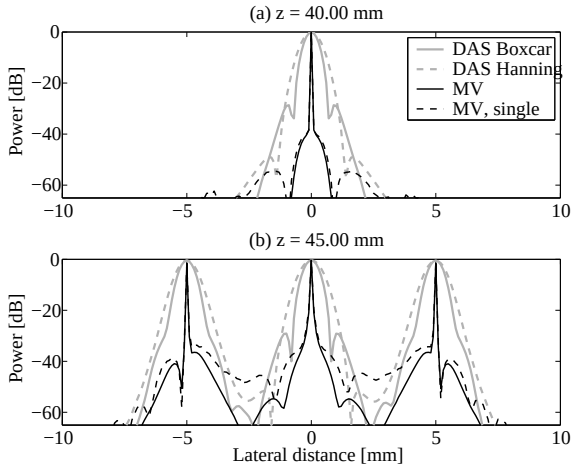

Figure 4.2: Lateral variation at depths of 40 mm and 45 mm of the beamformed responses shown in Fig. 4.1(a)-(d).

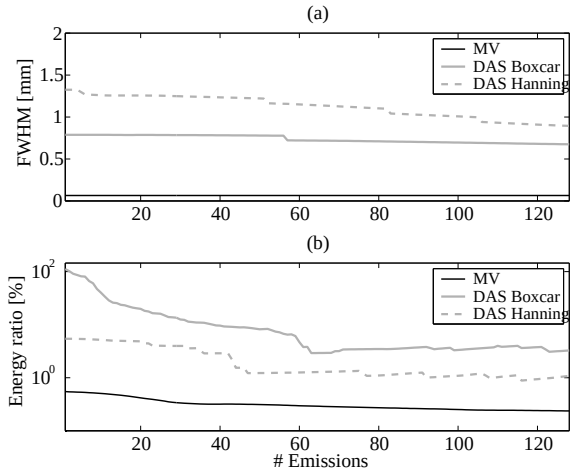

Figure 4.3: Full Width at Half Maximum (FWHM) and the energy ratio above and below -40 dB of the beamformed responses with respect to the number of emissions.

several emissions.

In Fig. 4.4(a)-(c), the beamformed responses for a simulation of a cyst in speckle are shown. The circular cyst has a radius of 5 mm and center at $(0, 40)$ mm. These images show the beamformed responses from a single emission, corresponding to element #64.

These single emission images emphasize the differences between the three beamforming approaches. It is seen that the high side-lobe level of the DAS

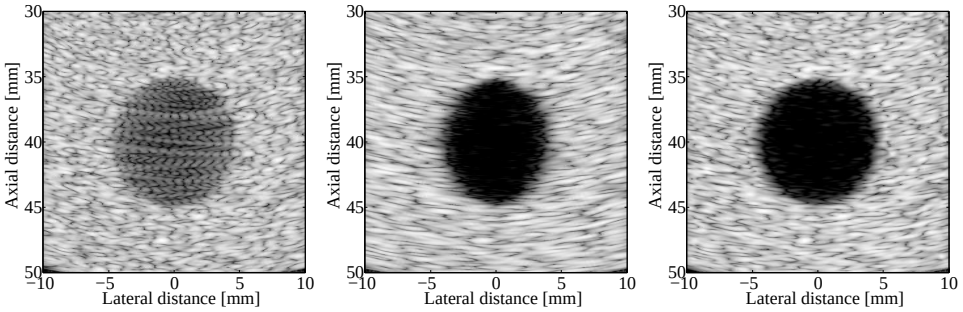

(a) DAS Boxcar (b) DAS Hanning (c) MV

Figure 4.4: Circular cyst with radius of 5 mm and center at $(0, 40)$ mm. (a) DAS using Boxcar weights; (b) DAS using Hanning weights; and (f) MV. The images are the responses to a single element emission (element #64). All images are shown with a dynamic range of 50 dB.

Boxcar apodization results in a rather poor contrast. Furthermore, it is seen that the DAS response using Hanning apodization does not result in a circular shape of the cyst. The shape is rather oval due to the lateral broadening from the Hanning apodization. However, the Hanning apodization does provide a suitable contrast level, as the side-lobes are lowered significantly.

The MV response from a single emission, Fig. 4.4(c), shows a circular shape of the cyst as well as a suitable contrast difference between the inner part of the cyst and the speckle pattern. From this investigation, it is seen that the MV beamformer provides a lowering of the side-lobe level without smoothing the responses laterally.

It should be noted that the beamformed responses for the full SA sequence of the circular cyst can be found in Paper I. In the combined images, these effects have been averaged out. Thus, the side-lobe level has reduced for the DAS Boxcar response, and the circular shape of the cyst has been recovered for DAS Hanning response.

4.2 Plane Wave Ultrasound Imaging

In the previous section, it was shown that the MV beamformer provides a significantly reduced main-lobe width compared to the DAS beamformer. A reduced main-lobe width was observed using only a single unfocused emission. This idea has been investigated further by using a plane wave emission in stead of a unfocused emission from a single element. The results in this

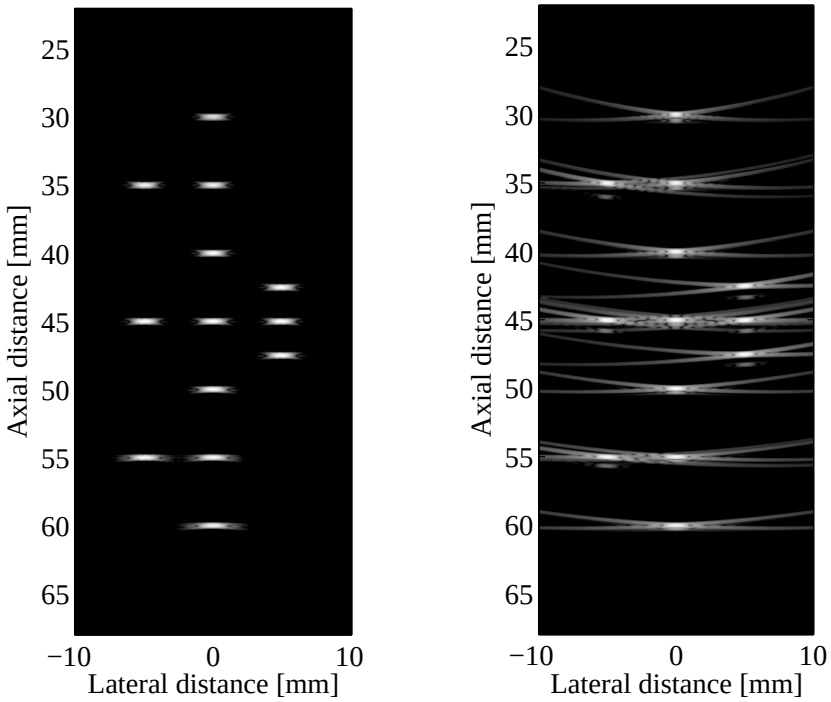

(a) Linear Scan (b) DAS Boxcar

section has been published in Paper III [15] and as a part of Paper I [14].

A plane wave (PW) emission can be achieved by using all elements as both the transmitting and receiving aperture. In this way, the entire image region can be covered in a single emission, as illustrated in Fig. 3.4(b).

The MV beamformed response is compared to DAS using Boxcar and Hanning weights. The beamformed DAS responses for the 13 point targets are seen in Fig. 4.5(b)-(c), and the MV response is seen in Fig. 4.5(d).

Furthermore, the PW emission responses are compared to a conventional linear scan response. The linear scan image in Fig. 4.5(a) is obtained with a sliding aperture size of 128 elements and a fixed transmit focus at a depth of 45 mm. The response is beamformed using DAS and dynamic Hanning apodization with $f/2$. The lateral variation of the beamformed responses, Fig. 4.5(a)-(d), are shown in Fig. 4.6(a)-(b) at depths of 40 mm and 45 mm.

The PW data is obtained with Boxcar apodization both in transmit and receive. This provides unwanted side-lobes below the point targets, as seen in Fig. 4.5(b)-(c). These could have been removed by using a transmit apodiza-

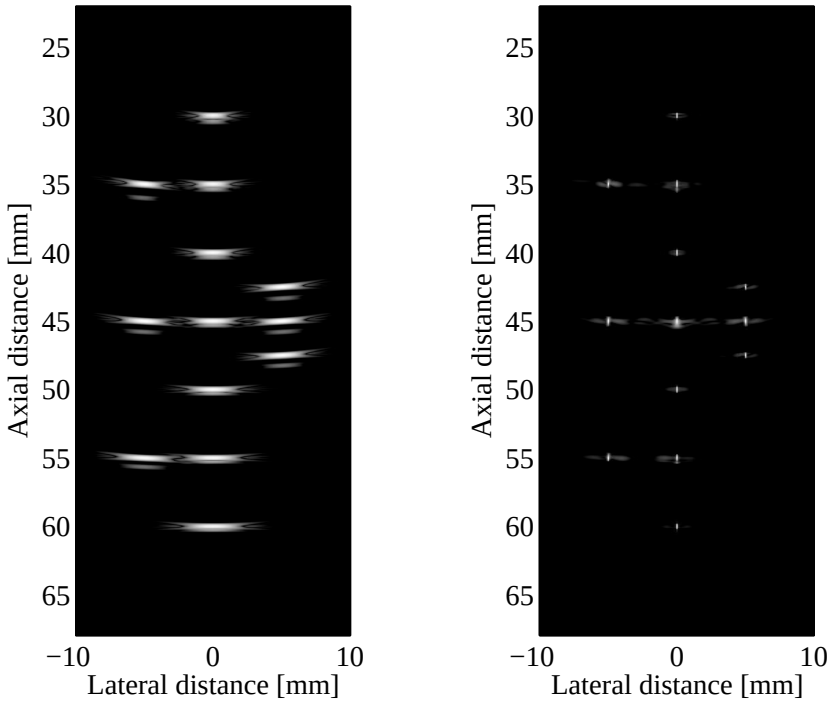

(c) DAS Hanning (d) MV

Figure 4.5: Beamformed responses of the 13 point targets. (a) Linear scan, DAS with dynamic apodization using Hanning weights. (b) Plane wave transmission, DAS using Boxcar weights. (c) Plane wave transmission, DAS using Hanning weights. (d) Plane wave transmission, MV. All images are shown with a dynamic range of 50 dB.

tion, such as a Tukey window with 70% tapering as in [36]. However, this has not been done, to demonstrate that the MV beamformer successfully eliminates these, as seen in Fig. 4.5(d).

Due to the focused emissions and the dynamic Hanning apodization, the linear scan sequence provides a more homogeneous image than the unfocused PW transmissions. The resolution and contrast of the PW data are degraded and the DAS beamformed images are not acceptable for ultrasound imaging.

However, the MV beamformer provides an increase of the resolution and contrast, as seen in Fig. 4.5(d) and Fig. 4.6(a)-(b). Even compared to the linear scan image, the MV beamformer provides a significant reduction of the FWHM and PSL. From this investigation, it is seen that the increase of resolution and contrast, provided by the MV beamformer, yields the possibility of high resolution and high contrast PW imaging, where an image region can be covered in a single emission.

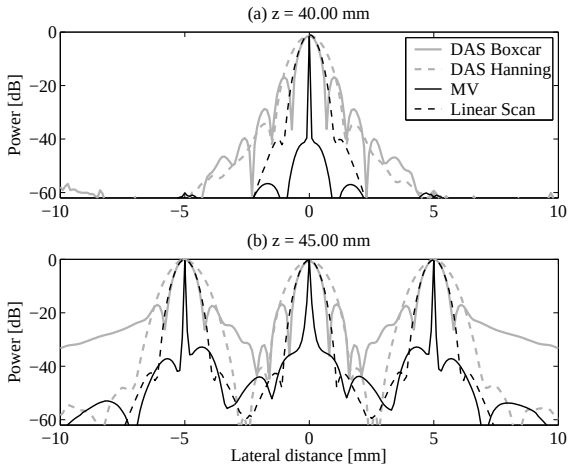

Figure 4.6: Lateral variation at depths of 40 mm and 45 mm of the beamformed responses shown in Fig. 4.5(a)-(d).

4.3 Subband and Temporal Implementation Comparison

The previous sections have shown the performance of the MV beamformer implemented in the frequency domain. This section demonstrates the difference between a direct temporal implementation and a subband implementation.

The two MV beamforming approaches are tested on simulated SA data, obtained using Field II [30, 31]. For the simulations, a 7 MHz, 128-element, linear array transducer with $\lambda/2$-spacing was used. A single element is used as the transmitting aperture and all 128 elements as the receiving aperture. The transmitting element is slid across the array, and for each single emission an image is created.

The subband MV beamformer is implemented in the frequency domain using the short time Fourier transform with a segment size corresponding to the length of the excitation pulse convolved with the two-way impulse response of the transducer. For both approaches, a subarray size of $L = \frac{M}{4} = 32$ was used. Before beamforming, additional white, zero-mean, Gaussian distributed noise with a signal-to-noise ratio (SNR) of 60 dB was added to each of the sensor signals. The performance of MV is compared to DAS using Boxcar and Hanning weights. The performance is quantified by the Full Width at Half Maximum (FWHM) and the peak-side-lobe level (PSL), which is defined as the peak value of the first side-lobe.

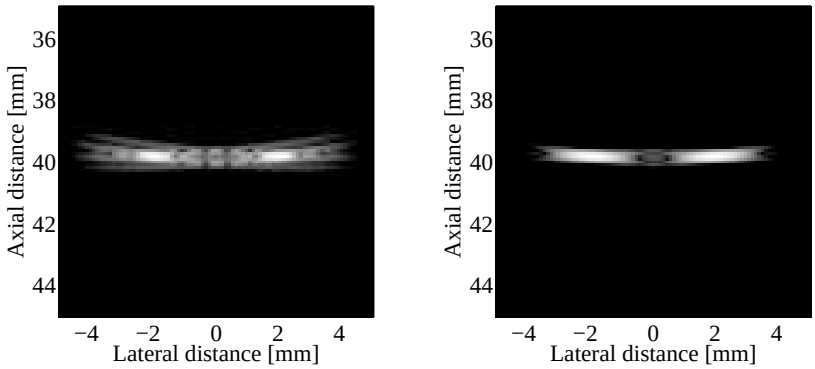

(a) DAS Boxcar

(b) DAS Hanning

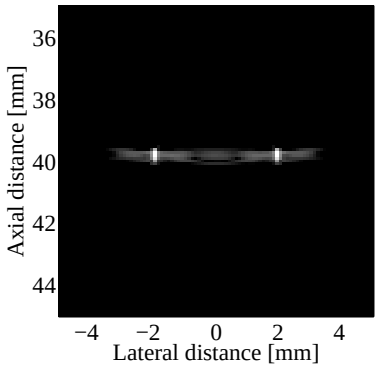

(c) MV, subband

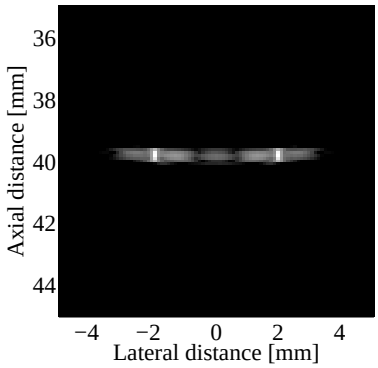

(d) MV, temporal

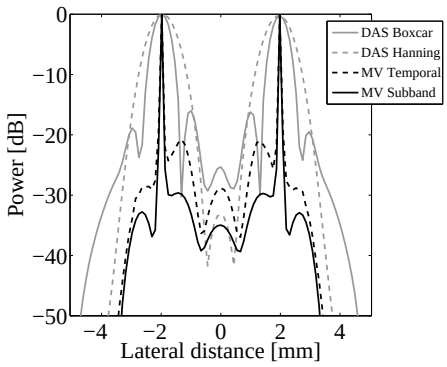

(e) Lateral variation at 40 mm

Figure 4.7: Beamformed responses for two point targets at $(\pm 2, 40)$ mm. The images are shown with a dynamic range of 50 dB. (a) DAS using Boxcar weights. (b) DAS using Hanning weights. (c) MV using subband implementation. (d) MV using temporal implementation. (e) Lateral variation of the four beamformed responses at a depth of 40 mm.

The beamformed responses of 2 point targets are shown in Fig. 4.7(a)-(d) with a dynamic range of 50 dB. Fig. 4.7(a)-(b) show the DAS beamformer responses using Boxcar and Hanning apodization weights, respectively. The two MV approaches are shown in Fig. 4.7(c)-(d). All images in Fig. 4.7 show the beamformed responses from a single emission, where a single element (element #64) was used as the transmitting aperture. The lateral variation of the beamformed responses, Fig. 4.7(a)-(d), are shown in Fig. 4.7(e) at a depth of 40 mm.

The four beamformers {DAS Boxcar, DAS Hanning, subband MV (using 12 subbands), temporal MV} provide FWHM of $\{0.81, 1.34, 0.03, 0.04\}$ mm and PSL of $\{-16, -34, -51, -43\}$ dB. The two approaches both provide a significant decrease of FWHM compared to DAS. No significant difference between the obtained FWHM of the two approaches is observed. The subband MV provide a reduction of PSL of 10 dB compared to the temporal MV. However, the reduced PSL comes at the expense of an increased processing time.

4.4 Adaptive Receive and Transmit Apodization

Previously, the adaptive beamformers have been applied on the receiving aperture, only. In this section, a method for applying adaptive beamforming on both the transmitting and receiving apertures is suggested. The results in this section has been published in Paper IV [19].

The suggested method is based on an SA framework, see Sec. 3.3 or [34]. The principle of the method is illustrated in Fig. 4.8. The method consists of two parts. First, adapted apodization weights are applied to the received data, one weight for each receive channel. This provides a set of adaptively weighted low-resolution images; one image for each emission. Subsequently, the chosen transmitting apodization weights are applied across these single emission images to form the combined SA image. This first part has previously been demonstrated in Paper I [14], where only data-independent apodization weights have been applied on the transmitting aperture.

The second part of the suggested method is to introduce data-dependent, adapted apodization weights on the transmitting aperture. In this way, the number of adapted weights and thereby the number of degrees of freedom are increased by a factor proportional to the number of SA emissions. Thus, the achievable resolution is assumed to increase significantly compared to both the data-independent transmitting apodization method and the conventional DAS method.

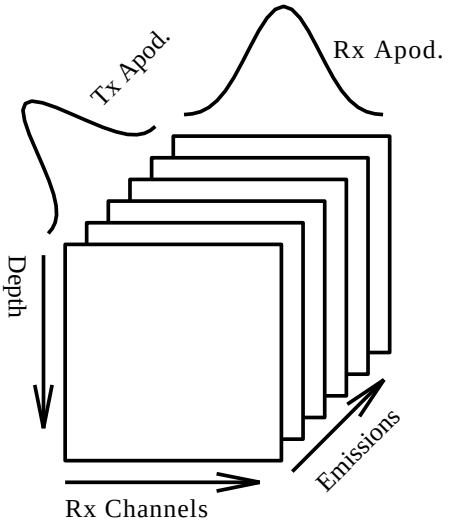

Figure 4.8: Using a synthetic aperture (SA) imaging sequence a number of emissions are acquired. For each emission a data set is obtained, from each of these a single emission image created using a beamformer with the receiving (Rx) apodization function. Weighting these images with the chosen transmitting (Tx) apodization function provides the combined SA image.

The covariance matrix for the receive apodization is estimated from the sensor signals, $\mathbf{y}_i$. For the ith low-resolution image, the covariance matrix estimate is found as

$$\hat{\mathbf{R}}_{Rx} = \mathcal{E}\left\{\mathbf{y}_i \mathbf{y}_i^H\right\} \ , \tag{4.1}$$

where $\mathcal{E}\{\cdot\}$ denotes the expectation value. For the transmit apodization, the adaptively weighted low-resolution images, $\boldsymbol{\ell}$, are used to estimate the covariance matrix as

$$\hat{\mathbf{R}}_{Tx} = \mathcal{E}\left\{\boldsymbol{\ell}\boldsymbol{\ell}^H\right\} \ . \tag{4.2}$$

Note that $\hat{\mathbf{R}}_{Rx}$ and $\hat{\mathbf{R}}_{Tx}$ are both dependent on the image point, $\vec{r}_p$, however this dependency has been omitted to simplify notation.

Using Field II [30, 31], simulated SA data of 13 point targets has been obtained. The points are distributed at depths ranging from 40 mm to 70 mm. For the simulations, a 5.5 MHz, 64-element linear array transducer with 300 μm pitch is used. The SA sequence consisting of 64 emissions is obtained using virtual sources with 11 active elements. For the MV beamforming, diagonal loading and a subarray size of $L = 32$ are used both on the receiving and the transmitting apertures.

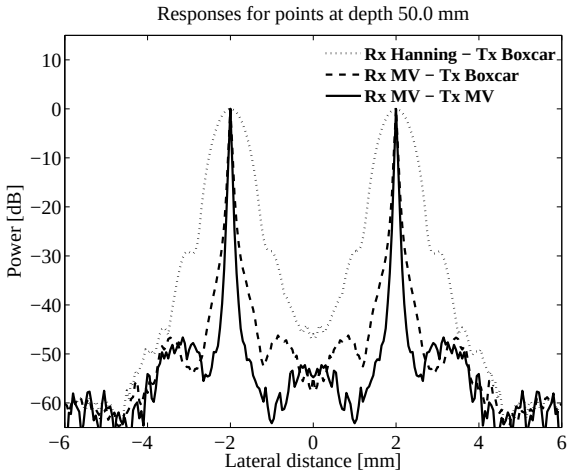

Figure 4.9: Lateral variation of the beamformed responses in Fig. 4.10(a)-(c) along two points at a depth of 50 mm.

The proposed method (Rx MV – Tx MV) is compared to two methods using data-independent apodization weighted on the transmitting aperture. These two methods are DAS using dynamic Hanning apodization weights with $f/2.5$ on the receiving aperture and Boxcar weights on the transmitting aperture (Rx Hanning – Tx Boxcar), and MV on the receiving aperture and Boxcar weights on the transmitting aperture (Rx MV – Tx Boxcar).

The lateral variation of the three beamformed responses along two points placed laterally at a depth of 50 mm are shown in Fig. 4.9. It is seen that the MV beamformer provides significantly reduced main-lobe width compared to the conventional DAS beamformer. This has previously been demonstrated in Paper I [14].

Note that in Paper I [14], the MV beamformer was implemented in the frequency domain. That provided an increased number of degrees of freedom compared to the implementation in the time domain, which is used in this paper.

Furthermore, it is seen that the introduction of the data-dependent apodization weights on the transmitting aperture provides a reduction of the main-lobe width compared to these two methods.

For these two point targets placed laterally at a depth of 50 mm, the three methods provide main-lobe widths (at -30 dB) of $\{2.20, 0.47, 0.26\}$ mm. Thus, the introduction of adaptive transmit apodization provides a reduction

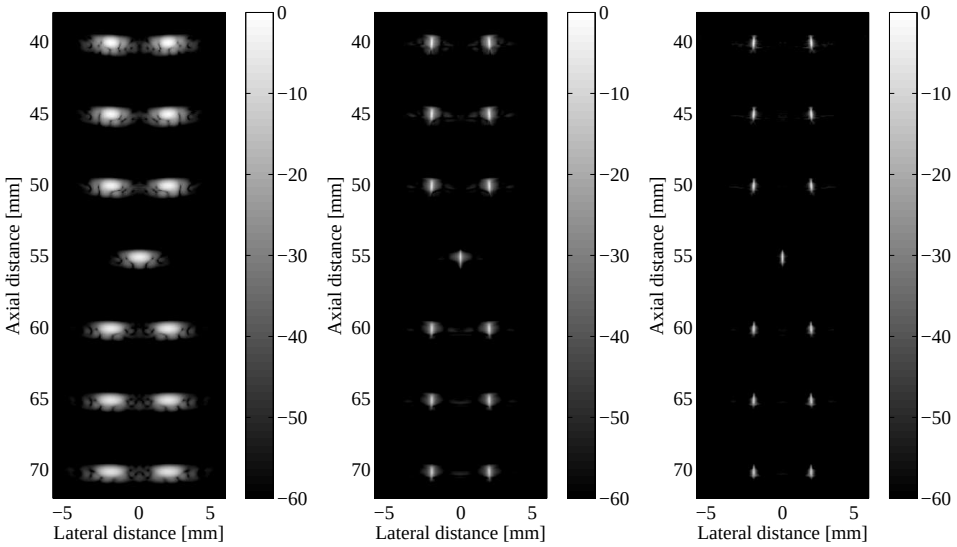

(a) Rx Hanning – Tx Boxcar (b) Rx MV – Tx Boxcar (c) Rx MV – Tx MV

Figure 4.10: Beamformed responses for 13 discrete point targets. (a) Hanning apodization on the receiving and Boxcar on the transmitting aperture. (b) MV apodization on the receiving and Boxcar on the transmitting aperture. (c) MV apodization on both the receiving and transmitting apertures.

of the main-lobe width (at -30 dB) by a factor of 1.8.

The three beamformed responses of the 13 point targets are shown in Fig. 4.10(a)-(c). It is seen that the main-lobe width has reduced significantly for the two adaptively beamformed responses in Fig. 4.10(b)-(c) compared to the data-independent DAS beamformed response in Fig. 4.10(a).

Furthermore, it is observed that the adaptively beamformed response using adaptive apodization weights on both the receiving and the transmitting apertures in Fig. 4.10(c) provides a reduced main-lobe width. These observations are in consistency with Fig. 4.9 and with the fact that the number of degrees of freedom has increased significantly with the introduction of the data-dependent apodization weights on the transmitting aperture.

4.5 Considerations on the Size of the Transducer Footprint

Due to near-field properties, the energy of the ultrasound data reduces towards the edges of the transducer. In this section, the influence of this near-

field effect is demonstrated, and a method to reduce this influence is proposed. The results in this section has been published in Paper V [16].

By reducing the number of active sensor elements, an increased resolution can be obtained with the MV beamformer. This observation is directly opposite the well-known relation between the spatial extent of the aperture and the achievable resolution. The investigations are based on Field II [30, 31] simulated data using a 128-element transducer with a large spatial extent.

The results show that an increased resolution can be obtained, when using only the central part of the transducer compared to using the entire spatial extent. Using the central 32 or 48 elements provides an increased resolution compared to using all 128 elements.

Different number of active elements are used; corresponding to $\{128, 64, 48, 32\}$ elements. This means that the spatial extent of the aperture has been reduced virtually down to 75% of the full size.

The beamformed responses in this section corresponds to a single SA emission, and data are obtained using Field II [30, 31] for two point targets positioned at $(2, 50)$ mm and $(-2, 50)$ mm. For the simulations, a 128-element, 5.5 MHz linear array transducer with 0.3 μm pitch is used. Data is obtained using an SA approach with a virtual source, where 11 elements are used as the transmitting aperture and all elements are used as the receiving aperture.

The MV beamformer is implemented in the frequency domain using the short-time Fourier transform with a segment size corresponding to the length of the excitation pulse convolved with the two-way impulse response of the transducer. And a subarray size of $L = 16$ is used for all calculations.

As indicated in (2.15) and (2.21), the definition of the signal of interest is of great influence on the MV beamformer output. This signal of interest characterizes the signal emerging from the focus point, which will resemble a plane wave, where all sensor signals are in phase, impinging directly onto the array. Thus, standard procedure is to denote the presteered signal of interest by a vector of ones, which indicates a constant phase and constant amplitude across the array.

However, in near-field situations, the amplitude is not necessarily constant across the array. Fig. 4.11(a)-(b) show the received sensor signals for a point positioned at $(0, 50)$ mm using two 128-element transducers with different spatial extents; a transducer with (a) 0.15 μm pitch and (b) 0.3 μm pitch. For the small transducer, the plane wave resemblance nearly holds. However,

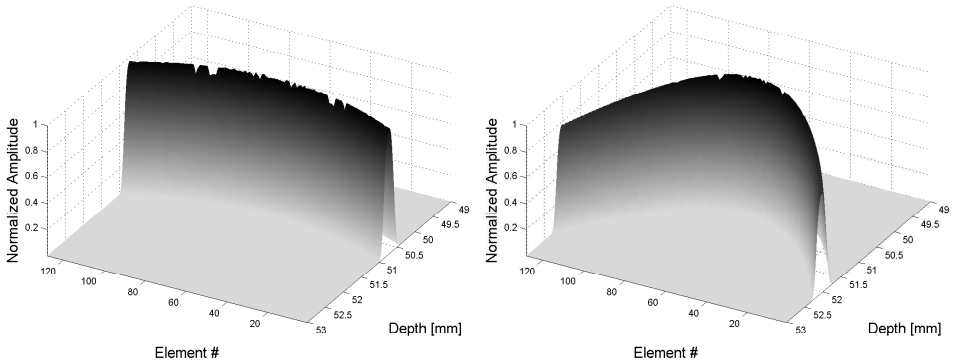

(a) 128 elements, 0.15 μm pitch

(b) 128 elements, 0.3 μm pitch

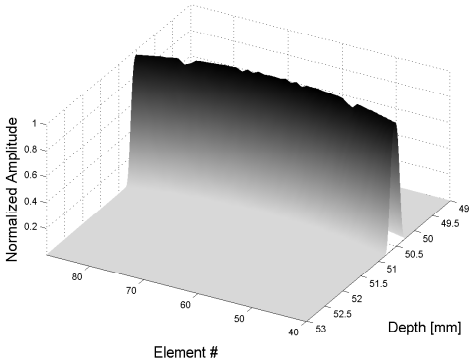

(c) 48 elements, 0.3 μm pitch

Figure 4.11: Received sensor signals for a point positioned at $(0, 50)$ mm using two different transducers with (a) 128 elements, 0.15 μm pitch, and (b) 128 elements, 0.3 μm pitch. (c) The transducer is identical to the one used in (b). However only the center 48 elements are displayed.

for the large transducer, the amplitude drops significantly towards the edges of the transducer; and the constant amplitude plane wave assumption does not hold. Thus, the signal emerging from the focus point will not be passed without distortion as intended. And as seen in the following, the amplitude difference across the array influences the achievable resolution.

There are several approaches to reduce the influence of the amplitude drop; e.g. changing the analytical expression of the signal of interest, normalizing the amplitudes across the array or virtually reducing the spatial extent of the transducer by reducing the number of active elements. Instead of using all 128 elements, we will only use e.g. the central 48 elements, as shown in Fig. 4.11(c). The transducer parameters used to create Fig. 4.11(b)-(c) are ex-

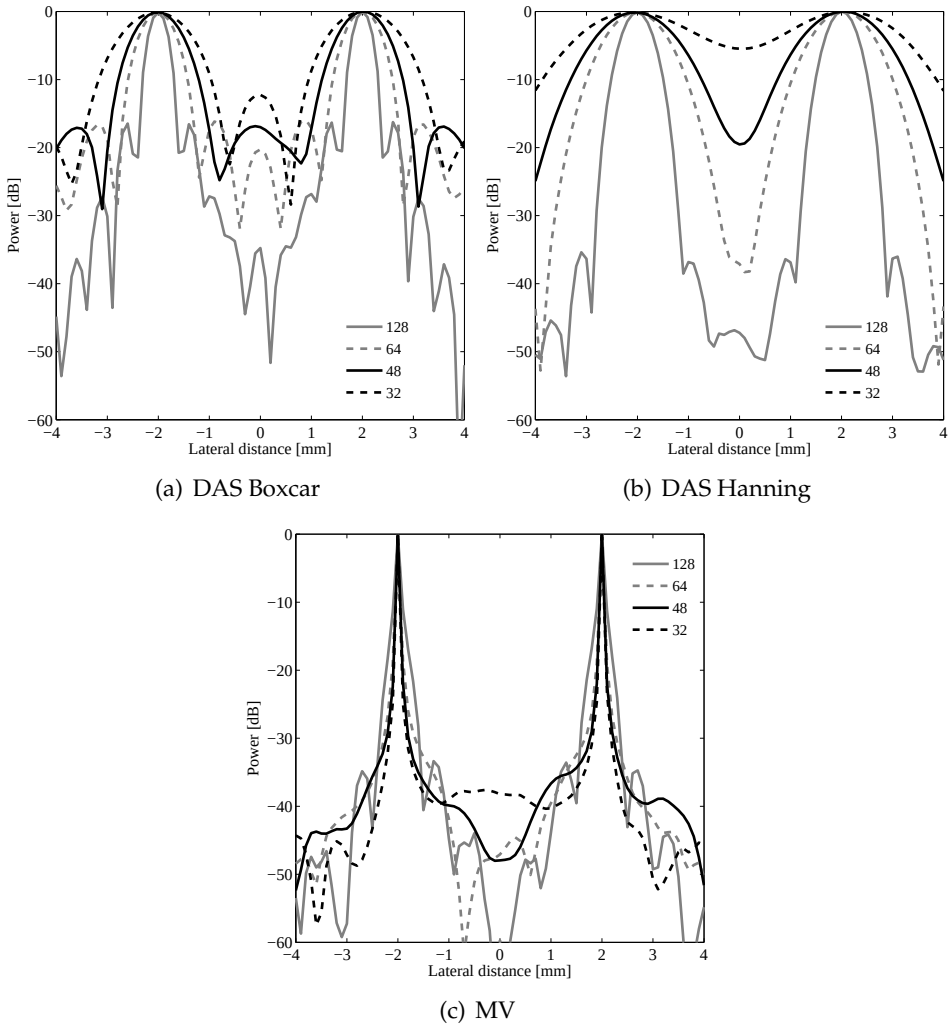

(a) DAS Boxcar

(b) DAS Hanning

(c) MV

Figure 4.12: Beamformed responses for two points positioned at $(-2, 50)$ mm and $(2, 50)$ mm using different numbers of active elements, $\{128, 64, 48, 32\}$. (a) DAS with Boxcar apodization. (b) DAS with Hanning apodization. (c) MV response.

actly identical; the only difference is the number of elements used to display the sensor signals. It is seen that the amplitude difference across the array has decreased significantly, and the plane wave assumption now holds.

Fig. 4.12(a) shows the DAS beamformed responses with Boxcar weights. As expected the responses using the highest number of elements provide the highest resolution and contrast; in terms of narrow main-lobe and low side-lobes. And obviously, the DAS beamformed responses with Hanning

weights, Fig. 4.12(b), show exactly the same.

The MV beamformed responses are shown in Fig. 4.12(c). It is seen that the MV beamformer provides an increased resolution compared to the responses in Fig. 4.12(a)-(b). Furthermore, it is seen that the highest resolution is not obtained using the largest number of active elements. It is seen that the broadest main-lobe is obtained using 128 elements; and the fewer active elements, the more narrow the main-lobe becomes.

Obviously, the number of active elements has a lower bound, and an inherent compromise between the number of active elements and the achievable resolution and contrast exists. The optimum compromise is dependent on the f-number, the transducer parameters, and the size of the subarray for the covariance matrix estimation. The purpose of this paper is to illustrate this rather peculiar observation, which is strictly contradicting both the expectation and is directly opposite the observation of the DAS beamformer in Fig. 4.12(a)-(b).

4.6 Influence of Sound Speed Errors

The adaptive beamformers are sensitive towards imperfections of the measured wave field, such as incorrect sensor positions and incorrect estimates of the sound speed. In this section, an investigation is carried out of the sensitivity of the MV and APES beamformers to errors in the sound speed. The results in this section has been published in Paper VI [17].

The sound speed estimate is changed percentage-wise from the true value (1540 m/s) by 2%, 4%, and 6%, which correspond to velocities of $\{1571, 1602, 1632\}$ m/s. The adaptive beamformers with the three covariance matrix estimation approaches are compared to the DAS beamformer using Boxcar and Hanning weights. The lateral variation of the beamformed responses of a single point target are seen in Fig. 4.13. Furthermore, a selection of the MV and APES beamformed responses can be found in Paper VI.

At the top in Fig. 4.13(a)-(c), the beamformed responses for the correct sound speed are shown. The inherent compromise between main-lobe width and side-lobe level is evident from these figures; the Hanning weights lower the side-lobe level at the expense of a broader main-lobe compared to the Boxcar weights.

It is seen that the MV and APES beamformers provide a significant increase

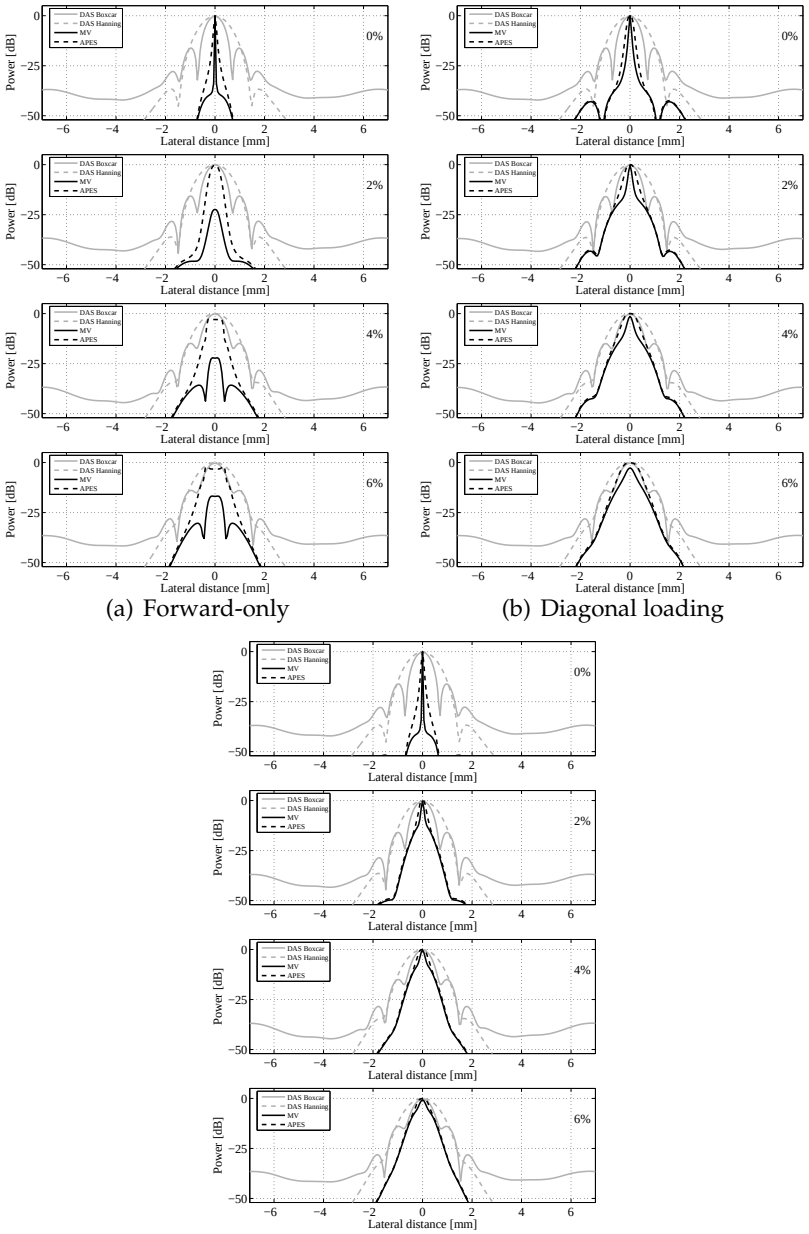

(a) Forward-only (b) Diagonal loading

(c) Forward-Backward

Figure 4.13: Lateral variation of the beamformed responses at depth $z = 40$ mm. The beamformed responses are DAS, Boxcar (gray solid), DAS, Hanning (gray dashed), MV (black solid) and APES (black dashed). (a) Forward-only, no diagonal loading has been applied. (b) Forward-only, diagonal loading factor of $\varepsilon = 10^{-3}\text{Tr}\{\mathbf{R}\}$ is used. (c) Forward-backward averaging is used (no diagonal loading). The percentage error of the sound speed is given at the top right in each figure.

in both resolution and contrast. Furthermore, it is noted that diagonal loading results in a slightly decreased resolution; as would be expected due to the convergence to the DAS solution. As seen the forward-backward (FB) approach does not diminish the resolution significantly. However, these investigations are based on single point targets; as adaptive beamformers are strictly data-dependent, a truly thorough investigation should include a variety of simulations.

As the percentage error increases, the MV and APES beamformers are not as robust compared to the DAS beamformer. Using the forward-only approach without diagonal loading, MV and APES provide amplitude drops on the signal strength of 17 dB and 3 dB, respectively. This amplitude drop can be avoided by using either diagonal loading or FB as seen in Fig. 4.13(b)-(c). However, a slight amplitude drop is seen for MV at 4% and 6% error using diagonal loading.

In general, it is observed that the APES beamformer provide more robust estimates than MV; in terms of less amplitude drop at the expense of a slightly decreased resolution. However, the resolution decrement seems insignificant compared to the robustness gained from using this beamformer.

The investigations have shown that the performance of the adaptive beamformers are significantly decreased for increasing sound speed errors. However, it is noted that the conventional DAS beamformer does not outperform the adaptive beamformers within the investigated region of errors. Thus, incorrect sound speed sound estimates will not lead to a performance degradation worse than that of the DAS beamformer.

The influence of sound speed errors cannot be neglected in medical ultrasound imaging. However, it is seen that the prospective degradation of the performance of the MV beamformer does not lead to further concerns than for the DAS beamformer. Thus, the adaptive beamformer can be implemented into the field of medical ultrasound imaging with the potential of increasing the resolution and contrast. This paper shows that incorrect speed of sound estimates will not lead to a performance degradation worse than that of the conventional DAS beamformer.

To obtain the potential increase in resolution and contrast, robust methods should be applied. Or the sound speed should be estimated and compensated for. The latter topic is a widely studied research topic within medical ultrasound imaging.

4.7 APES Beamforming for Ultrasound Imaging

This section will present a summary of the results published in Paper VII [18], which was carried out in collaboration with A. Blomberg, A. Austeng, J.-F. Synnevåg and S. Holm from the University of Oslo, Norway.

The APES beamformer has been applied to simulated ultrasound data and compared to the DAS and MV beamformers. The three beamforming approaches are in this paper all implemented in the temporal domain. The performance of the methods have been compared based on the resolvability, beam width, amplitude control and speckle statistics. The resolvability is defined as the relative difference between the peak amplitude of two laterally spaced point targets and the saddle point in between.

Data has been obtained using Field II [30, 31]. For the simulations a 96-element, 3.5 MHz, 18.5 mm transducer is used. Data for discrete point targets and for a 3 mm cyst in speckle are simulated. Subarray sizes of $L = \{24, 36, 48\}$ and diagonal loading have been used.

The investigations show that MV and APES provide significantly reduced main-lobe width and resolvability compared to DAS; with MV providing the largest reduction. It is observed that as the subarray size increases, APES performs rather constant, while MV provides reduced main-lobe width and increased resolvability. However, the increased performance of MV comes at the expense of a less robust amplitude estimates.

APES provides a more clear definition of the edges of the cyst than MV. Furthermore, it is observed that APES provides a different statistics of the speckle pattern than MV, and the temporal averaging suggested by Synnevåg *et al.* [37] can be omitted.

The computational load of APES is comparable to that of MV, and thus directly dependent on the subarray size, L. The investigations have shown that the performance of APES is less dependent on L. Thus, the subarray size, and thereby the computational load, can be reduced without sacrificing resolution.

4.8 Summary and Discussion

The purpose of the investigations presented in this chapter is to demonstrate the performance of adaptive beamforming in ultrasound imaging.

Paper I-III showed that the adaptive MV beamformer provides a significant reduction of the main-lobe width. The MV beamformer was implemented in the frequency domain and applied to SA and PW data, respectively. It was observed that MV introduced the possibility of obtaining data using a single emission, either SA or PW, while reducing the main-lobe width.

However, it should be noted that the SNR has not been considered. Obviously, the emission of an unfocused beam will yield a low SNR, compared to a conventional, focused measurement sequence. Nevertheless, it does introduce the possibility of very high frame-rate imaging.

A comparison of a frequency domain and a temporal domain implementation of the MV beamformer showed no significant difference in the main-lobe width of the two approaches. However, the frequency domain implementation provided a reduced side-lobe level, which does come at the expense of an increased computational load.

Paper IV introduced a framework for utilizing adapted apodization weights on both the receiving and transmitting apertures. The concept of the suggested approach was proved using simulated data with discrete point targets. The investigation showed that the proposed method is capable of providing additional reductions of the main-lobe width.

Paper V provided an investigation of the influence of the physical size of the transducer footprint. Due to near-field effects, a reduced main-lobe width can – dependent on the size of the footprint – be obtained, when using a reduced number of active transducer elements in the beamforming process. This observation is directly contradicting the expectation and the DAS results.

An investigation of the influence of errors in the sound speed estimate was presented in Paper VI, where both the MV and the APES beamformers were analyzed. It was seen that the adaptive beamformers did not perform worse than the conventional DAS beamformer. And as also shown in Paper VII, the APES beamformer seems to provide an increased robustness of the amplitude estimate compared to MV.

In general, it should be noted that the presented investigations do indeed suffer from being focused mainly on simulated data. Furthermore, discrete

point targets are rarely present in an ultrasound imaging scenario. To fully investigate and document the performance of adaptive beamformers in ultrasound imaging, experimental and clinical in-vivo data are necessary. Thus, further work in this field of research ought to include such investigations.

CHAPTER

FIVE

Adaptive Spectral Doppler Techniques

Spectral Doppler techniques are used commonly in the clinic for blood velocity estimation using ultrasound. A spectrogram is provided, which shows the blood flow velocity distribution at a certain depth with respect to time.

The spectrograms are conventionally obtained using the averaged periodogram, also referred to as Welch's method [38,39]. As is well-known from spectral estimation theory, the windowing function and the length of the segments directly determine the amount of leakage and broadening of the mainlobe. The segment size, and thus the number of ultrasonic emissions, must be increased in order to accommodate a desired resolution of the velocity distribution.

To obtain an increased resolution of the spectrogram without increasing the segment size, adaptive spectral Doppler techniques were proposed by Gran *et al.* [39]. In [40–42], in-vivo investigations on the Carotid Artery were carried out. These investigations have shown that it is in fact possible to obtain a comparable resolution, when reducing the segment size from 128 emissions to 16 emissions.

In this chapter, the in-vivo study is expanded to include both arterial and venous flow patterns. Furthermore, a deeper penetration depth is obtained using a convex array with lower center frequency compared to the one used in the previous work [40–42].

For the blood flow measurements, two healthy male volunteers, aged 33 and 35 years, are used. The blood flow in the Aorta, the Portal Vein, and the

Superior Mesenteric Artery are measured.

5.1 Methods

A spectrogram showing the velocity distribution of the blood flow using ultrasound is obtained by repeatedly emitting a pulse into the subject of interest. There are two temporal axis in a blood flow measurement setup; one corresponding to the depth within the tissue, and one along the repeated emissions. To distinguish between these two temporal axes, these will be referred to as *fast*-time and *slow*-time, respectively.

Due to the movement of the blood scatterers, the reflected signals will be shifted in time, as illustrated in Fig. 5.1. The blood scatterer moves away from the skin surface, providing a temporal shift along fast-time of the contributing signal.

The velocity distribution at a certain depth (indicated by the dotted vertical line), can according to [22] be found from the spectrum of the signal across emissions. The slow-time sampled signal across the repeated emissions is

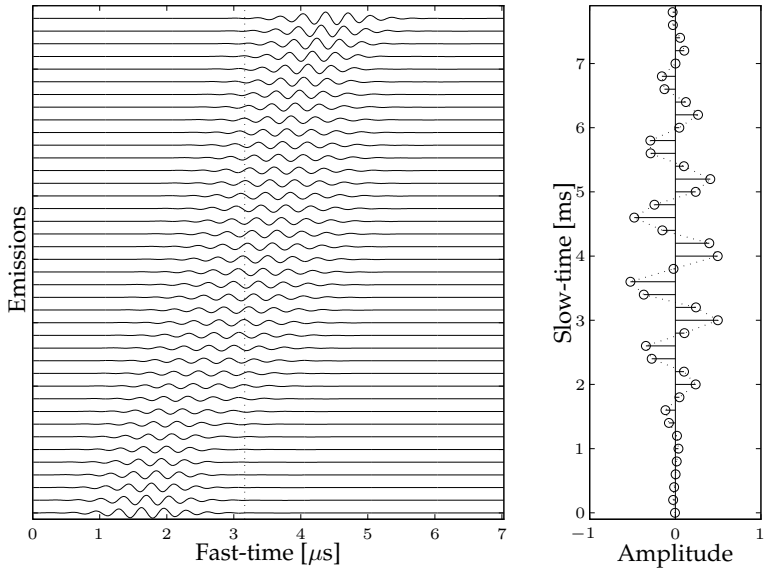

Figure 5.1: (left) Illustration of repeatedly emitted and received sensor signals obtained from a moving scatterer. (right) Slow-time signal, obtained from a specific depth, sampled across emissions. From [22].

shown on the right. In the following the different methods for estimating the spectrum will be introduced, for further description please consult [39].

5.1.1 Welch

Welch's method for estimating the power spectrum is calculated by averaging modified periodograms using windowed and overlapping data segments [38].

The pth data segment consisting of L samples (slow-time) is given by

$$\mathbf{y}_p = \begin{bmatrix} y_p & y_{p+1} & \dots & y_{p+L-1} \end{bmatrix}^T \tag{5.1}$$

for $p = 0, 1, \dots, P-1$, where $\{\cdot\}^T$ denotes the transpose. The corresponding Fourier vector is defined as

$$\mathbf{e}(f) = \begin{bmatrix} 1 & \exp\{j2\pi f\} & \dots & \exp\{j2\pi f(L-1)\} \end{bmatrix}^T , \tag{5.2}$$

and a weight vector for windowing the segment is defined as

$$\mathbf{w} = \begin{bmatrix} w_0 & w_1 & \dots & w_{L-1} \end{bmatrix}^T . \tag{5.3}$$

For later notational convenience, the weight vector is substituted into a diagonal weight matrix given by

$$\mathbf{W} = \text{diag}\{\mathbf{w}^H\} = \begin{bmatrix} w_0^* & & & 0 \\ & w_1^* & & \\ & & \ddots & \\ 0 & & & w_{L-1}^* \end{bmatrix} \tag{5.4}$$

where $\{\cdot\}^*$ denotes the complex conjugate operator, and $\{\cdot\}^H$ denotes the Hermitian transpose. Note that the segmented data vector in (5.1) has been Hilbert transformed, and thus consists of complex values.

The Welch power spectral estimate is according to [38, 43] given as the averaged periodogram of the weighted data segment, expressed as

$$\hat{\mathcal{P}}_{\text{WELCH}}(f) = \frac{1}{P} \sum_{p=0}^{P-1} \left| \sum_{\ell=0}^{L-1} y_{p+\ell} w_\ell \exp\{-j2\pi f \ell\} \right|^2 , \tag{5.5}$$

where the normalization of the inner sum has been omitted. Using matrix-vector notation, (5.5) rewrites into

$$\hat{\mathcal{P}}_{\text{WELCH}}(f) = \frac{1}{P}\sum_{p=0}^{P-1}\left|\mathbf{e}^H(f)\mathbf{W}^H\mathbf{y}_p\right|^2 \tag{5.6}$$

$$= \frac{1}{P}\sum_{p=0}^{P-1}\mathbf{e}^H(f)\mathbf{W}^H\mathbf{y}_p\mathbf{y}_p^H\mathbf{W}\mathbf{e}(f) \tag{5.7}$$

$$= \mathbf{e}^H(f)\mathbf{W}^H\left[\frac{1}{P}\sum_{p=0}^{P-1}\mathbf{y}_p\mathbf{y}_p^H\right]\mathbf{W}\mathbf{e}(f) \tag{5.8}$$

$$= \mathbf{e}^H(f)\mathbf{W}^H\hat{\mathbf{R}}_y\mathbf{W}\mathbf{e}(f)\,, \tag{5.9}$$

where $\hat{\mathbf{R}}_y$ denotes the estimated covariance matrix given by

$$\hat{\mathbf{R}}_y = \frac{1}{P}\sum_{p=0}^{P-1}\mathbf{y}_p\mathbf{y}_p^H\,. \tag{5.10}$$

5.1.2 Blood Spectral Power Capon

The Power Capon Method [1] is also referred to as the Minimum Variance method, and is equivalent to the beamforming method described in Chap. 2. In this section the method used for blood flow estimation, and it is referred to as Blood spectral Power Capon (BPC).

A set of optimized weights is found for each frequency component such that it minimizes the weighted output power, while passing the frequency component without distortion. Mathematically, this can be expressed as

$$\begin{array}{c}\min\limits_{\mathbf{w}(f)}\mathcal{E}\left\{\left|\mathbf{w}^H(f)\mathbf{y}_p\right|^2\right\} \\ \text{subject to } \mathbf{w}^H(f)\mathbf{e}(f)=1\end{array}\,, \tag{5.11}$$

where $\mathcal{E}\{\cdot\}$ denotes the expectation value. Note the equivalence of (5.11) to (2.15). The weighted output power is rewritten as

$$\mathcal{E}\left\{\left|\mathbf{w}^H(f)\mathbf{y}_p\right|^2\right\} = \mathbf{w}^H(f)\mathcal{E}\left\{\mathbf{y}_p\mathbf{y}_p^H\right\}\mathbf{w}(f) = \mathbf{w}^H(f)\hat{\mathbf{R}}_y\mathbf{w}(f)\,, \tag{5.12}$$

where $\hat{\mathbf{R}}_y$ is given by (5.10). The closed-form solution to (5.11) is equivalent to (2.21), and it yields the BPC estimate

$$\hat{\mathcal{P}}_{\text{BPC}}(f) = \frac{1}{\mathbf{e}^H(f)\hat{\mathbf{R}}_y^{-1}\mathbf{e}(f)}\,. \tag{5.13}$$

5.1.3 Blood Spectral Amplitude and Phase Estimation

The Blood spectral Amplitude and Phase EStimation (BAPES) method is equivalent to the previously described APES method. It is based on the optimization problem (5.11), where the covariance matrix estimate in (5.12) is replaced by

$$\hat{\mathbf{Q}} = \hat{\mathbf{R}}_y - \mathcal{E}\left\{\hat{\mathbf{g}}\hat{\mathbf{g}}^H\right\}, \text{ where } \hat{\mathbf{g}} = \frac{1}{P}\sum_{p=0}^{P-1}\mathbf{y}_p \exp\{j2\pi fp\}\,. \tag{5.14}$$

The closed-form solution is thus equivalent to (2.21), yielding the BAPES power spectral estimate

$$\hat{\mathcal{P}}_{\text{BAPES}}(f) = \left|\mathbf{w}^H(f)\hat{\mathbf{g}}\right|^2. \tag{5.15}$$

5.2 Measurement Setup

The measurements are carried out by an experienced radiologist using the experimental ultrasound scanner, RASMUS [44]. Two healthy male volunteers, aged 33 and 35 years, were used in the in-vivo measurements. The relevant parameters for the measurement setup are provided in Table 5.1.

The measurements are carried out using a standard transmission equivalent to the one used in [42], where a focused beam is emitted into the body with a fixed transmit focus. The main difference from the previous measurements in [42] is the use of a convex array instead of the linear array transducer, and the center frequency has been lowered to 4 MHz, which provides a deeper penetration depth.

Furthermore, the emission sequence is changed so that the B-mode and the Doppler emissions are interleaved. The emission sequence is as follows

$$\underbrace{D \;\; D \;\; \cdots \;\; D}_{\text{60 Doppler emissions}} \;\; \underbrace{B}_{\text{B-mode}} \;\; \underbrace{D \;\; D \;\; \cdots \;\; D}_{\text{60 Doppler emissions}} \;\; \underbrace{B}_{\text{B-mode}} \;\; \cdots \tag{5.16}$$

which is repeated 65 times for each image. In the previous work [39, 42], the Doppler emissions and the B-mode emissions were emitted in two separate blocks, so that the Doppler emissions were emitted first, and afterwards the 65 B-mode emissions were emitted. During a B-mode emission, no information of the blood velocities can be estimated. Thus, this emission sequence provided gaps in the resulting spectrograms. Using interpolation, the emission sequence (5.16) avoids these gaps in the spectrograms.

Parameter	Value
Transducer type	Convex
Transducer element pitch	245 μm
Transducer element kerf	35 μm
Transducer element height	10 mm
Elevation focus	70 mm
Center frequency, f_0	4 MHz
Bandwidth	60% fractional
Speed of sound, c	1540 m/s
Wavelength, $\lambda = c/f_0$	385 μm
Excitation pulse	8-cycle sinusoid at f_0
Number of elements, Transmit|Receive	32|64
Apodization, Transmit|Receive	Boxcar|Hanning
Pulse repetition frequency (PRF), f_{prf}	$\{6.8, 7.2\}$ kHz[†]
Wall motion filter	Mean-subtraction

[†]The PRF is changed to accommodate the desired depth of interest.

Table 5.1: Parameters for Measurement Setup

5.3 Results

Five measurements have been carried out in-vivo with the help from an experienced radiologist and two healthy male volunteers, aged 33 and 35 years old. The arterial flow patterns have been examined from measurements of the Aorta and the Superior Mesenteric Artery. And the venous flow has been examined from measurements of the Portal Vein

The four spectral estimation methods, Welch using Boxcar weights (W.BOX) and Hanning weights (W.HAN), BPC and BAPES, have been used for the estimation of the spectrograms. And five different window sizes, $L = \{128, 64, 32, 16, 8\}$, have been used.

The performance of the four methods have been quantified using the Full Width at Half Maximum (FWHM) and the Ratio of the relative side-lobe level. At one time instance, one spectrum from the entire spectrogram has been eliminated. For this spectrum, the FWHM has been found as the width of the velocity distribution, and is thus given in m/s. The relative side-lobe level was found as the ratio between the peak amplitude and the median value of the distributed amplitudes outside the main-lobe, outlined by the FWHM.

Arterial Flow

A selection of the estimated spectrograms for the measurement of the Superior Mesenteric Artery of a 35-year-old healthy male volunteer is shown in Fig. 5.2(a)-(e). The flow is estimated at a depth of 44.0 mm.

Fig. 5.2(a)-(d) show the four spectral estimation methods, W.BOX, W.HAN, BPC, BAPES, for a window size of $L = 16$. For comparison, Fig. 5.2(e) shows the spectrogram obtained using W.BOX for a window size of $L = 128$.

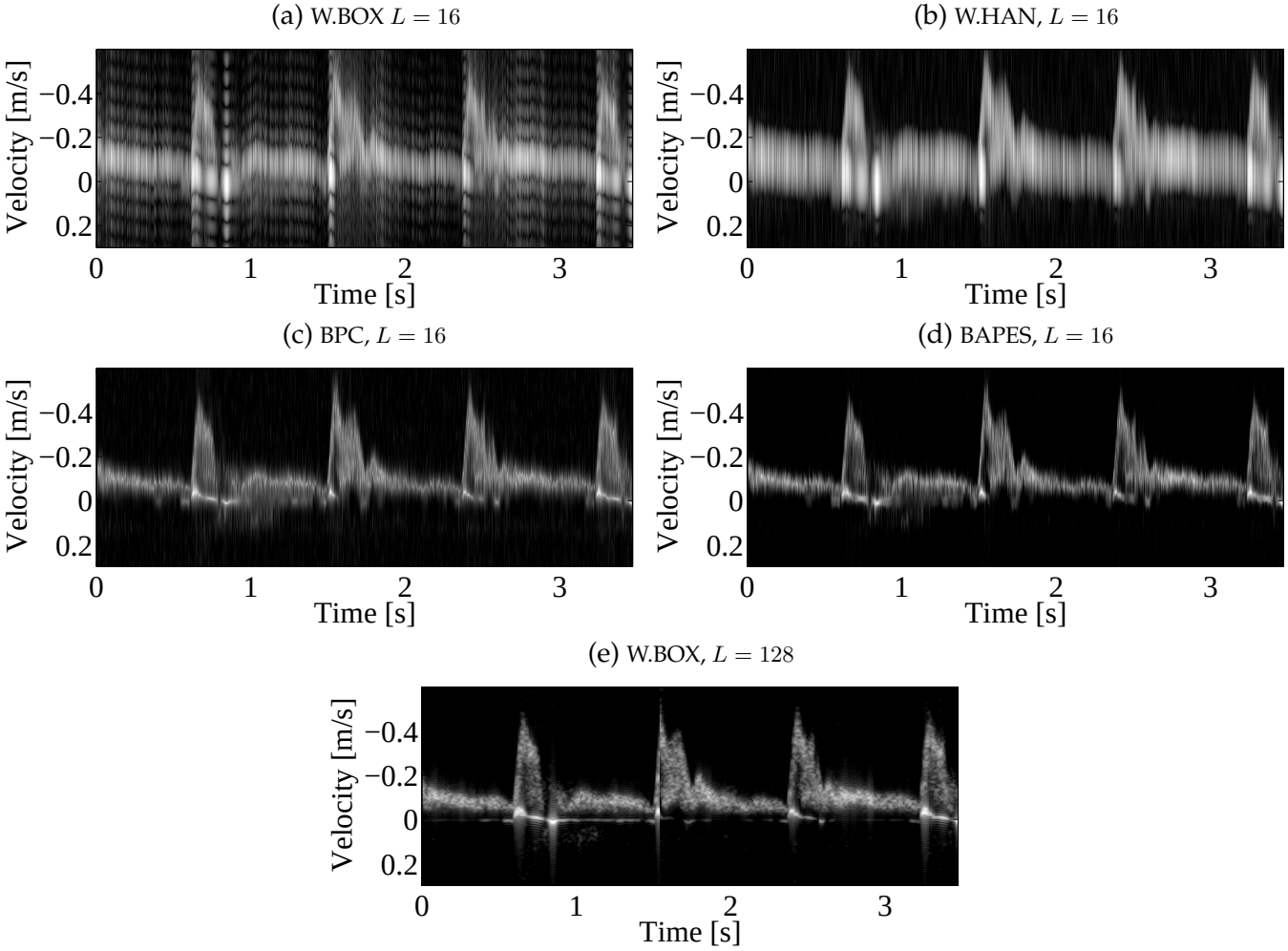

Figure 5.2: Spectrograms showing arterial flow from the Superior Mesenteric Artery measured on a 35-year-old healthy male volunteer. (a)-(d) Window size $L = 16$. (e) Window size $L = 128$. The images are shown with a dynamic range of 40 dB.

It is observed that using a window size of $L = 16$, W.BOX and W.HAN do not provide adequate resolution or contrast to the spectrograms. In Fig. 5.2(a), the sinc-structure is distinct, and in Fig. 5.2(b) the broadening of the main-lobe from the Hanning weights is evident. Compared to the spectrogram using $L = 128$, these two are far from acceptable for blood velocity estimation.

However, the two adaptive spectral methods, in Fig. 5.2(c)-(d), provide spectrograms with a resolution and contrast that are equivalent to that of Fig. 5.2(e).

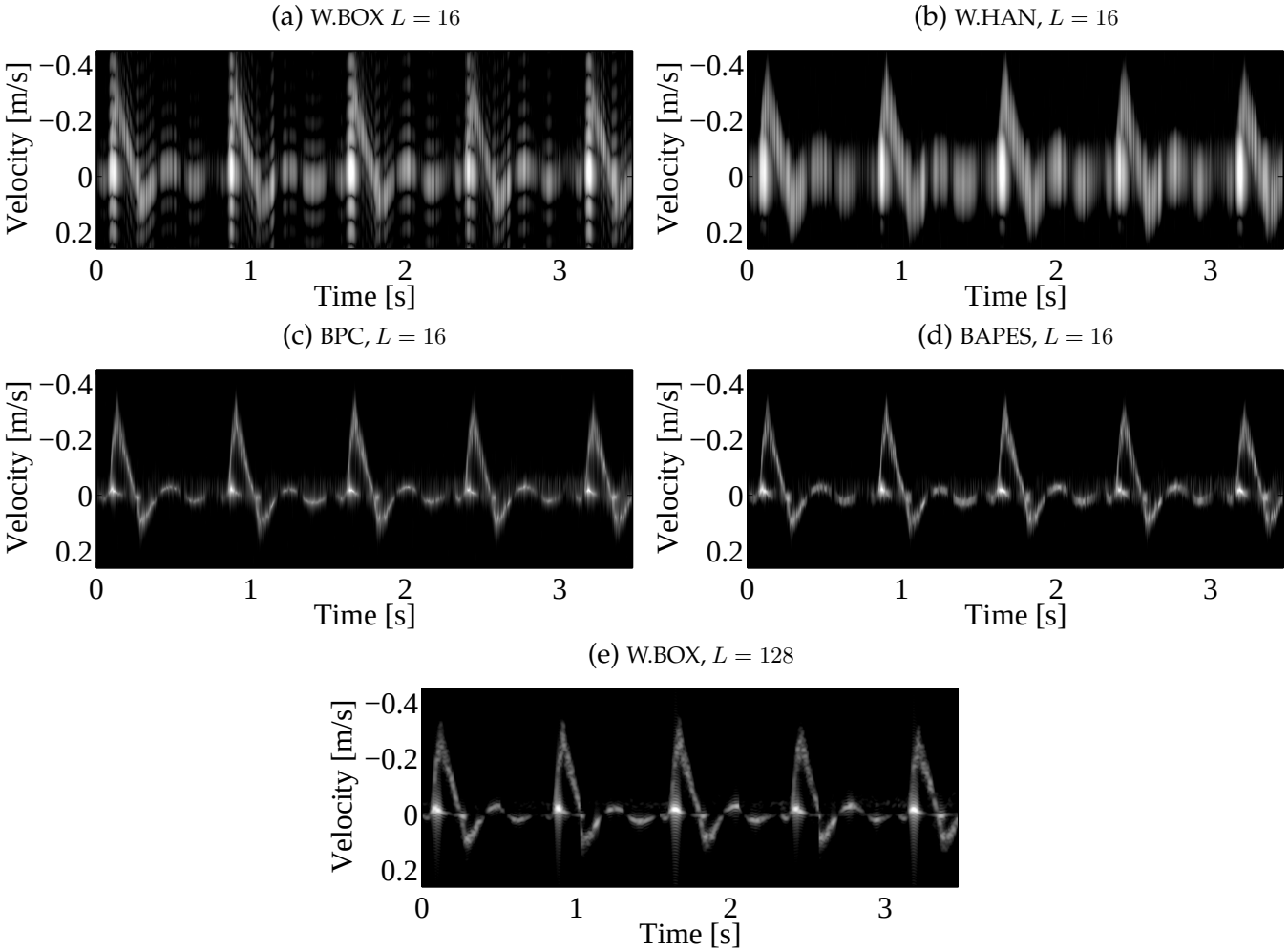

Figure 5.3: Spectrograms showing arterial flow from the Aorta measured on a 33-year-old healthy male volunteer. (a)-(d) Window size $L = 16$. (e) Window size $L = 128$. The images are shown with a dynamic range of 40 dB.

The equivalent trend is evident from the spectrograms in Fig. 5.3(a)-(e). These are estimated from the measurement of the Aorta of a 33-year-old healthy male volunteer. Furthermore, the spectrograms from the measurement of the Aorta of a 35-year-old volunteer indicate the same tendency. However, those

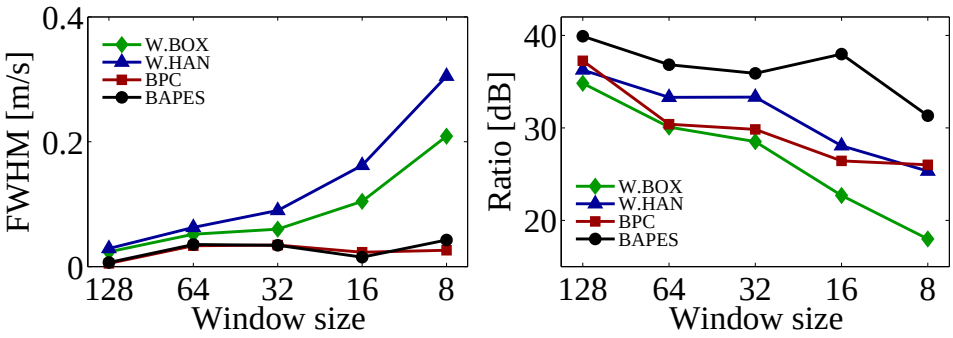

(a) From the Superior Mesenteric Artery of a 35-year-old healthy male volunteer.

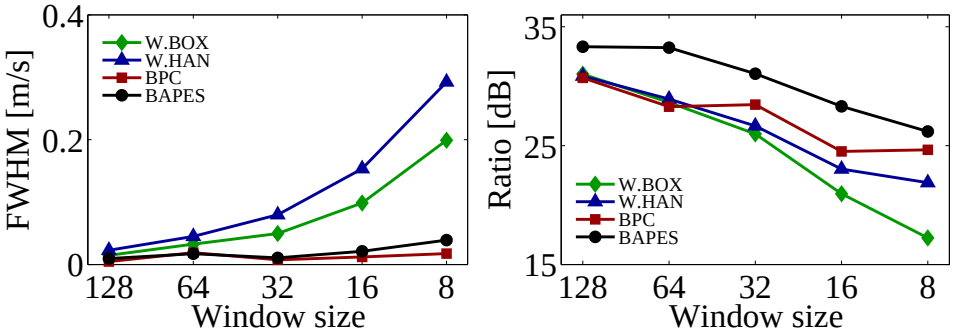

(b) From the Aorta of a 35-year-old healthy male volunteer.

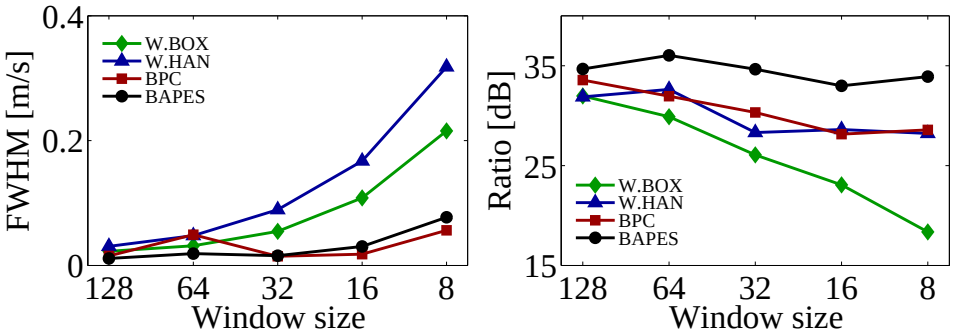

(c) From the Aorta of a 33-year-old healthy male volunteer.

Figure 5.4: (left) Full Width at Half Maximum (FWHM) and (right) the Ratio of the relative side-lobe level for the arterial flow measurements.

spectrograms are not showed in this section.

The performance of the four spectral estimation methods are quantified using the FWHM and the Ratio of the relative side-lobe level. These have been calculated for the five used window sizes, and the variation with respect to the window sizes are shown in Fig. 5.4(a)-(c).

As would be expected, the main-lobe width, in terms of the FWHM, increases as the window size is reduced. And the broadening of the main-lobe due to the Hanning weights is evident, as W.HAN provide the largest FWHM for all window sizes. Furthermore, it is observed that the FWHM for BPC and BAPES are rather constant for all window sizes.

The ratio of the relative side-lobe level indicates that BAPES provide contrast that is significantly higher than the remaining three methods. These observations are evident for all of the three arterial flow measurements.

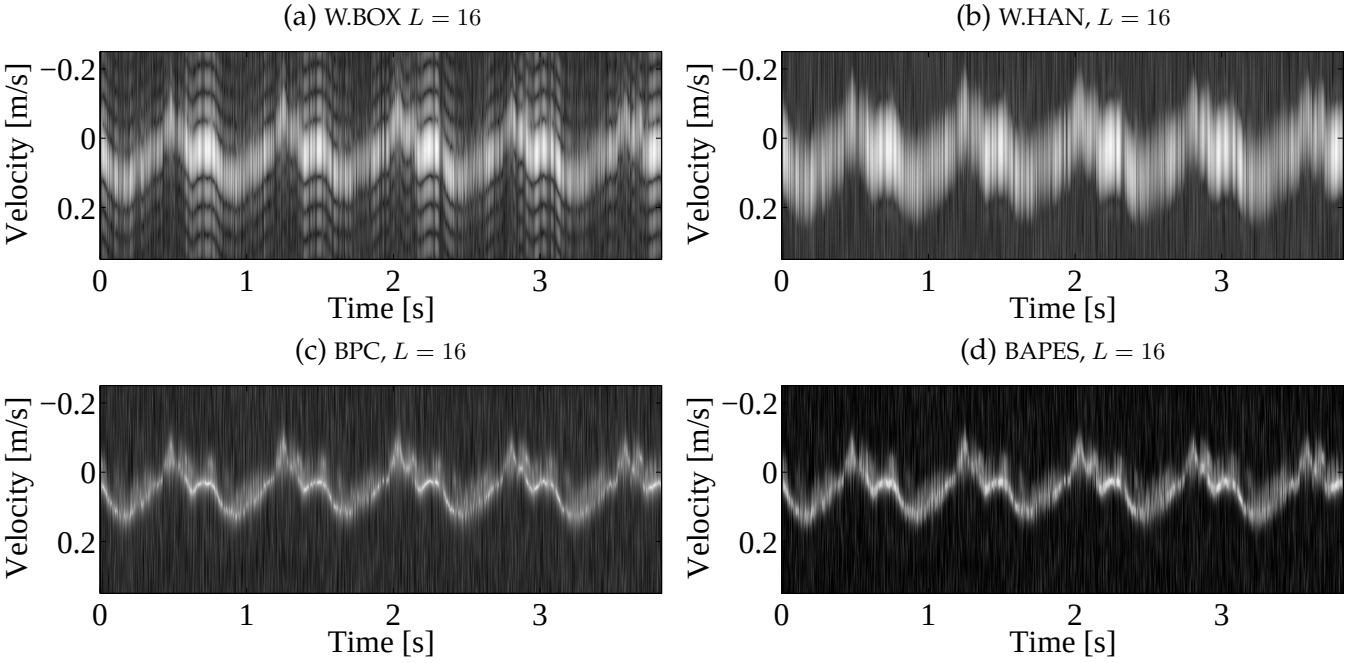

Figure 5.5: Spectrograms showing venous flow from the Portal Vein measured on a 33-year-old healthy male volunteer. Window size $L = 16$. The images are shown with a dynamic range of 40 dB.

Venous Flow

Fig. 5.5(a)-(d) show a selection of spectrograms estimated from the measurement of the flow in the Portal Vein of a 33-year-old healthy male volunteer. The blood flow estimation for this measurement is carried out at a depth of 73.0 mm. Note that the blood flow measurements in the previous study [42] were carried out at depths around approx. 20 mm.

Fig. 5.5(a)-(d) show the spectrograms for the four methods using a window size of $L = 16$. Again, the characteristic sinc-structure is observed for W.BOX, and the broadening of the main-lobe is evident for W.HAN. As also observed for the arterial flow, the two adaptive spectral estimators provide a significantly increased resolution of the velocity distribution.

The FWHM and Ratio of the relative side-lobe level for the two venous mea-

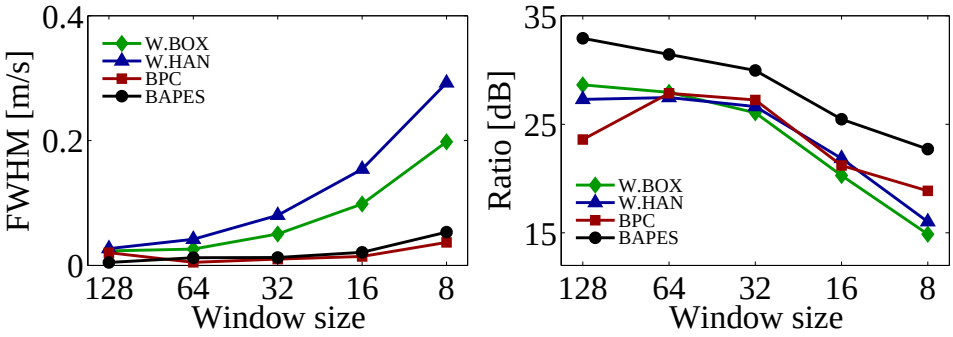

(a) From the Portal Vein of a 33-year-old healthy male volunteer.

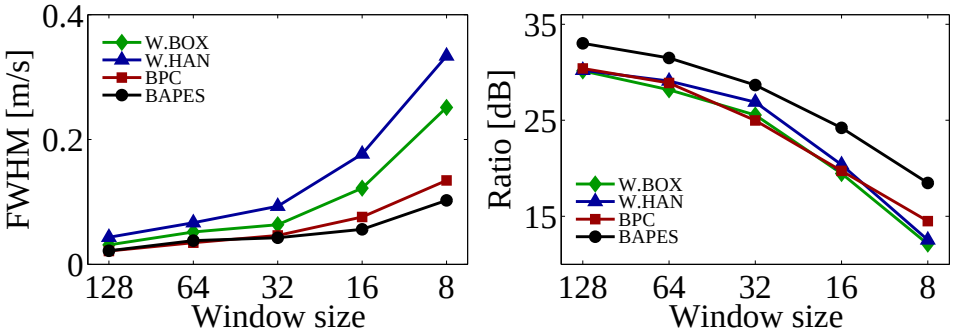

(b) From the Portal Vein of a 35-year-old healthy male volunteer.

Figure 5.6: (left) Full Width at Half Maximum (FWHM) and (right) the Ratio of the relative side-lobe level for the venous flow measurements.

surements are shown in Fig. 5.6(a)-(b). The FWHM indicate a trend equivalent to that of the arterial flow. And it is observed that BAPES does provide an increased Ratio of the relative side-lobe level compared to the remaining three methods.

5.4 Summary and Discussion

The results in this chapter are part of a work in progress, where an in-vivo study of the performance of these adaptive spectral estimators are investigated. It will be continued by PhD, MD Kristoffer Lindskov Hansen. The work will be expanded to include a qualitative evaluation of the spectra by medical doctors.

The investigations in this chapter have included in-vivo measurements of both arterial and venous flow patterns at depths ranging from 44.0 mm to 73.0 mm.

Is was observed that the two adaptive spectral estimators, BPC and BAPES, provide a significantly increased performance, in terms of resolution and contrast, compared to the conventional Welch method. The resolution and contrast were quantified using the FWHM and the ratio of the relative side-lobe level.

The investigations have shown that the adaptive spectral estimators provide the possibility of obtaining spectrograms using window sizes that are significantly shorter than when using Welch's method. This observation is in consistency with the previous in-vivo investigations of the Carotid Artery in [42].

Finally, it should be mentioned that the adaptive spectral Doppler methods do require an increased computational load, which has not been addressed in this chapter. For considerations on the computational cost, please consult [39].

CHAPTER

SIX

Conclusions

This dissertation has investigated the application of adaptive beamforming for medical ultrasound imaging. The investigations have been concentrated primarily on the Minimum Variance (MV) beamformer. A broadband implementation of the MV beamformer has been described, and simulated data have been used to demonstrate the performance.

The MV beamformer has been applied to both Synthetic Aperture (SA) and Plane Wave (PW) data. These applications have shown that MV is capable of providing a significantly reduced main-lobe width compared to the conventional Delay and Sum (DAS) beamformer, even when using considerably fewer emissions in the measurement sequence. This introduces the possibility for high frame-rate ultrasound imaging without sacrificing resolution.

A comparison of a frequency domain and a temporal domain implementation of the MV beamformer showed no significant difference in the main-lobe width of the two approaches. However, the frequency domain implementation provided a reduced side-lobe level, which does come at the expense of an increased computational load.

A frame-work for utilizing adapted apodization weights on both the receiving and the transmitting apertures has been suggested. This method introduces an increased number of degrees of freedom, which was shown to provide an additional reduction of the main-lobe width.

Near-field effects influence the performance of MV. An investigation of the influence of the size of the transducer footprint has been carried out. This investigation showed that in some cases, it is possible to obtain a reduced main-lobe width, when reducing the number of elements used in the adaptation process. This observation is directly contradicting the expectation and

the DAS results.

The sensitivity towards sound speed errors was investigated for both the MV and the Amplitude and Phase EStimation (APES) beamformer. And furthermore, an investigation of the performance of APES was carried out. These investigations showed that APES provides a more robust amplitude estimate than MV at the expense of a slightly increased main-lobe width.

Additionally, an in-vivo study of the performance of two previously suggested adaptive spectral Doppler techniques has been carried out. This study included in-vivo measurements of both arterial and venous flow from vessel located at depths ranging from 44.0 mm to 73.0 mm. These investigations showed that the adaptive spectral Doppler techniques were indeed capable of providing spectrograms with increased resolution and contrast compared to the conventional methods based on Welch's spectral estimator.

Future Work

The results in this dissertation are characterized by a proof-of-concept principle, where the applications are explored using simulated data. Thus, an extension of these investigations ought to include measurements, both experimental and in-vivo. Due to its more robust nature, is it assumed that the APES beamformer will provide a better performance than MV in an experimental setup.

A continuation of the work on the adaptive spectral Doppler techniques can hopefully lead to the implementation of the methods on a commercial platform in the future. These suggested approaches proves very efficient for high resolution spectral Doppler investigations, where the number of ultrasonic emissions into the patient is reduced.

Additionally, Synnevåg *et al.* have in [10] suggested a semi-adaptive, low-complexity approach that uses several sets of predefined apodization weights. Using this approach, a set of images is obtained using the conventional DAS beamformer, and afterwards the resulting image is chosen based on an MV criterion. This approach seems very interesting, rather straightforward to explore and definitely worth the effort to investigate clinically. However, the choice of the predefined sets of apodization weights might need further investigation before this approach is applied experimentally.

Finally, there might be an aspect in investigating adaptive beamformers in connection with Transverse Oscillation (TO) [45–47]. The TO approach is

used for blood flow estimation, where both the axial and the lateral velocity components are estimated using a specific apodization function that forces lateral oscillation of the point spread function. Using adaptive beamforming, one can obtain apodization weights and thus point spread functions that exhibit properties that satisfy any criterion defined by the designated optimization statement.

Paper I

Broadband Minimum Variance Beamforming for Ultrasound Imaging

I. K. Holfort, F. Gran and J. A. Jensen

IEEE Transactions on Ultrasonics, Ferroelectrics, and Frequency Control, Vol. 56, No. 2, pp. 314-325, Feb. 2009

Broadband Minimum Variance Beamforming for Ultrasound Imaging

Iben Kraglund Holfort, *Student Member, IEEE*, Fredrik Gran, and Jørgen Arendt Jensen, *Senior Member, IEEE*

***Abstract*—A minimum variance (MV) approach for near-field beamforming of broadband data is proposed. The approach is implemented in the frequency domain, and it provides a set of adapted, complex apodization weights for each frequency subband. The performance of the proposed MV beamformer is tested on simulated data obtained using Field II. The method is validated using synthetic aperture data and data obtained from a plane wave emission. Data for 13 point targets and a circular cyst with a radius of 5 mm are simulated. The performance of the MV beamformer is compared with delay-and-sum (DS) using boxcar weights and Hanning weights and is quantified by the full width at half maximum (FWHM) and the peak-side-lobe level (PSL). Single emission {DS boxcar, DS Hanning, MV} provide a PSL of {−16, −36, −49} dB and a FWHM of {0.79, 1.33, 0.08} mm. Using all 128 emissions, {DS boxcar, DS Hanning, MV} provides a PSL of {−32, −49, −65} dB, and a FWHM of {0.63, 0.97, 0.08} mm. The contrast of the beamformed single emission responses of the circular cyst was calculated as {−18, −37, −40} dB. The simulations have shown that the frequency subband MV beamformer provides a significant increase in lateral resolution compared with DS, even when using considerably fewer emissions. An increase in resolution is seen when using only one single emission. Furthermore, the effect of steering vector errors is investigated. The steering vector errors are investigated by applying an error of the sound speed estimate to the ultrasound data. As the error increases, it is seen that the MV beamformer is not as robust compared with the DS beamformer with boxcar and Hanning weights. Nevertheless, it is noted that the DS does not outperform the MV beamformer. For errors of 2% and 4% of the correct value, the FWHM are {0.81, 1.25, 0.34} mm and {0.89, 1.44, 0.46} mm, respectively.**

I. Introduction

In medical ultrasound imaging, beamforming is conventionally carried out using the delay-and-sum (DS) beamformer. The aim of the DS beamformer is to maximize its output by delaying, weighting, and summing the individual sensor signals. The DS beamformer uses predefined, fixed apodization weights, which are independent of the input data. As is commonly known, an inherent compromise between the main-lobe width and the side-lobe level exists. Choosing a smoothing apodization function, such as Hanning, the side-lobe level can be reduced at the expense of a lateral broadening of the main-lobe.

For decades, data-dependent, adaptive beamformers have been used in other fields of array signal processing, e.g., sonar and radar. Whereas the conventional beamformer is a passive process using predefined, fixed, data-independent apodization weights, the adaptive beamformer actively updates a set of new apodization weights for each point in the image. These apodization weights are dependent on the input data. One of the widely used methods was originally introduced by Capon in 1969 [1]. The Capon or minimum variance (MV) beamformer continuously updates the apodization weights, so that the variance (or power) of the weighted sensor signals is minimized under the constraint that the signal emerging from the point of interest is passed without distortion.

Recently, the application of adaptive beamforming to the field of medical ultrasound imaging has become an area of increased interest. The adaptive beamformers potentially provide improvements of the image quality, in terms of lateral resolution and contrast. In 2002, Mann and Walker [2] introduced the linearly constrained adaptive beamformer, also referred to as the Frost beamformer [3]. They applied the method to experimental data of a single point target and a cyst phantom using diagonal loading to ensure a well-conditioned covariance matrix. Another approach to obtain a well-conditioned covariance matrix is to use spatial averaging, which was introduced to ultrasound data by Sasso and Cohen-Bacrie in 2005 [4]. They apply the minimum variance beamformer on a simulated cyst. Four different adaptive beamformers were introduced by Viola and Walker [5], and these were applied to simulated data. Synnevåg *et al.* [6] applied the MV beamformer to simulated and experimental ultrasound data, and they proposed a robust approach using diagonal loading. Wang *et al.* [7] also applied the MV beamformer as well as the MUltiple SIgnal Classification (MUSIC) approach. They introduce yet another approach to obtain a well-conditioned covariance matrix by averaging over several emissions from different spatial positions.

The previous work within this field is characterized by the fact that narrowband methods have been applied directly on broadband ultrasound data. Instead, this paper proposes an approach for near-field, adaptive beamforming of broadband data. Preliminary results of this method were presented in [8]. This approach is implemented in the frequency domain, and it provides a set of adapted, complex apodization weights for each frequency subband. Whereas the conventional method and the previous imple-

Manuscript received May 26, 2008; accepted September 6, 2008. This work was supported by grant 26-04-0024 from the Danish Science Foundation; grant 274-05-0327 from the Danish Research Agency, the Radiopartsfoundation, the Technical University of Denmark; and by B-K Medical ApS, Denmark.

I. K. Holfort and J. A. Jensen are with the Center for Fast Ultrasound Imaging, Department of Electrical Engineering, Technical University of Denmark, Lyngby, Denmark (e-mail: ikh@elektro.dtu.dk).

F. Gran is with GN ReSound A/S, Ballerup, Denmark.

Digital Object Identifier 10.1109/TUFFC.2009.1040

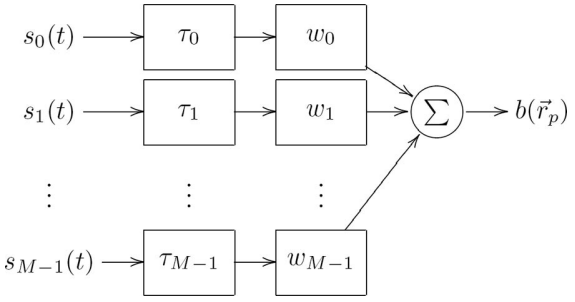

Fig. 1. Block diagram of the conventional delay-and-sum beamformer. The sensor signals are delayed, weighted, and subsequently summed to form the beamformer output.

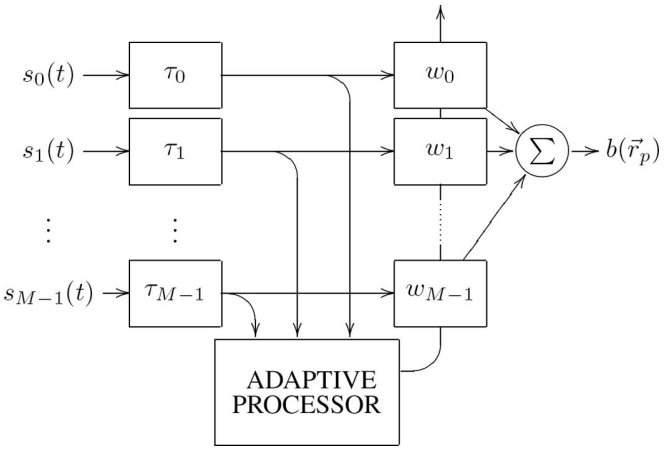

Fig. 2. Block diagram of an adaptive narrowband beamformer. The adaptive processor determines a set of optimized apodization weights from the delayed sensor signals.

mentations of the MV beamformer provide a single weight value for each sensor, this proposed method continuously updates a set of spatial filters for each sensor signal.

The outline of the paper is as follows: The method is presented in Section II. It is validated on simulated synthetic aperture ultrasound data and plane wave emission data. The results are given in Section III. In Section IV, the degradation of the point spread function dependent on incorrect sound speed estimates is investigated. Concluding remarks are given in Section V.

II. Method

Conventionally, beamforming is carried out on each of the sensor signals independently. As shown in Fig. 1, each sensor signal is delayed and weighted; and they are consecutively summed to form the beamformer output. The DS beamformer is a passive process using predefined, fixed, data-independent apodization weights. Because the phase-shift can be implemented as a time-delay, the DS beamformer works for both narrowband and broadband signals.

For narrowband signals, an adaptive beamformer is simply an extension to the DS beamformer, where the only difference is the choice of weights. Instead of using predefined weights, the adaptive processor actively updates a set of new apodization weights that are dependent on the delayed sensor signals. As illustrated in Fig. 2, the delayed sensor signals are fed to the adaptive processor, which determines a set of optimized weights for the specific, delayed sensor signals.

The adaptive process differs for the different adaptive beamformers. This paper concentrates on the minimum variance (MV) beamformer, which is described in Section II-C. For broadband signals, the signals are divided into a set of narrowband signals using the discrete Fourier transform; this approach is described in Section II-B.

A. Presteering

As in conventional beamforming, the sensor signals are presteered at the focus point, so that the sensor responses from the focus point will sum in phase, and the DS beamformer output from the current point will be maximized. Presteering at point $\vec{r}_p = (x_p, z_p)$ is carried out by compensating for the propagation delay profile for this point. The delay is calculated as the propagation path from the transmit element to the focus point and back to the mth receiving element. For a transducer array of M elements, the delay is given by

$$\tau_m(\vec{r}_p) = \frac{\| \vec{r}^{\,(\mathrm{xmt})} - \vec{r}_p \| + \| \vec{r}_m^{\,(\mathrm{rcv})} - \vec{r}_p \|}{c}, \qquad (1)$$

for $m = 0, 1, \ldots, M-1$, where c is the speed of sound, and $\vec{r}^{\,(\mathrm{xmt})}$ and $\vec{r}^{\,(\mathrm{rcv})}$ are the spatial positions of the transmitting and receiving elements, respectively. By compensating for the delay, the mth presteered sensor signal is given by

$$y_m(t) = s_m(t + \tau_m(\vec{r}_p)), \qquad (2)$$

where $s_m(t)$ is the received waveform on the mth sensor. By definition, the presteered signals, $y_m(t)$, are dependent on the focus point, $\vec{r}_p$. However, to simplify the notation, this dependence is omitted.

The concept of presteering is illustrated in Figs. 3(a)-(b), which show the responses from 3 point targets located at $(x,z) = \{(0.40), (5,42), (-2,45)\}$ mm. The responses are simulated for a transducer of $M = 128$ elements using Field II [9], [10]. Fig. 3(a) shows the received sensor signals, $s_m(t)$, for $m = 0,1,\ldots,M-1$. In Fig. 3(b), the sensor signals are presteered at the point $\vec{r}_p = (0,40)$ mm. Due to the compensation for the delay line, the response from the focus point resembles a plane wave impinging directly onto the array. Thus, the presteered sensor signals will sum in phase, maximizing the DS beamformer output power at the focus point.

In the beamformer, the presteered sensor signals are weighted and subsequently summed. The amplitude of the

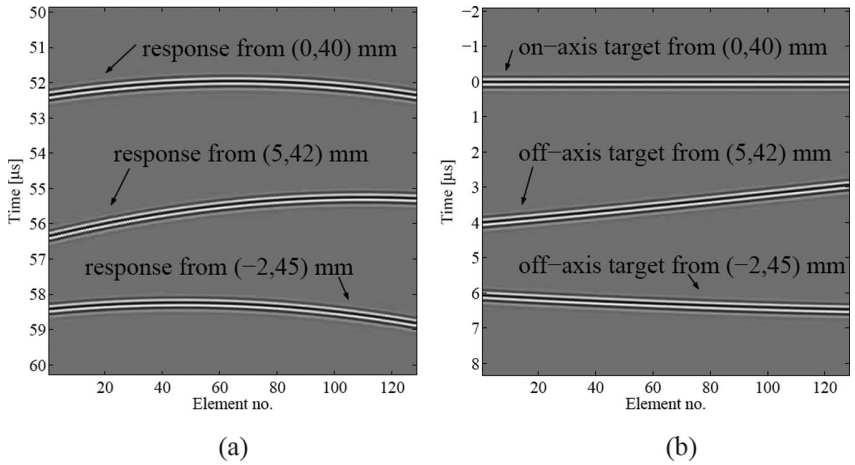

Fig. 3. (a) The received sensor signals, $s_m(t)$, for $m = 0,1,\ldots,M-1$. The figure shows the responses from 3 point targets located at $(x,z) = \{(0,40),(5,42),(-2,45)\}$ mm. (b) Sensor signals presteered at the focus point $\vec{r}_p = (0, 40)$ mm. After presteering, the response from the focus point resembles a plane wave impinging directly onto the array.

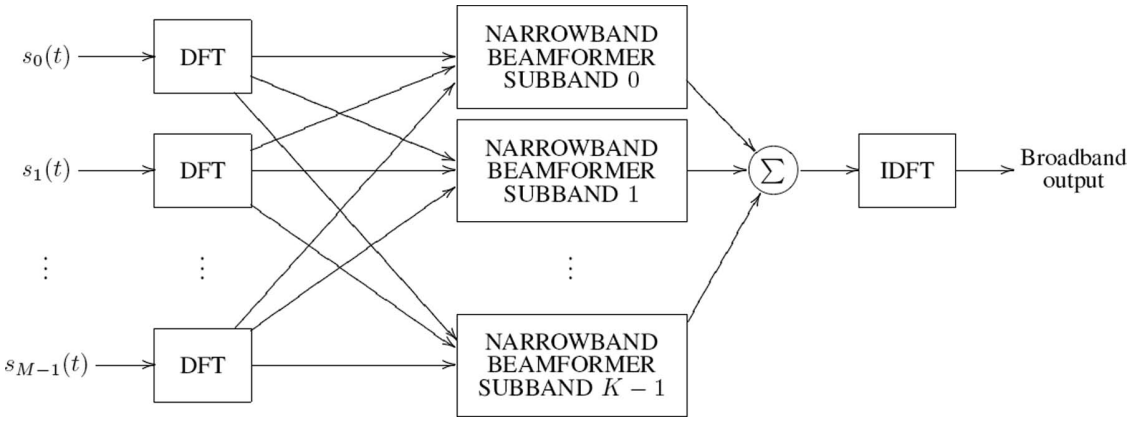

Fig. 4. Block diagram of a broadband beamformer. Each broadband sensor signal is divided into a set of narrowband signals using the discrete Fourier transform (DFT). Each frequency subband is processed independently by a narrowband beamformer. Subsequently, the processed subband responses are summed to provide the broadband beamformer output.

beamformer output at $t = 0$, provides the amplitude at the focus point $\vec{r}_p$ in the resulting beamformed image. Thus, the beamformer output is given by

$$b(\vec{r}_p) = \sum_{m=0}^{M-1} w_m y_m(0) = \sum_{m-0}^{M-1} w_m s_m(\tau_m(\vec{r}_p)), \qquad (3)$$

where w_m are the apodization weight on the mth sensor. Note that the apodization weights can be different for each focus point, but the dependence on $\vec{r}_p$ is here omitted. Whereas the conventional beamformer uses a set of predefined weights, the adaptive beamformer finds a set of optimized weights. The adaptive process for optimizing the apodization weights is described in Section II-C.

B. Subband Beamforming

The MV beamformer [1] was originally developed for narrow-band applications. As described in [11], the adaptive beamformer can be applied to broadband data by dividing the sensor signals into frequency subbands using the short-time, discrete Fourier transform (DFT). Each separate subband satisfies the narrowband condition of the adaptive beamformer and is processed independently, as illustrated in Fig. 4. First, the processed subband responses are summed, and then the inverse DFT is used to obtain the MV response from the focus point.

For each focus point, the DFT is applied on a segment of the presteered sensor signals. Due to the compensation for the delay line, the response from the focus point will be centered around $t = 0$, as seen in Fig. 3(b). The mth segmented, presteered sensor signal is thus given by

$$y_m(t) \text{ for } t \in [-t_d/2; t_d/2], \qquad (4)$$

where t_d is the time duration of the segment size. To sustain the axial resolution, t_d should not exceed the pulse length, which is given by the convolution of the excitation pulse and the 2-way impulse response of the transducer.

For the given focus point, the beamformer output for each frequency subband, ω, is given by

$$B(\omega,\vec{r}_p)=\sum_{m=0}^{M-1} w^*_m(\omega)Y_m(\omega), \tag{5}$$

where $Y_m(\omega)$ is the Fourier transform of the mth segmented sensor signal (4), and $\{\cdot\}^*$ denotes the complex conjugate. By defining the vectors

$$\mathbf{w}(\omega)=[w_0(\omega)\quad w_1(\omega)\quad \ldots\quad w_{M-1}(\omega)]^T \tag{6}$$

$$\mathbf{Y}(\omega)=[Y_0(\omega)\quad Y_1(\omega)\quad \ldots\quad Y_{M-1}(\omega)]^T, \tag{7}$$

the beamformer output (5) rewrites as

$$B(\omega,\vec{r}_p)=\mathbf{w}(\omega)^H\mathbf{Y}(\omega), \tag{8}$$

where the superscripts $\{\cdot\}^T$ and $\{\cdot\}^H$ denote the nonconjugate and the conjugate transpose, respectively. Note that the subband division provides the possibility of weighting both each subband and each point differently.

C. Minimum Variance Beamforming

The adaptive beamformer uses a set of apodization weights, which are dependent on the frequency content of the specific sensor signals. In the following, it is assumed that the sensor signals have been divided into frequency subbands as described in Section II-B

The MV beamformer continuously updates the weights, so that the power of the beamformer output is minimized, while the response from the focus point is passed without distortion. The power of the beamformer output is given by

$$\mathcal{P}(\vec{r}_p)=\mathcal{E}\left\{|B(\omega,\vec{r}_p)|^2\right\} \tag{9}$$

$$=\mathcal{E}\left\{|\mathbf{w}(\omega)^H\mathbf{Y}(\omega)|^2\right\} \tag{10}$$

$$=\mathcal{E}\left\{\mathbf{w}(\omega)^H\mathbf{Y}(\omega)\mathbf{Y}(\omega)^H\mathbf{w}(\omega)\right\} \tag{11}$$

$$=\mathbf{w}(\omega)^H\mathbf{R}(\omega)\mathbf{w}(\omega), \tag{12}$$

where $\mathcal{E}\{\cdot\}$ denotes the expectation value, and $\mathbf{R}(\omega)$ is the covariance matrix given by

$$\mathbf{R}(\omega)=\mathcal{E}\left\{\mathbf{Y}(\omega)\mathbf{Y}(\omega)^H\right\}. \tag{13}$$

Omitting the dependency on ω, the MV beamformer is expressed as [2]

$$\begin{aligned}&\min_{\mathbf{w}}\ \mathbf{w}^H\mathbf{R}\mathbf{w}\\ &\text{subject to } \mathbf{w}^H\mathbf{e}=1,\end{aligned} \tag{14}$$

where $\mathbf{e}$ is the so-called steering vector, which characterizes the response from the focus point. The steering vector defines the signal that should be passed distortionless through the beamformer and is given by

$$e=\begin{bmatrix}\exp\{j\omega(\tau_0(\vec{r}_p)-\tau_0(\vec{r}_p))\}\\ \exp\{j\omega(\tau_1(\vec{r}_p)-\tau_1(\vec{r}_p))\}\\ \vdots\\ \exp\{j\omega(\tau_{M-1}(\vec{r}_p)-\tau_{M-1}(\vec{r}_p))\}\end{bmatrix}=\begin{bmatrix}1\\1\\\vdots\\1\end{bmatrix}, \tag{15}$$

where $\tau_m(\vec{r}_p)$ is the delay line given in (1). Due to presteering, the sensor signals have already been compensated for the delay line, $\tau_m(\vec{r}_p)$. Thus, as illustrated in Fig. 3, the response from the focus point will resemble a plane wave incident directly onto the array. Thus, the steering vector is constant across the array and independent on the frequency, and it simply becomes a $M\times 1$-vector of ones.

The constrained optimization problem (14) can be solved analytically using Lagrangian multiplier theory [12]. Provided that $\mathbf{R}^{-1}$ exists, the MV optimized apodization weights are given by [1]

$$\mathbf{w}=\frac{\mathbf{R}^{-1}\mathbf{e}}{\mathbf{e}^H\mathbf{R}^{-1}\mathbf{e}}. \tag{16}$$

The subband MV beamformer output is found by applying these MV-optimized weights to the delayed sensor signals using (8). This yields an MV-optimized spectrum, and the amplitude corresponding to the focus point is found from the inverse Fourier transform of this spectrum and choosing the sample at $t=0$.

D. Subarray Averaging

In real applications, the covariance matrix is unknown and must be replaced by the sample covariance matrix, which is estimated from the data. To estimate the sample covariance matrix, several realizations of data are required. In this paper, these realizations are obtained by dividing the data from a single acquisition into several subgroups. This follows the spatial smoothing approach suggested in [13].

As illustrated in Fig. 5, the spatially smoothed covariance matrix estimate is obtained by dividing the array into P overlapping subarrays of size $M_p\le M/2$. For each subarray, a subcovariance matrix is estimated, and these are averaged across the array. The covariance matrix estimate can be expressed as

$$\mathbf{R}=\frac{1}{P}\sum_{p=0}^{P-1}\mathbf{G}_p\mathbf{G}_p^H, \tag{17}$$

where $\mathbf{G}_p$ denotes the pth subarray given by

TABLE I. PARAMETERS USED FOR THE FIELD II SIMULATIONS.

Transducer	
Transducer type	Linear array
Transducer element pitch	110 μm
Transducer element kerf	35 μm
Transducer element height	6 mm
Center frequency, f_0	7 MHz
Bandwidth	60% fractional
Speed of sound, C	1540 m/s
Wavelength, $\lambda = c/f_0$	220 μm
Excitation pulse	Two-cycle sinusoid at f_0
Synthetic Aperture Emission	
Transmit apodization	Hanning
Receive apodization	Boxcar/Hanning/MV
Number of transmitting elements	1
Number of receiving elements, M	128
Number of emissions	128
Plane Wave Emission	
Transmit apodization	Boxcar
Receive apodization	Boxcar/Hanning/MV
Number of transmitting elements	128
Number of receiving elements, M	128
Number of emissions	1
Linear Scan Emission	
Transmit apodization	Hanning
Transmit focus depth	45 mm
Receive apodization	Dynamic Hanning with $f/2.0$
Number of transmitting elements	128
Number of receiving elements, M	128
Number of emissions	185

$$\mathbf{G}_p = [Y_p(\omega) \quad Y_{p+1}(\omega) \quad \ldots \quad Y_{p+L-1}(\omega)]^T, \tag{18}$$

for $p = 0, 1, \ldots, P-1$. Note that this reduces the dimension of the covariance matrix, and thus the number of weights will be reduced correspondingly. The reduced weight vector $\tilde{\mathbf{w}}$ is applied to the data by averaging over the P subarrays, which is expressed as

$$B(\vec{r}_p) = \tilde{\mathbf{w}}^H \frac{1}{P} \sum_{p=0}^{P-1} \mathbf{G}_p, \tag{19}$$

Note that the reduced dimension also influences the resolution due to the inherent compromise between the width of the array and the achievable resolution [14].

III. APPLICATION TO ULTRASOUND DATA

The proposed MV beamformer is tested on simulated ultrasound data, obtained using Field II [9], [10]. For the simulations, a 7-MHz, 128-element linear array transducer with $\lambda/2$-spacing was used. The parameters for the simulations are given in Table I. In Section III-A, the method is applied to synthetic aperture data, and in Section III-B, data from a plane wave emission are used.

The MV beamformer is implemented in the frequency domain using the short time Fourier transform with a segment size corresponding to the length of the excitation pulse convolved with the 2-way impulse response of the transducer. A subarray size of $L = M/4 = 32$ was used. Before beamforming, additional white, zero-mean, Gaussian distributed noise with a signal-to-noise ratio (SNR) of 60 dB was added to each of the sensor signals.

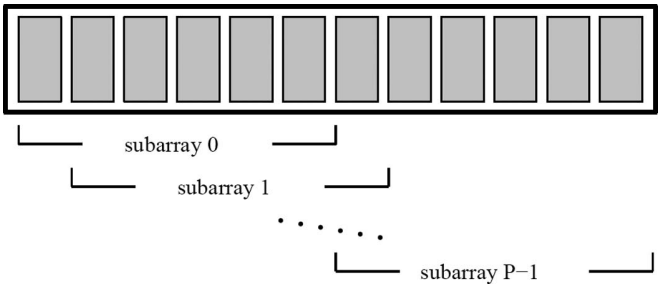

Fig. 5. Spatial smoothing. The array is divided into P overlapping subarrays, and the covariance matrix is averaged across the array.

The performance of MV is compared with DS using boxcar weights and Hanning weights. The performance is quantified by the full width at half maximum (FWHM) and the peak-side-lobe level (PSL), which is defined as the peak value of the first side-lobe.

A. Synthetic Aperture Emission

In this section, the proposed MV beamformer is tested using simulated synthetic aperture (SA) data. The concept of SA imaging is indicated in Fig. 6; a single element is used as the transmitting aperture and all $M = 128$ elements as the receiving aperture. The transmitting element is slid across the array, and for each single emission an image is created; these are traditionally referred to as low-resolution images [15]. Combining the single-emission images, obtained from the different spatial positions, provides an image with a higher resolution and contrast. A full SA sequence consisting of 128 emissions was simulated. Data for 13 point targets and for a circular cyst with a radius of 5 mm were simulated.

1) Point Targets: The beamformed responses of 13 point targets are shown in Fig. 8 with a dynamic range of 50 dB. Fig. 8(a) and (b) shows the DS beamformer responses using boxcar and Hanning apodization weights, respectively. The 3 responses in Fig. 8(a)–(c) are combined images from a full SA sequence. Thus, these have been averaged over 128 emissions. The MV response on the right, Fig. 8(d), is the response from a single emission, where a single element (element #64) was used as the transmitting aperture.

The lateral variation of the beamformed responses, Fig. 8, are shown in Fig. 7(a) and (b) at the depths $z = \{40, 45\}$ mm. As expected, it is seen that applying Hanning apodization weights to the DS beamformer reduces the side-lobe level at the expense of a lateral broadening of the main-lobe, compared with DS using boxcar weights.

The resolution and contrast improvements are quantified using the FWHM and PSL. These quantitative measures are calculated at a depth of 40 mm and are given in Table II. The measures are given for the single-element

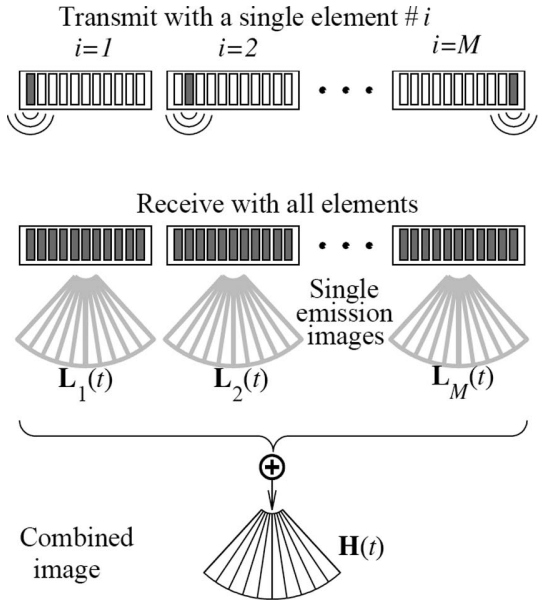

Fig. 6. Concept of synthetic aperture imaging. Several images are created from a single emission. These single emission images are averaged to obtain an image with a higher resolution and contrast. From [15].

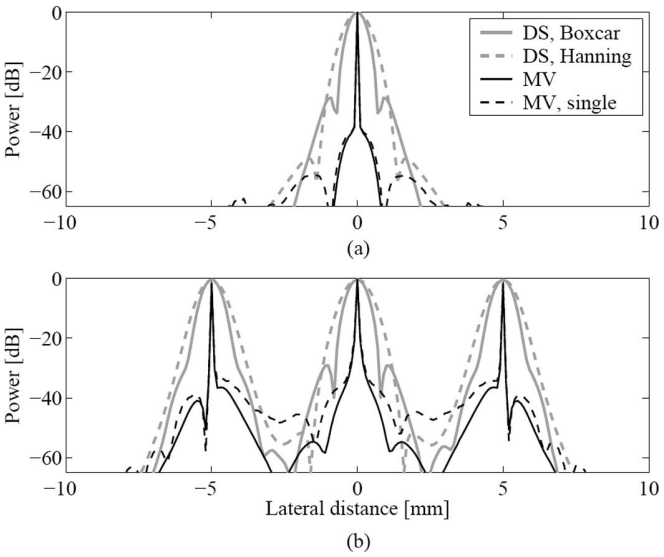

Fig. 7. Lateral variation at $z = 40$ mm (a), and 45 mm (b) of the beamformed responses shown in Fig. 8(a)–(d).

emission and for the full SA sequence. Only the lateral resolution has been considered, because the axial resolution does not change from that of the DS beamformer.

From Figs. 7 and 8 and Table II, it is seen that the MV beamformer provides a significant increase in the lateral resolution and a lowering of the side-lobes; it thus represents a significant improvement in terms of both resolution and contrast. The FWHM of MV from a single emission response comprise only {12.7%, 8.2%} of the FWHM from the full DS sequence using DS{boxcar, Hanning}.

As seen in Figs. 7(a)–(b), the MV response does not change significantly in the interval of [−40;0] dB. The FWHM is calculated at a level of −6 dB and will not change for MV, when averaging over all 128 emissions. This is shown in Fig. 10(a), where the FWHM for DS and MV are shown with respect to the number of emissions. Furthermore, the ratio of energy above and below −40 dB has been calculated relative to the number of emissions, shown in Fig. 10(b). A reduction of the relative energy within the main-lobe could mean that the width of the main-lobe decreases. It is seen that this ratio reduces with the number of emissions. However, the reduction for MV is not as large as for DS. Thus, the MV response does not improve significantly, when averaging over several emissions.

2) Circular Cyst: In this section, simulated data of a circular cyst in a speckle pattern are considered. The circular cyst has a radius of 5 mm and center at $(x,z) = (0,40)$ mm. The speckle pattern is simulated with 10 randomly placed scatterers within a resolution cell of $\lambda \times \lambda \times \lambda$ to ensure fully developed speckle, where λ is the wavelength given in Table I.

The beamformed responses for the full SA sequence are shown in Fig. 9(a)–(c). Thus, these responses are averaged over 128 emissions. In Fig. 9(d)–(f), the beamformed responses from a single emission are shown. These responses are from a emission using element #64 as the transmitting aperture. Furthermore, the lateral variation at a depth of $z = 40$ mm is seen in Fig. 11.

The single emission images, Figs. 9(d)–(f), emphasize the differences between the 3 beamforming approaches. It is seen that the high side-lobe level of the DS boxcar apodization results in a rather poor contrast. Furthermore, it is seen that the DS response using Hanning apodization does not result in a circular shape of the cyst. The shape is rather oval due to the lateral broadening from the Hanning apodization. However, the Hanning apodization does provide a suitable contrast level, because the side-lobes are lowered significantly. Note that in the combined images, Figs. 9(a)–(c), these effects have been averaged out. Thus, the side-lobe level has reduced for the DS boxcar response, and the circular shape of the cyst has been recovered for DS Hanning response.

The MV response from a single emission, Fig. 9(f), shows a circular shape of the cyst as well as a suitable contrast difference between the inner part of the cyst and the speckle pattern. From this investigation, it is seen that the MV beamformer provides a lowering of the side-lobe level without smoothing the responses laterally.

Only a slight difference can be observed between the single-emission MV response, Fig. 9(f), and the full SA sequence MV response, Fig. 9(c). In Fig. 11, this difference is easier to recognize. It is seen that the averaged responses have a reduced side-lobe level compared with the single emission responses. This is valid for all 3 approaches. However, it is seen that the single-emission MV response provides a side-lobe level, which is comparable to the averaged DS responses. Thus, the averaged MV

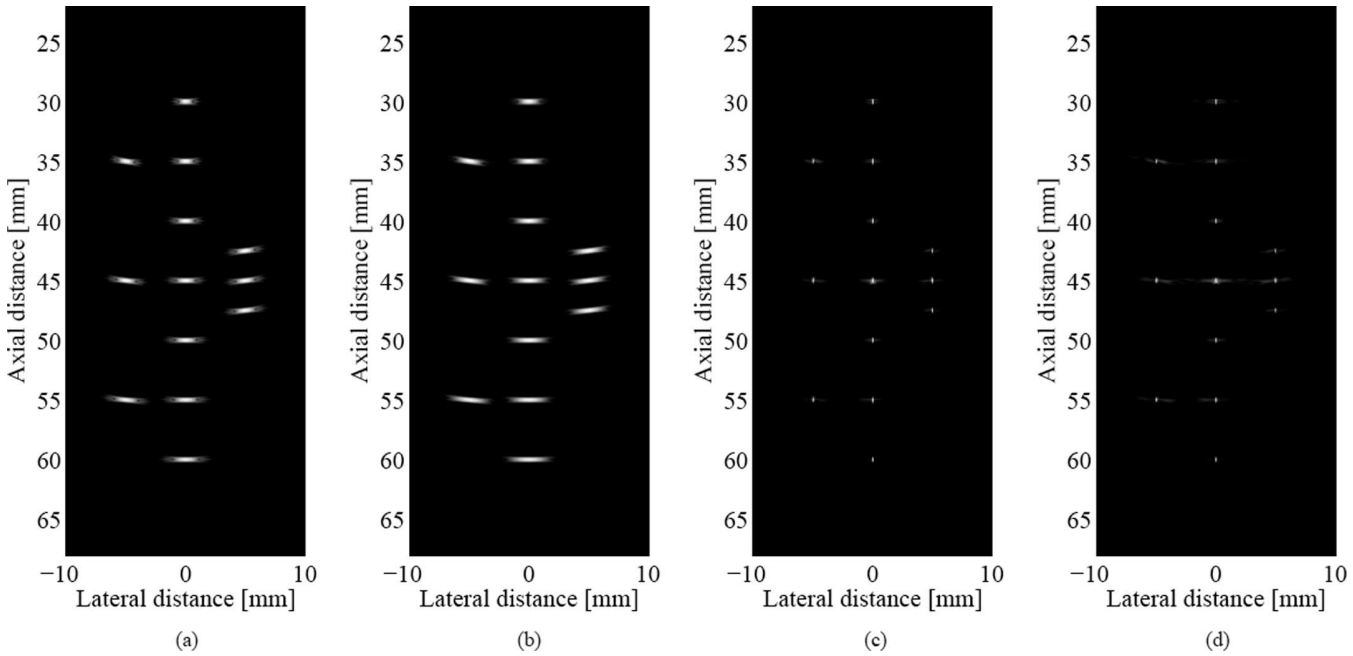

Fig. 8. Beamformed responses of the 13 point targets using simulated synthetic aperture data. (a) DS, Boxcar; (b) DS, Hanning; and (c) MV; the images are averaged over 128 emissions. (d) Response from a single element emission (element #64). All images are shown with a dynamic range of 50 dB.

TABLE II. FULL WIDTH AT HALF MAXIMUM (FWHM) AND PEAK-SIDE-LOBE LEVEL (PSL) FOR THE BEAMFORMED RESPONSES AT $z = 40$ MM.

	PSL	FWHM	
Single emission (element #64)			
DS, boxcar	−16 dB	0.79 mm	3.59λ
DS, Hanning	−36 dB	1.33 mm	6.05λ
MV	−49 dB	0.08 mm	0.36λ
Full sequence (averaged over 128 emissions)			
DS, boxcar	−32 dB	0.63 mm	2.86λ
DS, Hanning	−49 dB	0.97 mm	4.41λ
MV	−65 dB	0.08 mm	0.36λ

$\lambda = c/f_0 = 220$ μm.

response does provide a further reduction of the side-lobe level. This is substantiated by the estimated contrast levels for the 3 approaches, which are given in Table III. The contrast is computed as the ratio between the mean power within the cyst and outside the cyst.

B. Plane Wave Emission

A plane wave (PW) emission can be achieved by using all elements as both the transmitting and receiving aperture. In this way, the entire image region can be covered in a single emission. Note that when using PW, the propagation path from the transmitting element, $\vec{r}^{\,(\mathrm{xmt})}$, to the current image point, $\vec{r}_p = (x_p, z_p)$, in (1) simply becomes the axial distance, z_p, from the array to the image point

$$\left\| \vec{r}^{\,(\mathrm{xmt})} - \vec{r}_p \right\| = z_p. \tag{20}$$

The MV-beamformed response is compared with DS using boxcar and Hanning weights. The beamformed DS responses for the 13 point targets are seen in Fig. 12(b) and (c), and the MV response is seen in Fig. 12(d). The PW emission responses are compared with a conventional linear scan response. The linear scan image in Fig. 12(a) is obtained with a sliding aperture size of 128 elements and a fixed transmit focus at a depth of $z = 45$ mm. The response is beamformed using DS and dynamic Hanning apodization with $f/2$. The lateral variation of the beamformed responses, Fig. 12, are shown in Fig. 13 at depths of $z = \{40, 45\}$ mm. The FWHM and PSL are estimated at a depth of $z = 40$ mm and given in Table IV.

The PW data are obtained with boxcar apodization both in transmit and receive. This provides unwanted side-lobes below the point targets, as seen in Fig. 12(b) and (c). These could have been removed by using a transmit

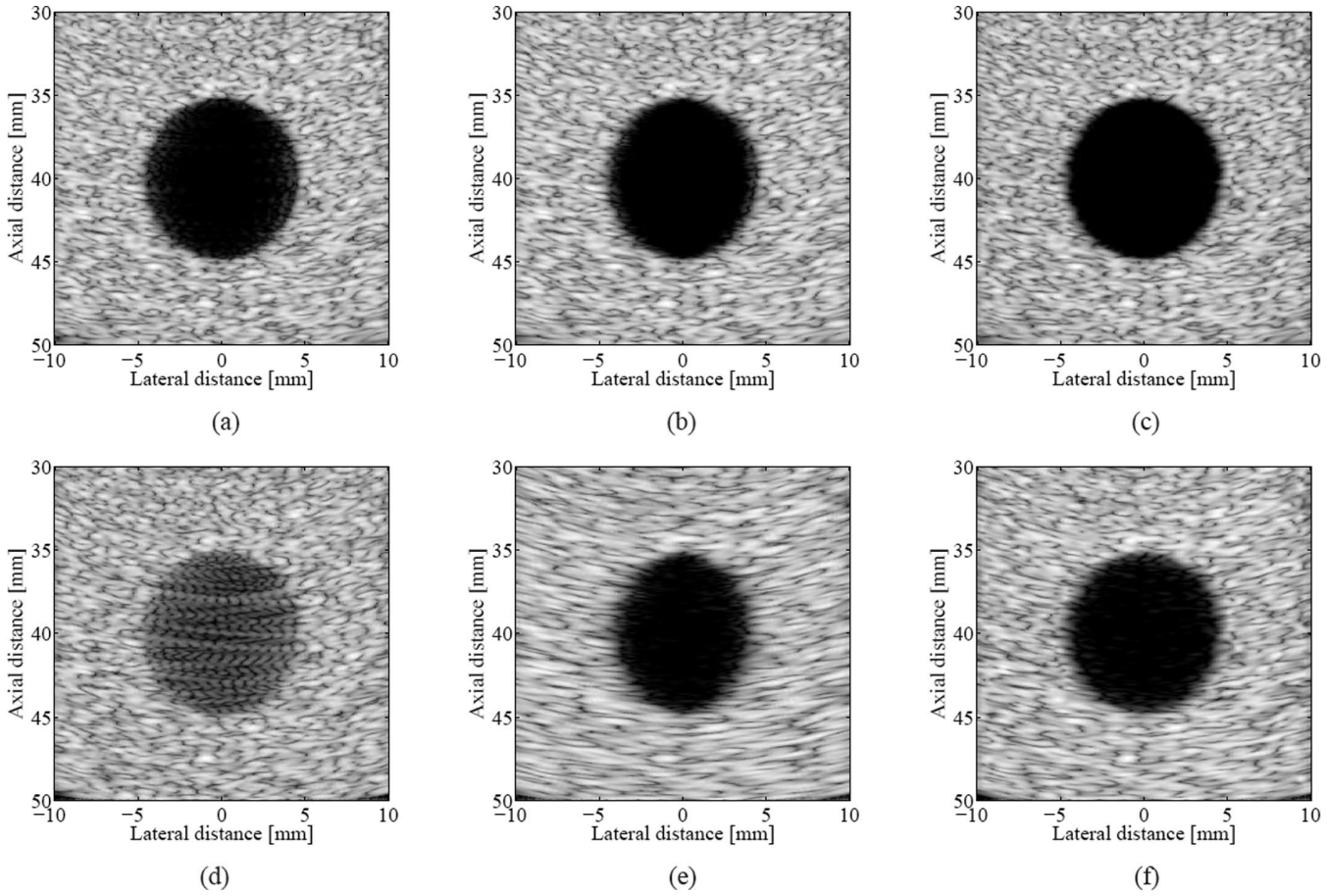

Fig. 9. Circular cyst with radius of 5 mm and center at $(x,z) = (0.40)$ mm. (a) DS, Boxcar; (b) DS, Hanning; and (c) MV; the images are the responses averaged over the full sequence of 128 emissions. (d) DS, Boxcar; (e) DS, Hanning; and (f) MV; the images are the responses to a single element emission (element #64). All images are shown with a dynamic range of 50 dB.

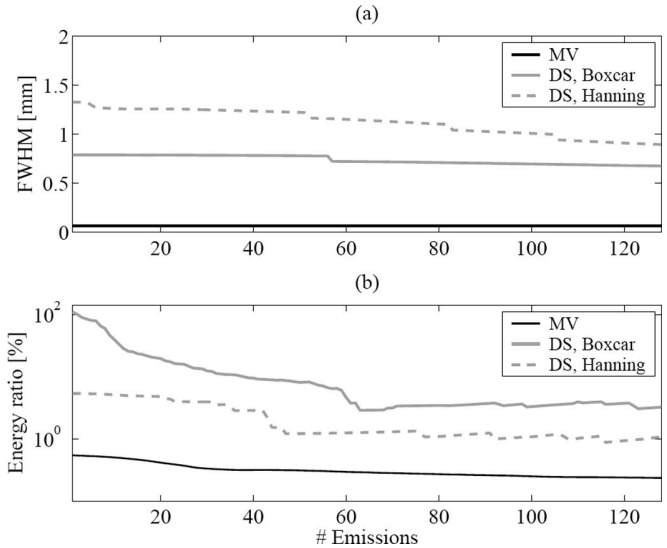

Fig. 10. Full Width at Half Maximum (FWHM) and the energy ratio above and below −40 dB of the beamformed responses with respect to the number of emissions.

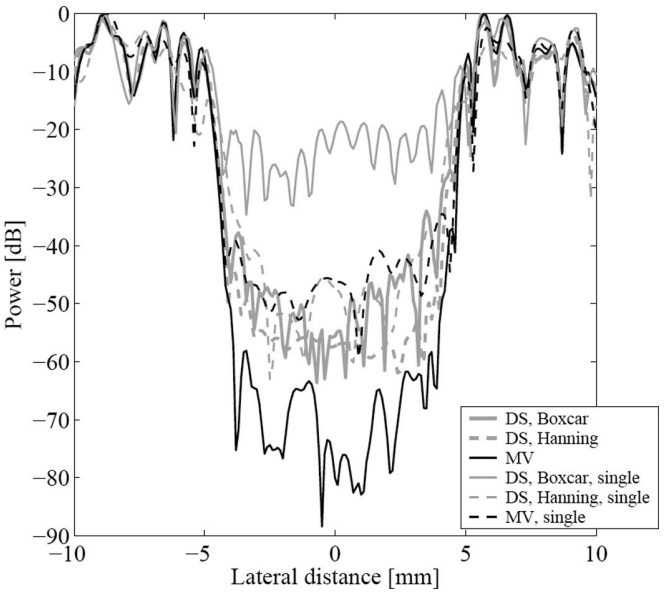

Fig. 11. Lateral variation at $z = 40$ mm of the beamformed responses in Fig. 9. The beamformed reponses in Fig. 9(a)–(c) are averaged over 128 emissions, and the responses in Fig. 9(d)–(f) are from a single emission.

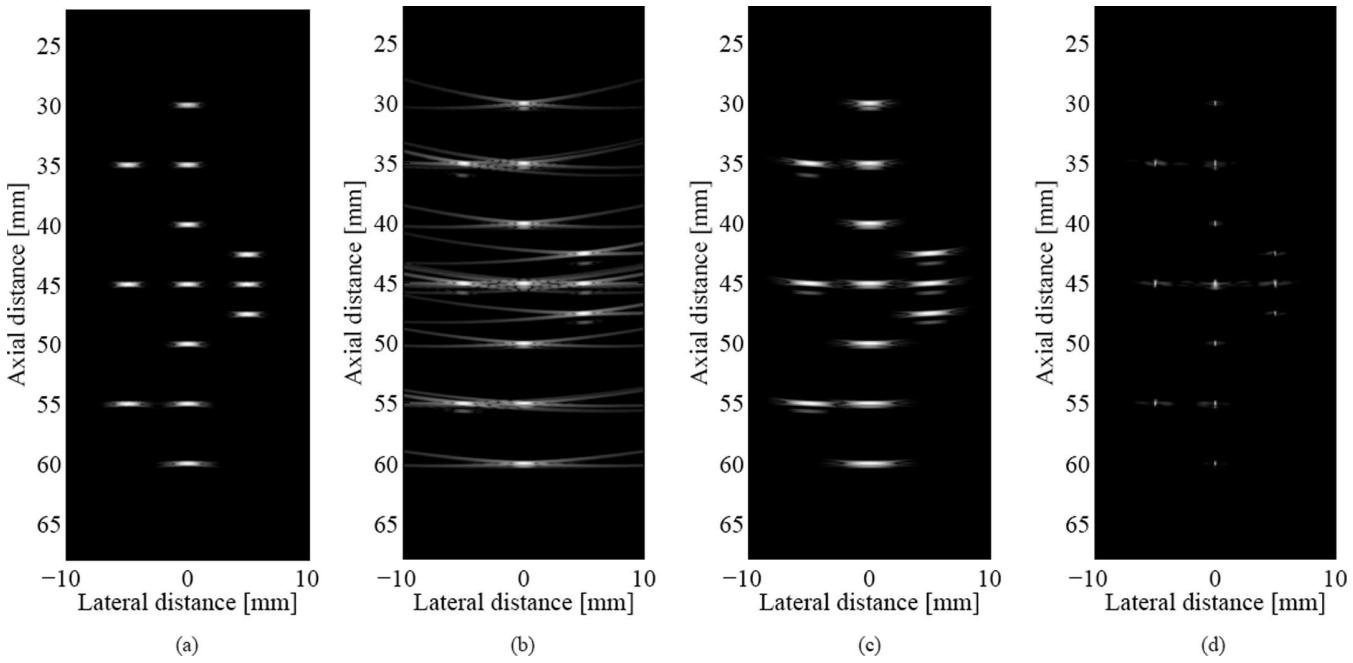

Fig. 12. Beamformed responses of the 13 point targets using simulated plane wave emission data. (a) Linear scan, DS beamformed using dynamic Hanning apodization with $f/2$; (b) DS, Boxcar; (c) DS, Hanning; and (d) MV plane wave emission images. All images are shown with a dynamic range of 50 dB.

TABLE III. CONTRAST LEVEL FOR THE CYST RESPONSES IN FIG. 9(A)–(F).

	Single emission	Full sequence
DS, Boxcar	−18 dB	−40 dB
DS, Hanning	−37 dB	−47 dB
MV	−40 dB	−60 dB

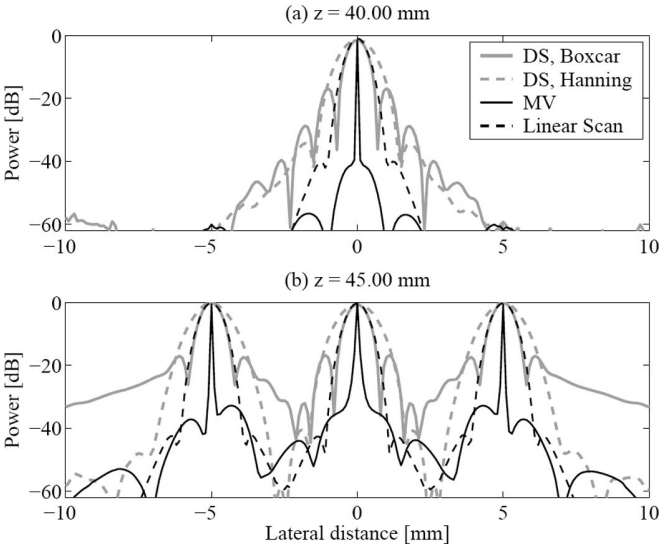

Fig. 13. Lateral variation at $z = 40$ mm (a) and 45 mm (b) of the beamformed responses shown in Fig. 8.

apodization, such as a Tukey window with 70% tapering as in [16]. However, this has not been done, to demonstrate the MV beamformer successes in eliminating these, as seen in Fig. 12(d).

Due to the focused emissions and the dynamic Hanning apodization, the linear scan sequence provides a more homogenous image than the unfocused PW transmissions. The resolution and contrast of the PW data are degraded, and the DS beamformed images are not acceptable for ultrasound imaging. The MV beamformer provides an increase of the resolution and contrast, as seen in Fig. 12(d) and Fig. 13. Even compared with the linear scan image, the MV beamformer provides a significant increase of the FWHM and PSL. From this investigation, it is seen that the increase of resolution and contrast, provided by the MV beamformer, yields the possibility of high-resolution and high-contrast PW imaging, where an image region can be covered in a single emission.

IV. THE EFFECT OF SOUND SPEED ERRORS

Adaptive beamformers are highly sensitive to steering vector errors. Robust approaches for adaptive beamforming are widely studied; see e.g., [11]. In medical ultrasound imaging, the primary cause of steering vector errors is incorrect sound speed estimates. Because this estimate varies with the characteristics of the different tissue types within the human body [17], the variation cannot be eliminated.

In the field of medical ultrasound imaging, robust methods for adaptive beamforming have been suggested by Wang *et al.* [7] and Synnevåg *et al.* [6]. However, no investigations on the performance reduction due to steering vector errors have yet been carried out.

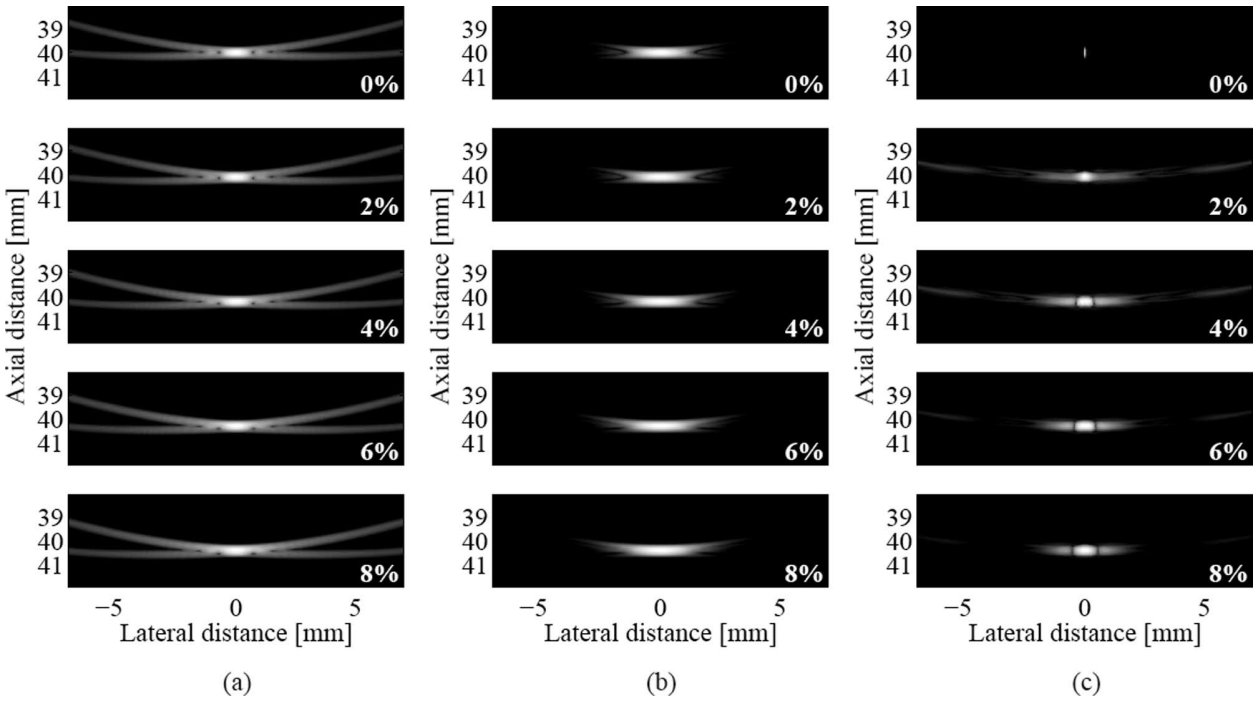

Fig. 14. Point spread functions (PSF) for the DS beamformer using boxcar (a) and Hanning (b) weights, and the MV beamformer (c) subjected to errors in the sound speed estimate. The percentage error is indicated on the lower right of each image. All images are shown with a dynamic range of 50 dB.

This section will investigate the effect of steering vector errors. The sound speed estimate is changed percentagewise from 0% to 20% of the true value. A selection of the resulting PSFs are seen in Fig. 14 with the lateral variation of the PSFs shown in Fig. 15(a)–(c). Furthermore, the FWHM with respect to the percentage error is shown in Fig. 15(d).

As described in the previous section, the top images of Fig. 14 and Fig. 15(a) show that the MV beamformer provides a significant increase in resolution and contrast compared with the DS beamformer. However, the sound speed estimate is required to be correct, an error of only a few percent degrades the potential performance significantly. As the error increases, it is seen that the MV beamformer is not as robust compared with the DS beamformer.

The FWHM in Table V is a measure of the main-lobe width and thus a measure of the resolution. It is seen that up to approximately 10%, the DS beamformer is rather robust, because the FWHM is rather constant with the percentage error of the sound speed estimate. It is noted that the DS does not outperform the MV beamformer within the investigated region of errors. In Fig. 15(d), it is seen that the FWHM for the MV beamformer does not become larger than that of the conventional beamformer.

The influence of sound speed errors cannot be ignored in medical ultrasound imaging. However, it is seen that the degradation of the performance of the MV beamformer does not lead to additional concerns beyond those that affect the DS beamformer. Thus, the adaptive beamformer can be implemented in the field of medical ultrasound imaging with the potential of increasing the resolution and contrast. This paper shows that incorrect speed of sound estimates will not lead to a performance degradation worse than that of the conventional DS beamformer.

TABLE IV. Full Width at Half Maximum (FWHM) and Peak-Side Lobe Level (PSL) for the Beamformed Responses at $z = 40$ mm.

	PSL	FWHM	
Linear Scan	−40.1 dB	0.82 mm	3.71λ
DS, Boxcar	−16.8 dB	0.71 mm	3.23λ
DS, Hanning	−34.4 dB	1.28 mm	5.81λ
MV	−57.0 dB	0.12 mm	0.53λ

$\lambda = c/f_0 = 220$ μm.

To obtain the potential increase in resolution and contrast, either robust methods should be applied or the sound speed should be estimated and compensated for [18].

V. Conclusions

An approach for near-field, adaptive beamforming of broadband data based on the minimum variance (MV) beamformer has been proposed. The approach is implemented in the frequency domain, and it provides a set of adapted, complex apodization weights for each frequency subband. The method is validated using Field II simulated synthetic aperture (SA) data and plane wave (PW) data. The performance of the MV beamformer is compared with the DS beamformer using boxcar and Hanning weights.

The adaptive subband beamformer provides a significant increase in resolution and contrast compared with

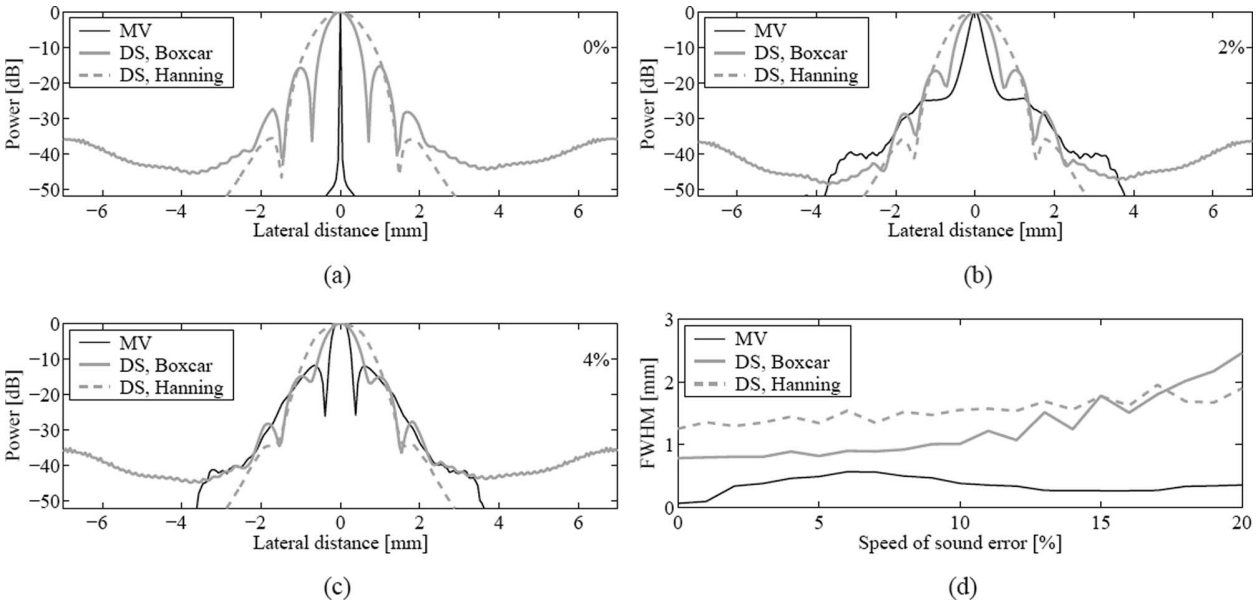

Figure 15. (a)–(c) Lateral variation of the PSF shown in Fig. 14(a)–(c), 0, 2, and 4%, respectively; (d) the FWHM with respect to the percentage error in the sound speed estimate.

TABLE V. Full Width at Half Maximum (FWHM) for the PSFs at the Depth of the Maximum Peak.

Error [%]		FWHM	
0%	DS, boxcar	0.78 mm	3.56λ
0%	DS, Hanning	1.25 mm	5.69λ
0%	MV	0.06 mm	0.29λ
2%	DS, boxcar	0.81 mm	3.67λ
2%	DS, Hanning	1.25 mm	5.89λ
2%	MV	0.34 mm	1.54λ
4%	DS, boxcar	0.89 mm	4.04λ
4%	DS, Hanning	1.44 mm	6.57λ
4%	MV	0.46 mm	2.10λ
6%	DS, boxcar	0.90 mm	4.08λ
6%	DS, Hanning	1.54 mm	7.00λ
6%	MV	0.57 mm	2.58λ
8%	DS, Boxcar	0.92 mm	4.18λ
8%	DS, Hanning	1.52 mm	6.91λ
8%	MV	0.50 mm	2.27λ
20%	DS, boxcar	2.46 mm	11.19λ
20%	DS, Hanning	1.90 mm	8.63λ
20%	MV	0.36 mm	1.61λ

$\lambda = c/f_0 = 220$ μm.

the conventional beamformer, even when using a single emission. It is seen that the resolution does not increase significantly when averaging several single emission images for MV. Thus, the MV beamformer introduces the possibility of imaging the entire region in a single emission using only a single emission.

Furthermore, the effect of steering vector errors originating from incorrect sound speed estimates on the performance of the MV beamformer has been investigated. The influence of sound speed errors cannot be ignored in medical ultrasound imaging. However, it is seen that the degradation of the performance of the MV beamformer does not lead to additional concerns beyond those that affect the DS beamformer. The achievable performance of MV is not outperformed by the conventional method.

References

[1] J. Capon, "High-resolution frequency-wavenumber spectrum analysis," *Proc. IEEE*, vol. 57, no. 8, pp. 1408–1418, Aug. 1969.

[2] J. A. Mann and W. F. Walker, "A constrained adaptive beamformer for medical ultrasound: Initial results," in *Proc. IEEE Ultrasonics Symp.*, Oct. 2002, vol. 2, pp. 1807–1810.

[3] O. L. Frost III, "An algorithm for linearly constrained adaptive array processing," *Proc. IEEE*, vol. 60, no. 8, pp. 926–935, 1972.

[4] M. Sasso and C. Cohen-Bacrie, "Medical ultrasound imaging using the fully adaptive beamformer," in *Proc. IEEE Int. Conf. Acoustics, Speech, and Signal Processing*, Mar. 2005, vol. 2, pp. 489–492.

[5] F. Viola and W. F. Walker, "Adaptive signal processing in medical ultrasound beamforming," in *Proc. IEEE Ultrasonics Symp.*, 2005, vol. 4, pp. 1980–1983.
[6] J.-F. Synnevåg, A. Austeng, and S. Holm, "Adaptive beamforming applied to medical ultrasound imaging," *IEEE Trans. Ultrason. Ferroelectr. Freq. Control*, vol. 54, no. 8, pp. 1606–1613, Aug. 2007.
[7] Z. Wang, J. Li, and R. Wu, "Time-delay- and time-reversal-based robust capon beamformers for ultrasound imaging," *IEEE Trans. Med. Imaging*, vol. 24, no. 10, pp. 1308–1322, Oct. 2005.
[8] I. K. Holfort, F. Gran, and J. A. Jensen, "Minimum variance beamforming for high frame-rate ultrasound imaging," in *Proc. IEEE Ultrasonics Symp.*, Oct. 2007, pp. 1541–1544.
[9] J. A. Jensen and N. B. Svendsen, "Calculation of pressure fields from arbitrarily shaped, apodized, and excited ultrasound transducers," *IEEE Trans. Ultrason. Ferroelectr. Freq. Control*, vol. 39, pp. 262–267, Mar. 1992.
[10] J. A. Jensen, "Field: A program for simulating ultrasound systems," *Med. Biol. Eng. Comp.*, 10th Nordic-Baltic Conference on Biomedical Imaging, vol. 4, suppl. 1, part 1, pp. 351–353, 1996b.
[11] J. Li and P. Stoica, *Robust Adaptive Beamforming*. New York: John Wiley & Sons, 2006.
[12] J. S. Arora, *Introduction to Optimum Design*. New York: McGraw-Hill, Inc., 1989.
[13] T.-J. Shan and T. Kailath, "Adaptive beamforming for coherent signals and interference," *IEEE Trans. Acoust. Speech. Sig. Pro.*, vol. 33, no. 3, pp. 527–536, Jun. 1985.
[14] D. H. Johnson and D. E. Dudgeon, *Array Signal Processing. Concepts and Techniques.* Englewood Cliffs, NJ: Prentice-Hall, 1993.
[15] S. I. Nikolov and J. A. Jensen, "In-vivo synthetic aperture flow imaging in medical ultrasound," *IEEE Trans. Ultrason. Ferroelectr. Freq. Control*, vol. 50, no. 7, pp. 848–856, 2003.
[16] J. Udesen, F. Gran, and J. A. Jensen, "Fast color flow mode imaging using plane wave excitation and temporal encoding," in *Proc. SPIE—Progress in Biomedical Optics and Imaging*, 2005, vol. 5750, pp. 427–436.
[17] S. A. Goss, R. L. Johnston, and F. Dunn, "Comprehensive compilation of empirical ultrasonic properties of mammalian tissues," *J. Acoust. Soc. Am.*, vol. 64, pp. 423–457, Aug. 1978.
[18] D. Robinson, J. Ophir, and C. Chen, "Pulse-echo ultrasound speed measurements: Progress and prospects," *Ultrasound Med. Biol.*, vol. 17, no. 6, pp. 633–646, 1991.

Iben Kraglund Holfort (S'08) was born in Viborg, Denmark, in 1980. She earned her M.Sc. degree in electrical engineering from the Technical University of Denmark in 2006. She is currently pursuing a Ph.D. degree in signal processing at the Technical University of Denmark.

Her research interests include array signal processing, adaptive beamforming, and blood flow estimation.

Fredrik Gran earned his M.Sc. in engineering physics from Lund University in 2002. In 2005, Dr. Gran received the Ph.D. degree from the Technical University of Denmark for work on ultrasound signal processing. From 2005 to 2008, he was employed as Assistant Professor at the Technical University of Denmark. In January 2008, Dr. Gran joined GN ReSound A/S as a research scientist in hearing aid signal processing.

His research interests include adaptive signal processing, adaptive beamforming, and acoustics.

Jørgen Arendt Jensen earned his Master of Science degree in electrical engineering in 1985 and the Ph.D. degree in 1989, both from the Technical University of Denmark. He received the Dr.Techn. degree from the university in 1996. He has published more than 160 journal and conference papers on signal processing and medical ultrasound and the book *Estimation of Blood Velocities Using Ultrasound*, Cambridge University Press in 1996. He is also developer of the Field II simulation program. He has been a visiting scientist at Duke University, Stanford University, and the University of Illinois at Urbana-Champaign. He is currently full professor of Biomedical Signal Processing at the Technical University of Denmark at the Department of Electrical Engineering and head of Center for Fast Ultrasound Imaging and the Group for Biomedical Engineering. He is also adjunct full professor at the Faculty of Health Sciences at the University of Copenhagen. He has given courses on blood velocity estimation at both Duke University and University of Illinois and teaches biomedical signal processing and medical imaging at the Technical University of Denmark. He has given several short courses on simulation, synthetic aperture imaging, and flow estimation at international scientific conferences. He has received several awards for his research.

He is also the co-organizer of B.Sc./M.Sc. education in biomedical engineering offered jointly by the Technical University of Denmark and the University of Copenhagen. His research is centered around simulation of ultrasound imaging, synthetic aperture imaging, vector blood flow estimation, and construction of ultrasound research systems.

Paper II

Minimum Variance Beamforming for High Frame-Rate Ultrasound Imaging

I. K. Holfort, F. Gran and J. A. Jensen

Proceedings of the IEEE International Ultrasonics Symposium

Presented in New York, USA, Oct. 2007

Minimum Variance Beamforming for High Frame-Rate Ultrasound Imaging

Iben Kraglund Holfort, Fredrik Gran and Jørgen Arendt Jensen

Center for Fast Ultrasound Imaging, Ørsted•DTU, Bldg. 349,
Technical University of Denmark, DK-2800 Kgs. Lyngby, Denmark

***Abstract*— This paper investigates the application of adaptive beamforming in medical ultrasound imaging. A minimum variance (MV) approach for near-field beamforming of broadband data is proposed. The approach is implemented in the frequency domain, and it provides a set of adapted, complex apodization weights for each frequency sub-band. As opposed to the conventional, Delay and Sum (DS) beamformer, this approach is dependent on the specific data.**

The performance of the proposed MV beamformer is tested on simulated synthetic aperture (SA) ultrasound data, obtained using Field II. For the simulations, a 7 MHz, 128-element, phased array transducer with $\lambda/2$-spacing was used. Data is obtained using a single element as the transmitting aperture and all 128 elements as the receiving aperture. A full SA sequence consisting of 128 emissions was simulated by sliding the active transmitting element across the array. Data for 13 point targets and a circular cyst with a radius of 5 mm were simulated. The performance of the MV beamformer is compared to DS using boxcar weights and Hanning weights, and is quantified by the Full Width at Half Maximum (FWHM) and the peak-side-lobe level (PSL). Single emission $\{$DS Boxcar, DS Hanning, MV$\}$ provide a PSL of $\{-16, -36, -49\}$ dB and a FWHM of $\{0.79, 1.33, 0.08\}$ mm = $\{3.59\lambda, 6.05\lambda, 0.36\lambda\}$. Using all 128 emissions, $\{$DS Boxcar, DS Hanning, MV$\}$ provide a PSL of $\{-32, -49, -65\}$ dB, and a FWHM of $\{0.63, 0.97, 0.08\}$ mm = $\{2.86\lambda, 4.41\lambda, 0.36\lambda\}$. The contrast of the beamformed single emission responses of the circular cyst were calculated to $\{-18, -37, -40\}$ dB.

The simulations have shown that the frequency sub-band MV beamformer provides a significant increase in lateral resolution compared to DS, even when using considerably fewer emissions. An increase in resolution is seen when using only one single emission. Furthermore, it is seen that an increase of the number of emissions does not alter the FWHM. Thus, the MV beamformer introduces the possibility for high frame-rate imaging with increased resolution.

I. Introduction

Recently, the application of adaptive beamforming methods to the field of medical ultrasound imaging has been an increasingly area of interest. In recent literature [1]–[6] adaptive beamformers have been applied to medical ultrasound imaging with significant improvements in terms of lateral resolution and contrast.

In traditional beamforming, the Delay and Sum (DS) beamformer uses a fixed, predefined set of apodization weights. Whereas the adaptive methods actively finds a set of apodization weights, which is adapted to the specific data.

One of these adaptive methods is the Minimum Variance (MV) beamformer, which finds a set of weights that minimizes the variance of the weighted sensor signals under the constraint that the signal emerging from the point of interest is passed without distortion. The MV optimized weights are found in a single iteration, but it does require a matrix inversion, which increases the computational cost compared to DS.

In this paper an approach for near-field beamforming of broad-band data is proposed. This approach is implemented in the frequency domain, and it provides a set of adapted, complex apodization weights for each frequency sub-band.

II. Method

A. Presteering

As in conventional beamforming, the sensor signals are presteered, so that each scan line is dynamically focused. Considering a linear array transducer with M sensor elements, the mth dynamically focused sensor signal along the ℓth scan line is given by

$$y_{m,\ell}(z) = s\left(\frac{\|\vec{r}_{\ell}^{\,(xmt)}(z)\| + \|\vec{r}_{m,\ell}^{\,(rcv)}(z)\|}{c}\right) \qquad (1)$$

for $m = 0, 1, \ldots, M-1$ and $\ell = 0, 1, \ldots, L-1$, where z denotes the spatial position along the ℓth scan line, $s(t)$ is the received waveform, $\vec{r}^{\,(xmt)}$ and $\vec{r}^{\,(rcv)}$ are the spatial positions of the transmitting and the receiving sensor elements, and c is the speed of sound.

The output of the beamformer is given by the weighted sum of the dynamically focused scan lines, so that the ℓth scan line is given by

$$b_{\ell}(z) = \sum_{m=0}^{M-1} w_{m,\ell}\, y_{m,\ell}(z)\,, \qquad (2)$$

where $w_{m,\ell}$ is the apodization weight for the mth sensor signal.

B. Sub-Band Beamforming

The MV beamformer [7] is originally developed for narrow-band applications. Applying MV to broad-band ultrasound data, the sensor signals are divided into sub-bands using the short-time Fourier transform. For each point, z_0, along the ℓth scan line, the Fourier transform is applied on a segment of the sensor signals. The mth segmented sensor signal is given by

$$\tilde{y}_{m,\ell}(z, z_0) = y_{m,\ell}(z - z_0), \quad z \in [-Z/2; Z/2]\,, \qquad (3)$$

where Z is the size of the segment. For the given point, z_0, the beamformer output for each spatial frequency sub-band, k, is given by

$$B_\ell(k, z_0) = \sum_{m=0}^{M-1} w^*_{m,\ell}(k, z_0) Y_{m,\ell}(k, z_0) \,, \tag{4}$$

where $Y_{m,\ell}(k, z_0)$ is the Fourier transform of the mth segmented sensor signal, $\tilde{y}_{m,\ell}(z, z_0)$, given in (3), and $\{\cdot\}^*$ denotes the complex conjugate. By defining the vectors

$$\mathbf{w}_\ell(k, z_0) = \begin{pmatrix} w_{0,\ell}(k, z_0) & w_{1,\ell}(k, z_0) & \cdots & w_{M-1,\ell}(k, z_0) \end{pmatrix}^T$$
$$\mathbf{Y}_\ell(k, z_0) = \begin{pmatrix} Y_{0,\ell}(k, z_0) & Y_{1,\ell}(k, z_0) & \cdots & Y_{M-1,\ell}(k, z_0) \end{pmatrix}^T$$

the beamformer output (4) rewrites into

$$B_\ell(k, z_0) = \mathbf{w}_\ell(k, z_0)^H \mathbf{Y}_\ell(k, z_0) \,, \tag{5}$$

where the superscripts, $\{\cdot\}^T$ and $\{\cdot\}^H$, denote the non-conjugate and the conjugate transpose, respectively.

Note that the sub-band division provides the possibility of weighting both each sub-band and each point differently.

C. Minimum Variance Beamforming

The adaptive beamformer uses a set of apodization weights, which are dependent on the frequency content of the specific sensor signals. The MV beamformer continuously updates the weights, so that the variance (or power) of the beamformer output is minimized, while the response from the focus point is passed without distortion. The power of the beamformer output is given by

$$\mathcal{P}_\ell(k, z_0) = \mathcal{E}\left\{|B_\ell(k, z_0)|^2\right\} \tag{6}$$
$$= \mathbf{w}_\ell(k, z_0)^H \mathbf{R}_\ell(k, z_0) \mathbf{w}_\ell(k, z_0) \,, \tag{7}$$

where $\mathcal{E}\{\cdot\}$ denotes the expectation value, and $\mathbf{R}_\ell(k, z_0)$ is the covariance matrix given by

$$\mathbf{R}_\ell(k, z_0) = \mathcal{E}\left\{\mathbf{Y}_\ell(k, z_0) \mathbf{Y}_\ell(k, z_0)^H\right\} \,. \tag{8}$$

Mathematically, the MV beamformer is expressed as [7]

$$\min_{\mathbf{w}_\ell(k,z_0)} \mathbf{w}_\ell(k, z_0)^H \mathbf{R}_\ell(k, z_0) \mathbf{w}_\ell(k, z_0)$$
$$\text{subject to } \mathbf{w}_\ell(k, z_0)^H \mathbf{e}(k, z_0) = 1 \,, \tag{9}$$

where $\mathbf{e}(k, z_0)$ is the so-called steering vector, which characterizes the response from the focus point.

The solution to the optimization problem (9) can be found in a single iteration using Lagrangian multiplier theory as [7]

$$\mathbf{w}_\ell(k, z_0) = \frac{\mathbf{R}_\ell(k, z_0)^{-1} \mathbf{e}(k, z_0)}{\mathbf{e}(k, z_0)^H \mathbf{R}_\ell(k, z_0)^{-1} \mathbf{e}(k, z_0)} \,, \tag{10}$$

provided that $\mathbf{R}_\ell(k, z_0)^{-1}$ exists. Due to presteering and sub-band division, the response from the focus point will resemble a plane wave incident directly onto the array. Thus, the steering vector is constant across the array and independent on the frequency, and it simply becomes a $M \times 1$-vector of ones.

D. Subarray Averaging

In real applications, the covariance matrix is unknown and must be estimated from data. To obtain a useful estimate, the array is divided into overlapping subarrays, and the subcovariance matrices are averaged across the array. According to [8] the spatially smoothed covariance matrix estimate will always become non-singular, if the size of the subarray satisfies $M_p \leq \frac{M}{2}$. The covariance matrix estimate can be expressed as

$$\mathbf{R}_\ell(k, z_0) = \sum_{p=0}^{M-M_p+1} \mathbf{G}_{p,\ell}(k, z_0) \mathbf{G}_{p,\ell}(k, z_0)^H \,, \tag{11}$$

where $\mathbf{G}_{p,\ell}(k, z_0)$ denotes the pth subarray given by

$$\mathbf{G}_{p,\ell}(k, z_0) = \begin{pmatrix} Y_{p,\ell}(k, z_0) & Y_{p+1,\ell}(k, z_0) & \cdots & Y_{p+M_p-1,\ell}(k, z_0) \end{pmatrix}^T$$

for $p = 0, 1, \ldots, M_p - 1$. Note that this reduces the dimension of the covariance matrix, and thus the number of weights will be reduced correspondingly.

III. Results

The proposed MV beamformer is tested on simulated synthetic aperture (SA) ultrasound data, obtained using Field II [9], [10]. For the simulations, a 7 MHz, 128-element, phased array transducer with $\lambda/2$-spacing was used. Data is obtained using a single element as the transmitting aperture and all $M = 128$ elements as the receiving aperture. A full SA sequence consisting of 128 emissions was simulated by sliding the active transmitting element across the array. Data for 13 point targets and a circular cyst with a radius of 5 mm were simulated.

The MV beamformer is implemented in the frequency domain using the short time Fourier transform with a segment size corresponding to the length of the excitation pulse convolved with the two-way impulse response of the transducer. A subarray size of $M_p = \frac{M}{4} = 32$ was used, and before beamforming, additional white, Gaussian noise with a signal-to-noise ratio (SNR) of 60 dB was added to each of the sensor signals.

The performance of MV is compared to DS using boxcar weights and Hanning weights. The performance is quantified by the Full Width at Half Maximum (FWHM) and the peak-side-lobe level (PSL), which is defined as the peak value of the first side-lobe.

A. Point Targets

The beamformed responses of the 13 point targets are shown in Fig. 1(a)-(d) with a dynamic range of -50 dB. The three responses in Fig. 1(a)-(c) are averaged over 128 emissions, and the MV response on the right, Fig. 1(d), is from a single element emission (corresponding to element #64). The lateral variation of the beamformed responses at $z = \{40, 45\}$ mm are seen in Fig. 3(a)-(b). It is seen that MV provides a significant increase of the lateral resolution and a lowering of the side-lobes.

The resolution and contrast improvements are quantified using the FWHM and PSL. These quantitative measures are calculated at a depth of 40 mm and are given in Table I. The

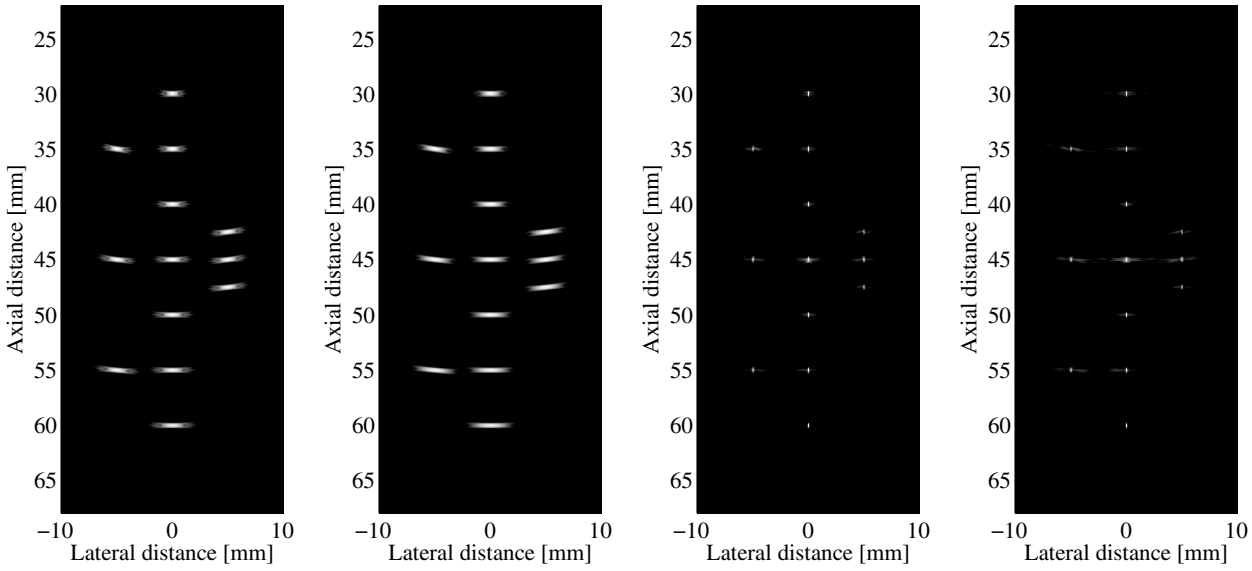

(a) DS, Boxcar (b) DS, Hanning (c) MV (d) MV, single element

Fig. 1. Beamformed responses of the 13 point targets. (a)-(c) The images are averaged over 128 emissions. (d) No averaging is applied, response from a single element emission (element #64). All images are shown with a dynamic range of -50 dB.

measures are given for the single element emission and for the full SA sequence. It is seen that the MV beamformer provides a significant improvement in terms of both FWHM and PSL. The FWHM of MV from a single emission response comprise only $\{12.7\%, 8.2\%\}$ of the FWHM from the full DS sequence using DS{Boxcar,Hanning}.

The MV response does not change significantly in the interval of $[-40; 0]$ dB. The FWHM is calculated at a level of -6 dB and will not change for MV, when averaging over all 128 emissions. This is shown in Fig. 2(a), where the FWHM for DS and MV are shown with respect to the number of emissions. Furthermore, the ratio of energy above

	PSL	FWHM	
Single emission (element #64)			
DS, Boxcar	-16 dB	0.79 mm	3.59λ
DS, Hanning	-36 dB	1.33 mm	6.05λ
MV	-49 dB	0.08 mm	0.36λ
Full sequence (averaged over 128 emissions)			
DS, Boxcar	-32 dB	0.63 mm	2.86λ
DS, Hanning	-49 dB	0.97 mm	4.41λ
MV	-65 dB	0.08 mm	0.36λ

$\lambda = c/f_0 = 220$ μm

TABLE I

FULL WIDTH AT HALF MAXIMUM (FWHM) AND PEAK-SIDE-LOBE LEVEL (PSL) FOR THE BEAMFORMED RESPONSES AT $z = 40$ MM.

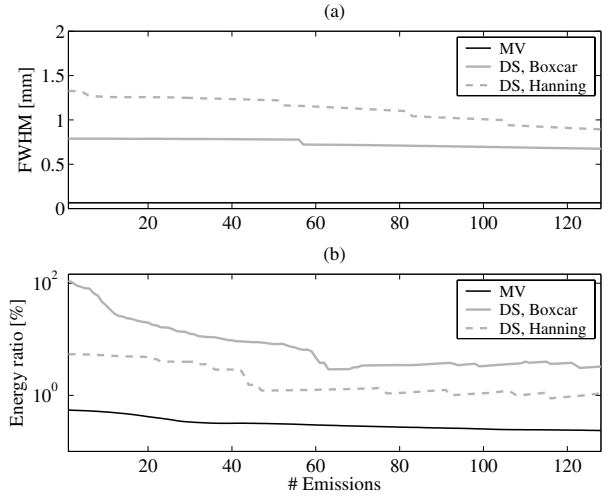

Fig. 2. Full Width at Half Maximum (FWHM) and the energy ratio above and below -40 dB of the beamformed responses with respect to the number of emissions.

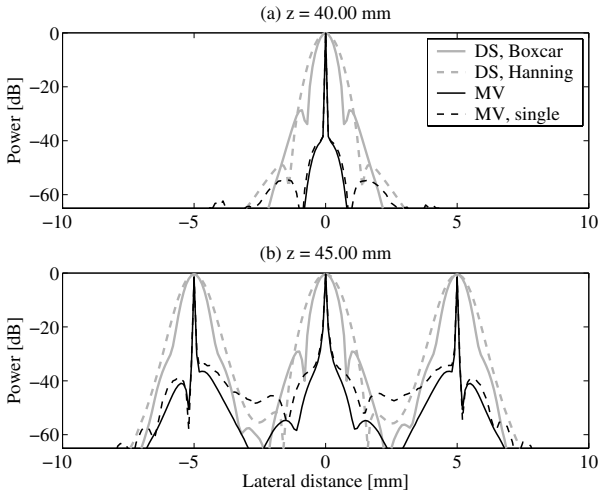

Fig. 3. Lateral variation at $z = \{40, 45\}$ mm of the beamformed responses shown in Fig. 1(a)-(d).

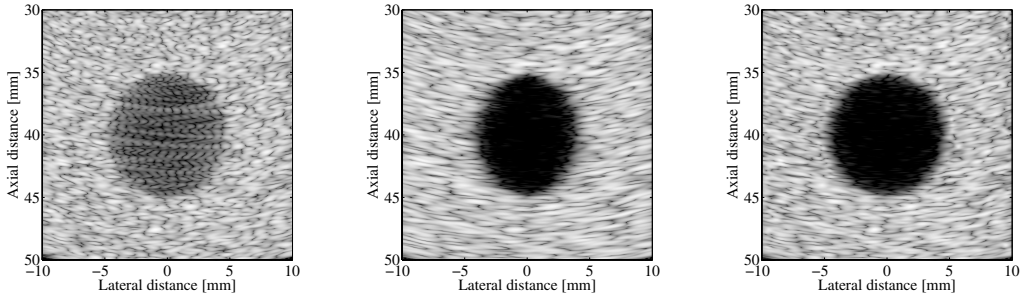

(a) DS, Boxcar Contrast: -18 dB (b) DS, Hanning Contrast: -37 dB (c) MV Contrast: -40 dB

Fig. 4. Circular cyst with radius of 5 mm and center at $(x, z) = (0, 40)$ mm. (a)-(c) The images are responses to a single element emission (element #64). All images are shown with a dynamic range of -50 dB.

and below -40 dB has been calculated relative to the number of emissions, shown in Fig. 2(b). This ratio is a measure of the relative energy within the main-lobe. As it reduces, the relative energy within the main-lobe reduces, which could mean that the width of the main-lobe decreases. It is seen that this ratio reduces with the number of emissions. However, the reduction for MV is not as immense as for DS. Thus, the MV response does not improve significantly, when averaging over several emissions.

B. Circular Cyst

In this section, simulated data of a circular cyst in a speckle pattern is considered. The circular cyst has a radius of 5 mm and center at $(x, z) = (0, 40)$ mm. The speckle pattern is simulated with 10 randomly placed scatterers within a resolution cell of λ^3 to ensure fully developed speckle.

The beamformed responses from a single element emission (corresponding to element #64) are shown in Fig. 4(a)-(c). The resulting contrast for each of the three responses are $\{-18, -37, -40\}$ dB. The contrast is computed as the ratio between the mean energy within the cyst and outside the cyst.

In real applications, the DS responses will be averaged over several emissions to obtain a better contrast. Furthermore, averaging emissions from different spatial positions would also result in a circular cyst using DS with Hanning weights. However, these single emission responses are shown to emphasize the differences between the three beamforming approaches.

It is seen that the high side-lobe level of the DS Boxcar apodization results in a rather poor contrast. Furthermore, it is seen that the DS response using Hanning apodization does not result in a circular shape of the cyst. The shape is rather oval due to the lateral broadening from the Hanning apodization. However, the Hanning apodization provides a suitable contrast level, as the side-lobes are lowered to the SNR level at -60 dB. The MV response shows a circular shape of the cyst as well as a suitable contrast difference between the inner part of the cyst and the speckle pattern. From this investigation, it is seen that the MV beamformer provides a lowering of the side-lobe level without smoothing the responses laterally.

IV. Conclusions

The proposed approach for near-field, broad band adaptive beamforming was implemented in the frequency domain and investigated based on simulated ultrasound data. The investigations have shown that each frequency sub-band can be treated independently. The adaptive sub-band beamformer provides a significant increase in lateral resolution and contrast compared to the conventional beamformer, even when using considerably fewer emissions. An increase in resolution is seen when using only one single emission. Furthermore, it is seen that an increase of the number of emissions does not alter the FWHM. Thus, the MV beamformer introduces the possibility for high frame-rate imaging with increased resolution.

V. Acknowledgment

This work was supported by grant 9700883, 9700563 and 26-01-0178 from the Danish Science Foundation and by B-K Medical A/S, Denmark.

References

[1] M. Sasso and C. Cohen-Bacrie, "Medical Ultrasound Imaging Using the Fully Adaptive Beamformer," in *Proc. IEEE Int. Conf. Acous., Speech, Sig. Pro.*, March 2005, vol. 2, pp. 489–492.

[2] J. A. Mann and W. F. Walker, "A Constrained Adaptive Beamformer for Medical Ultrasound: Initial Results," in *Proc. IEEE Ultrason. Symp.*, Oct. 2002, vol. 2, pp. 1807–1810.

[3] F. Viola and W. F. Walker, "Adaptive Signal Processing in Medical Ultrasound Beamforming," in *Proc. IEEE Ultrason. Symp.*, 2005, vol. 4, pp. 1980–1983.

[4] J.-F. Synnevåg, A. Austeng, and S. Holm, "Minimum Variance Adaptive Beamforming Applied to Medical Ultrasound Imaging," in *Proc. IEEE Ultrason. Symp.*, Sept. 2005, vol. 2, pp. 1199–1202.

[5] J.-F. Synnevåg, A. Austeng, and S. Holm, "High frame-rate and high resolution medical imaging using adaptive beamforming," in *Proc. IEEE Ultrason. Symp.*, Oct. 2006, vol. 2.

[6] J.-F. Synnevåg, A. Austeng, and S. Holm, "Adaptive Beamforming Applied to Medical Ultrasound Imaging," *IEEE Trans. Ultrason., Ferroelec., Freq. Contr.*, vol. 54, no. 8, pp. 1606–1613, August 2007.

[7] J. Capon, "High-Resolution Frequency-Wavenumber Spectrum Analysis," *Proc. IEEE*, vol. 57, no. 8, pp. 1408–1418, August 1969.

[8] T.-J. Shan and T. Kailath, "Adaptive Beamforming for Coherent Signals and Interference," *IEEE Trans. Acous., Speech, Sig. Pro.*, vol. 33, no. 3, pp. 527–536, June 1985.

[9] J. A. Jensen and N. B. Svendsen, "Calculation of pressure fields from arbitrarily shaped, apodized, and excited ultrasound transducers," *IEEE Trans. Ultrason., Ferroelec., Freq. Contr.*, vol. 39, pp. 262–267, 1992.

[10] J. A. Jensen, "Field: A program for simulating ultrasound systems," *Med. Biol. Eng. Comp.*, vol. 10th Nordic-Baltic Conference on Biomedical Imaging, Vol. 4, Supplement 1, Part 1, pp. 351–353, 1996b.

Paper III

Plane Wave Medical Ultrasound Imaging Using Adaptive Beamforming

I. K. Holfort, F. Gran and J. A. Jensen

Proceedings of the 5th IEEE Sensor Array and Multichannel Signal Processing Workshop

Presented in Darmstadt, Germany, July 2008

PLANE WAVE MEDICAL ULTRASOUND IMAGING USING ADAPTIVE BEAMFORMING

Iben Kraglund Holfort[*], *Fredrik Gran*[†] *and Jørgen Arendt Jensen*[*]

[*]Center for Fast Ultrasound Imaging, Department of Electrical Engineering,
Technical University of Denmark, DK-2800 Kgs. Lyngby, Denmark

[†]GN ReSound A/S, Lautrupbjerg 9, DK-2750 Ballerup, Denmark

ABSTRACT

In this paper, the adaptive, minimum variance (MV) beamformer is applied to medical ultrasound imaging. The significant resolution and contrast gain provided by the adaptive, minimum variance (MV) beamformer, introduces the possibility of plane wave (PW) ultrasound imaging. Data is obtained using Field II and a 7 MHz, 128-elements, linear array transducer with $\lambda/2$-spacing. MV is compared to the conventional delay-and-sum (DS) beamformer with Boxcar and Hanning weights. Furthermore, the PW images are compared to the a conventional ultrasound image, obtained from a linear scan sequence. The four approaches, $\{$Linear Scan, DS Boxcar, DS Hanning, MV$\}$, have full width at half maximum of $\{0.82, 0.71, 1.28, 0.12\}$ mm and peak side-lobe levels of $\{-40.1, -16.8, -34.4, -57.0\}$ dB.

1. INTRODUCTION

A conventional ultrasound image is formed from several focused ultrasound transmissions, so that each scan line in the image is obtained from an additional, focused ultrasound transmission. To cover the entire image region, the aperture is slid along the scan plane.

An alternative approach is to use a single unfocused transmission, also referred to as a plane wave transmission. In this way, the entire image region is covered in a single transmission. However, this approach traditionally provides images with poor contrast and resolution due to the limitations of the conventional, delay-and-sum (DS) beamformer.

For decades data-dependent, adaptive beamformers have been used in other fields of array signal processing, e.g. sonar and radar. Whereas the conventional beamformer is a passive process using predefined, fixed, data-independent (apodization) weights, the adaptive beamformer actively updates a set of new apodization weights for each point in the image. These apodization weights are dependent on the input data. One of the widely used methods was originally introduced by Capon in 1969 [1].

Recently, the application of adaptive beamforming to the field of medical ultrasound imaging has been an area of increased interest. In recent literature [2, 3, 4, 5, 6], adaptive beamformers have been applied to medical ultrasound imaging with significant improvements in terms of lateral resolution and contrast.

Previously, an approach for near-field beamforming of broad-band ultrasound data has been proposed [6]. This approach is implemented in the frequency domain, and it provides a set of adapted, complex apodization weights for each frequency sub-band.

The purpose of this paper is to apply the proposed beamformer to ultrasound data obtained from a plane wave (PW) transmission. The performance of the proposed beamformer is compared to the DS beamformer using Boxcar and Hanning weights. Furthermore, the resulting image from the PW sequence is compared to an image obtained using a conventional ultrasound, focused transmission sequence.

2. METHOD

As in conventional beamforming, the sensor signals are presteered, so that each scan line is dynamically focused. Considering a linear array transducer with M sensor elements, the mth dynamically focused sensor signal along the ℓth scan line is given by

$$y_{m,\ell}(z) = s\left(\tau_{m,\ell}(z)\right) \ , \tag{1}$$

for $m = 0, 1, \ldots, M-1$ and $\ell = 0, 1, \ldots, L-1$, where z denotes the spatial position along the ℓth scan line, $s(t)$ is the received waveform. The delay line, $\tau_{m,\ell}(z)$, is found from the propagation path of the sound waves from the transmitting element to the focal point and returning to the receiving element, and is given by

$$\tau_{m,\ell}(z) = \frac{\|\vec{r}^{\,(xmt)} - \vec{r}_\ell(z)\| + \|\vec{r}_m^{\,(rcv)} - \vec{r}_\ell(z)\|}{c} \ , \tag{2}$$

where $\vec{r}^{\,(xmt)}$ and $\vec{r}_m^{\,(rcv)}$ are the spatial positions of the transmitting and the mth receiving sensor elements, $\vec{r}_\ell(z)$

This work was supported by grant 26-04-0024 from the Danish Science Foundation, grant 274-05-0327 from the Danish Research Agency, the Radio-parts foundation and by B-K Medical ApS, Denmark.

denotes the focal point, and c is the speed of sound. The output of the beamformer is given by the weighted sum of the dynamically focused scan lines.

2.1. Sub-Band Beamforming

The MV beamformer [1] is originally developed for narrow-band applications. Applying MV to broad-band ultrasound data, the sensor signals are divided into sub-bands using the short-time Fourier transform. For each point, z_0, along the ℓth scan line, the Fourier transform is applied on a segment of the sensor signals. The mth segmented sensor signal is given by

$$\tilde{y}_{m,\ell}(z, z_0) = y_{m,\ell}(z + z_0), \quad z \in [-Z/2; Z/2] \ , \tag{3}$$

where Z is the size of the segment. For the given point, z_0, the beamformer output for each spatial frequency sub-band, k, is given by

$$B_\ell(k, z_0) = \sum_{m=0}^{M-1} w^*_{m,\ell}(k, z_0) Y_{m,\ell}(k, z_0) \ , \tag{4}$$

where $Y_{m,\ell}(k, z_0)$ is the Fourier transform of the mth segmented sensor signal, $\tilde{y}_{m,\ell}(z, z_0)$, given in (3), and $\{\cdot\}^*$ denotes the complex conjugate. By defining the vectors

$$\mathbf{w}_\ell(k, z_0) = \begin{pmatrix} w_{0,\ell}(k, z_0) & w_{1,\ell}(k, z_0) & \cdots & w_{M-1,\ell}(k, z_0) \end{pmatrix}^T$$
$$\mathbf{Y}_\ell(k, z_0) = \begin{pmatrix} Y_{0,\ell}(k, z_0) & Y_{1,\ell}(k, z_0) & \cdots & Y_{M-1,\ell}(k, z_0) \end{pmatrix}^T$$

the beamformer output (4) rewrites into

$$B_\ell(k, z_0) = \mathbf{w}_\ell(k, z_0)^H \mathbf{Y}_\ell(k, z_0) \ , \tag{5}$$

where the superscripts, $\{\cdot\}^T$ and $\{\cdot\}^H$, denote the non-conjugate and the conjugate transpose, respectively. Note that the sub-band division provides the possibility of weighting both each sub-band and each point differently.

2.2. Minimum Variance Beamforming

The adaptive beamformer uses a set of apodization weights, which are dependent on the frequency content of the specific sensor signals. The MV beamformer continuously updates the weights, so that the variance (or power) of the beamformer output is minimized, while the response from the focus point is passed without distortion. The power of the beamformer output is given by

$$\mathcal{P}_\ell(k, z_0) = \mathcal{E}\left\{|B_\ell(k, z_0)|^2\right\} \tag{6}$$
$$= \mathcal{E}\left\{|\mathbf{w}(k, z_0)^H \mathbf{Y}_\ell(k, z_0)|^2\right\} \tag{7}$$
$$= \mathbf{w}_\ell(k, z_0)^H \mathbf{R}_\ell(k, z_0) \mathbf{w}_\ell(k, z_0) \ , \tag{8}$$

where $\mathcal{E}\{\cdot\}$ denotes the expectation value, and $\mathbf{R}_\ell(k, z_0)$ is the covariance matrix given by

$$\mathbf{R}_\ell(k, z_0) = \mathcal{E}\left\{\mathbf{Y}_\ell(k, z_0) \mathbf{Y}_\ell(k, z_0)^H\right\} \ . \tag{9}$$

Mathematically, the MV beamformer is expressed as [1]

$$\min_{\mathbf{w}_\ell(k, z_0)} \mathbf{w}_\ell(k, z_0)^H \mathbf{R}_\ell(k, z_0) \mathbf{w}_\ell(k, z_0)$$
$$\text{subject to } \mathbf{w}_\ell(k, z_0)^H \mathbf{e}(k, z_0) = 1 \ , \tag{10}$$

where $\mathbf{e}(k, z_0)$ is the so-called steering vector, which characterizes the response from the focus point.

The solution to the optimization problem (10) can be found in a single iteration using Lagrangian multiplier theory as [1]

$$\mathbf{w}_\ell(k, z_0) = \frac{\mathbf{R}_\ell(k, z_0)^{-1} \mathbf{e}(k, z_0)}{\mathbf{e}(k, z_0)^H \mathbf{R}_\ell(k, z_0)^{-1} \mathbf{e}(k, z_0)} \ , \tag{11}$$

provided that $\mathbf{R}_\ell(k, z_0)^{-1}$ exists. Due to presteering and sub-band division, the response from the focus point will resemble a plane wave incident directly onto the array. Thus, the steering vector is constant across the array and independent on the frequency, and it simply becomes a $M \times 1$-vector of ones.

2.3. Covariance Matrix Estimation

In real applications, the covariance matrix is unknown and must be replaced by the sample covariance matrix, which is estimated from the data. To estimate the sample covariance matrix a number of realizations of data is required. In this paper, these realizations are obtained by dividing the data from a single acquisition into a number of subgroups. This follows the spatial smoothing approach suggested in [7].

As illustrated in Fig. 1, the spatially smoothed covariance matrix estimate is obtained by dividing the array into P overlapping subarrays of size $M_p \leq \frac{M}{2}$. For each subarray, a sub-covariance matrix is estimated, and these are averaged across the array. The covariance matrix estimate

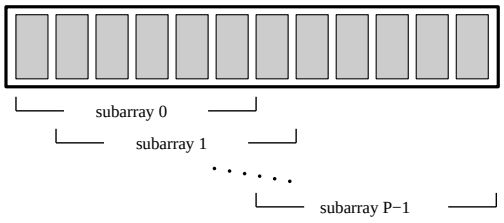

Fig. 1. Spatial smoothing. The array is divided into P overlapping subarrays, and the covariance matrix is averaged across the array.

can be expressed as

$$\mathbf{R}_\ell(k,z_0) = \frac{1}{P}\sum_{p=0}^{P-1} \mathbf{G}_{p,\ell}(k,z_0)\mathbf{G}_{p,\ell}(k,z_0)^H \,, \qquad (12)$$

where $\mathbf{G}_{p,\ell}(k,z_0)$ denotes the pth subarray given by

$$\mathbf{G}_{p,\ell}(k,z_0) = \begin{bmatrix} Y_{p,\ell}(k,z_0) \\ Y_{p+1,\ell}(k,z_0) \\ \vdots \\ Y_{p+M_p-1,\ell}(k,z_0) \end{bmatrix}$$

for $p = 0, 1, \ldots, P-1$. Note that this reduces the dimension of the covariance matrix, and thus the number of weights will be reduced correspondingly. The reduced weight vector, $\widetilde{\mathbf{w}}_\ell(k,z_0)$, is applied to the data by averaging over the P subarrays, which is expressed as

$$\mathbf{R}_\ell(k,z_0) = \widetilde{\mathbf{w}}_\ell(k,z_0)^H \frac{1}{P}\sum_{p=0}^{P-1} \mathbf{G}_{p,\ell}(k,z_0)\,. \qquad (13)$$

Note that the reduced dimension also influences the resolution due to the inherent compromise between the width of the array and the achievable resolution [8].

3. RESULTS

The MV beamformer is applied to simulated medical ultrasound data, obtained using the ultrasound simulation program, Field II [9, 10]. For the simulations, a linear array transducer with a center frequency of $f_0 = 7$ MHz, $\lambda/2$-spacing and $M = 128$ sensor elements was used. Data of 13 point targets is obtained using two different transmission sequences; a conventional, linear scan, see Sec. 3.1, and a PW transmission, see Sec. 3.2.

The MV beamformer is implemented in the frequency domain using the short-time Fourier transform with a segment size corresponding to the length of the excitation pulse convoluted with the two-way impulse response of the transducer. A subarray size of $M_p = \frac{M}{4} = 32$ was used, and the signal-to-noise ratio was 60 dB.

3.1. Linear Scan

Conventionally ultrasound imaging is carried out by transmitting several focused ultrasound beams, e.g. using a linear scan sequence as illustrated in Fig. 2(a). The transmitted pulses from each of the transducer elements are delayed so that they add up constructively in phase in a single point in space, the transmit focus.

To cover the entire image region, a large array is used and a part of the aperture is slid electronically along the scan plane. The image in Fig. 3(a) is obtained with a sliding aperture size of 128 elements and a fixed transmit focus at a depth of $z = 45$ mm. The response is beamformed using DS and dynamic Hanning apodization weights with $f/2$.

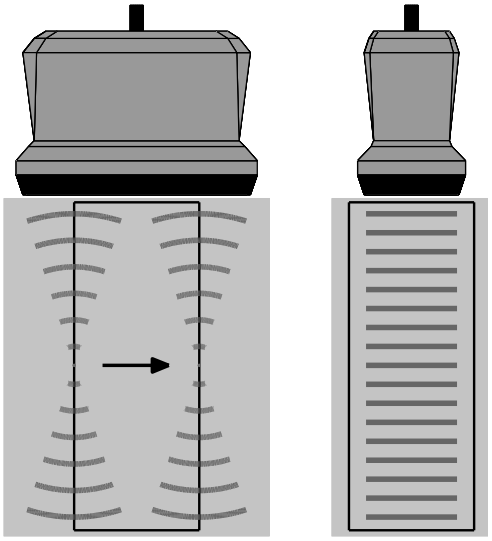

(a) Linear Scan (b) Plane Wave

Fig. 2. Illustration of scan sequences, the transducer is shown in the top and the image region is indicated by the black lines. (a) A linear scan is carried out using a large array and transmitting several focused beams, while sliding the active part of the aperture along the scan plane. (b) Using a plane wave transmission the entire image region is obtained from a single transmission. Courtesy of Dr. J. Udesen.

3.2. Plane Wave Transmission

A plane wave (PW) transmission can be achieved by using all elements are as both the transmitting and receiving aperture. In this way, the entire image region can be covered in a single transmission, as illustrated in Fig. 2(b). Note that when using PW, the propagation path from the transmitting element to the current image point, $\vec{r}_\ell(z_0)$, in (2) simply becomes the axial distance, z_0, from the array to the image point

$$\|\vec{r}^{\,(xmt)} - \vec{r}_\ell(z_0)\| = z_0 \,, \qquad (14)$$

which is independent on the scan line, ℓ.

The MV beamformed response is compared to DS using Boxcar and Hanning weights. The beamformed responses are seen in Fig. 3(b)-(d) with the lateral variation at $z = \{40, 45\}$ mm shown in Fig. 4. The resolution and contrast are quantified by the Full Width at Half Maximum (FWHM) and the Peak-Side-lobe Level (PSL), which is defined as the peak of the first side-lobe. These are given in Table 1.

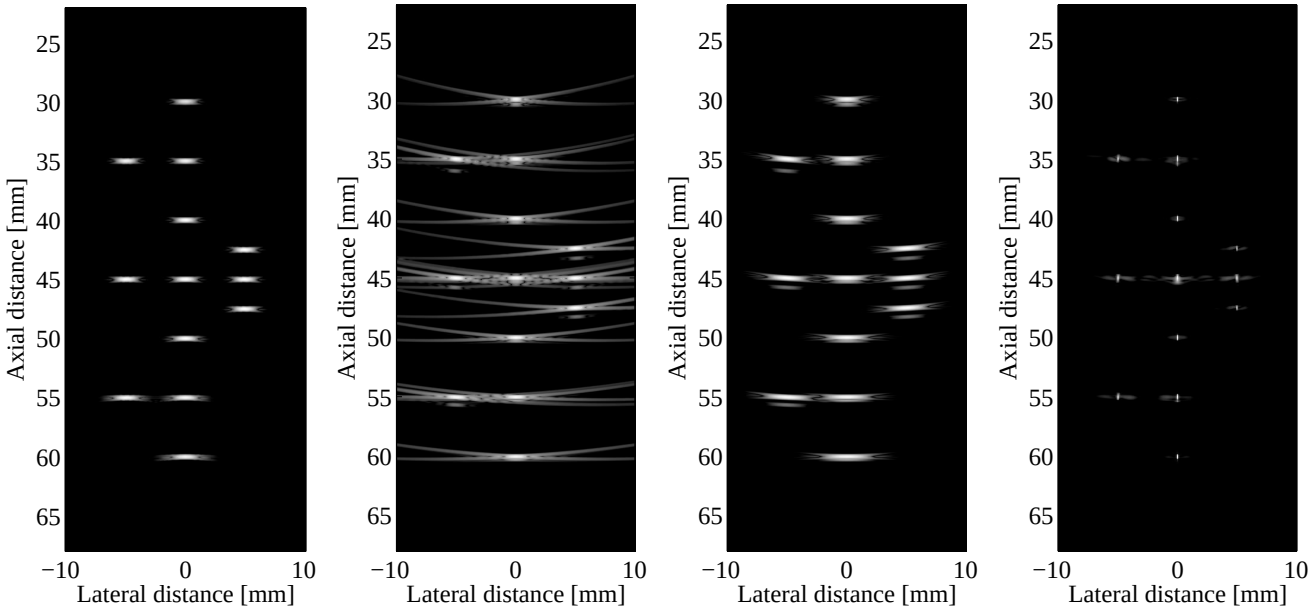

(a) Linear Scan (b) DS, Boxcar (c) DS, Hanning (d) MV

Fig. 3. Beamformed responses of the 13 point targets. (a) Linear scan, DS with dynamic apodization using Hanning weights. (b)-(d) Plane wave transmission. All images are shown with a dynamic range of 50 dB.

	PSL	FWHM	
Linear Scan	-40.1 dB	0.82 mm	3.71λ
DS, Boxcar	-16.8 dB	0.71 mm	3.23λ
DS, Hanning	-34.4 dB	1.28 mm	5.81λ
MV	-57.0 dB	0.12 mm	0.53λ

$\lambda = c/f_0 = 220$ μm

Table 1. Full Width at Half Maximum (FWHM) and Peak-side-lobe level (PSL) for the beamformed responses found at a depth of $z = 40$ mm.

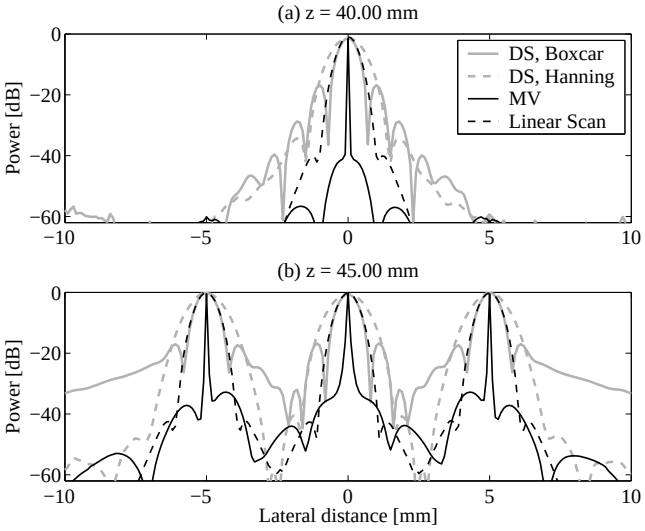

Fig. 4. Lateral variation at a depth of $z = \{40, 45\}$ mm of the beamformed responses shown in Fig. 3(a)-(d).

The PW data is obtained with Boxcar apodization both in transmit and receive. This provides unwanted side-lobes below the point targets, as seen in Fig. 3(b)-(c). These could have been removed by using a transmit apodization, such as a Tukey window with 70% tapering as in [11]. However, this has not been done, to demonstrate that the MV beamformer successes in eliminating these, as seen in Fig. 3(d).

Due to the focused transmissions and the dynamic Hanning apodization, the linear scan sequence provides a more homogeneous image than the unfocused PW transmissions. The resolution and contrast of the PW data are degraded and the images are not acceptable for ultrasound imaging.

The MV beamformer provides an increase of the resolution and contrast, as seen in Fig. 3(d) and Fig. 4. Even compared to the linear scan image, the MV beamformer provides a significant increase of the FWHM and PSL. From this investigation, it is seen that the increase of resolution and contrast, provided by the MV beamformer, yields the possibility of high resolution and contrast PW imaging, where an image region can be covered in a single transmission.

4. CONCLUSIONS

The adaptive MV beamformer has been applied to simulated ultrasound data obtained from a PW transmission. The performance of the MV beamformer is compared to the DS beamformer using Boxcar and Hanning weights. The results have shown that the MV beamformer provides a significant increase in resolution and contrast compared to the DS beamformer. Furthermore, the MV beamformed PW response is compared to data obtained from a conventional ultrasound sequence, where several focused transmission are used. These results have shown that the significant increase in resolution and contrast, provided by the MV beamformer, yields the possibility of PW medical ultrasound imaging with increased resolution and contrast.

5. REFERENCES

[1] J. Capon, "High-Resolution Frequency-Wavenumber Spectrum Analysis," *Proc. IEEE*, vol. 57, no. 8, pp. 1408–1418, August 1969.

[2] J. A. Mann and W. F. Walker, "A Constrained Adaptive Beamformer for Medical Ultrasound: Initial Results," in *Proc. IEEE Ultrason. Symp.*, Oct. 2002, vol. 2, pp. 1807–1810.

[3] M. Sasso and C. Cohen-Bacrie, "Medical Ultrasound Imaging Using the Fully Adaptive Beamformer," in *Proc. IEEE Int. Conf. Acous., Speech, Sig. Pro.*, March 2005, vol. 2, pp. 489–492.

[4] Z. Wang, J. Li, and R. Wu, "Time-Delay- and Time-Reversal-Based Robust Capon Beamformers for Ultrasound Imaging," *IEEE Trans. Med. Imag.*, vol. 24, no. 10, pp. 130–1322, Oct. 2007.

[5] J.-F. Synnevåg, A. Austeng, and S. Holm, "Adaptive Beamforming Applied to Medical Ultrasound Imaging," *IEEE Trans. Ultrason., Ferroelec., Freq. Contr.*, vol. 54, no. 8, pp. 1606–1613, Aug. 2007.

[6] I. K. Holfort, F. Gran, and J. A. Jensen, "Minimum Variance Beamforming for High Frame-Rate Ultrasound Imaging," in *Proc. IEEE Ultrason. Symp.*, Oct. 2007, pp. 1541–1544.

[7] T.-J. Shan and T. Kailath, "Adaptive Beamforming for Coherent Signals and Interference," *IEEE Trans. Acous., Speech, Sig. Pro.*, vol. 33, no. 3, pp. 527–536, June 1985.

[8] D. H. Johnson and D. E. Dudgeon, *Array Signal Processing: Concepts and Techniques*, Prentice-Hall., Englewood Cliffs, New Jersey, 1993.

[9] J. A. Jensen and N. B. Svendsen, "Calculation of pressure fields from arbitrarily shaped, apodized, and excited ultrasound transducers," *IEEE Trans. Ultrason., Ferroelec., Freq. Contr.*, vol. 39, pp. 262–267, 1992.

[10] J. A. Jensen, "Field: A program for simulating ultrasound systems," *Med. Biol. Eng. Comp.*, vol. 10th Nordic-Baltic Conference on Biomedical Imaging, Vol. 4, Supplement 1, Part 1, pp. 351–353, 1996b.

[11] J. Udesen, F. Gran, and J. A. Jensen, "Fast color flow mode imaging using plane wave excitation and temporal encoding," in *Proc. SPIE - Progress in biomedical optics and imaging*, 2005, vol. 5750, pp. 427–436.

Paper IV

Adaptive Receive and Transmit Apodization for Synthetic Aperture Ultrasound Imaging

I. K. Holfort, A. Austeng, J.-F. Synnevåg, S. Holm, F. Gran and J. A. Jensen

Proceedings of the IEEE International Ultrasonics Symposium

Presented in Rome, Italy, Sep. 2009

Adaptive Receive and Transmit Apodization for Synthetic Aperture Ultrasound Imaging

Iben Kraglund Holfort[1], Andreas Austeng[2], Johan-Fredrik Synnevåg[2,3], Sverre Holm[2], Fredrik Gran[1,4] and Jørgen Arendt Jensen[1]

[1]Department of Electrical Engineering, Technical University of Denmark, DK-2800 Kgs. Lyngby, Denmark
[2]Department of Informatics, University of Oslo, P. O. Box 1080, N-0316 Oslo, Norway
[3]Bergen Oilfield Services AS, Sandviksbodene 1E, NO-5035 Bergen, Norway
[4]GN ReSound A/S, Lautrupbjerg 9, DK-2750 Ballerup, Denmark

***Abstract*— This paper suggests a framework for utilizing adaptive, data-dependent apodization weights on both the receiving and transmitting aperture for Synthetic Aperture (SA) ultrasound imaging. The suggested approach is based on the Minimum Variance (MV) beamformer and consists of two steps. A set of uniquely designed receive apodization weights are applied to pre-summed element data forming a set of adaptively weighted images; these are in SA literature conventionally referred to as low-resolution images. The adaptive transmit apodization is obtained by applying MV across the full set of single emission images before summation. The method is investigated using simulated SA ultrasound data obtained using Field II. Data of 13 point targets distributed at depths from 40 mm to 70 mm, and a 5.5 MHz, 64-element linear array transducer have been used. The investigation has shown that the introduction of adaptive apodization weights on the transmitting aperture provides a main-lobe reduction (estimated at -30 dB) by a factor of 1.8 compared to the method using adaptive apodization weights on the receiving aperture only.**

I. Introduction

Recently, the application of adaptive, data-dependent beamformers to the field of ultrasound imaging has become an area of increasing interest. These have provided significant results in terms of increased resolution and contrast compared to the conventional, delay-and-sum (DAS) beamformer [1]–[7].

Previously, the adaptive minimum variance (MV) beamformer has been applied to the receiving aperture of synthetic aperture ultrasound (SA) data [5]. This has provided single emission images with increased resolution. The set of single emission images are combined by a weighted sum to form the full SA image; these weights represent the transmit apodization. So-far only data-independent transmit apodization weights have been used.

This paper suggests a framework for utilizing adaptive, data-dependent apodization weights both on the receiving and transmitting aperture. The suggested approach is based on the MV beamformer and consists of two steps. A set of uniquely designed receive apodization weights are applied to pre-summed element data forming a set of adaptively weighted images; these are in SA literature conventionally referred to as low-resolution images. The adaptive transmit apodization is obtained by applying MV across the full set of single emission images before summation.

This paper investigates, whether the additional data-dependent, adaptive apodization weights on the transmitting aperture provides an increased resolution compared to the data-independent transmitting apodization methods.

II. Method

The suggested method is based on a synthetic aperture ultrasound imaging framework, where a number of so-called low-resolution images are created from unfocused emissions; one image for each emission. These are combined by a weighted sum to form an image with an increased resolution. For more on SA see e.g. [8].

The principle of the proposed method is illustrated in Fig. 1. The method consists of two parts. First, adapted apodization weights are applied to the received data, one weight for each receive channel. This provides a set of adaptively weighted low-resolution images; one image for each emission. Subsequently, the chosen transmitting apodization weights

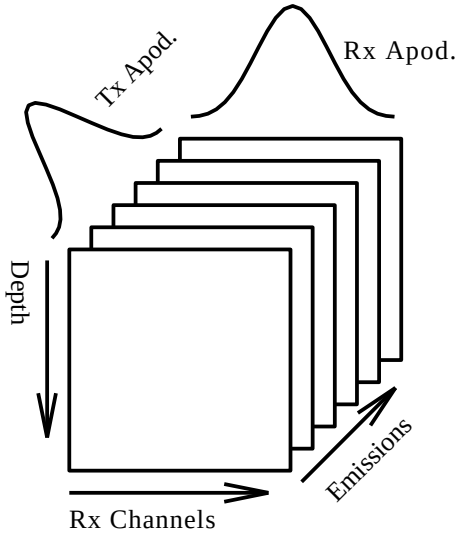

Fig. 1. Using a synthetic aperture (SA) imaging sequence a number of emissions are acquired. For each emission a data set is obtained, from each of these a single emission image created using a beamformer with the receiving (Rx) apodization function. Weighting these images with the chosen transmitting (Tx) apodization function provides the combined SA image.

are applied across these single emission images to form the combined SA image. This first part has previously been demonstrated in [5], where only data-independent apodization weights have been applied on the transmitting aperture.

The second part of the suggested method is to introduce data-dependent, adapted apodization weights on the transmitting aperture. In this way, the number of adapted weights and thereby the number of degrees of freedom are increased by a factor proportional to the number of SA emissions. Thus, the achievable resolution is assumed to increase significantly compared to both the data-independent transmitting apodization method and the conventional DAS method.

A. Beamforming

An ultrasound image is obtained using beamforming, where a specific set of time samples, $\Delta_{m,i}$, are chosen from the received sensor signals, $y_{m,i}(n)$. Which samples to choose is determined by the time-of-flight from the transmitting elements to the image point, $\vec{r}_p$, and back to the receiving elements. These samples are weighted and subsequently summed to form the beamformer output. To obtain an SA image, the set of so-called low-resolution images are furthermore weighed and summed to form the combined SA image, as illustrated in Fig. 1. Mathematically, an SA image is expressed by

$$b(\vec{r}_p) = \sum_{i=0}^{I-1} a_i^*(\vec{r}_p) \sum_{m=0}^{M-1} w_{m,i}^*(\vec{r}_p) y_{m,i}(\Delta_{m,i}(\vec{r}_p)) \quad (1)$$

$$= \sum_{i=0}^{I-1} a_i^*(\vec{r}_p) \ell_i(\vec{r}_p)\,, \quad (2)$$

where a and w denote the apodization weights on the transmitting and receiving apertures, respectively. The superscript, $\{\cdot\}^*$, denotes the complex conjugate.[i] I and M are the number of emissions and receiving elements, respectively. And $\ell_i(\vec{r}_p)$ denotes the ith low-resolution image. In matrix-vector notation, (2) becomes

$$b(\vec{r}_p) = \mathbf{a}^H(\vec{r}_p)\boldsymbol{\ell}(\vec{r}_p) = \mathbf{a}^H(\vec{r}_p) \begin{bmatrix} \mathbf{w}_0^H \mathbf{y}_0(\vec{r}_p) \\ \mathbf{w}_1^H \mathbf{y}_1(\vec{r}_p) \\ \vdots \\ \mathbf{w}_{I-1}^H \mathbf{y}_{I-1}(\vec{r}_p) \end{bmatrix}, \quad (3)$$

where $\mathbf{a}$ and $\{\mathbf{w}_i\}_{i=0}^{I-1}$ are vectors containing the apodization weights, $\boldsymbol{\ell}$ contains the stacked low-resolution images, $\{\ell_i(\vec{r}_p)\}_{i=0}^{I-1}$, and the superscript, $\{\cdot\}^H$, denotes the Hermitian transpose.

B. Adaptive Beamforming for both Receive and Transmit Apodization

The adaptive apodization weights are found using the Minimum Variance (MV) beamformer, which was introduced by Capon in 1969 [9]. In the following, the apodization weight vector is denoted $\mathbf{u}$; it refers to and can be substituted for the apodization weights on either the receiving aperture or the transmitting aperture.

The data-dependent MV beamformer uses apodization weights that are found from the measured wave field, as opposed to DAS, which uses pre-defined apodization weights. The MV beamformer finds a set of optimized weights that minimize the variance (or power) of the beamformer output, while passing the signal of interest without distortion. Thus, it passes the signal from the current receive focal point with unit gain. According to [9], the MV beamformer can mathematically be expressed as

$$\min_{\mathbf{u}} \mathbf{u}^H \mathbf{R} \mathbf{u} \quad \text{subject to } \mathbf{u}^H \mathbf{e} = 1 \quad (4)$$

where $\mathbf{e}$ is the so-called steering vector that defines the signal from the current receive focal point, $\vec{r}_p$, which should be passed with unit gain. $\mathbf{R}$ is the covariance matrix, described in Sec. II-B.1-II-B.2. The closed-form solution to (4) can be found using Lagrangian multiplier [10] theory as [9]

$$\hat{\mathbf{u}} = \frac{\mathbf{R}^{-1}\mathbf{e}}{\mathbf{e}^H \mathbf{R}^{-1} \mathbf{e}}\,, \quad (5)$$

provided that $\mathbf{R}^{-1}$ exists.

The apodization weight vector, $\mathbf{u}$, refers to apodization on either the receiving aperture or the transmitting aperture. For optimization of the receive apodization weights for the ith low-resolution image, $\mathbf{u}$ should be substituted by $\mathbf{w}_i$. For adapting the apodization weight on the transmitting aperture, $\mathbf{u}$ should be substituted by $\mathbf{a}$.

Furthermore, the covariance matrix should be interchanged with either $\hat{\mathbf{R}}_{Rx}$ or $\hat{\mathbf{R}}_{Tx}$ according to which of the two apertures, Receive (Rx) or Transmit (Tx), is used. The estimation of the covariance matrices is described in the following.

1) Covariance Matrix Estimation for Receive Apodization: The covariance matrix for the receive apodization is estimated from the sensor signals, $\mathbf{y}_i(\vec{r}_p)$. For the ith low-resolution image, the covariance matrix estimate is found as

$$\hat{\mathbf{R}}_{Rx} = \mathcal{E}\left\{\mathbf{y}_i(\vec{r}_p)\mathbf{y}_i(\vec{r}_p)^H\right\}\,, \quad (6)$$

where $\mathcal{E}\{\cdot\}$ denotes the expectation value.

2) Covariance Matrix Estimation for Transmit Apodization: For the transmit apodization, the adaptively weighted low-resolution images, $\boldsymbol{\ell}(\vec{r}_p)$, are used to estimate the covariance matrix as

$$\hat{\mathbf{R}}_{Tx} = \mathcal{E}\left\{\boldsymbol{\ell}(\vec{r}_p)\boldsymbol{\ell}(\vec{r}_p)^H\right\}\,. \quad (7)$$

Note that $\hat{\mathbf{R}}_{Rx}$ and $\hat{\mathbf{R}}_{Tx}$ are both dependent on the image point, $\vec{r}_p$, however this dependency has been omitted to simplify notation.

3) Spatial Smoothing and Diagonal Loading: In real applications, the covariance matrix is unknown and must be estimated from data. Several realizations of data are required; these are obtained by smoothing the covariance matrix estimate spatially as suggested in [11]. Fig. 2 illustrates how the array is divided into P overlapping subarrays of length L. For each subarray, a sub-covariance matrix is estimated. The

[i] Note that the complex conjugate operator is only introduced here to have a notation in consistency with the conventional matrix-vector notation. Using real apodization weights, the conjugation can be neglected.

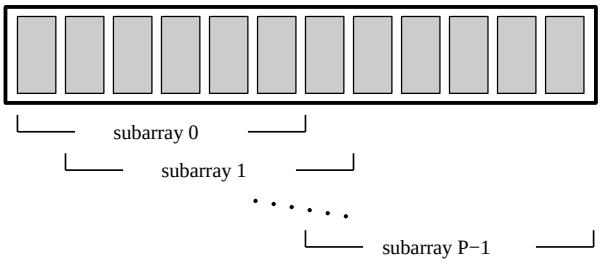

Fig. 2. Spatial smoothing. The array is divided into P overlapping subarrays, and the covariance matrix is averaged across the array.

resulting covariance matrix is then given as the average over the subarrays

$$\hat{\mathbf{R}} = \frac{1}{P}\sum_{p=0}^{P-1}\hat{\mathbf{R}}_p\,, \tag{8}$$

where $\hat{\mathbf{R}}_p$ is the pth sub-covariance matrix estimate. Note that the spatial smoothing reduces the dimension of the covariance matrix to $L \times L$, and the dimension of the weight vector is reduced correspondingly. Thus, the number of degrees of freedom is reduced, which mean that the achievable resolution is also reduced.

For both the Rx and Tx apertures, diagonal loading is added to the covariance matrix. This introduces a robustness towards small disalignments. For more on robust adaptive beamforming methods see [12]. The diagonal loaded covariance matrix is given as

$$\mathbf{R} = \hat{\mathbf{R}} + \epsilon\mathbf{I}\,, \tag{9}$$

where ϵ is small scalar value, and $\mathbf{I}$ is the $L \times L$ identity matrix.

III. Results

Using Field II [13], [14], simulated SA data of 13 point targets has been obtained. The points are distributed at depths ranging from 40 mm to 70 mm. For the simulations, a 5.5 MHz, 64-element linear array transducer with 300 μm pitch is used. The SA sequence consisting of 64 emissions is obtained using virtual sources with 11 active elements. For the MV beamforming, diagonal loading and a subarray size of $L = 32$ are used both on the receiving and the transmitting apertures.

The proposed method (Rx MV – Tx MV) is compared to two methods using data-independent apodization weighted on the transmitting aperture. These two methods are DAS using dynamic Hanning apodization weights with f-number of 2.5 on the receiving aperture and Boxcar weights on the transmitting aperture (Rx Hanning – Tx Boxcar), and MV on the receiving aperture and Boxcar weights on the transmitting aperture (Rx MV – Tx Boxcar).

The lateral variation of the three beamformed responses along two points placed laterally at a depth of 50 mm are shown in Fig. 3. It is seen that the MV beamformer provides significantly reduced main-lobe width compared to the conventional DAS beamformer. This has previously been demonstrated in [5].[ii] Furthermore, it is seen that the introduction of the data-dependent apodization weights on the transmitting aperture provides a reduction of the main-lobe width compared to these two methods.

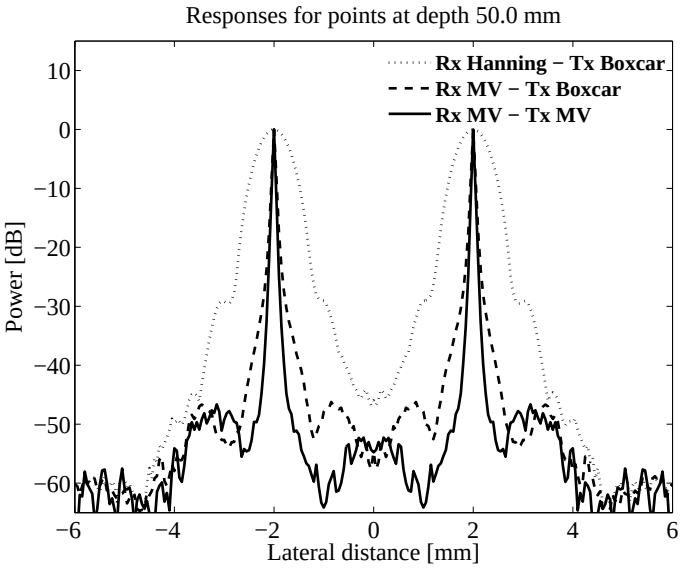

Fig. 3. Lateral variation of the beamformed responses in Fig. 4(a)-(c) along two points at a depth of 50 mm.

For these two point targets placed laterally at a depth of 50 mm, the three methods provide main-lobe widths (at -30 dB) of $\{2.20, 0.47, 0.26\}$ mm. Thus, the introduction of adaptive transmit apodization provides a reduction of the main-lobe width (at -30 dB) by a factor of 1.8.

The three beamformed responses of the 13 point targets are shown in Fig. 4(a)-(c). It is seen that the main-lobe width has reduced significantly for the two adaptively beamformed responses in Fig. 4(b)-(c) compared to the data-independent DAS beamformed response in Fig. 4(a). Furthermore, it is observed that the adaptively beamformed response using adaptive apodization weights on both the receiving and the transmitting apertures in Fig. 4(c) provides a reduced main-lobe width. These observations are in consistency with Fig. 3 and with the fact that the number of degrees of freedom has increased significantly with the introduction of the data-dependent apodization weights on the transmitting aperture.

IV. Discussion

As mentioned previously, the introduction of data-dependent transmit apodization weights increases the number of degrees of freedom. Thus, the achievable resolution is potentially increased. These increments come at the expense of additional computational load. In the proposed method, it is suggested to carry out the two optimizations in two separate, subsequent steps. This introduces a matrix inversion for each step, and thus an increase of the computational load compared to the data-independent transmit apodization methods. Another

[ii]Note that in [5], the MV beamformer was implemented in the frequency domain. That provided an increased number of degrees of freedom compared to the implementation in the time domain, which is used in this paper.

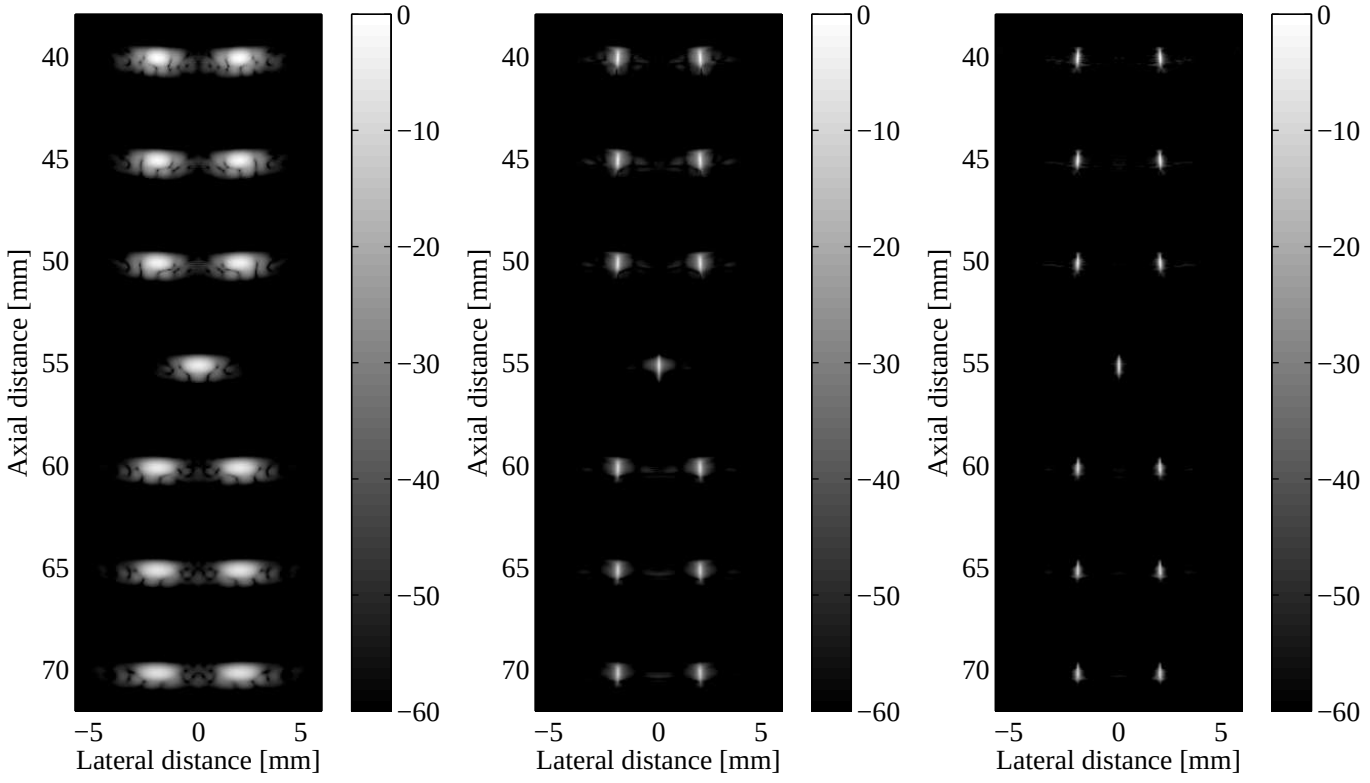

(a) Rx Hanning – Tx Boxcar (b) Rx MV – Tx Boxcar (c) Rx MV – Tx MV

Fig. 4. Beamformed responses for 13 discrete point targets. (a) Hanning apodization on the receiving and Boxcar on the transmitting aperture. (b) MV apodization on the receiving and Boxcar on the transmitting aperture. (c) MV apodization on both the receiving and transmitting apertures.

approach is to implement the optimization of the apodization weights on the receiving and transmitting apertures in one single optimization problem. However, that will introduce a significantly increased dimension of the covariance matrix. As the computational load of the matrix inversion is directly dependent on matrix dimension, it should be investigated further, whether or not the combination into one optimization problem will in fact reduce the computational load.

V. Conclusions

In this paper, a framework for applying adaptive, data-dependent apodization weights on both the receiving and the transmitting aperture has been introduced. The suggested method has been validated using simulated synthetic aperture ultrasound data. The investigation has shown that the introduction of adaptive apodization weights on the transmitting aperture provides a main-lobe reduction (estimated at -30 dB) by a factor of 1.8 compared to the method using adaptive apodization weights on the receiving aperture only.

Acknowledgment

This work was supported by grant 26-04-0024 from the Danish Science Foundation and by B-K Medical ApS, Denmark.

References

[1] J. A. Mann and W. F. Walker, "A Constrained Adaptive Beamformer for Medical Ultrasound: Initial Results," in *Proc. IEEE Ultrason. Symp.*, Oct. 2002, vol. 2, pp. 1807–1810.

[2] M. Sasso and C. Cohen-Bacrie, "Medical Ultrasound Imaging Using the Fully Adaptive Beamformer," in *Proc. IEEE Int. Conf. Acous., Speech, Sig. Pro.*, March 2005, vol. 2, pp. 489–492.

[3] F. Viola and W. F. Walker, "Adaptive Signal Processing in Medical Ultrasound Beamforming," in *Proc. IEEE Ultrason. Symp.*, 2005, vol. 4, pp. 1980–1983.

[4] J.-F. Synnevåg, A. Austeng, and S. Holm, "Adaptive Beamforming Applied to Medical Ultrasound Imaging," *IEEE Trans. Ultrason., Ferroelec., Freq. Contr.*, vol. 54, no. 8, pp. 1606–1613, Aug. 2007.

[5] I. K. Holfort, F. Gran, and J. A. Jensen, "Broadband Minimum Variance Beamforming for Medical Ultrasound Imaging," *IEEE Trans. Ultrason., Ferroelec., Freq. Contr.*, vol. 56, no. 2, pp. 314–325, 2009.

[6] Z. Wang, J. Li, and R. Wu, "Time-Delay- and Time-Reversal-Based Robust Capon Beamformers for Ultrasound Imaging," *IEEE Trans. Med. Imag.*, vol. 24, no. 10, pp. 1308–1322, 2005.

[7] F. Vignon and M. R. Burcher, "Capon Beamforming in Medical Ultrasound Imaging with Focused Beams," *IEEE Trans. Ultrason., Ferroelec., Freq. Contr.*, vol. 50, no. 4, pp. 619–628, March 2008.

[8] S. I. Nikolov, *Synthetic Aperture Tissue and Flow Ultrasound Imaging*, Ph.D. thesis, Ørsted•DTU, Technical University of Denmark, 2800, Lyngby, Denmark, 2001.

[9] J. Capon, "High-Resolution Frequency-Wavenumber Spectrum Analysis," *Proc. IEEE*, vol. 57, no. 8, pp. 1408–1418, August 1969.

[10] J. S. Arora, *Introduction to Optimum Design*, McGraw-Hill, Inc., 1989.

[11] T.-J. Shan and T. Kailath, "Adaptive Beamforming for Coherent Signals and Interference," *IEEE Trans. Acous., Speech, Sig. Pro.*, vol. 33, no. 3, pp. 527–536, June 1985.

[12] J. Li and P. Stoica, *Robust Adaptive Beamforming*, John Wiley & Sons, New York, 2006.

[13] J. A. Jensen and N. B. Svendsen, "Calculation of pressure fields from arbitrarily shaped, apodized, and excited ultrasound transducers," *IEEE Trans. Ultrason., Ferroelec., Freq. Contr.*, vol. 39, pp. 262–267, 1992.

[14] J. A. Jensen, "Field: A program for simulating ultrasound systems," *Med. Biol. Eng. Comp.*, vol. 10th Nordic-Baltic Conference on Biomedical Imaging, Vol. 4, Supplement 1, Part 1, pp. 351–353, 1996b.

Paper V

High Resolution Ultrasound Imaging Using Adaptive Beamforming with Reduced Number of Active Elements

I. K. Holfort, F. Gran and J. A. Jensen

Proceedings of the International Congress on Ultrasonics

Presented in Santiago, Chile, Jan. 2009

Paper #1111 Presented at the International Congress on Ultrasonics, Santiago, Jan. 11 - 17, 2009, Session R04: Adaptive Imaging and Focusing

High Resolution Ultrasound Imaging Using Adaptive Beamforming with Reduced Number of Active Elements

Iben Kraglund Holfort[1], Fredrik Gran[2] and Jørgen Arendt Jensen[1]

[1]Technical University of Denmark, Dept. Electrical Engineering,
Center for Fast Ultrasound Imaging, DK-2800 Kgs. Lyngby, Denmark
[2]GN ReSound A/S, Lautrupvej 7, DK-2750 Ballerup, Denmark

Abstract: In this paper, the adaptive, minimum variance (MV) beamformer is applied to ultrasound data. Due to near-field properties, the energy of the ultrasound data reduces towards the edges of the transducer. The influence of this near-field effect is demonstrated, and a method to reduce this influence is proposed. By reducing the number of active sensor elements, an increased resolution can be obtained with the MV beamformer. This observation is directly opposite the well-known relation between the spatial extent of the aperture and the achievable resolution. The investigations are based on Field II simulated data using a 128-element transducer with a large spatial extent. The results show that an increased resolution can be obtained, when using only the central part of the transducer compared to using the entire spatial extent. Using the central 32 or 48 elements provides an increased resolution compared to using all 128 elements.

Key words: Adaptive Array Processing, Adaptive Beamforming, High Resolution Beamforming, Minimum Variance Beamforming, Ultrasound Imaging.

A. Introduction

In medical ultrasound imaging, beamforming is conventionally carried out using the Delay and Sum (DS) beamformer, which works by delaying, weighting and summing the individual sensor signals. The DS beamformer uses pre-defined and fixed apodization weights. It is a well-known fact that the achievable resolution is directly dependent on the choice of apodization weights and the number of sensor elements.

Within recent years, the application of adaptive beamforming to ultrasound imaging has become an area of increasing interest. The primary focus has been on the so-called Minimum Variance (MV) or Capon beamformer [1]. Despite the fact that adaptive beamformers originally were developed for far-field applications, previous investigations in the field of ultrasound imaging have shown promising results; in terms of significantly increased resolution [2]-[8].

Due to near-field properties, the energy of the ultrasound data reduces towards the edges of the transducer. In this paper, the influence of this near-field effect on the MV beamformer is demonstrated using simulated Field II [9]-[10] data. Furthermore, a method to reduce this influence is proposed by reducing the number of sensor signals.

B. Adaptive Beamforming

A beamformer works by delaying, weighting and subsequently summing each of the sensor signals. As illustrated in Fig. 1, an adaptive beamformer is similar to DS with the only difference being the choice of weights. The adaptive weights are continuously updated and are directly dependent on the measured sensor signals.

B.1. Pre-steering

As in conventional beamforming, the sensor signals are pre-steered at the focus point, so that the sensor responses from the focus point will sum in phase, and the DS beamformer output from the current point will be maximized. Pre-steering at a point is carried out by compensating for the propagation delay for this point. The delay is calculated as the propagation path from the transmit element to the focus point and back to the receiving element.

The concept of pre-steering is illustrated in Fig. 2(a)-(b), which show the responses from three point targets located at (x,z)={(0,40), (5,42), (-2,45)} mm. The responses are simulated for a transducer with 128 elements. Fig. 2(a) shows the received sensor signals, and in Fig. 2(b), the sensor signals are pre-steered at the point (x,z)= (0,40) mm. Due to the compensation for the delay, the response from the focus point resembles a plane wave impinging directly onto the array. Thus, the signals will sum in phase, and the DS beamformer output will be

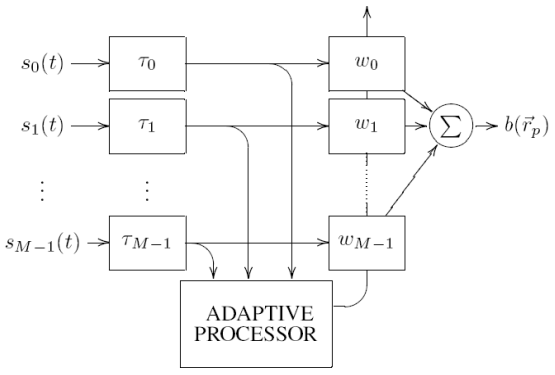

Fig.1. Block diagram of an adaptive, narrowband beamformer. The adaptive processor determines a set of optimized apodization weights from the delayed sensor signals.

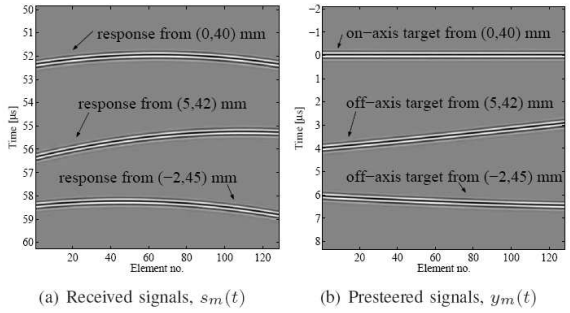

(a) Received signals, $s_m(t)$ (b) Presteered signals, $y_m(t)$

Fig. 2. (a) The received sensor signals. The figure shows the responses from three point targets located at (*x*,*z*) = {(0,40),(5,42),(-2,45)} mm. (b) Sensor signals pre-steered at the focus point (*x*,*z*) = (0,40) mm. After pre-steering, the response from the focus point resembles a plane wave impinging directly onto the array.

maximized. This plane wave resemblance is exploited in the adaptive beamformer, see Sec. B.3.

B.2. Beamforming

Denoting the *m*th pre-steered sensor signals $y_m(t)$, the beamformer output is given as a weighted sum of the sensor signals

$$b(r) = \sum_{m=0}^{M-1} w_m y_m(0) = w^H y \qquad (1)$$

where *r* denotes the current focus point and the superscript $\{\}^H$ denotes the Hermitian transpose. Using pre-defined and fixed apodization weights, w_m, yields the DS response.

B.3. Minimum Variance Beamforming

In adaptive beamforming, the apodization weights are varying and are directly dependent on the sensor signals. The Minimum Variance (MV) beamformer continuously updates the weights, so that the variance (or power) of the beamformer output is minimized, while the response from the focus point is passed without distortion. Mathematically, this is expressed as [1]

$$\min w^H R w \ \text{ subject to } \ w^H e = 1 \qquad (2)$$

where *R* is the covariance matrix of the pre-steered sensor signals, and *e* is the so-called steering vector. The steering vector characterizes the signal of interest, which is not to be distorted.

The constrained optimization problem (2) can be solved analytically using Lagrangian multiplier theory. Provided that R^{-1} exists, the MV optimized apodization weights are given by [1]

$$\hat{w} = \frac{R^{-1}e}{e^H R^{-1} e} \qquad (3)$$

B.3.1. Covariance Matrix Estimation

The covariance matrix is unknown and must be replaced by the sample covariance matrix, which is estimated from the data. To estimate the sample covariance matrix a number of realizations of data is required. In this paper, these realizations are obtained by dividing the data from a single acquisition into a number of groups. This follows the spatial smoothing approach suggested in [11].

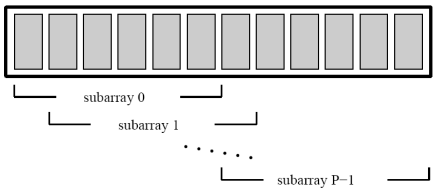

Fig. 3. Spatial smoothing. The array is divided into *P* overlapping sub-arrays, and the covariance matrix is averaged across the array.

As illustrated in Fig. 3, the spatially smoothed covariance matrix estimate is obtained by dividing the array into *P* overlapping sub-arrays. For each sub-array, a sub-covariance matrix is estimated, and these are averaged across the array. Note that this reduces the dimension of the covariance matrix, and thus the number of weights will be reduced correspondingly. The reduced dimension also influences the resolution due to the inherent compromise between the width of the array and the achievable resolution [12].

B.3.2. Signal of Interest

As indicated in (2)-(3), the definition of the signal of interest, *e*, is of great influence on the MV beamformer output. This signal of interest characterizes the signal emerging from the focus point. As seen in Fig. 2(b) the signal from the focus point will resemble a plane wave, where all sensor signals are in phase, impinging directly onto the array. Thus, standard procedure is to denote the pre-steered signal of interest by a vector of ones, which indicates a constant phase and constant amplitude across the array.

However, in near-field situations, the amplitude is not necessarily constant across the array. Fig. 4-5 show the received sensor signals for a point positioned at (0,50) mm using two 128-element transducers with different

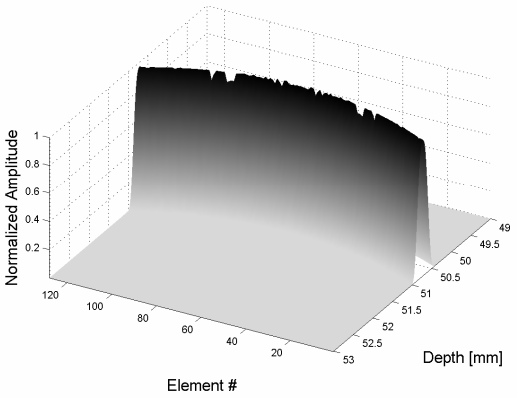

Fig. 4. Received sensor signals for a point positioned at (0,50) mm using a 128-element transducer with 0.15 μm pitch.

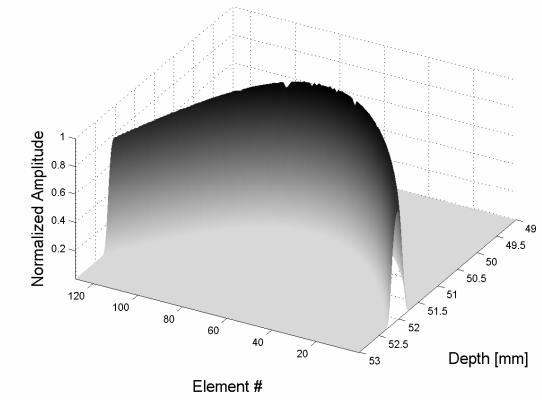

Fig. 5. Received sensor signals for a point positioned at (0,50) mm using a 128-element transducer with 0.3 µm pitch.

spatial extents; a transducer with 0.15 µm pitch (Fig. 4) and 0.3 µm pitch (Fig. 5). For the small transducer, the plane wave resemblance nearly holds. However, for the large transducer, the amplitude drops significantly towards the edges of the transducer; and the constant amplitude plane wave assumption does not hold. Thus, the signal emerging from the focus point will not be passed without distortion as intended. And as seen in the following section, the amplitude difference across the array influences the achievable resolution.

There are several approaches to reduce the influence of the amplitude drop; e.g. changing the analytical expression of the signal of interest, normalizing the amplitudes across the array or virtually reducing the spatial extent of the transducer by reducing the number of active elements. Instead of using all 128 elements, we will only use e.g. the center 48 element, as shown in Fig. 6. The transducer parameters used to create Fig. 5-6 are exactly identical; the only difference is the number of elements used to display the sensor signals. It is seen that the amplitude difference across the array has decreased significantly, and the plane wave assumption now holds.

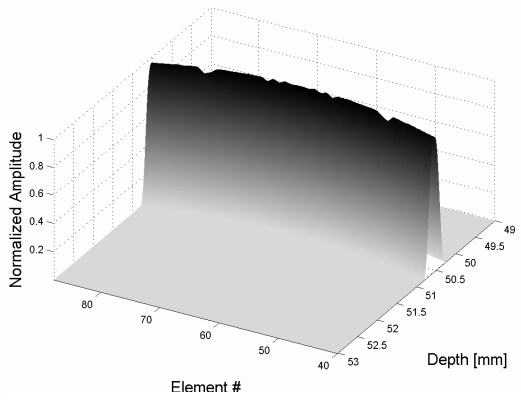

Fig. 6. Received sensor signals for a point positioned at (0,50) mm using a 128-element transducer with 0.3 µm pitch. Only the center 48 elements are displayed.

The majority of the transducers available in our lab has relatively large spatial extents and provides sensor signals with amplitude differences across the array. Thus, a reduction of this influence is of great interest for our future work in this area.

In this paper, we propose an approach using a reduced number of sensor signals to form the adaptive beamformer output. The following section will demonstrate that it is possible to obtain an increased resolution, despite a decreased number of active sensor signals. Note that this principle is directly contradicting the well-known relationship between the number of elements and the achievable resolution.

C. Results

In this section the MV beamformer is applied to Field II [9]-[10] simulated ultrasound data. For the simulations, a 128-element, 5.5 MHz linear array transducer with 0.3 µm pitch is used. These parameters correspond to a transducer, which is physically present in our lab. Data is obtained using a synthetic aperture approach [13], where 11 elements are used as the transmitting aperture and all elements are used as the receiving aperture.

The MV beamformer is implemented in the frequency domain using the short-time Fourier transform with a segment size corresponding to the length of the excitation pulse convolved with the two-way impulse response of the transducer. This provides a set of adapted apodization weights for each frequency bin. Before beamforming white Gaussian noise is added to each of the sensor signals; and a sub-array size of $L = 16$ is used for all calculations.

The beamformed responses in this section corresponds to a single synthetic aperture emission, and data are obtained for two point targets positioned at (2,50) mm and (-2,50) mm. Different number of active elements are used; corresponding to {128, 64, 48, 32} elements. This means that the spatial extent of the aperture has been reduced virtually down to 75% of the full size.

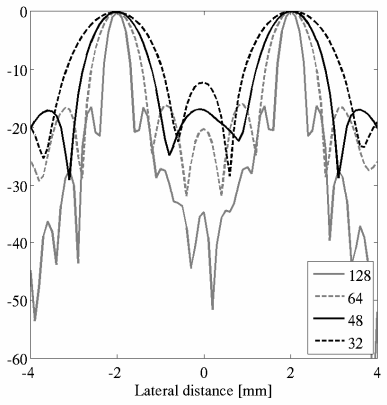

Fig. 7. DS beamformed responses with Boxcar weights for two points positioned at (-2,50) mm and (2,50) mm. Different number of active elements, {128, 64, 48, 32} are used.

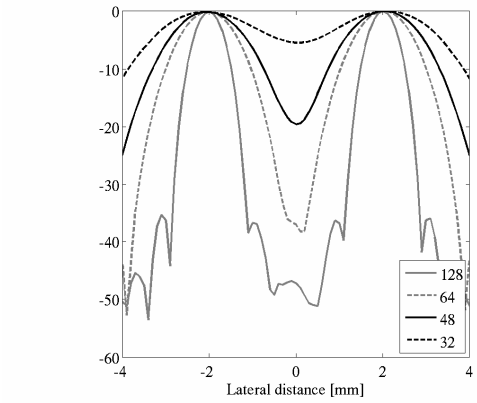

Fig. 8. DS beamformed responses with Hanning weights for two points positioned at (-2,50) mm and (2,50) mm. Different number of active elements, {128, 64, 48, 32} are used.

Fig. 7 shows the DS beamformed responses with Boxcar weights. As expected the responses using the highest number of elements provide the highest resolution and contrast; in terms of narrow main-lobe and low side-lobes. And obviously, the DS beamformed responses with Hanning weights, Fig. 8, show exactly the same.

The MV beamformed responses are shown in Fig. 9. It is seen that the MV beamformer provides an increased resolution compared to the responses in Fig. 7-8. Furthermore, it is seen that the highest resolution is not obtained using the largest number of active elements. It is seen that the broadest main-lobe is obtained using 128 elements; and the fewer active elements, the more narrow the main-lobe becomes. Obviously, the number of active elements has a lower bound, and a inherent compromise between the number of active elements and the achievable resolution and contrast exists. The optimum compromise is dependent on the *f*-number, the transducer parameters, and the size of the sub-array for the covariance matrix estimation.

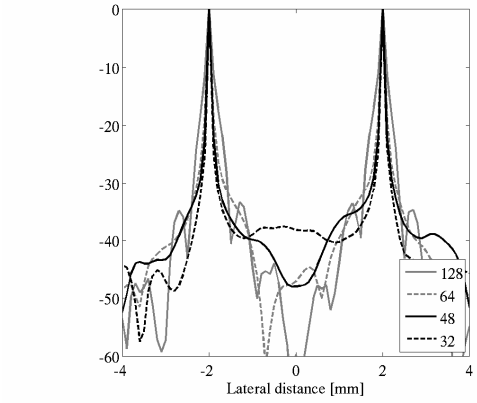

Fig. 9. MV beamformed responses for two points positioned at (-2,50) mm and (2,50) mm. Different number of active elements {128, 64, 48, 32} are used.

The purpose of this paper is to illustrate this rather peculiar observation, which is strictly contradicting both the expectation and is directly opposite the observation of the DS beamformer in Fig. 7-8.

D. Conclusions

From the investigations in this paper it is concluded that the near-field effects of ultrasound data has influence on the achievable resolution of the MV beamformer. An approach to reduce the influence of this effect has been proposed using fewer receiving elements. This observation is strictly opposite the expectation.

E. Acknowledgment

This work was supported by grant 26-04-0024 from the Danish Science Foundation and by B-K Medical ApS, Denmark.

F. Literature

[1] J. Capon, “High-Resolution Frequency-Wavenumber Spectrum Analysis,” Proc. IEEE, vol. 57, no. 8, pp. 1408–1418, August 1969.

[2] I. K. Holfort, F. Gran, and J. A. Jensen, “Minimum Variance Beamforming for High Frame-Rate Ultrasound Imaging,” in Proc. IEEE Ultrason. Symp., Oct. 2007, pp. 1541–1544.

[3] I. K. Holfort, F. Gran, and J. A. Jensen, “Plane Wave Medical Ultrasound Imaging using Adaptive Beamforming,” in Proc. 5th IEEE Sensor Array and Multichannel Signal Proc., July 2008, pp. 288-292.

[4] I. K. Holfort, F. Gran, and J. A. Jensen, “Investigations of Sound Speed Errors in Adaptive Beamforming,” in Proc. IEEE Ultrason. Symp., Nov. 2008.

[5] M. Sasso and C. Cohen-Bacrie, “Medical Ultrasound Imaging Using the Fully Adaptive Beamformer,” in Proc. IEEE Int. Conf. Acous., Speech, Sig. Pro., March 2005, vol. 2, pp. 489–492.

[6] F. Viola and W. F. Walker, “Adaptive Signal Processing in Medical Ultrasound Beamforming,” in Proc. IEEE Ultrason. Symp., 2005, vol. 4, pp. 1980–1983.

[7] J.-F. Synnevåg, A. Austeng, and S. Holm, “Adaptive Beamforming Applied to Medical Ultrasound Imaging,” IEEE Trans. Ultrason., Ferroelec., Freq. Contr., vol. 54, no. 8, pp. 1606–1613, Aug. 2007.

[8] Z. Wang, J. Li, and R. Wu, “Time-Delay- and Time-Reversal-Based Robust Capon Beamformers for Ultrasound Imaging,” IEEE Trans. Med. Imag., vol. 24, no. 10, pp. 130–1322, Oct. 2007.

[9] J. A. Jensen and N. B. Svendsen, “Calculation of pressure fields from arbitrarily shaped, apodized, and excited ultrasound transducers,” IEEE Trans. Ultrason., Ferroelec., Freq. Contr., vol. 39, pp. 262–267, 1992.

[10] J. A. Jensen, “Field: A program for simulating ultrasound systems,” Med. Biol. Eng. Comp., vol. 10th Nordic-Baltic Conference on Biomedical Imaging, Vol. 4, Supplement 1, Part 1, pp. 351–353, 1996b.

[11] T.-J. Shan and T. Kailath, “Adaptive Beamforming for Coherent Signals and Interference,” IEEE Trans. Acous., Speech, Sig. Pro., vol. 33, no. 3, pp. 527–536, June 1985.

[12] D. H. Johnson and D. E. Dudgeon, Array Signal Processing. Concepts and Techniques., Prentice-Hall., Englewood Cliffs, New Jersey, 1993.

[13] S. I. Nikolov and J. A. Jensen, “In-vivo synthetic aperture flow imaging in medical ultrasound,” IEEE Trans. Ultrason., Ferroelec., Freq. Contr., vol. 50, no. 7, pp. 848–856, 2003.

Paper VI

Investigation of Sound Speed Errors in Adaptive Beamforming

I. K. Holfort, F. Gran and J. A. Jensen

Proceedings of the IEEE International Ultrasonics Symposium

Presented in Beijing, China, Nov. 2008

Digital Object Identifier: 10.1109/ULTSYM.2008.0260

Investigation of Sound Speed Errors in Adaptive Beamforming

Iben Kraglund Holfort*, Fredrik Gran† and Jørgen Arendt Jensen*

*Center for Fast Ultrasound Imaging, Department of Electrical Engineering, Technical University of Denmark, DK-2800 Kgs. Lyngby, Denmark

†GN ReSound A/S, Lautrupbjerg 9, DK-2750 Ballerup, Denmark

***Abstract*— Previous studies have shown that adaptive beamformers provide a significant increase of resolution and contrast, when the propagation speed is known precisely. This paper demonstrates the influence of sound speed errors on two adaptive beamformers; the Minimum Variance (MV) beamformer and the Amplitude and Phase (APES) beamformer. Simulations of a single point target are carried out in Field II, and a percentage error is applied on the speed of sound. As the error increases, MV and APES provide amplitude drops of 17 dB and 3 dB on the signal strength. Two approaches to overcome this amplitude drop is proposed; diagonal loading (DL) and forward-backward (FB) averaging of the covariance matrix. The investigations show that DL provides a slightly decreased resolution and amplitude compared to FB. It is noted that APES provides more robust estimates than MV at the mere expense of a slight decrease of resolution. From the investigations, it is concluded the performance of the adaptive beamformers are not outperformed by the conventional delay-and-sum beamformer.**

I. Introduction

In medical ultrasound imaging beamforming is conventionally carried out using the delay-and-sum (DS) beamformer. Thus, the achievable resolution, and contrast is dependent on the inherent compromise between the main-lobe width and the side-lobe level. Although data-dependent, adaptive beamformers have been used in other fields of array signal processing for decades, the application of adaptive beamforming to the field of medical ultrasound imaging has only recently become an area of increasing interest [1]–[4].

Adaptive beamformers are highly sensitive to steering vector errors; and robust approaches for adaptive beamforming is a widely studied subject, see e.g. [5]. In medical ultrasound imaging, the primary cause of steering vector errors is incorrect sound speed estimates. As this estimate varies with the characteristics of the different tissue types within the human body [6], the variation cannot be eliminated. In the field of medical ultrasound imaging, robust methods for adaptive beamforming have been suggested by e.g. Wang *et al.* [3] and Synnevåg *et al.* [4].

In this paper, we demonstrate the influence of sound speed errors on two adaptive beamformers; the Minimum Variance (MV) beamformer and the APES beamformer. The adaptive beamformers are implemented in the frequency domain as suggested in [7], and it provides a set of data-dependent, complex weights for each frequency sub-band. Furthermore, three different covariance matrix estimation approaches are compared; these are forward-only spatial smoothing, diagonal loading and forward-backward averaging.

II. Sub-Band Minimum Variance Beamforming

As in conventional beamforming, the sensor signals are presteered, so that each scan line is dynamically focused. Considering a linear array transducer with M sensor elements, the mth dynamically focused sensor signal along the ℓth scan line is given by

$$y_{m,\ell}(z) = s\left(\tau_{m,\ell}(z)\right) \,, \tag{1}$$

for $m = 0, 1, \ldots, M-1$ and $\ell = 0, 1, \ldots, L-1$, where z denotes the spatial position along the ℓth scan line, $s(t)$ is the received waveform. The delay, $\tau_{m,\ell}(z)$, is found from the propagation path of the sound waves from the transmitting element to the focal point and returning to the receiving element, and is given by

$$\tau_{m,\ell}(z) = \frac{\|\vec{r}^{\,(xmt)} - \vec{r}_\ell(z)\| + \|\vec{r}_m^{\,(rcv)} - \vec{r}_\ell(z)\|}{c} \,, \tag{2}$$

where $\vec{r}^{\,(xmt)}$ and $\vec{r}_m^{\,(rcv)}$ are the spatial positions of the transmitting and the mth receiving sensor elements, $\vec{r}_\ell(z)$ denotes the focal point, and c is the speed of sound.

The MV beamformer [8] is originally developed for narrowband applications. Applying MV to broad-band ultrasound data, the sensor signals are divided into sub-bands using the short-time Fourier transform. For a given point, $\vec{r}_\ell(z_0)$, the beamformer output for each spatial frequency sub-band, k, is given by

$$B_\ell(k, z_0) = \mathbf{w}_\ell(k, z_0)^H \mathbf{Y}_\ell(k, z_0) \,, \tag{3}$$

where $\mathbf{w}_\ell(k, z_0)$ is a vector of sensor weights, $\mathbf{Y}_\ell(k, z_0)$ is a vector of short-time Fourier transforms of the segmented sensor signals, $y_{m,\ell}(z + z_0)$, $z \in [-Z/2; Z/2]$. The superscripts, $\{\cdot\}^T$ and $\{\cdot\}^H$, denote the non-conjugate and the conjugate transpose, respectively. Note that the sub-band division provides the possibility of weighting both each sub-band and each point differently.

The MV beamformer continuously updates the weights, so that the variance (or power) of the beamformer output is minimized, while the response from the focus point is passed

without distortion. The power of the beamformer output is given by

$$\mathcal{P}_\ell(k,z_0) = \mathcal{E}\left\{|B_\ell(k,z_0)|^2\right\} \quad (4)$$
$$= \mathbf{w}_\ell(k,z_0)^H \mathbf{R}_\ell(k,z_0)\mathbf{w}_\ell(k,z_0)\,, \quad (5)$$

where $\mathcal{E}\{\cdot\}$ denotes the expectation value, and $\mathbf{R}_\ell(k,z_0)$ is the covariance matrix given by

$$\mathbf{R}_\ell(k,z_0) = \mathcal{E}\left\{\mathbf{Y}_\ell(k,z_0)\mathbf{Y}_\ell(k,z_0)^H\right\}\,. \quad (6)$$

Mathematically, the MV beamformer is expressed as [8]

$$\min_{\mathbf{w}_\ell(k,z_0)} \mathbf{w}_\ell(k,z_0)^H \mathbf{R}_\ell(k,z_0)\mathbf{w}_\ell(k,z_0)$$
$$\text{subject to } \mathbf{w}_\ell(k,z_0)^H \mathbf{e}(k,z_0) = 1\,, \quad (7)$$

where $\mathbf{e}(k,z_0)$ is the so-called steering vector, which characterizes the response from the focus point. The solution to the optimization problem (7) can be found in a single iteration using Lagrangian multiplier theory as [8]

$$\mathbf{w}_\ell(k,z_0) = \frac{\mathbf{R}_\ell(k,z_0)^{-1}\mathbf{e}(k,z_0)}{\mathbf{e}(k,z_0)^H\mathbf{R}_\ell(k,z_0)^{-1}\mathbf{e}(k,z_0)}\,, \quad (8)$$

provided that $\mathbf{R}_\ell(k,z_0)^{-1}$ exists. Due to presteering and subband division, the response from the focus point will resemble a plane wave incident directly onto the array. Thus, the steering vector is constant across the array and independent on the frequency, and it simply becomes a $M\times 1$-vector of ones.

A. Spatial Smoothing

To obtain a useful estimate of the covariance matrix, a number of realizations is needed. Here, data from a single acquisition is divided into a number of subgroups and averaged spatially, as suggested in [9]. The spatially smoothed covariance matrix estimate is obtained by dividing the array into P overlapping subarrays of length L. For each subarray, a sub-covariance matrix is estimated, and these are averaged across the array. The covariance matrix estimate can be expressed as

$$\hat{\mathbf{R}} = \frac{1}{P}\sum_{p=0}^{P-1}\mathbf{G}_p\mathbf{G}_p^H\,, \quad (9)$$

where $\mathbf{G}_p$ denotes the pth subarray given by

$$\mathbf{G}_p = \begin{bmatrix} Y_p(\omega) & Y_{p+1}(\omega) & \dots & Y_{p+L-1}(\omega)\end{bmatrix}^T\,, \quad (10)$$

for $p = 0, 1, \dots, P-1$. Note that this reduces the dimension of the covariance matrix, and thus the number of weights will be reduced correspondingly. The reduced weight vector, $\tilde{\mathbf{w}}$, is applied to the data by averaging over the P subarrays, which is expressed as

$$B(\vec{r}_p) = \tilde{\mathbf{w}}^H\frac{1}{P}\sum_{p=0}^{P-1}\mathbf{G}_p\,. \quad (11)$$

B. APES Beamforming

The APES (Amplitude and Phase Estimation) Beamformer is based on the analogue spectral estimator [10]. The APES estimate can be found by replacing the covariance matrix in (8) by

$$\mathbf{Q} = \hat{\mathbf{R}} - \hat{\mathbf{G}}\hat{\mathbf{G}}^H\,, \quad \hat{\mathbf{G}} = \frac{1}{P}\sum_{p=0}^{P-1}\mathbf{G}_p \quad (12)$$

with $\hat{\mathbf{R}}$ and $\mathbf{G}_p$ given in (9)-(10). For more on the APES algorithm see e.g. [11].

C. Diagonal Loading

A commonly used approach for robust adaptive beamforming is to use diagonal loading [5], where a small scalar value, ε, is added to the diagonal of the covariance matrix estimate.

$$\hat{\mathbf{R}}_\varepsilon = \hat{\mathbf{R}} + \varepsilon\mathbf{I}\,, \quad (13)$$

where $\mathbf{I}$ denotes the identity matrix. The choice of ε will have a large influence on the provided weights. The larger ε becomes, the more the diagonal will dominate the result; and as shown in e.g. [4], the result will converge to the DS result. As suggested in [4], ε is chosen to be relative to the trace, $\mathrm{Tr}\{\cdot\}$, of $\hat{\mathbf{R}}$. In Sec. III, a value of $\varepsilon = 10^{-3}\mathrm{Tr}\{\hat{\mathbf{R}}\}$ is used.

D. Forward-Backward Averaging

The covariance matrix estimate in (9) is sometimes referred to as the *forward-only* estimate. Yet another covariance matrix estimate is the Forward-Backward (FB) average [11] defined by

$$\tilde{\mathbf{R}} = \frac{1}{2}(\hat{\mathbf{R}} + \mathbf{J}\hat{\mathbf{R}}^T\mathbf{J})\,, \quad \mathbf{J} = \begin{bmatrix} 0 & & 1\\ & \iddots & \\ 1 & & 0\end{bmatrix}\,. \quad (14)$$

This approach has previously been used in radar imaging in combination with APES by Wang *et al.* [12].

III. Application to Ultrasound Data

The two adaptive beamformers are applied on simulated ultrasound data, obtained using Field II [13], [14]. For the simulations, a 7 MHz linear array transducer with $\lambda/2$-spacing was used. Data is obtained using a single element as the transmitting aperture and all $M = 128$ elements as the receiving aperture. The MV and APES beamformers are implemented in the frequency domain using the short-time Fourier transform with a segment size corresponding to the length of the excitation pulse convolved with the two-way impulse response of the transducer. A subarray size of $L = \frac{M}{4} = 32$ was used, and before beamforming, additional white, Gaussian noise was added to each of the sensor signals. The signal-to-noise ratio was 60 dB, and the correct sound speed was 1540 m/s.

The sound speed estimate is changed percentage-wise from the true value by 2%, 4%, and 6%, which correspond to velocities of $\{1571, 1602, 1632\}$ m/s. The adaptive beamformers with the three covariance matrix estimation approaches are

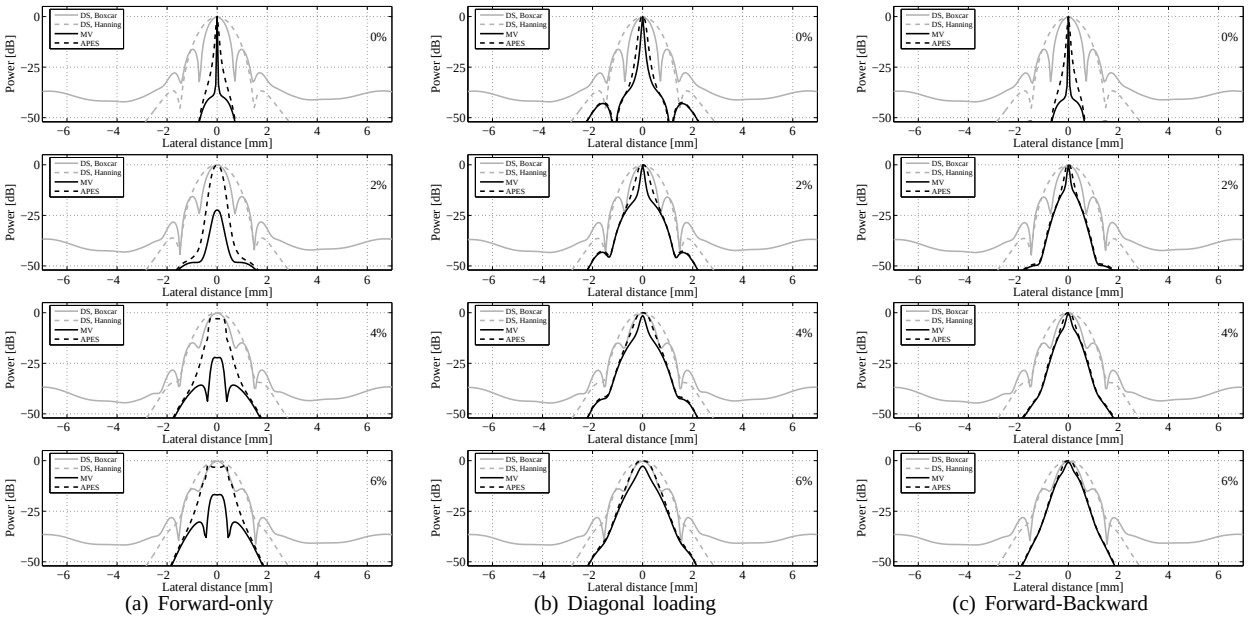

(a) Forward-only (b) Diagonal loading (c) Forward-Backward

Fig. 1. Lateral variation of the beamformed responses at depth $z = 40$ mm. The beamformed responses are DS, Boxcar (gray solid), DS, Hanning (gray dashed), MV (black solid) and APES (black dashed). (a) Forward-only, no diagonal loading has been applied. (b) Forward-only, diagonal loading factor of $\varepsilon = 10^{-3}\mathrm{Tr}\{\mathbf{R}\}$ is used. (c) Forward-backward averaging is used (no diagonal loading). The percentage error of the sound speed is given at the top right in each figure.

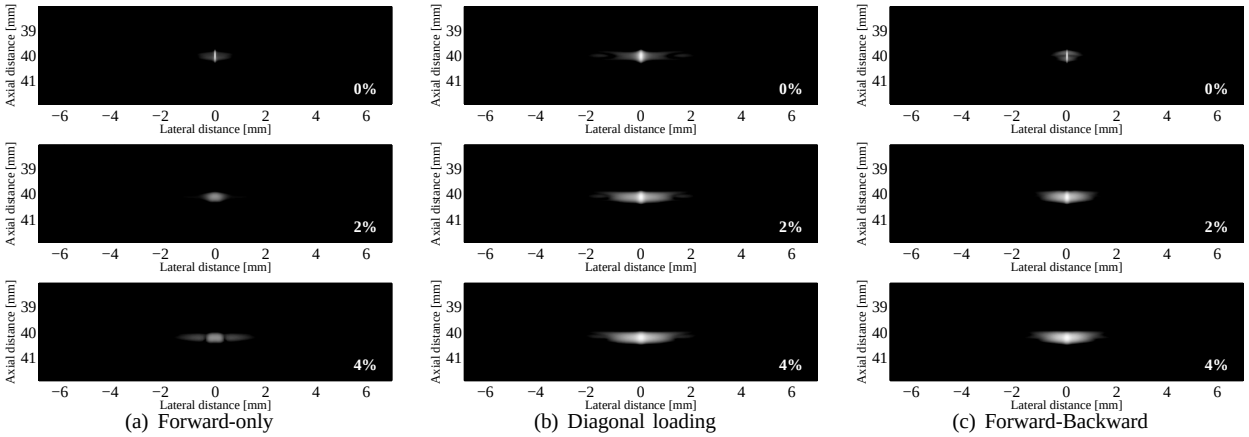

(a) Forward-only (b) Diagonal loading (c) Forward-Backward

Fig. 2. Minimum variance beamformed responses from a single point target for different percentage error on the sound speed. Images are shown with a dynamic range of 50 dB.

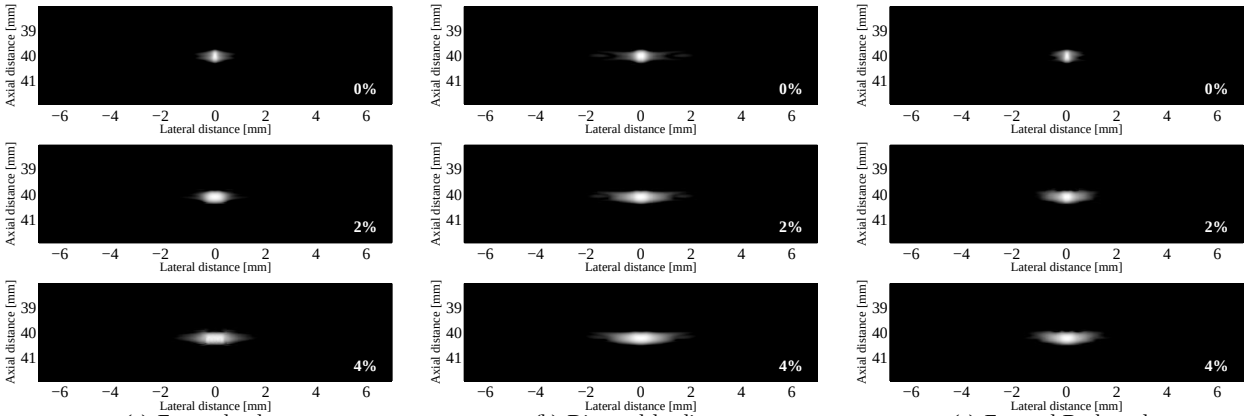

(a) Forward-only (b) Diagonal loading (c) Forward-Backward

Fig. 3. APES beamformed responses from a single point target for different percentage error on the sound speed. Images are shown with a dynamic range of 50 dB.

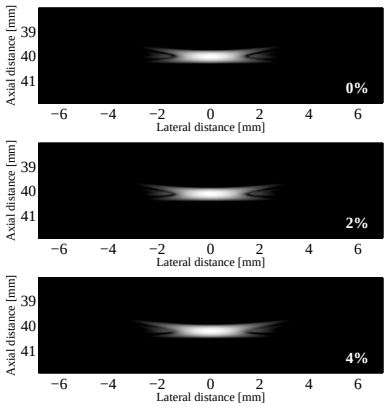

Fig. 4. Delay-and-sum (Hanning weights) beamformed responses from a single point target for different percentage error on the sound speed. Images are shown with a dynamic range of 50 dB.

compared to the DS beamformer using Boxcar and Hanning weights. The lateral variation of the beamformed responses os a single point target are seen in Fig. 1. Furthermore, a selection of the MV and APES beamformed responses are seen in Fig. 2 and Fig. 3. For comparison the DS beamformed responses using Hanning weights are shown in Fig. 4.

At the top in Fig. 1(a)-(c), the beamformed responses for the correct sound speed are shown. The inherent compromise between main-lobe width and side-lobe level is evident from these figures; the Hanning weights lower the side-lobe level at the expense of a broader main-lobe compared to the Boxcar weights.

It is seen that the MV and APES beamformers provide a significant increase in both resolution and contrast. Furthermore, it is noted that diagonal loading results in a slightly decreased resolution; as would be expected due to the convergence to the DS solution. As seen the forward-backward (FB) approach does not diminish the resolution significantly. However, these investigations are based on single point targets; as adaptive beamformers are strictly data-dependent, a truly thorough investigation should include a variety of simulations.

As the percentage error increases, the MV and APES beamformers are not as robust compared to the DS beamformer. Using the forward-only approach without diagonal loading, MV and APES provide amplitude drops on the signal strength of 17 dB and 3 dB, respectively. This amplitude drop can be avoided by using either diagonal loading or FB as seen in Fig. 1(b)-(c). However, a slight amplitude drop is seen for MV at 4% and 6% error using diagonal loading.

In general, it is observed that the APES beamformer provide more robust estimates than MV; in terms of less amplitude drop at the expense of a slightly decreased resolution. However, the resolution decrement seems insignificant compared to the robustness gained from using this beamformer.

The investigations have shown that the performance of the adaptive beamformers are significantly decreased for increasing sound speed errors. However, it is noted that the conventional DS beamformer does not outperform the adaptive beamformers within the investigated region of errors. Thus, incorrect sound speed sound estimates will not lead to a performance degradation worse than that of the conventional DS beamformer.

IV. Conclusions

The adaptive MV and APES beamformers have been applied to simulated ultrasound data with three different covariance matrix estimation approaches; forward-only spatial smoothing, diagonal loading (DL), and forward-backward (FB) averaging. For correct speed of sound estimates, both MV and APES provide significant performance gains with respect to resolution and contrast. As the sound speed error increases, MV and APES provide 17 dB and 3 dB amplitude drops on the signal strength. However, using DL or FB the amplitude drop is avoided. Furthermore, it is seen that APES provides more robust estimates than MV. In general, it is observed that even though the performance of the adaptive beamformers is much degraded, when incorrect speed of sound is used in the beamforming. However, the performance was shown to outperform the conventional delay-and-sum beamformer.

Acknowledgment

A thanks goes to Prof. Sverre Holm, Dr. Andreas Austeng and PhD Students Johan-Fredrik Synnevåg and Ann Blomberg for valuable input. They are all with the University of Oslo, Norway. This work was supported by grant 26-04-0024 from the Danish Science Foundation and by B-K Medical ApS, Denmark.

References

[1] J. A. Mann and W. F. Walker, "A Constrained Adaptive Beamformer for Medical Ultrasound: Initial Results," in *Proc. IEEE Ultrason. Symp.*, Oct. 2002, vol. 2, pp. 1807–1810.

[2] M. Sasso and C. Cohen-Bacrie, "Medical Ultrasound Imaging Using the Fully Adaptive Beamformer," in *Proc. IEEE Int. Conf. Acous., Speech, Sig. Pro.*, March 2005, vol. 2, pp. 489–492.

[3] Z. Wang, J. Li, and R. Wu, "Time-Delay- and Time-Reversal-Based Robust Capon Beamformers for Ultrasound Imaging," *IEEE Trans. Med. Imag.*, vol. 24, no. 10, pp. 130–1322, Oct. 2007.

[4] J.-F. Synnevåg, A. Austeng, and S. Holm, "Adaptive Beamforming Applied to Medical Ultrasound Imaging," *IEEE Trans. Ultrason., Ferroelec., Freq. Contr.*, vol. 54, no. 8, pp. 1606–1613, Aug. 2007.

[5] J. Li and P. Stoica, *Robust Adaptive Beamforming*, John Wiley & Sons, New York, 2006.

[6] S. A. Goss, R. L. Johnston, and F. Dunn, "Comprehensive compilation of empirical ultrasonic properties of mammalian tissues," *J. Acoust. Soc. Am.*, vol. 64, pp. 423–457, 1978.

[7] I. K. Holfort, F. Gran, and J. A. Jensen, "Minimum Variance Beamforming for High Frame-Rate Ultrasound Imaging," in *Proc. IEEE Ultrason. Symp.*, Oct. 2007, pp. 1541–1544.

[8] J. Capon, "High-Resolution Frequency-Wavenumber Spectrum Analysis," *Proc. IEEE*, vol. 57, no. 8, pp. 1408–1418, August 1969.

[9] T.-J. Shan and T. Kailath, "Adaptive Beamforming for Coherent Signals and Interference," *IEEE Trans. Acous., Speech, Sig. Pro.*, vol. 33, no. 3, pp. 527–536, June 1985.

[10] J. Li and P. Stoica, "An Adaptive Filtering Approach to Spectral Estimation and SAR Imaging," *IEEE Trans. Sig. Pro.*, vol. 44, pp. 1469–1484, 1996.

[11] P. Stoica and R. Moses, *Spectral Analysis of Signals*, Pearson Prentice Hall, New Jersey, 2005.

[12] Y. Wang, X. Li, Y. Sun, J. Li, and P. Stoica, "Adaptive Imaging for Forward-Looking Ground Penetrating Radar," *IEEE Trans. Aero. Electron. Sys.*, vol. 41, pp. 922–936, 2005.

[13] J. A. Jensen and N. B. Svendsen, "Calculation of pressure fields from arbitrarily shaped, apodized, and excited ultrasound transducers," *IEEE Trans. Ultrason., Ferroelec., Freq. Contr.*, vol. 39, pp. 262–267, 1992.

[14] J. A. Jensen, "Field: A program for simulating ultrasound systems," *Med. Biol. Eng. Comp.*, vol. 10th Nordic-Baltic Conference on Biomedical Imaging, Vol. 4, Supplement 1, Part 1, pp. 351–353, 1996b.

Bibliography

[1] J. Capon. High-Resolution Frequency-Wavenumber Spectrum Analysis. *Proc. IEEE*, 57(8):1408–1418, August 1969.

[2] J. A. Mann and W. F. Walker. A Constrained Adaptive Beamformer for Medical Ultrasound: Initial Results. In *Proc. IEEE Ultrason. Symp.*, pages 1807–1810, Oct. 2002.

[3] O. L. Frost III. An Algorithm for Linearly Constrained Adaptive Array Processing. *IEEE Proc.*, 60(8):926–935, 1972.

[4] M. Sasso and C. Cohen-Bacrie. Medical Ultrasound Imaging Using the Fully Adaptive Beamformer. In *Proc. IEEE Int. Conf. Acous., Speech, Sig. Pro.*, volume 2, pages 489–492, March 2005.

[5] F. Viola and W. F. Walker. Adaptive Signal Processing in Medical Ultrasound Beamforming. In *Proc. IEEE Ultrason. Symp.*, pages 1980–1983, 2005.

[6] F. Viola, M. A. Ellis, and W. F. Walker. Time-Domain Optimized Near-Field Estimator for Ultrasound Imaging: Initial Development and Results. *IEEE Trans. Med. Imag.*, 27(1):99–110, Jan. 2008.

[7] M. A. Ellis and W. F. Walker. Super-Resolution Image Reconstruction With Reduced Computational Complexity. In *Proc. IEEE Ultrason. Symp.*, Sep. 2009.

[8] J.-F. Synnevåg, A. Austeng, and S. Holm. Adaptive Beamforming Applied to Medical Ultrasound Imaging. *IEEE Trans. Ultrason., Ferroelec., Freq. Contr.*, 54(8):1606–1613, Aug. 2007.

[9] Z. Wang, J. Li, and R. Wu. Time-Delay- and Time-Reversal-Based Robust Capon Beamformers for Ultrasound Imaging. *IEEE Trans. Med. Imag.*, 24(10):1308–1322, 2005.

[10] J.-F. Synnevåg, S. Holm, and A. Austeng. A Low Complexity Data-Dependent Beamformer. In *Proc. IEEE Ultrason. Symp.*, pages 1084–1087, Nov. 2008.

[11] F. Vignon and M. R. Burcher. Capon Beamforming in Medical Ultrasound Imaging with Focused Beams. *IEEE Trans. Ultrason., Ferroelec., Freq. Contr.*, 50(4):619–628, March 2008.

[12] F. Vignon and M. R. Burcher. Preserving Speckle Statistics in Minimum-Variance Beamformed Images: The Effectiveness of Spatial Compounding. In *Proc. IEEE Ultrason. Symp.*, Sep. 2009.

[13] I. K. Holfort, F. Gran, and J. A. Jensen. Minimum Variance Beamforming for High Frame-Rate Ultrasound Imaging. In *Proc. IEEE Ultrason. Symp.*, pages 1541–1544, Oct. 2007.

[14] I. K. Holfort, F. Gran, and J. A. Jensen. Broadband Minimum Variance Beamforming for Medical Ultrasound Imaging. *IEEE Trans. Ultrason., Ferroelec., Freq. Contr.*, 56(2):314–325, 2009.

[15] I. K. Holfort, F. Gran, and J. A. Jensen. Plane Wave Medical Ultrasound Imaging Using Adaptive Beamforming. In *Proc. 5th IEEE Sensor Array and Multichannel Sig. Proc. Workshop*, 2008.

[16] I. K. Holfort, F. Gran, and J. A. Jensen. High Resolution Ultrasound Imaging Using Adaptive Beamforming with Reduced Number of Active Elements. In *Proc. Int. Cong. on Ultrasonics*, 2009.

[17] I. K. Holfort, F. Gran, and J. A. Jensen. Investigation of Sound Speed Errors in Adaptive Beamforming. In *Proc. IEEE Ultrason. Symp.*, pages 1080–1083, 2008.

[18] A. E. A. Blomberg, I. K. Holfort, A. Austeng, J.-F. Synnevåg, S. Holm, and J. A. Jensen. APES Beamforming Applied to Medial Ultrasound Imaging. In *Proc. IEEE Ultrason. Symp.*, 2009.

[19] I. K. Holfort, A. Austeng, J.-F. Synnevåg, S. Holm, F. Gran, and J. A. Jensen. Adaptive Receive and Transmit Apodization for Synthetic Aperture Ultrasound Imaging. In *Proc. IEEE Ultrason. Symp.*, 2009.

[20] D. H. Johnson and D. E. Dudgeon. *Array Signal Processing. Concepts and Techniques.* Prentice-Hall., Englewood Cliffs, New Jersey, 1993.

[21] L. E. Kinsler, A. R. Frey, A. B. Coppens, and J. V. Sanders. *Fundamentals of Acoustics*. John Wiley & Sons, New York, third edition, 1982.

[22] J. A. Jensen. *Estimation of Blood Velocities Using Ultrasound: A Signal Processing Approach*. Cambridge University Press, New York, 1996.

[23] Canadian SKA Consortium. *The Square Kilometre Array*. http://www.skatelescope.ca/, 2009.

[24] P. Stoica and R. Moses. *Spectral Analysis of Signals*. Pearson Prentice Hall, New Jersey, 2005.

[25] J. S. Arora. *Introduction to Optimum Design*. McGraw-Hill, Inc., 1989.

[26] T.-J. Shan and T. Kailath. Adaptive Beamforming for Coherent Signals and Interference. *IEEE Trans. Acous., Speech, Sig. Pro.*, 33(3):527–536, June 1985.

[27] J. Li and P. Stoica. *Robust Adaptive Beamforming*. John Wiley & Sons, New York, 2006.

[28] A. Jakobsson and P. Stoica. On the Forward-Backward Spatial APES. *Signal Processing*, 86:710–715, 2006.

[29] S. Holm, J.-F. Synnevåg, and A. Austeng. Capon Beamforming for Active Ultrasound Imaging Systems. In *Proc. IEEE 13th Dig. Sig. Proc. Workshop*, pages 60–65, Jan. 2009.

[30] J. A. Jensen and N. B. Svendsen. Calculation of Pressure Fields from Arbitrarily Shaped, Apodized, and Excited Ultrasound Transducers. *IEEE Trans. Ultrason., Ferroelec., Freq. Contr.*, 39:262–267, 1992.

[31] J. A. Jensen. Field: A Program for Simulating Ultrasound Systems. *Med. Biol. Eng. Comp.*, 10th Nordic-Baltic Conference on Biomedical Imaging, Vol. 4, Supplement 1, Part 1:351–353, 1996b.

[32] F. Gran. *Spatio-Temporal Encoding in Medical Ultrasound Imaging*. PhD thesis, Ørsted•DTU, Technical University of Denmark, Lyngby, Denmark, 2005.

[33] M. I. Skolnik. *Introduction to Radar Systems*. McGraw-Hill, New York, 1980.

[34] S. I. Nikolov. *Synthetic Aperture Tissue and Flow Ultrasound Imaging*. PhD thesis, Ørsted•DTU, Technical University of Denmark, 2800, Lyngby, Denmark, 2001.

[35] S. I. Nikolov and J. A. Jensen. In-vivo Synthetic Aperture Flow Imaging in Medical Ultrasound. *IEEE Trans. Ultrason., Ferroelec., Freq. Contr.*, 50(7):848–856, 2003.

[36] J. Udesen, F. Gran, and J. A. Jensen. Fast Color Flow Mode Imaging Using Plane Wave Excitation and Temporal Encoding. In *Proc. SPIE - Progress in biomedical optics and imaging*, volume 5750, pages 427–436, Feb. 2005.

[37] J.-F. Synnevåg, C.-I. C. Nielsen, and S. Holm. Speckle Statistics in Adaptive Beamforming. In *Proc. IEEE Ultrason. Symp.*, Oct. 2007.

[38] P. D. Welch. The Use of Fast Fourier Transform for the Estimation of Power Spectra: A Method Based on Time Averaging Over Short, Modified Periodograms. *IEEE Trans. Au. Electroacous.*, AU-15:70–73, 1967.

[39] F. Gran, A. Jakobsson, and J. A. Jensen. Adaptive Spectral Doppler Estimation. *IEEE Trans. Ultrason., Ferroelec., Freq. Contr.*, 56(4):700–714, 2009.

[40] K. L. Hansen, F. Gran, I. K. Holfort, M. M. Pedersen, J. A. Jensen, and M. B. Nielsen. In-vivo Validation of Fast Spectral Velocity Estimation Techniques – Preliminary Results. In *Proc. IEEE Ultrason. Symp.*, pages 1615–1618, 2008.

[41] K. L. Hansen, F. Gran, M. M. Pedersen, I. K. Holfort, J. A. Jensen, and M. B. Nielsen. Evaluation Study of Fast Spectral Estimators Using In-vivo Data. In *Proc. IEEE Ultrason. Symp.*, 2009.

[42] K. L. Hansen, F. Gran, M. M. Pedersen, I. K. Holfort, J. A. Jensen, and M. B. Nielsen. In-vivo Validation of Fast Spectral Velocity Estimation Techniques. *Ultrasonics*, 2009.

[43] J. G. Proakis and D. G. Manolakis. *Digital Signal Processing: Principles, Algorithms, and Applications*. Pearson Education, Inc., Pearson Prentice Hall, New Jersey, fourth edition, 2007.

[44] J. A. Jensen, O. Holm, L. J. Jensen, H. Bendsen, S. I. Nikolov, B. G. Tomov, P. Munk, M. Hansen, K. Salomonsen, J. Hansen, K. Gormsen, H. M. Pedersen, and K. L. Gammelmark. Ultrasound Research Scanner for Real-time Synthetic Aperture Image Acquisition. *IEEE Trans. Ultrason., Ferroelec., Freq. Contr.*, 52 (5):881–891, May 2005.

[45] J. A. Jensen and P. Munk. A New Method for Estimation of Velocity Vectors. *IEEE Trans. Ultrason., Ferroelec., Freq. Contr.*, 45:837–851, 1998.

[46] J. A. Jensen. A New Estimator for Vector Velocity Estimation. *IEEE Trans. Ultrason., Ferroelec., Freq. Contr.*, 48(4):886–894, 2001.

[47] J. Udesen and J. A. Jensen. Investigation of Transverse Oscillation Method. *IEEE Trans. Ultrason., Ferroelec., Freq. Contr.*, 53:959–971, 2006.

APPENDIX

A

Additional Publications

This appendix includes additional papers. Except for Paper VII, these papers are not covered in the dissertation.

Paper VII was carried out in collaboration with A. Blomberg, A. Austeng, J.-F. Synnevåg and S. Holm from the University of Oslo, Norway. The paper was presented at the Ultrasonics Symposium 2009 in Rome, Italy by Ann Blomberg.

Paper VIII, IX and X are based on the adaptive spectral estimators developed in [39]. These papers present quantitative and qualitative evaluations of the adaptively estimated spectrograms.

Paper VIII is accepted for publication in Ultrasonics. Paper IX-X were presented at the Ultrasonics Symposium 2009 in Rome, Italy and 2008 in Beijing, China by Kristoffer Lindskov Hansen.

Note that Paper VIII-X form a part of a PhD dissertation by MD Kristoffer Lindskov Hansen. The dissertation was handed-in May 2009.

Paper XI is the product of a BSc project carried out by Gertrud Laura Sørensen and Julie Brinck Jensen, whom I co-supervised during my PhD project period. The paper was presented at the Ultrasonics Symposium 2008 in Beijing, China by Gertrud Laura Sørensen and Julie Brinck Jensen.

Paper XII-XIII are the product of a one-year research project by the then student, Lasse Henze, whom I co-supervised during my PhD project period. These papers were presented at the Ultrasonics Symposium 2008 in Beijing, China and 2007 in New York, NY, USA by Lasse Henze.

Paper XIV is based on my Master's thesis on blood flow estimation using an approach based on cross-correlation of directional signals. This paper was presented at the Ultrasonics Symposium 2006 in Vancouver, BC, Canada.

Paper VII

APES Beamforming Applied to Medical Ultrasound Imaging

A. E. A. Blomberg, I. K. Holfort, A. Austeng, J.-F. Synnevåg, S. Holm and J. A. Jensen

Proceedings of the IEEE International Ultrasonics Symposium

Presented in Rome, Italy, Sep. 2009

APES Beamforming Applied to Medical Ultrasound Imaging

Ann E.A. Blomberg*, Iben Kraglund Holfort† Andreas Austeng*, Johan-Fredrik Synnevåg*,
Sverre Holm*, Jørgen Arendt Jensen†,
*Department of Informatics, University of Oslo, P.O. Box 1080, NO-0316 Oslo, Norway
†Department of Electrical Engineering, Technical University of Denmark, DK-2800 Kgs. Lyngby, Denmark

***Abstract*—Recently, adaptive beamformers have been introduced to medical ultrasound imaging. The primary focus has been on the minimum variance (MV) (or Capon) beamformer. This work investigates an alternative but closely related beamformer, the Amplitude and Phase Estimation (APES) beamformer. APES offers added robustness at the expense of a slightly lower resolution. The purpose of this study was to evaluate the performance of the APES beamformer on medical imaging data, since correct amplitude estimation often is just as important as spatial resolution. In our simulations we have used a 3.5 MHz, 96 element linear transducer array. When imaging two closely spaced point targets, APES displays nearly the same resolution as the MV, and at the same time improved amplitude control. When imaging cysts in speckle, APES offers speckle statistics similar to that of the DAS, without the need for temporal averaging.**

I. Introduction

The minimum variance (MV) beamformer was originally used in passive systems for e.g. direction finding [1], and later extended to active systems such as medical ultrasound imaging [2], [3], [4]. It has been shown that the MV beamformer, when used with the right parameters, significantly improves the image resolution compared to the conventional delay-and-sum (DAS) beamformer. However, the MV is sensitive to errors in the steering vector and also suffers from signal cancellation in the case of coherent sources. Diagonal loading [5] and sub-array averaging [6] are necessary in order to address these issues. Still, the MV tends to under-estimate the amplitude of scatterers in some cases.

The closely related Amplitude and Phase Estimation (APES) beamformer was developed for improved amplitude control at the expense of slightly lower resolution. In [7], it is shown that APES is more robust against sound speed errors than MV when imaging single point targets. In this work, we have investigated the performance of the APES beamformer when imaging single and double point targets, as well as a cyst phantom. We have compared the APES beamformer to the MV and the DAS beamformers, with respect to resolvability, beamwidth, amplitude control and speckle appearance and statistics. In this context, resolvability is defined as the relative difference between the peak amplitude of the two laterally spaced point targets and the saddle point between them.

II. Methods

A. The DAS beamformer

In the conventional DAS beamformer, a time delay is applied to the received signal from each of the sensors to steer and focus the beam in a given direction, before coherently combining the signals. Given an array of M sensors, the output of a general beamformer may be written as

$$z\left[n\right] = \sum_{m=0}^{M-1} w_m^* y_m\left[n - \Delta_m\right], \tag{1}$$

where n denotes the time sample index and Δ_m is the time delay applied to sensor m. $y_m[n - \Delta_m]$ is the received and delayed signal at element m. The signal received at each sensor is multiplied by a weight, w_m. In conventional, non-adaptive beamformers such as DAS, these weights are pre-defined and thus data-independent. Often, the sensor weights are defined by a window function such as a Hanning or a Kaiser window.

B. The MV beamformer

The MV beamformer differs from the DAS beamformer in the way in which the weights, w_m in (1), are calculated. Instead of using a set of pre-defined weights, the MV beamformer uses the recorded data field in order to compute the weights which minimize the variance of the output from the beamformer, while maintaining unit gain in the direction of interest. The MV beamformer computes the aperture weights by solving the following minimization problem [1]

$$\min_{\mathbf{w}} \mathbf{w}[n]^H \hat{\mathbf{R}}[n]\mathbf{w}[n] \text{ subject to } \mathbf{w}[n]^H \ \mathbf{a} = 1, \tag{2}$$

where $\mathbf{w}$ is an Mx1 vector containing the complex sensor weights, $\hat{\mathbf{R}}$ is the estimated spatial covariance matrix, and $\mathbf{a}$ is the *steering vector*. Eq. (2) has an analytical solution given by

$$\mathbf{w}_{MV}[n] = \frac{\hat{\mathbf{R}}[n]^{-1}\mathbf{a}}{\mathbf{a}^H\hat{\mathbf{R}}[n]^{-1}\mathbf{a}}. \tag{3}$$

In active imaging systems, sub-array averaging is used to address the problem of signal cancellation caused by coherent sources. This involves dividing the transducer array into sub-arrays of length L, computing the spatial covariance matrix of each of the sub-arrays and using the averaged covariance matrix in (3). The parameter L should be chosen with care, as discussed in [3] and [4]. While long sub-arrays result in improved resolution, shorter sub-arrays tend to give more robust amplitude estimates. Diagonal loading, i.e. adding a

small amount of energy to the diagonal of the covariance matrix, is often necessary to ensure an invertible and robust estimate of the covariance matrix.

C. The APES beamformer

The APES beamformer is designed such that the output is as close as possible to a plane wave with wavenumber k_x, where k_x represents the direction in which the beam is steered. The APES beamformer computes the weights which solve the following minimization problem

$$\min_{\mathbf{w},\alpha} \frac{1}{M-L+1} \sum_{m=0}^{M-L+1} |w^H y_m[n] - \alpha e^{jk_x x_m}|^2 \quad \text{subject to } \mathbf{w}[n]^H \mathbf{a} = 1, \tag{4}$$

where n denotes the time sample index, $\mathbf{w}$ is a vector of apodization weights, m denotes the element number, x_m is the x-coordinate of element m and α is the complex amplitude of the desired plane wave. Let $G(k_x) = \frac{1}{M}\sum_{m=0}^{M-1} y_m[n] e^{-jk_x x_m}$. The expression to be minimized in (4) can be re-written as [8]

$$\begin{aligned} &\frac{1}{M-L+1} \sum_{m=0}^{M-L} |w^H y_m[n] - \alpha e^{jk_x x_m}|^2 \\ &= \mathbf{w}^H \hat{\mathbf{R}} \mathbf{w} - \alpha^* \mathbf{w}^H \mathbf{G}(k_x) - \alpha \mathbf{G}^H(k_x)\mathbf{w} + |\alpha|^2 \\ &= |\alpha - \mathbf{w}^H \mathbf{G}(k_x)|^2 + \mathbf{w}^H \hat{\mathbf{R}} \mathbf{w} - |\mathbf{w}^H \mathbf{G}(k_x)|^2. \end{aligned} \tag{5}$$

Minimizing (5) with respect to α, gives $\hat{\alpha} = \mathbf{w}^H G(k_x)$. Inserting this in (5) results in the following minimization problem

$$\min_{\mathbf{w}} \mathbf{w}^H \hat{\mathbf{Q}} \mathbf{w} \text{ subject to } \mathbf{w}[n]^H \mathbf{a} = 1, \tag{6}$$

where $\hat{\mathbf{Q}} = \hat{\mathbf{R}} - \mathbf{G}(k_x)\mathbf{G}^H(k_x)$. Eq. (6) has a solution given by [8]

$$\mathbf{w}_{APES} = \frac{\hat{\mathbf{Q}}^{-1}\mathbf{a}(k_x)}{\mathbf{a}^H(k_x)\hat{\mathbf{Q}}^{-1}\mathbf{a}(k_x)}. \tag{7}$$

The APES solution is equivalent in form to the MV solution, with the exception that the spatial covariance matrix, $\hat{\mathbf{R}}$, is replaced by $\hat{\mathbf{Q}}$, which may be interpreted as the noise covariance matrix.

III. Results and Discussion

We have used Field II [9], [10] for the simulations. Data was obtained for point targets and for a cyst phantom in speckle, using a 96-element, 3.5 MHz, 18.5 mm transducer. Dynamic focusing was used both on transmission and on reception. The cyst was modelled as a cylindrical area with a radius of 3 mm, within which the reflection coefficient of the scatterers is zero. Homogeneous tissue surrounding the cyst region was modelled by placing 350 000 randomly distributed point scatterers within a volume defined by a radial distance of 3 to 5 cm, a lateral angle of -90 ° to 90 ° and an elevation angle of -3.9 ° to 3.9 °, corresponding to the sezond zero point of the array beampattern. Two strong point reflectors were also placed inside the tissue region. Diagonal loading corresponding to $\frac{5\%}{L}$ of the received power was used, in accordance with previously recommended parameter sets [4].

Fig. 1 shows the steered response from two closely spaced point reflectors imaged using the DAS with uniform weighting (dashed line), the MV (solid line) and the APES (solid line with crosses) beamformer. The point reflectors are placed 3 mm apart, at a depth of 5 cm. In the leftmost plot, a sub-array length of L=24 is used, in the middle L=36 and on the right L = 48. For all choices of L, The MV and APES bamformers display significantly narrower mainlobes than the DAS, as well as better resolvability. Between the MV and the APES beamformers, the MV displays the narrowest mainlobe and the highest resolvability. The performance of the MV and the APES beamformers are similar for short sub-arrays (L=24). As the sub-array length increases, the performance of the APES beamformer stays relatively constant while the MV displays increasing resolvability and a narrower mainlobe, at the expense of less robust amplitude estimates (underestimated by up to 5 dB).

In Fig. 2, the resolvability (left), full width at half maximum (FWHM) (middle), and normalized peak amplitude (right) for each of the beamformers are plotted for sub-array lengths ranging from 24 to 48 in steps of 4. The DAS beamformer is able to resolve the two points by 17 dB, while the APES beamformer resolves them by about 19 dB. For the MV, the resolvability improves significantly with the sub-array length, resolving the points by about 20 dB (L=24) to 25 dB (L=48). The FWHM values for the APES and MV beamformers are both much smaller than for the DAS beamformer, but again the MV beamformer shows a slightly narrower mainlobe than the APES beamformer. The peak amplitude of the APES beamformer stays nearly constant and very close to that of DAS, while it drops down to 5 dB (L=48) below that of the DAS, for the MV.

In medical ultrasound imaging, resolution and contrast as well as reliable amplitude estimates are of importance. Also, the speckle pattern caused by scattering from micro-structures within the tissue may be of clinical interest. Fig. 3 shows a cyst phantom in speckle together with two strong point reflectors. The DAS beamformer with a rectangular window (a), and with a Hanning window (b) result in some smearing of the point reflectors, as expected due to the wide mainlobe of the conventional beamformer. The Hanning window in (b) reduces the sidelobes, resulting in less energy leakage into the cyst region, but the resolution is decreased as can be seen from the point reflectors. The MV beamformer (c) gives well-defined point targets, but there is considerable leakage into the cyst region, and the speckle pattern looks quite different from what could be expected. Temporal averaging (as in (d) where averaging over one pulse length is used) has been suggested as a way to improve the speckle statistics when using the MV [11]. The APES beamformer (e) results in a clear definition of the edges of the cyst as well as the point reflectors. Also, there is less energy leakage from sidelobes. The increased amplitude

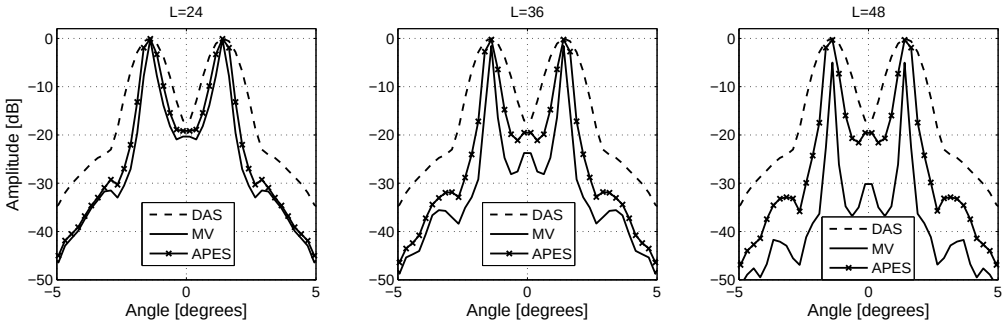

Figure 1: Steered response for the DAS (dashed), the MV (solid) and the APES (solid with crosses) beamformers, with L=24 (left), L=36 (middle) and$L$=48 (right).A 3.5 MHz 96 element array was used. The point targets are placed at a depth of 5 cm.

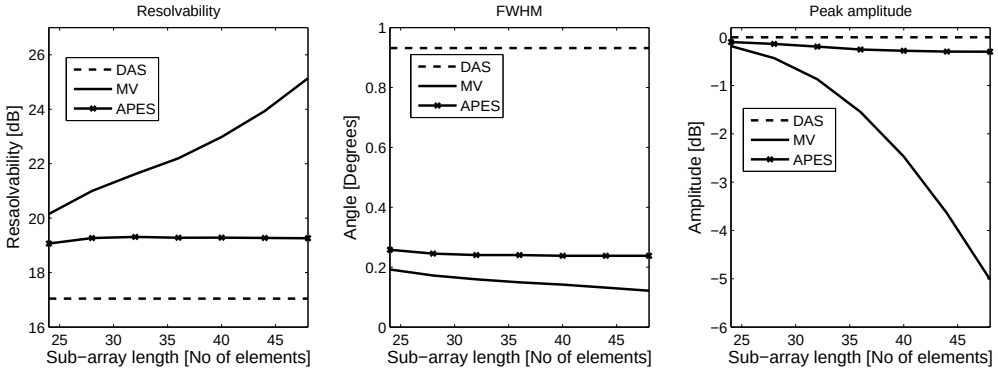

Figure 2: Resolvability (left), FWHM (middle) and normalized peak amplitude (right) for sub-array lengths from 24 to 48 in steps of four. The resolvability is measured as the relative distance between the peaks of two scatterers and the saddle point between them. FWHM is measured from the response of a single point scatterer. The peak amplitude is computed for double point reflectors ans is normalized by the peak amplitude of the DAS beamformer.

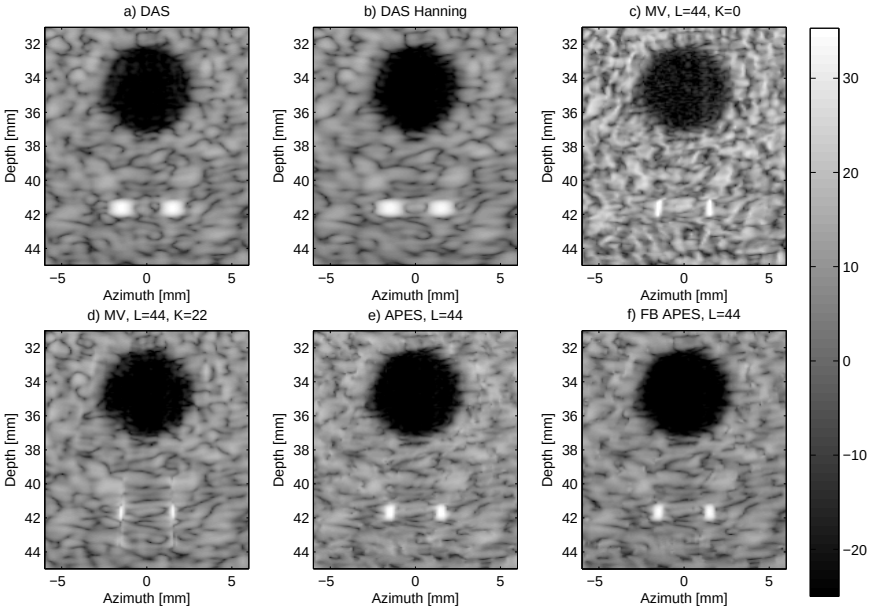

Figure 3: A simulated cyst phantom in speckle together with two strong reflectors, imaged using a 96 element, 18.5 mm, 3.5 MHz transducer. Each image is normalized by its mean speckle value. (a): DAS with a rectangular window, (b): MV with temporal averaging over one pulse length, (c): MV with temporal averaging over one pulse-length, (d): APES, (e): Forward-backward APES.

control of the APES beamformer results in a speckle pattern similar to that of the DAS beamformer, without the need for temporal averaging. Forward-backward averaging has been proposed by several authors, see e.g. [12], in order to further improve the APES estimate. APES with forward-backward averaging is shown in e).

To ensure stable results, we have run 100 simulations on a cluster of Linux workstations, randomly distributing the point scatterers each time. Fig. 4 shows a horizontal slice through the center of the cyst, created by averaging the images from the 100 simulations. 15 depth samples were averaged for each of the beamformers ((a), (d), and (e) from Fig. 3). Among these beamformers, APES provided the lowest value inside the cyst region together with the MV with temporal averaging, indicating a low amount of energy leakage into this area.

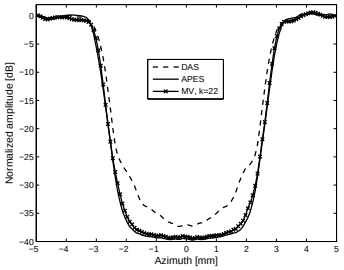

Figure 4: Horizontal slice through the center of the cyst, imaged using DAS rectangular window (dashed), APES (solid) and MV with temporal averaging (solid with crosses). Images from 100 simulations were averaged.

Speckle statistics are quantified using the pixel signal-to-noise ratio (SNR_p) (1.91 for fully developed speckle), defined as the mean value divided by the standard deviation within a speckle region [13]. Table I summarizes these values for each of the beamformers. The statistics in Table I are average values from the 100 simulations. These measurements show that the APES beamformer offers speckle statistics close to the theoretical value for fully developed speckle, without the need for temporal averaging. For the MV beamformer, temporal averaging over one pulse length is necessary in order to achieve speckle statistics comparable to that of the DAS.

Beamformer	mean	std	SNR_p
DAS	0.31	0.16	1.91
DAS Hanning	0.31	0.12	1.91
MV, K=0	0.16	0.13	1.21
MV, K=22	0.30	0.16	1.90
APES	0.28	0.14	1.91
FB APES	0.29	0.15	1.91

Table I: Speckle statistics (mean, standard deviation and SNR_p) computed from a speckle region for each of the beamformers. The values are averaged over 100 realizations of speckle.

IV. Conclusion

The APES beamformer may be preferable to the MV beamformer in applications where robustness and reliable amplitude estimates are of importance. The MV beamformer can achieve higher resolution than the APES beamformer, but it suffers from sensitivity to assumed parameters such as the propagation velocity, the choice of sub-array length and the amount of diagonal loading applied. The MV beamformer also suffers from signal cancellation in the presense of coherent sources, which is the case in an active system such as medical ultrasound imaging. Because of the way the minimization criterion is formulated in the APES beamformer, it does not suffer from signal cancellation to the same extent [12]. Also, the APES beamformer is less dependent on the choice of model parameters, and the improved amplitude control results in speckle patterns similar to that of the DAS beamformer. The computational burden of the APES beamformer is only marginally larger than that of the MV beamformer. The most demanding computational step of the MV and APES beamformers, is the matrix inversion in (3) and (7). Since the dimensions of the matrices $\hat{\mathbf{R}}$ and $\hat{\mathbf{Q}}$ are directly proportional to the sub-array lengths, L, using a shorter sub-array length will reduce the computational burden. As illustrated by Fig. 2, the performance of the APES beamformer is less dependent on L, so the sub-array length may be reduced without sacrificing performance. The fact that temporal averaging is unnecessary further reduces the number of computations. The APES beamformer is therefore a strong candidate for applications in medical ultrasound, offering high image resolution and contrast as well as robustness and speckle patterns similar to that of the DAS beamformer.

References

[1] J. Capon. High-resolution frequancy-wavenumber spectrum analysis. *Proc. IEEE*, pages 1408–1418, August 1969.

[2] I. K. Holfort, F. G., and J. A. Jensen. Broadband minimum variance beamforming for ultrasound imaging. *IEEE Trans. on Ultrason., Ferroelec., and Freq. Contr.*, February 2009.

[3] J.-F. Synnevåg, A. Austeng, and S. Holm. Adaptive beamforming applied to medical ultrasound imaging. *IEEE Trans. Ultrason., Ferroelec., Freq. Contr.*, pages 1606–1613, August 2007.

[4] J.-F. Synnevåg, A. Austeng, and S. Holm. Benefits of minimum variance beamformning in medical ultrasound imaging. *IEEE Trans. Ultrason., Ferroelec., Freq. Contr.*, September 2009.

[5] T.-J. Shan, M. Wax, and T. Kailath. On spatial smoothing for direction-of-arrival estimation of coherent signals. *IEEE Trans. Acoust., Speech, Signal Process.*, pages 806–811, August 1985.

[6] T.-J. Shan and T. Kailah. Adaptive beamforming for coherent signals and interference. *IEEE Trans. Acoust., Speech, Signal Process.*, pages 527–536, June 1985.

[7] I. K Holfort, F. Gran, and J. A. Jensen. Investigation of sound speed errors in adaptive beamforming. In *Proc. IEEE Ultrason. Symp.*, 2008.

[8] P. Stoica, H. Li, and J. Li. A new derivation of the apes filter. *IEEE Signal Processing Letters*, August 1999.

[9] J. A. Jensen and N. B. Svendsen. Calculation of pressure fields from arbitrarily shaped, apodized, and excited ultrasound transducers. *IEEE Trans. Ultrason., Ferroelec., Freq. Contr.*, pages 262–267, 1992.

[10] J. A. Jensen. A program for simulating ultrasound systems. *Med. Biol. Eng. Comp., vol. 10th Nordic-Baltic Conference on Biomedical Imaging*, pages 351–353, 1996.

[11] J.-F. Synnevåg, C. I. C. Nilsen, and S. Holm. Speckle statistics in adaptive beamforming. *Proc. IEEE Ultrason. Symp.*, pages 1545–1548, October 2007.

[12] A. Jakobsson and P. Stoica. On the forward-backward spatial APES. *Signal Process.*, 86(4):710–715, 2006.

[13] J. M. Thijssen, G. Weijers, and C. L. de Korte. Objective performance testing and quality assurance of medical ultrasound equipment. *Ultrasound in Med. & Biol.*, pages 460–471, March 2007.

Paper VIII

In-vivo Validation of Fast Spectral Velocity Estimation Techniques

K. L. Hansen, F. Gran, M. M. Pedersen, I. K. Holfort, J. A. Jensen and M. B. Nielsen

Ultrasonics, 2009

Ultrasonics xxx (2009) xxx–xxx

Contents lists available at ScienceDirect

Ultrasonics

journal homepage: www.elsevier.com/locate/ultras

In-vivo validation of fast spectral velocity estimation techniques

K.L. Hansen [a,c,*], F. Gran [b,c], M.M. Pedersen [a,c], I.K. Holfort [c], J.A. Jensen [c], M.B. Nielsen [a]

[a] Section of Ultrasound, Department of Radiology, Rigshospitalet, Blegdamsvej 9, DK-2100 Kbh. Ø, Denmark
[b] GN Resound, Lautrupbjerg 9, DK-2750 Ballerup, Denmark
[c] Center for Fast Ultrasound Imaging, DTU Elektro, Bldg. 349, Technical University of Denmark, DK-2800 Lyngby, Denmark

ARTICLE INFO

Article history:
Received 9 May 2009
Received in revised form 9 July 2009
Accepted 16 July 2009
Available online xxxx

PACS:
87.63.dk

Keywords:
Blood flow
Spectral Doppler
BAPES
BPC
Welch's method

ABSTRACT

Spectrograms in medical ultrasound are usually estimated with Welch's method (WM). WM is dependent on an observation window (OW) of up to 256 emissions per estimate to achieve sufficient spectral resolution and contrast. Two adaptive filterbank methods have been suggested to reduce the OW: Blood spectral Power Capon (BPC) and the Blood Amplitude and Phase EStimation method (BAPES). Ten volunteers were scanned over the carotid artery. From each data set, 28 spectrograms were produced by combining four approaches (WM with a Hanning window (W.HAN), WM with a boxcar window (W.BOX), BPC and BAPES) and seven OWs (128, 64, 32, 16, 8, 4, 2). The full-width-at-half-maximum (FWHM) and the ratio between main and side-lobe levels were calculated at end-diastole for each spectrogram. Furthermore, all 280 spectrograms were randomized and presented to nine radiologists for visual evaluation: useful/not useful. BAPES and BPC compared to WM had better resolution (lower FWHM) for all OW < 128 while only BAPES compared to WM had improved contrast (higher ratio). According to the scores given by the radiologists, BAPES, BPC and W.HAN performed equally well ($p > 0.05$) at OW 128 and 64, while W.BOX scored less ($p < 0.05$). At OW 32, BAPES and BPC performed better than WM ($p < 0.0001$) and BAPES was significantly superior to BPC at OW 16 ($p = 0.0002$) and 8 ($p < 0.0001$). BPC at OW 32 performed as well as BPC at OW 128 ($p = 0.29$) and BAPES at OW 16 as BAPES at OW 128 ($p = 0.55$). WM at OW 16 and 8 failed as all four methods at OW 4 and 2. The intra-observer variability tested for three radiologist showed on average good agreement (90%, $\kappa = 0.79$) and inter-observer variability showed moderate agreement (78%, $\kappa = 0.56$). The results indicated that BPC and BAPES had better resolution and BAPES better contrast than WM, and that OW can be reduced to 32 using BPC and 16 using BAPES without reducing the usefulness of the spectrogram. This could potentially increase the temporal resolution of the spectrogram or the frame-rate of the interleaved B-mode images.

1. Introduction

In ultrasound (US) imaging, visualization of blood motion can be achieved with color flow mapping, power Doppler imaging, and spectral Doppler. The three methods estimate the blood motion along the beam direction. Color flow mapping and power Doppler display the blood motion qualitatively using color coding on top of a B-mode image. The spectral Doppler method is a quantitative technique providing estimates of blood flow within a range gate on a single image line. Spectral Doppler is displayed next to the B-mode image in duplex mode where the B-mode image is used for navigation of the range gate and for flow angle correction. Alternatively, spectral Doppler is displayed in triplex mode with a B-mode image and a color flow mapping.

A typical B-mode image consists of about 64 image lines. Whether the technique is color flow mapping, power Doppler or spectral Doppler, the axial velocity of the blood is found by imaging the same image line repeatedly. In spectral Doppler, the estimates are angle-corrected by the operator and presented as blood velocities plotted against time, denoted a spectrogram. In most commercial scanners Welch's method (WM) [1,2] is used for estimation of the spectrogram. To obtain an acceptable spectral resolution with WM, an observation window (OW) of up to 256 consecutive emissions for each velocity estimate is used [3].

At the same time as showing a spectrogram of the blood velocity distribution, it is desirable to show a B-mode image of the surrounding tissue, which can be solved with or without interleaving of B-mode transmissions.

The first option is to let the scanner use an interleaving scheme where every other transmission is a B-mode transmission. This

* Corresponding author. Address: Section of Ultrasound, Department of Radiology, Rigshospitalet, Blegdamsvej 9, DK-2100 Kbh. Ø, Denmark. Tel.: +45 35 45 68 94; fax: +45 35 45 20 58.
E-mail address: lindskov@gmail.com (K.L. Hansen).

0041-624X/$ - see front matter © 2009 Elsevier B.V. All rights reserved.
doi:10.1016/j.ultras.2009.07.007

reduces the effective pulse repetition frequency (PRF) of the Doppler sequence and puts a limit on how fast the blood can move before the spectrogram shows aliasing. If the full PRF is to be exploited, to image fast flow without aliasing, this method can no longer be used. The spectrogram in turn has to be updated every 4–16 ms, which at 12 kHz PRF corresponds to every 48–192 samples. Since the observation window can be up to 256 samples long, it is no longer possible to interleave any B-mode transmissions. In this case, Doppler transmissions are carried out continuously, and the only way to create a B-mode image is to interrupt the Doppler sequence and acquire a full B-mode image. This creates a gap in the spectrogram, which naturally is undesirable and therefore done as seldom as possible. Thus, the frame-rate of the B-mode images will be low and can be decreased to the point where the examination is difficult to perform. The importance of a sufficiently high frame-rate has previously been addressed by a number of authors in relation to color flow mapping [3,4]. However, it is also valid for spectral Doppler as the operator can experience difficulties in placing the range gate in the vessel of interest as respiratory movements by the patient or involuntary transducer movements by the operator are not realized and corrected due to limited frame-rate of the B-mode image.

If the most extreme spectral line update period is chosen, the spectrogram has to be updated every 48th sample. B-mode transmissions could be interleaved without interrupting the spectrogram if the OW could be reduced below 48 samples. If it is assumed that a spectrum of sufficiently good quality can be attained in 32 samples, then there are 16 transmissions left, which can be used to acquire B-mode lines. A typical B-mode image in this context consists of 64 raw B-mode lines. Consequently, $64/16*48 = 192$ transmissions (both Doppler and B-mode transmissions) have to be carried out before a full B-mode image can be displayed. At 12 kHz PRF this is equal to a frame-rate of 62.5 images/s, which is fully acceptable. If this assumption holds, it is possible with a spectral line update of 4 ms to display a spectrogram continuously with the full velocity range and B-mode images with a frame-rate of 62.5 images/s.

Another interesting aspect of the long OW of conventional spectral estimation techniques is temporal resolution. The temporal resolution of the spectrogram in conventional spectral Doppler can be impaired to the point where the rapid changes of blood velocities in systole are difficult to measure. The events of upstroke, peak velocity and downstroke lie temporally so close that the different phases are merged together due to the long OW [5].

Alternative methods for fast velocity estimation have been proposed by several groups. Coats et al. used offline computation combined with a recursive spectral estimation approach [5], Tanaka and Ohtsuki used selected phase information [6], Gran et al. proposed a method with frequency splitting using Barker and Golay code excitation [7], Oddershede et al. used multi-frequency encoding [8] and Jensen used sparse data sequences [9]. Another approach is adaptive filtering, which previously has been tested in simulations [10–12] and in phantom validation studies [13,14]. Only Herment and Giovannelli has produced examples of adaptive spectral filtration on *in-vivo* data [15].

In this paper two adaptive spectral filtering methods are validated *in-vivo* against the conventional WM for blood velocity estimation. The Blood spectral Power Capon method (BPC), based on a minimum variance estimator, has been proposed by Stoica and Moses [2,16], and the Blood spectral Amplitude and Phase EStimation (BAPES) has been proposed by Gran et al. [17,18]. The algorithm used in BPC has previously been compared to the averaged periodogram used in the WM [19,20] and both BPC and BAPES have been evaluated in simulations using Field II [21], in a flow rig with steady laminar flow and in a single *in-vivo* experiment [18].

The purpose of this paper is to investigate the *in-vivo* performances of BPC and BAPES compared to WM. Ten volunteers were scanned on the common carotid artery. From each data set, spectrograms were found by using BPC, BAPES and WM on a series of different OWs. To investigate the methods quantitatively, a spectrum at end-diastole was taken out from each spectrogram and two parameters were calculated: the full-width-at-half-maximum (FWHM) and the ratio between main and side-lobe levels. To investigate the estimates qualitatively, a prospective trial was conducted where all the spectrograms were randomized and presented to nine radiologists blinded to method and OW for visual evaluation.

2. Materials and method

2.1. Volunteers

This prospective study was performed after approval by The Danish National Committee on Biomedical Research Ethics. Ten healthy volunteers (nine males and one female, mean age: 29.1 years, range: 24–36 years) entered the study after informed consent. The right common carotid artery was examined in all volunteers using US. All scans were carried out by an experienced radiologist.

2.2. Spectral estimators

WM is applied on data using two different weighting schemes to control contrast and resolution in the resulting spectrogram: WM with a Hanning window (W.HAN) and WM with a boxcar window (W.BOX) (Fig. 1). W.HAN is the preferred conventional spectral estimator. It is well known in digital signal processing [22] that due to Hanning weighting of data the resulting spectrogram has improved contrast at the expense of spectral resolution. On the contrary, spectrograms generated with the W.BOX approach have improved spectral resolution but decreased contrast compared to W.HAN.

BPC and BAPES are alternative methods using data-dependent adaptive filtering techniques based on a matched filterbank framework [2,23]. For a given data set, an optimal filter is calculated for

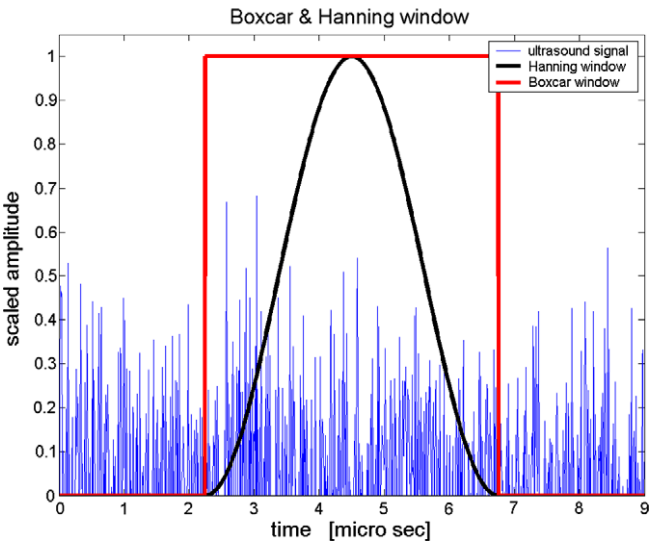

Fig. 1. The scattered signal is multiplied in the time domain with a bell-shaped Hanning window or with a rectangular boxcar window. Thus, the blood signal used for velocity estimation is found under the curve corresponding to the chosen window.

Please cite this article in press as: K.L. Hansen et al., *In-vivo* validation of fast spectral velocity estimation techniques, Ultrasonics (2009), doi:10.1016/j.ultras.2009.07.007

each velocity component to minimize noise and interference from other velocities. Such that to each data set a unique filterbank is generated. In BPC the filters are designed to minimize the total power of the filtered data, while in BAPES the filters are designed to minimize the power of the filtered noise; including interfering signals, such as contributions from additional velocity components. In general these methods display better velocity resolution than traditional methods like W.HAN and W.BOX. The details of the implementation can be found in [17,18].

2.3. Setup

Ten healthy volunteers were scanned on the right common carotid artery using the experimental scanner RASMUS [24] and a B-K Medical 8804, 7 MHz linear array transducer. The setup is given in Table 1. One data set of approximately 2.5 s was recorded for each volunteer where the sequential data acquisition alternated between a sequence for flow estimation of 3800 consecutive emissions and a sequence for B-mode imaging of 65 consecutive emissions. The recorded data was post processed using the four different methods: W.HAN, W.BOX, BPC and BAPES. For each method, spectrograms were estimated using different OWs: 128, 64, 32, 16, 8, 4 and 2 emissions/estimate. Hence, 28 spectrograms were calculated from every data set giving in total 280 spectrograms for all volunteers. Post processing was done offline with MATLAB (Mathworks, Natick, MA, USA) on a 100 CPU Linux cluster.

2.4. Quantitative evaluation

To investigate the methods quantitatively, a spectrum at end-diastole was found for each spectrogram. For each data set, the time instant was chosen by visually examining the spectrogram obtained with W.HAN at OW 128. For the selected time, spectra from all 28 spectrograms of the same data set were found. End-diastole was chosen to be the time of interest as it is easy to identify and used clinically for calculating e.g. resistive index [25]. From each spectrum, two parameters were calculated: the FWHM and the ratio between main and side-lobe levels. The FWHM was found as the width of the velocity distribution of the main lobe at half of the maximum amplitude. Thus, the FWHM, given in m/s, is a measure of spectral resolution. The main to side-lobe ratio was found as the relative difference between the side-lobe level and the peak amplitude. The side-lobe level was found as the median value of the distributed amplitudes outside the main lobe, outlined by the FWHM. The ratio, given in decibel (dB), is a measure of contrast in the spectrogram.

2.5. Qualitative evaluation

To investigate the methods qualitatively, nine experienced radiologists evaluated in a blinded trial the 280 randomized spectrograms by scoring each spectrogram as useful or not useful. Additionally, intra- and inter-observer variations were found. The intra-observer variability was assessed by comparing the scores given twice by three radiologists with >14 days between each session. The sequence of spectrograms was randomized to each session so judgement bias was minimized.

Table 1
Scanner and transducer setup.

Parameter	Value	Unit
Sampling frequency	40	MHz
Center frequency	7	MHz
Pulse repetition frequency	9.3	kHz
Number of transmitting elements	64	Elements
Apodization in transmit	Uniform	N/A
Number of receiving elements	64	Elements
Apodization in receive	Hanning	N/A
Wall motion filter	mean − subtraction	N/A

2.6. Statistics

A descriptive statistical analysis was computed on FWHM and ratio data of the 280 spectra finding mean value and standard deviation for each combination of method and window. The scores given by the radiologists were pooled by method and window. Useful and not useful were coded with the dummy variables 1 and 0, respectively. Before data analysis, Kolmogorov–Smirnov normality test and the Levene variance homogeneity test were applied to the data. No data transformation was needed. Bonferroni adjusted tests for multiple comparisons paired on volunteer level with $p < 0.05$ considered significant were performed [26]. The intra- and inter-observer variability were investigated using Cohen's and Fleiss' kappa, respectively [27,28]. Statistical analyses were performed using SAS (SAS Institute, Cary, NC, USA) and MATLAB (Mathworks, Natick, MA, USA).

3. Result

From the same data set with three systoles recorded, examples of spectrograms obtained with the four methods at OW 128 and 16, are presented (Fig. 2). The gaps in the spectrograms represent the necessary pulse emissions used for generating the interleaved B-mode images. Examples of spectra obtained from the spectrograms shown in Fig. 2 at end-diastole (time 2.2 s) are presented in Fig. 3. Mean and standard deviation of FWHM and ratio for the 280 spectra pooled by method and window are displayed in Table 2 and plotted in Fig. 4. For the qualitative evaluation, the total sum of scores given for each combination of method and window is displayed in Table 3 and illustrated in Fig. 5. The total sum of scores for each combination is found in the range between 0 and 90 as it is found by adding the scores given by nine radiologists on 10 volunteers.

The result of Bonferroni adjusted tests for multiple comparisons on the summed scores for each combination of method and window is shown in Table 4 and illustrated in Fig. 6. The sum of scores for each spectrogram is found from the scores given by nine radiologists, and therefore, in the range from 0 to 9. Thus, each combination includes 10 summed scores, one for each of the 10 spectrograms. The mean of the summed scores for each combination is given as well in Table 4 and Fig. 6.

For each method, tests for multiple comparisons were also used to investigate at which OWs the given scores were significantly different from the score given at OW 128. W.BOX performed significantly worse when OW was reduced to 64 compared to W.BOX at OW 128 ($p = 0.03$). W.HAN was not scored differently when reducing OW to 64 ($p = 0.55$) but was scored significantly less at OW 32 ($p < 0.0001$). BPC performed equally well at OW 32 compared to OW 128 ($p = 0.30$) while BAPES scored significantly higher at OW 32 compared to OW 128 ($p = 0.02$). Only BAPES performed as well for OW 16 as at OW 128 ($p = 0.55$). All four methods had decreased performances at OW 8, 4 and 2 compared to OW 128. The intra-observer variability for three radiologist evaluating the same 280 spectrograms with >14 days apart showed good agreement with an averaged Cohen's kappa value of 0.79 (94%, $\kappa = 0.88$; 83%, $\kappa = 0.67$; 93%, $\kappa = 0.81$). The inter-observer variability showed moderate agreement using Fleiss' kappa (78%, $\kappa = 0.57$).

Please cite this article in press as: K.L. Hansen et al., *In-vivo* validation of fast spectral velocity estimation techniques, Ultrasonics (2009), doi:10.1016/j.ultras.2009.07.007

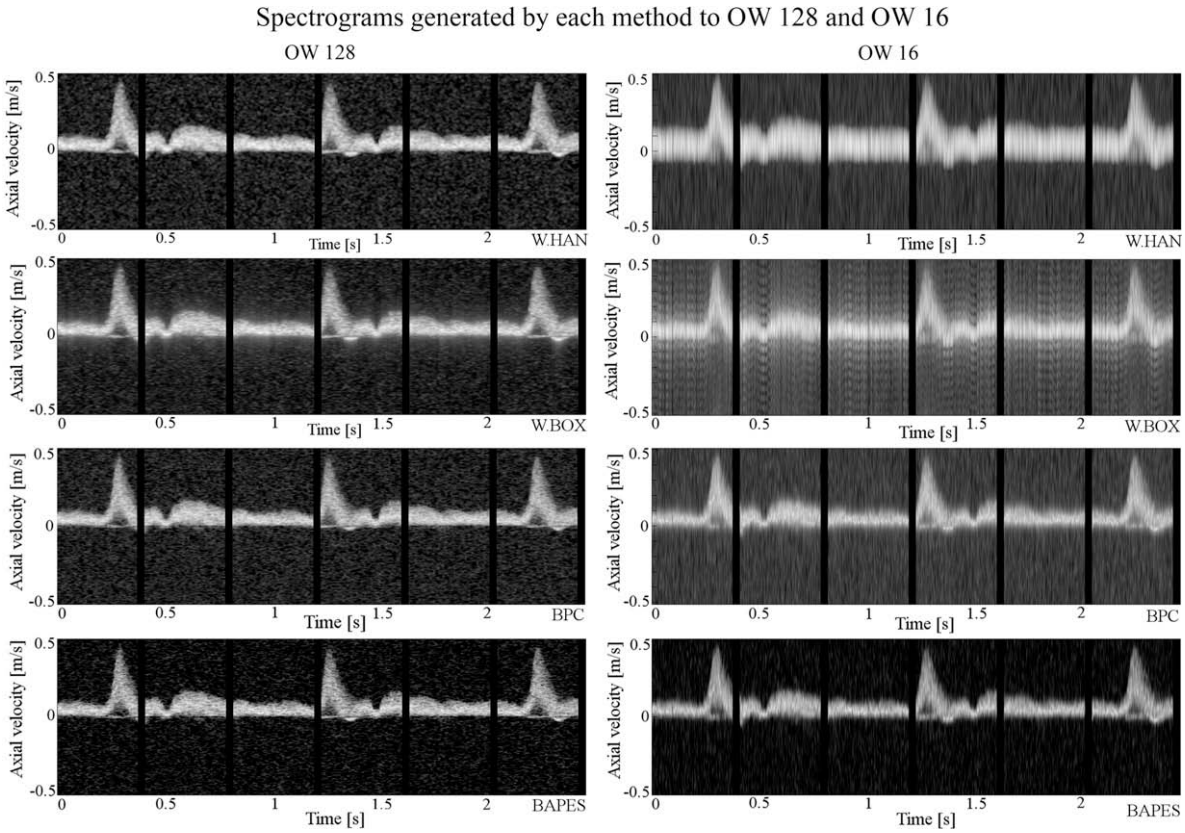

Fig. 2. Spectrograms were found using the four methods with an OW 128 (left frames) and 16 (right frames). At OW 128 all methods displayed good performances. At OW 16, W.HAN and W.BOX estimated spectrograms with decreased quality compared to BPC and BAPES.

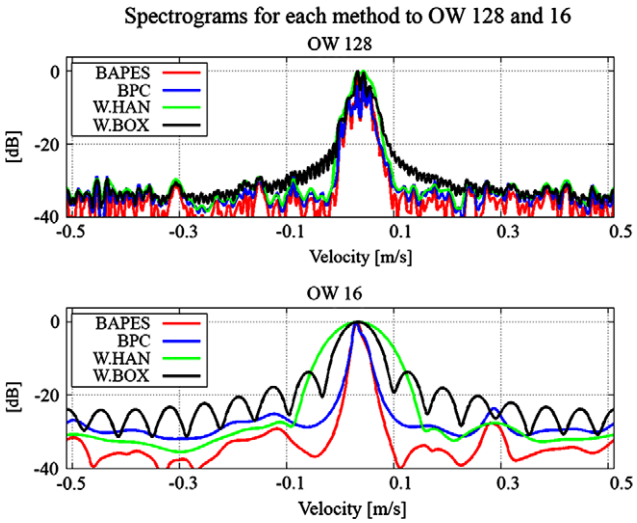

Fig. 3. From the same volunteer at one time instant, spectra were generated using the four methods with an OW 128 and 16.

Table 2
Mean (and standard deviation) of FWHM and ratio given for each combination OW/method over 10 volunteers.

ow	Parameter	BAPES	BPC	W.HAN	W.BOX
128	FWHM (m/s)	0.029 (0.01)	0.026 (0.01)	0.034 (0.01)	0.029 (0.01)
	Ratio (dB)	37.06 (3.19)	33.64 (3.16)	34.47 (3.20)	32.80 (2.45)
64	FWHM (m/s)	0.025 (0.01)	0.032 (0.01)	0.050 (0.01)	0.040 (0.01)
	Ratio (dB)	35.81 (3.91)	29.89 (2.76)	31.53 (2.63)	29.31 (1.87)
32	FWHM (m/s)	0.034 (0.02)	0.033 (0.02)	0.074 (0.01)	0.055 (0.01)
	Ratio (dB)	34.02 (4.47)	28.71 (2.94)	30.67 (4.63)	26.60 (2.25)
16	FWHM (m/s)	0.029 (0.01)	0.027 (0.01)	0.124 (0.00)	0.082 (0.01)
	Ratio (dB)	33.27 (5.24)	29.03 (4.41)	29.63 (5.81)	22.99 (1.73)
8	FWHM (m/s)	0.034 (0.01)	0.033 (0.02)	0.230 (0.00)	0.159 (0.01)
	Ratio (dB)	31.26 (5.17)	26.01 (4.18)	26.49 (5.33)	17.85 (0.81)
4	FWHM (m/s)	0.065 (0.02)	0.053 (0.03)	0.412 (0.01)	0.319 (0.00)
	Ratio (dB)	26.73 (4.73)	22.23 (4.01)	20.51 (3.29)	13.20 (0.60)
2	FWHM (m/s)	0.145 (0.03)	0.113 (0.06)	0.688 (0.01)	0.688 (0.01)
	Ratio (dB)	23.38 (4.13)	18.94 (4.18)	11.21 (0.51)	11.21 (0.51)

4. Discussion

FWHM is a measure of spectral resolution and should be as low as possible, while the ratio is a measure of spectral contrast and should be as high as possible. It is seen in Table 2 and Fig. 4 that on average for all OWs above 2, W.BOX performed with better resolution than W.HAN and W.HAN performed with better contrast than W.BOX. The adaptive methods outperformed WM in terms of resolution at all OWs below 128 and it is seen that BPC had a slightly better resolution than BAPES. In terms of contrast, BAPES was superior compared to both BPC and WM for all OWs. The W.HAN had better contrast than BPC for all OWs above 8.

In Fig. 2 examples of spectrograms obtained with the four approaches at OW 128 and 16 are shown. Spectral resolution in the spectrogram corresponds to the width of the white curve representing estimated blood velocities, while the difference between the white curve and the darker surroundings corresponds to contrast. The spectrograms underline the results of the quantitative tests. At OW 128 the four approaches produced spectrograms of good quality while the estimators differed in performance at OW

Please cite this article in press as: K.L. Hansen et al., *In-vivo* validation of fast spectral velocity estimation techniques, Ultrasonics (2009), doi:10.1016/j.ultras.2009.07.007

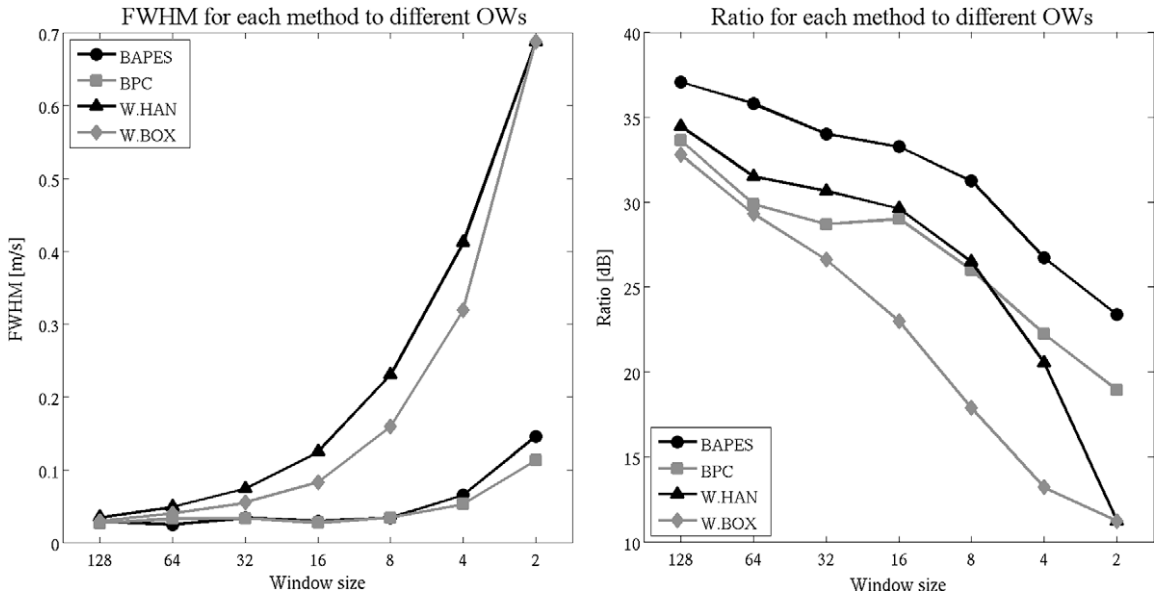

Fig. 4. FWHM (left frame) and ratio (right frame) are plotted against OW for each method.

Table 3
Each cell consists of the total sum of scores given by nine radiologists on 10 volunteers in the range 0 to 90 (and percentage) for the combination method/OW.

ow	BAPES	BPC	W.HAN	W.BOX
128	72 (80%)	73 (81.1%)	73 (81.1%)	62 (68.9%)
64	73 (81.1%)	78 (86.7%)	75 (83.3%)	55 (61.1%)
32	80 (88.9%)	77 (85.6%)	34 (37.8%)	23 (25.6%)
16	70 (77.8%)	50 (55.6%)	5 (5.6%)	5 (5.6%)
8	31 (34.4%)	13 (14.4%)	0 (0.0%)	0 (0.0%)
4	6 (6.7%)	6 (6.7%)	0 (0.0%)	0 (0.0%)
2	0 (0.0%)	0 (0.0%)	0 (0.0%)	0 (0.0%)

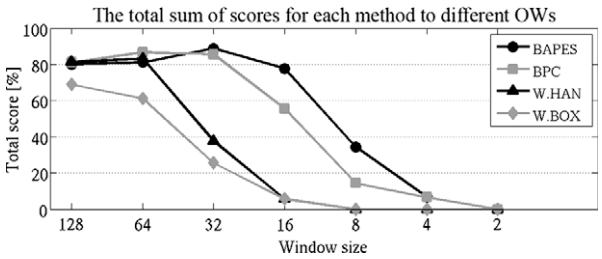

Fig. 5. The total sum of scores in percentage for each method to different OWs.

16. At OW 16, it is seen that W.BOX estimated with a higher spectral resolution than W.HAN and the adaptive methods with higher spectral resolution than WM. Furthermore, it is seen that the contrast decreased from BAPES to BPC and WM. W.BOX performed poorest among the four methods in terms of contrast and a so-called ringing phenomenon at OW 16 can be seen.

Spectra for the methods are shown in Fig. 3. The side lobes representing leakage from the true velocity were suppressed, while the main lobe representing the true velocity was broadened for W.HAN compared to W.BOX. The pronounced side lobes for W.BOX at OW 16 correspond to the ringing phenomenon shown in Fig. 2. The adaptive methods had a narrower main lobe at OW 16 compared to WM, and BAPES displayed better side-lobe levels compared to both BPC and WM.

The overall result of the qualitative evaluation displayed in Table 3 and Fig. 5 shows that the radiologists preferred the adaptive methods over WM, BAPES over BPC and W.HAN over W.BOX. The inter- and intra-observer variability were additionally tested and showed moderate and good agreement, respectively, indicating consistent scores given by each radiologists with a base-line difference among the radiologists. In Table 4 and Fig. 6 the results of the statistical analyses on the mean of scores using Bonferroni adjusted tests for multiple comparisons are displayed. It is seen that at OW 128 and 64, BAPES, BPC and W.HAN performed equally well while W.BOX scored significantly less. When reducing the OW to 32, the adaptive methods BAPES and BPC performed better than W.HAN and W.BOX. However, BAPES was superior to BPC at OW 16 and 8. At OW 16 and 8 the conventional methods were scored useless. When the OW was decreased to 4 and 2 all four methods failed according to the radiologists.

For each method, the scores given at window sizes below OW 128 were compared to the score given at OW 128 to evaluate how robust each method was to reduction of OW. At OW 64 only W.BOX scored significantly worse, while W.HAN significantly decreased in score at OW 32. At OW 32, BPC scored as at OW 128 while BAPES actually scored significantly better. At OW 16, only BAPES was scored equal to OW 128. Hence, W.HAN at OW 64, BPC at 32 and BAPES at 16 can produce spectrograms, according to the nine radiologists, which are as acceptable as if they were produced at OW 128.

Moreover, the radiologists preferred contrast to spectral resolution when comparing scores given for W.BOX and W.HAN at OW 128 and 64 and in most modern scanners the Hanning weighting scheme is accordingly implemented for spectral blood estimation. However, when comparing BPC and W.HAN the improved resolution in BPC was preferred to the improved contrast in W.HAN. This is seen in Table 4 and Fig. 6 at OW 32 and 16. It indicates that it is not only the raised side-lobe level in W.BOX, which reduces the quality of the spectrogram compared to W.HAN but also the accompanying ringing phenomenon.

The radiologists significantly preferred BAPES at OW 32 compared to BAPES at OW 128 ($p = 0.01$). The reason could be that the observers were disturbed visually by the high contrast and spectral resolution of the spectrograms obtained with BAPES/OW 128 and somewhat preferred the smoothing of details as presented in spectrograms obtained with BAPES/OW 32.

Please cite this article in press as: K.L. Hansen et al., *In-vivo* validation of fast spectral velocity estimation techniques, Ultrasonics (2009), doi:10.1016/j.ultras.2009.07.007

Table 4
The mean of the summed scores (and standard deviation) is given on volunteer level in the range 0 to 9 for each combination method/OW. For each OW, comparison tests between methods indicated by "X" were performed with 95% CI in difference of means and *p*-value given. Significant findings are marked by a "●". No comparison is done for OW 2 as all methods were scored useless.

	BAPES	BPC	W.HAN	W.BOX	95% CI	*p*-value
128 Emissions/estimate	7.2 (0.91)	7.3 (0.65)	7.3 (0.95)	6.2 (1.23)		
BAPES vs. BPC	X	X			(−1.03;0.83)	1.0
BAPES vs. W.HAN	X		X		(−1.03;0.83)	1.0
BAPES vs. W.BOX	X			X	(0.07;1.93)	0.03 ●
BPC vs. W.HAN		X	X		(−0.93;0.93)	1.0
BPC vs. W.BOX		X		X	(0.17;2.03)	0.01 ●
W.HAN vs. W.BOX			X	X	(0.17;2.03)	0.01 ●
64 Emissions/estimate	7.3 (0.82)	7.8 (0.79)	7.5 (0.97)	5.5 (0.71)		
BAPES vs. BPC	X	X			(−1.34;0.35)	0.63
BAPES vs. W.HAN	X		X		(−1.04;0.64)	1.0
BAPES vs. W.BOX	X			X	(0.95;2.65)	<0.0001 ●
BPC vs. W.HAN		X	X		(−0.54;1.15)	1.0
BPC vs. W.BOX		X		X	(1.45;3.15)	<0.0001 ●
W.HAN vs. W.BOX			X	X	(1.15;2.85)	<0.0001 ●
32 Emissions/estimate	8.0 (0.94)	7.7 (1.25)	3.4 (1.51)	2.3 (1.25)		
BAPES vs. BPC	X	X			(−1.24;1.84)	1.0
BAPES vs. W.HAN	X		X		(3.06;6.14)	<0.0001 ●
BAPES vs. W.BOX	X			X	(4.16;7.24)	<0.0001 ●
BPC vs. W.HAN		X	X		(2.76;5.84)	<0.0001 ●
BPC vs. W.BOX		X		X	(3.86;6.94)	<0.0001 ●
W.HAN vs. W.BOX			X	X	(−0.44;2.64)	0.31
16 Emissions/estimate	7.0 (1.15)	5.0 (1.15)	0.5 (0.53)	0.5 (0.53)		
BAPES vs. BPC	X	X			(0.84;3.16)	0.0002 ●
BAPES vs. W.HAN	X		X		(5.34;7.66)	<0.0001 ●
BAPES vs. W.BOX	X			X	(5.34;7.66)	<0.0001 ●
BPC vs. W.HAN		X	X		(3.34;5.66)	<0.0001 ●
BPC vs. W.BOX		X		X	(3.34;5.66)	<0.0001 ●
W.HAN vs. W.BOX			X	X	(-1.16;1.16)	1.0
8 Emissions/estimate	3.1 (1.10)	1.3 (0.94)	0 (0)	0 (0)		
BAPES vs. BPC	X	X			(0.99;2.61)	<0.0001 ●
BAPES vs. W.HAN	X		X		(2.29;3.91)	<0.0001 ●
BAPES vs. W.BOX	X			X	(2.29;3.91)	<0.0001 ●
BPC vs. W.HAN		X	X		(0.49;2.11)	0.0006 ●
BPC vs. W.BOX		X		X	(0.49;2.11)	0.0006 ●
W.HAN vs. W.BOX			X	X	(-0.81;0.81)	1.0
4 Emissions/estimate	0.6 (0.84)	0.6 (0.70)	0 (0)	0 (0)		
BAPES vs. BPC	X	X			(−0.62;0.62)	1.0
BAPES vs. W.HAN	X		X		(−0.02;1.21)	0.062
BAPES vs. W.BOX	X			X	(−0.02;1.21)	0.062
BPC vs. W.HAN		X	X		(−0.02;1.21)	0.062
BPC vs. W.BOX		X		X	(−0.02;1.21)	0.062
W.HAN vs. W.BOX			X	X	(−0.62;0.62)	1.0
2 Emissions/estimate	0 (0)	0 (0)	0 (0)	0 (0)		

Fig. 5 and Table 3 indicate that even at the presumably best condition, i.e. OW 128, only 80% of the spectrograms were accepted. No data set was consistently rejected indicating that the 10 data set were of equal quality. However, the ratings of the nine radiologists varied significantly. At OW 128, two of the nine radiologists only accepted 7.5% and 60% of the spectrograms, respectively, while the other seven radiologists on average accepted 90% of the spectrograms (range: 82–100%).

When evaluating the spectrograms acquired on the experimental system, the radiologists use their experience from daily practice on commercial systems as reference. Limitations in the experimental setup are believed to be reflected in the high rejection rate for some of the radiologists. Data was acquired using the experimental scanner RASMUS and the spectrograms were calculated using MATLAB on a 100 CPU Linux cluster. This combination provided a flexible environment for acquiring and processing the data from an experimental point of view, but, compared to commercial scanners, the signal-to-noise ratio of the resultant spectrograms were lower. Moreover, adjustment of PRF, spectral gain or baseline was not feasible in the evaluation setup.

The US examination of today can potentially be improved if the conventional WM for blood velocity estimation used in commercial scanners was to be replaced with one of adaptive spectral estimators BPC or BAPES. Consequently, the decreased OW could potentially be used to increase the temporal resolution of the spectrogram. Alternatively, depending on PRF, spectral line update period and desired B-mode frame-rate, the scheme suggested in the introduction could potentially be used to show the spectrogram and B-mode images simultaneously with the full velocity range. According to Gran et al. [7,18], the adaptive methods are more computationally demanding than the conventional WM, and BAPES is more computationally heavy than BPC. However, when reducing the OW, the computational costs decrease as well. Therefore, the BAPES method implemented with an OW 16 or the BPC method with an OW 32 may be as tractable as WM with a much longer OW. It should therefore be possible to implement the methods into commercial scanners and convert the methods to an actual real-time modality.

5. Conclusions

In this paper the performances of two adaptive spectral estimators BPC and BAPES were investigated *in-vivo*. It was shown that the adaptive methods were superior to the conventional WM and

Please cite this article in press as: K.L. Hansen et al., *In-vivo* validation of fast spectral velocity estimation techniques, Ultrasonics (2009), doi:10.1016/j.ultras.2009.07.007

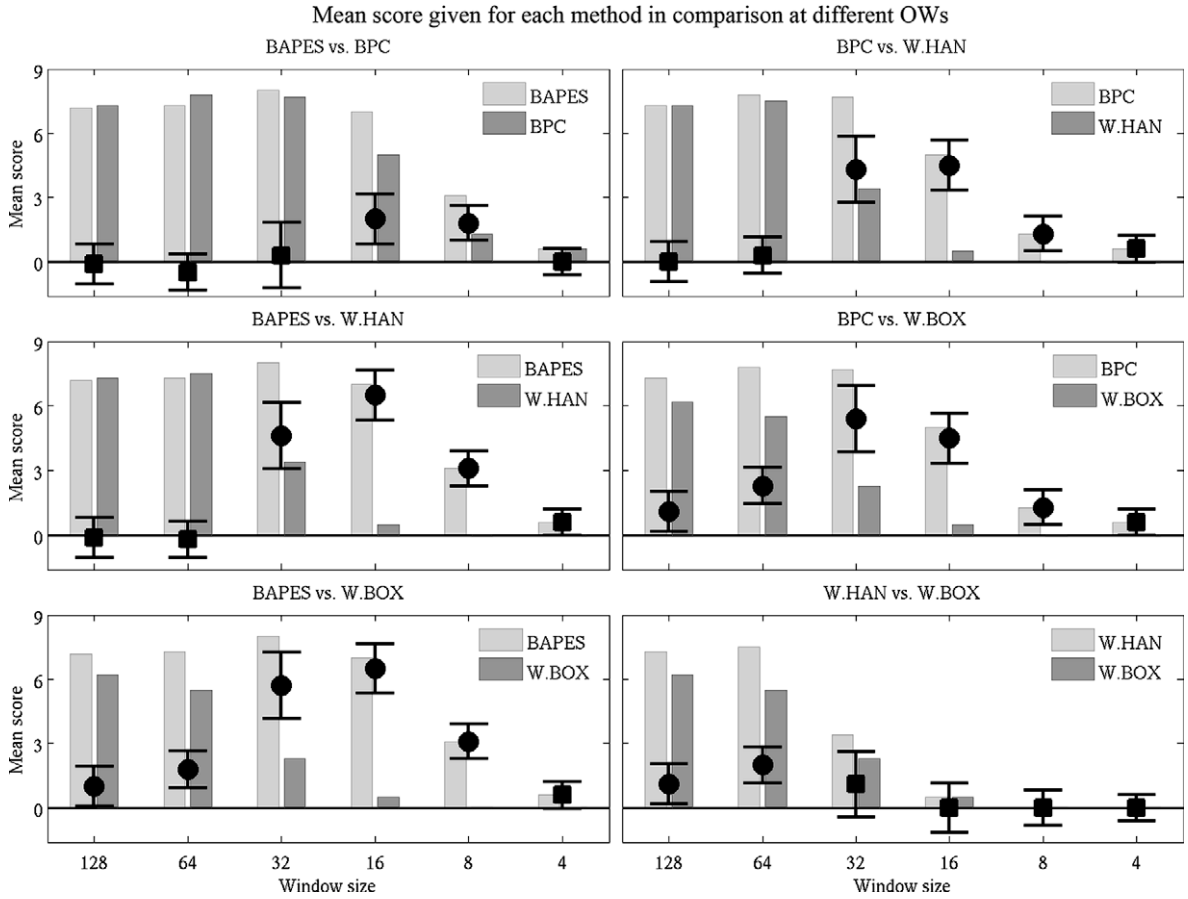

Fig. 6. The mean of scores for each method in comparison over different OWs is shown. The 95% confidence interval for the difference in means is illustrated with a bar and marked "■" if insignificant or "●" if significant. Comparisons to OW 2 are left out.

that BAPES was superior to BPC. The quantitative tests showed that BAPES and BPC had improved spectral resolution and BAPES had improved spectral contrast compared to WM. According to the given scores given by nine radiologists, OW can be reduced to 32 when using BPC, and 16 when using BAPES method for estimating spectrogram without losing performance. The results indicate that the adaptive methods BPC and BAPES potentially can bring improvements to spectral blood estimation as an increase of the temporal resolution of the spectrogram or as an increase of the frame-rate for the interleaved B-mode image. Further studies are needed to evaluate the adaptive spectral estimators in various *in-vivo* settings with different flow profiles, vessel geometries and scan depths using different transducers.

References

[1] P.D. Welch, The use of fast Fourier transform for the estimation of power spectra: a method based on time averaging over short, modified periodograms, IEEE Trans. Audio Electroacoust. AU-15 (1967) 70–73.
[2] P. Stoica, R. Moses, Spectral Analysis of Signals, Prentice Hall, Upper Saddle River, NJ, 2005.
[3] J.B. Kruskal, P.A. Newman, L.G. Sammons, R.A. Kane, Optimizing Doppler and color flow US: application to hepatic sonography, Radiographics 24 (2004) 657–675.
[4] K. Ferrara, G. DeAngelis, Color flow mapping, Ultrasound Med. Biol. 23 (1997) 321–345.
[5] A.J.S. Coats, C. Murphy, J. Conway, P. Sleight, Validation of the beat to beat measurement of blood velocity in the human ascending aorta by a new high temporal resolution Doppler ultrasound spectral analyser, Brit. Heart J. 68 (1992) 223–229.
[6] N. Tanaka, S. Ohtsuki, Estimation of Doppler shift frequency using selected phase information for high frame rate color flow mapping, J. Med. Ultrason. 31 (2004) 5–12.
[7] F. Gran, J. Udesen, M.B. Nielsen, J.A. Jensen, Coded ultrasound for blood flow estimation using subband processing, IEEE Trans. Ultrason. Ferroelectr. Freq. Contr. 55 (2009) 2211–2220.
[8] N. Oddershede, F. Gran, J.A. Jensen, Multi-frequency encoding for fast color flow or quadroplex imaging, IEEE Trans. Ultrason. Ferroelectr. Freq. Contr. 55 (2008) 778–786.
[9] J.A. Jensen, Spectral velocity estimation in ultrasound using sparse data sets, J. Acoust. Soc. Am. 120 (2006) 211–220.
[10] J. Li, P. Stoica, An adaptive filtering approach to spectral estimation and SAR imaging, IEEE Trans. Signal Process. 44 (1996) 1469–1484.
[11] N. Feng, J. Zhang, W. Wang, An adaptive clutter rejection method based on AR model in color flow imaging, Ultrasonics 44 (suppl. 1) (2006) e85–e88.
[12] D. Wang, Y. Shen, N.Z. Feng, A novel clutter rejection scheme in color flow imaging, Ultrasonics 44 (suppl. 1) (2006) e303–e305.
[13] M.E. Allam, J.F. Greenleaf, Isomorphism between pulsed-wave Doppler ultrasound and direction-of-arrival estimation – part I: basic principles, IEEE Trans. Ultrason. Ferroelectr. Freq. Contr. 43 (1996) 911–922.
[14] M.E. Allam, R.R. Kinnick, J.F. Greenleaf, Isomorphism between pulsed-wave Doppler ultrasound and direction-of-arrival estimation – part II: experimental results, IEEE Trans. Ultrason. Ferroelectr. Freq. Contr. 43 (1996) 923–935.
[15] A. Herment, J.F. Giovannelli, An adaptive approach to computing the spectrum and mean frequency of Doppler signals, Ultrason. Imaging 17 (1995) 1–26.
[16] P. Stoica, R. Moses, Introduction to Spectral Analysis, Prentice Hall, Upper Saddle River, NJ, 1997.
[17] F. Gran, A. Jakobsson, J.A. Jensen, Adaptive blood velocity estimation in medical ultrasound, Proc. IEEE ICASSP 1 (2007) 293–296.
[18] F. Gran, A. Jakobsson, J.A. Jensen, Adaptive spectral Doppler estimation, IEEE Trans. Ultrason. Ferroelectr. Freq. Contr. 56 (2009) 700–714.
[19] P.J. Vaikus, R.S.C. Cobbold, A comparative study and assessment of Doppler ultrasound spectral estimation techniques – part 1: estimation methods, Ultrasound Med. Biol. 14 (1988) 661–672.
[20] P.J. Vaikus, R.S.C. Cobbold, K.W. Johnston, A comparative study and assessment of Doppler ultrasound spectral estimation techniques – part 2: methods and results, Ultrasound Med. Biol. 14 (1988) 673–688.
[21] J.A. Jensen, N.B. Svendsen, Calculation of pressure fields from arbitrarily shaped, apodized, and excited ultrasound transducers, IEEE Trans. Ultrason. Ferroelectr. Freq. Contr. 39 (1992) 262–267.

Please cite this article in press as: K.L. Hansen et al., *In-vivo* validation of fast spectral velocity estimation techniques, Ultrasonics (2009), doi:10.1016/j.ultras.2009.07.007

[22] J.G. Proakis, D.G. Manolakis, Digital Signal Processing, Principles, Algorithms and Applications, Prentice Hall, Upper Saddle River, NJ, 2007.
[23] P. Stoica, A. Jakobsson, J. Li, Matched-filterbank interpretation of some spectral estimators, Signal Process. 66 (1998) 45–59.
[24] J.A. Jensen, O. Holm, L.J. Jensen, H. Bendsen, S. Nikolov, B.G. Tomov, P. Munk, M. Hansen, K. Salomonsen, J. Hansen, K. Gormsen, H.M. Pedersen, K.L. Gammelmark, Ultrasound research scanner for real-time synthetic aperture image acquisition, IEEE Trans. Ultrason. Ferroelectr. Freq. Contr. 52 (2005) 881–891.
[25] M.E. Tublin, R.O. Bude, J.F. Platt, Review. The resistive index in renal Doppler sonography: where do we stand?, AJR Am J. Roentgenol. 180 (2003) 885–892.
[26] D.G. Altman, Practical Statistics for Medical Research, Chapmann & Hall/CRC, London, 1991.
[27] J.R. Landis, G.G. Koch, The measurement of observer agreement for categorical data, Biometrics 33 (1977) 159–174.
[28] J.L. Fleiss, Measuring nominal scale agreement among many raters, Psychol. Bull. 76 (1971) 378–382.

Please cite this article in press as: K.L. Hansen et al., *In-vivo* validation of fast spectral velocity estimation techniques, Ultrasonics (2009), doi:10.1016/j.ultras.2009.07.007

Paper IX

Evaluation Study of Fast Spectral Estimators Using In-vivo Data

K. L. Hansen, F. Gran, M. M. Pedersen, I. K. Holfort, J. A. Jensen and M. B. Nielsen

Proceedings of the IEEE International Ultrasonics Symposium

Presented in Rome, Italy, Sep. 2009

Evaluation Study of Fast Spectral Estimators Using *In-vivo* Data

Hansen K.L.[1,2], Gran F.[2,3], Pedersen M.M.[1,2], Holfort I.K.[2], Jensen J.A.[2], Nielsen M.B.[1]

1) Department of Radiology, Section of Ultrasound, Rigshospitalet, Blegdamsvej 9, 2100 Kbh. Ø, Denmark
2) Center for Fast Ultrasound Imaging, DTU Elektro, Bldg. 349, Technical University of Denmark, 2800 Lyngby, Denmark
3) GN Resound, Lautrupbjerg 9, 2750 Ballerup, Denmark

Abstract – **Spectrograms in medical ultrasound are usually estimated with Welch's method (WM). To achieve sufficient spectral resolution and contrast, WM uses an observation window (OW) of up to 256 emissions per estimate. Two adaptive filterbank methods have been suggested to reduce the OW: Blood spectral Power Capon (BPC) and the Blood Amplitude and Phase EStimation method (BAPES). Ten volunteers were scanned over the carotid artery. From each dataset, 28 spectrograms were produced by combining four approaches (WM with a Hanning window (W.HAN), WM with a boxcar window (W.BOX), BPC and BAPES) and seven OWs (128, 64, 32, 16, 8, 4, 2). The full-width-at-half-maximum (FWHM) and the ratio between main and side lobe levels were calculated for each spectrogram. Furthermore, all 280 randomized spectrograms were presented to nine radiologists for visual evaluation: useful/not useful. BAPES and BPC compared to WM had better resolution (lower FWHM) for all OW<128 while only BAPES compared to WM had improved contrast (higher ratio). According to the scores given by the radiologists, BAPES, BPC and W.HAN performed equally well (p>0.05) at OW 128 and 64, while W.BOX scored less (p<0.05). At OW 32, BAPES and BPC performed better than WM (p<0.0001) and BAPES was significantly superior to BPC at OW 16 (p=0.0002) and 8 (p<0.0001). BPC at OW 32 (p=0.29) and BAPES at OW 16 (p=0.55) scored as at OW 128. WM at OW 16 and 8 failed as the four methods at OW 4 and 2. The intra-observer variability tested for three radiologist showed on average good agreement (90%, κ=0.79) and inter-observer variability showed moderate agreement (78%, κ=0.56). The overall result indicates that BPC and BAPES have better resolution and BAPES better contrast than WM, and that OW can be reduced to 32 using BPC and 16 using BAPES without reducing the usefulness of the spectrogram. This could potentially increase the temporal resolution of the spectrogram or the frame rate of the interleaved B-mode images.**

I. Introduction

Spectral Doppler in medical ultrasound is a quantitative technique providing estimates of blood velocity distribution within a range gate on a single image line. In most commercial scanners Welch's method (WM) [1] is used for the estimation. The axial velocity of the blood is found by imaging the same image line repeatedly, where WM uses up to 256 emissions per estimate [2]. The estimates are angle-corrected by the operator and presented as blood velocities plotted against time, denoted a spectrogram.

Conventional spectral estimation has limitations due to the long observation window (OW). The frame rate of the accompanying B-mode images will be low [2] and the temporal resolution of the spectrogram will be impaired [3].

Alternative methods for fast velocity estimation have been proposed by several groups. In this paper the performance of two adaptive filterbank methods are investigated: Blood spectral Power Capon method (BPC) proposed by Stoica et al. [4] and Blood spectral Amplitude and Phase EStimation (BAPES) proposed by Gran et al. [5].

The purpose of this paper is to evaluate the two adaptive filtering methods compared to the conventional WM using *in-vivo* data. Ten volunteers were scanned and from each data set, spectrograms were found by using BPC, BAPES and WM on a series of different OWs. The calculated spectrograms were evaluated quantitatively and qualitatively.

II. Materials and methods

A. Volunteers

This prospective study was performed after approval by The Danish National Committee on Biomedical Research Ethics. Ten healthy volunteers (nine males and one female, mean age: 29.1 years, range: 24-36 years) entered the study after informed consent.

B. Spectral estimators

WM is applied on data using two different weighting schemes to control contrast and resolution in the resulting spectrogram: WM with a Hanning window (W.HAN) and WM with a boxcar window (W.BOX). W.HAN is the preferred conventional spectral estimator for which the resulting spectrogram has improved contrast at the expense of spectral resolution. Spectrograms generated with the W.BOX approach have improved spectral resolution but decreased contrast.

BPC and BAPES are alternative methods using data-dependent adaptive filtering techniques based on a matched filterbank framework. For a given data set, an optimal filter is calculated for each velocity component to minimize noise and interference from other velocities, whereby a unique filterbank is generated. In BPC the filters are designed to minimize the total power of the filtered data, while in BAPES the filters are designed to minimize the power of the filtered noise. In general these methods display better velocity resolution than

traditional methods like W.HAN and W.BOX. Details of the implementation can be found in [5].

C. Setup

The volunteers were scanned on the right common carotid artery using the experimental scanner RASMUS [6] and a B-K Medical 8804, 7 MHz linear array transducer. The setup is provided in Table 1. One data set of 2.5 seconds was recorded for each volunteer, where the sequential data acquisition alternated between a sequence for flow estimation of 3800 consecutive emissions and a sequence for B-mode imaging of 65 consecutive emissions. The recorded data was post processed using the four different methods: W.HAN, W.BOX, BPC and BAPES. For each method, spectrograms were estimated using different OWs: 128, 64, 32, 16, 8, 4 and 2 emissions per estimate. Hence, 28 spectrograms were calculated from every data set giving in total 280 spectrograms for all volunteers. Post processing was done offline with MATLAB (Mathworks, Natick, MA, USA) on a 100 CPU Linux cluster.

TABLE I
Scanner and transducer setup

Parameter	Value	Unit
Sampling frequency	40	MHz
Center frequency	7	MHz
Pulse repetition frequency	9.3	kHz
Number of transmitting elements	64	elements
Apodization in transmit	Uniform	N/A
Number of receiving elements	64	elements
Apodization in receive	Hanning	N/A
Wall Motion Filter	Mean-subtraction	N/A

D. Quantitative evaluation

To investigate the methods quantitatively, a spectrum at end-diastole was found for each spectrogram. For each data set, the time instant was chosen by visually examining the spectrogram obtained with W.HAN at OW 128. For the selected time, spectra from all 28 spectrograms of the same data set were found. From each spectrum, two parameters were calculated: the FWHM and the ratio between main and side lobe levels. The FWHM was found as the width of the velocity distribution of the main lobe at half of the maximum amplitude. Thus, the FWHM, given in m/s, is a measure of spectral resolution and should be as low as possible. The main to side lobe ratio was found as the relative difference between the side-lobe level and the peak amplitude. The side-lobe level was found as the median value of the distributed amplitudes outside the main-lobe, outlined by the FWHM. The ratio, given in decibel (dB), is a measure of contrast in the spectrogram and should be as high as possible.

E. Qualitative evaluation

To investigate the methods qualitatively, nine experienced radiologists evaluated in a blinded trial the 280 randomized spectrograms by scoring each spectrogram: useful or not useful. Additionally, intra- and inter-observer variations were found. The intra-observer variability was assessed by comparing the scores given twice by three radiologists with more than 14 days between each session.

F. Statistics

A descriptive statistical analysis was computed on FWHM and ratio data. Scores given by the radiologists were pooled by method and window. Useful and not useful were coded with the dummy variables 1 and 0, and Bonferroni adjusted tests for multiple comparisons with $p<0.05$ considered significant were performed [7]. The intra- and inter-observer variability were found using Cohen's and Fleiss' kappa, respectively [8;9]. Statistical analyses were performed using SAS (SAS Institute, Cary, NC, USA) and MATLAB (Mathworks, Natick, MA, USA).

III. Results

From the same data set with three systoles recorded, examples of spectrograms obtained with the four methods at OW 128 and 16, are presented (Fig. 1). The gaps in the spectrograms represent the necessary pulse emissions used for generating the interleaved B-mode images.

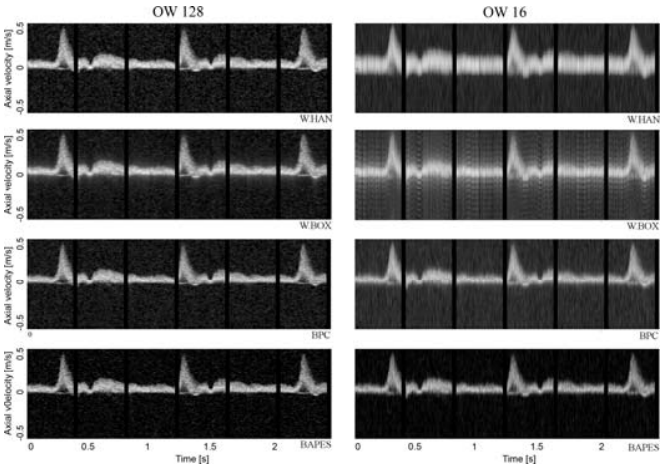

Figure 1: From the same volunteer spectrograms are found using the four methods with OW of 128 and 16.

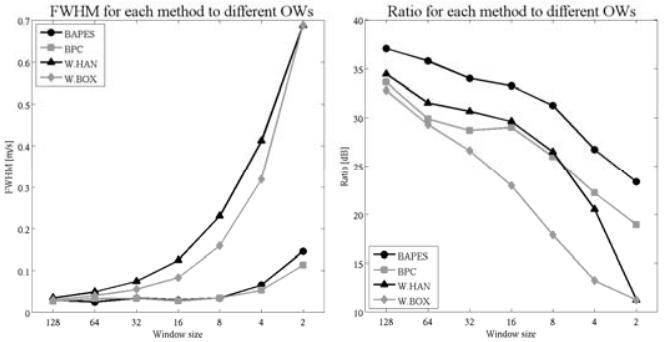

Figure 2: Means for FWHM and ratio are plotted to each window size (OW).

The means of FWHM and ratio for the 280 spectra pooled by method and window are plotted in Fig. 2. From the qualitative evaluation, the total score for each combination of method and OW is found by adding the scores given by nine

radiologists on ten volunteers, thus in the range between 0 and 90. The total score for each combination given in percentage is shown in Fig. 3.

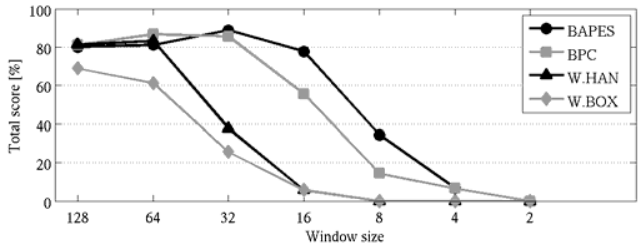

Figure 3: Total sum of scores in percentage for each method to different OWs

The mean of the summed scores for each combination of method and window along with the results of the multiple comparisons are shown in Fig. 4. The sum of scores for each spectrogram is found from the scores given by nine radiologists, and therefore, in the range from 0 to 9. Thus, each combination includes ten summed scores, one for each of the ten spectrograms.

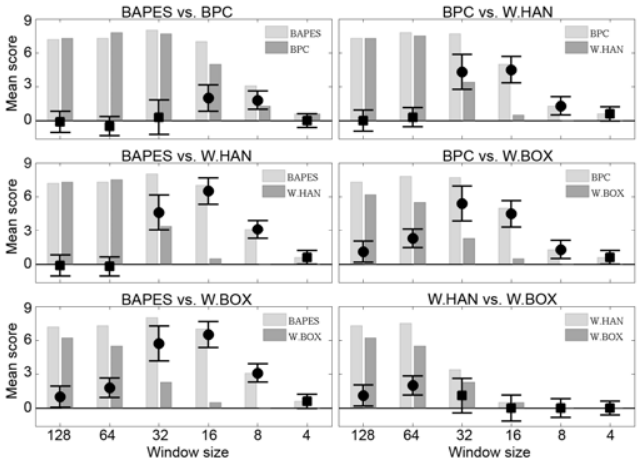

Figure 4: The mean of the summed scores for each method in comparison over different OWs is shown. The 95% confidence interval for the difference in means is illustrated with a bar and marked "■" if insignificant or "●" if significant.

For each method, tests for multiple comparisons were also employed to investigate at which OW the mean score was significantly different from the mean score given at OW 128. W.BOX performed significantly worse when OW was reduced to 64 (p=0.03) and W.HAN when OW was reduce to 32 (p <0.0001). BPC performed equally well at OW 32 compared to OW 128 (p=0.30) while BAPES scored significantly higher at OW 32 compared to OW 128 (p=0.02). Only BAPES had equal performance at OW 16 and OW 128 (p = 0.55). All four methods decreased in performance at OW 8, 4 and 2 compared to OW 128.

The intra-observer variability for three radiologist evaluating the same 280 spectrograms with more than 14 days apart showed good agreement with an averaged Cohen's kappa value of 0.79 (94%, κ=0.88; 83%, κ=0.67; 93%, κ=0.81). The inter-observer variability showed moderate agreement using Fleiss' kappa (78%, κ=0.57).

IV. Discussion

In Fig. 1 examples of spectrograms obtained with the four approaches at OW 128 and 16 are shown. Spectral resolution in the spectrogram corresponds to the width of the white curve representing estimated blood velocities, while the difference between the white curve and the darker surroundings corresponds to contrast. At OW 128 the four approaches produced spectrograms of good quality while the estimators differed in performance at OW 16. At OW 16, it is seen that W.BOX estimated with a higher spectral resolution than W.HAN and the adaptive methods with higher spectral resolution than WM. Furthermore, it is seen that the contrast decreased from BAPES to BPC and WM. W.BOX performed poorest among the four methods in terms of contrast and a so-called ringing phenomenon at OW 16 can be seen.

The quantitative tests illustrated in Fig. 2 confirmed the findings in Fig. 1. On average for all OWs above 2, W.BOX performed with better resolution than W.HAN, and W.HAN performed with better contrast than W.BOX. The adaptive methods outperformed WM in terms of resolution at all OWs below 128 and it is seen that BPC had a slightly better resolution than BAPES. In terms of contrast, BAPES was superior compared to both BPC and WM for all OWs. The W.HAN had better contrast than BPC for all OWs above 8.

The overall result of the qualitative evaluation displayed in Fig. 3 shows that the radiologists preferred the adaptive methods over WM, BAPES over BPC and W.HAN over W.BOX. The inter- and intra-observer variability were additionally tested and showed moderate and good agreement, respectively, indicating consistent scores given by each radiologists with a base-line difference among the radiologists. In Fig. 4 the results of the statistical analyses on the mean of the summed scores using Bonferroni adjusted tests for multiple comparisons are displayed. It is seen that at OW 128 and 64, BAPES, BPC and W.HAN performed equally well while W.BOX scored significantly less. When reducing the OW to 32, the adaptive methods BAPES and BPC performed better than W.HAN and W.BOX. However, BAPES was superior to BPC at OW 16 and 8. At OW 16 and 8 the conventional methods were scored useless. When the OW was decreased to 4 and 2 all four methods failed according to the radiologists.

For each method, the scores given at window sizes below OW 128 were compared to the score given at OW 128 to evaluate how robust each method was to reduction of OW. W.BOX scored significantly less at OW 64 while W.HAN at OW 64, BPC at 32 and BAPES at 16 scored as at OW 128.

The radiologists preferred contrast to spectral resolution when comparing scores given for W.BOX and W.HAN at OW 128 and 64 and in most modern scanners the Hanning

weighting scheme is accordingly implemented for spectral blood estimation. However, when comparing BPC and W.HAN the improved resolution in BPC was preferred to the improved contrast in W.HAN. This is seen in Fig. 4 at OW 32 and 16. It indicates that it is not only the raised side lobe level in W.BOX, which reduces the quality of the spectrogram compared to W.HAN but also the accompanying ringing phenomenon.

Moreover, the radiologists preferred BAPES at OW 32 compared to BAPES at OW 128 ($p = 0.01$). The reason could be that the observers were disturbed visually by the high contrast and spectral resolution of the spectrograms obtained with BAPES at OW 128 and somewhat preferred the smoothing of details as presented in spectrograms obtained with BAPES at OW 32.

Fig. 3 shows that even at the presumably best condition, i.e. OW 128, only 80% of the spectrograms were accepted. No dataset was consistently rejected indicating that the ten dataset were of equal quality. However, the ratings of the nine radiologists varied significantly. At OW 128, two of the nine radiologists only accepted 7.5% and 60% of the spectrograms, respectively, while the other seven radiologists on average accepted 90% of the spectrograms (range: 82%-100%). When evaluating the spectrograms acquired on the experimental system, the radiologists use their experience on commercial systems from daily practice as reference. Limitations in the experimental setup are believed to be reflected in the high rejection rate for some of the radiologists. Data was acquired using the experimental scanner RASMUS and the spectrograms were calculated using MATLAB on a 100 CPU Linux cluster. This combination provided a flexible environment for acquiring and processing the data from an experimental point of view, but, compared to commercial scanners, the signal-to-noise ratio of the spectrograms were lower. Furthermore, adjustments of PRF, spectral gain and baseline were not feasible in the evaluation setup.

The spectral ultrasound examination of today can potentially be improved if the conventional WM for blood velocity estimation used in commercial scanners was to be replaced with one of adaptive spectral estimators BPC or BAPES. The reduction in OW could potentially be used to increase the temporal resolution of the spectrogram or the frame rate of the accompanying B-mode images.

The adaptive methods are more computationally demanding than the conventional WM, and BAPES is more computationally demanding than BPC. However, when reducing the OW, the computational costs decrease as well. Therefore, the BAPES method implemented with an OW 16 or the BPC method with an OW 32 may be as tractable as WM with a much longer OW. It should therefore be possible to implement the methods into commercial scanners and convert the methods to an actual real-time modality.

V. Conclusion

In this paper the performances of two adaptive spectral estimators BPC and BAPES were investigated *in-vivo*. It was shown that the adaptive methods were superior to the conventional WM and that BAPES was superior to BPC. The quantitative tests showed that BAPES and BPC had improved spectral resolution and BAPES had improved spectral contrast compared to WM. According to the scores given by nine radiologists, OW can be reduced to 32 when using BPC, and 16 when using BAPES method for estimating spectrogram without losing performance. The results indicate that the adaptive methods BPC and BAPES potentially can bring improvements to spectral blood estimation as an increase of the temporal resolution of the spectrogram or as an increase of the frame rate for the interleaved B-mode images. Further studies are needed to evaluate the adaptive spectral estimators in various *in-vivo* settings with different flow profiles, vessel geometries and scan depths using different transducers.

Acknowledgement

This work was supported by grant 26-04-0024 from the Danish Science Foundation and by B-K Medical A/S, Herlev, Denmark.

References

[1] P.D.Welch, "The use of fast Fourier transform for the estimation of power spectra: A method based on time averaging over short, modified periodograms," IEEE Trans Audio Electroacoust., vol. AU-15, pp. 70-73, 1967.

[2] J.B.Kruskal, P.A.Newman, L.G.Sammons, and R.A.Kane, "Optimizing Doppler and color flow US: Application to hepatic sonography," Radiographics, vol. 24, no. 3, pp. 657-675, 2004.

[3] A.J.S.Coats, C.Murphy, J.Conway, and P.Sleight, "Validation of the beat to beat measurement of blood velocity in the human ascending aorta by a new high temporal resolution Doppler ultrasound spectral analyser," Br. Heart J, vol. 68, no. 8, pp. 223-229, Aug.1992.

[4] P.Stoica and R.Moses, Introduction to spectral analysis. Upper Saddle River, N.J: Prentice Hall, 1997.

[5] F.Gran, A.Jakobsson, and J.A.Jensen, "Adaptive spectral Doppler estimation," IEEE Trans Ultrason Ferroelec Freq Contr, vol. 56, no. 4, pp. 700-714, 2009.

[6] J.A.Jensen, O.Holm, L.J.Jensen, H.Bendsen, S.Nikolov, B.G.Tomov, P.Munk, M.Hansen, K.Salomonsen, J.Hansen, K.Gormsen, H.M.Pedersen, and K.L.Gammelmark, "Ultrasound research scanner for real-time synthetic aperture image acquisition," IEEE Trans Ultrason Ferroelec Freq Contr, vol. 52, no. 5, pp. 881-891, 2005.

[7] D.G.Altman, Practical statistics for medical research. London: Chapmann & Hall/CRC, 1991.

[8] J.R.Landis and G.G.Koch, "The measurement of observer agreement for categorical data," Biometrics, vol. 33, pp. 159-174, 1977.

[9] J.L.Fleiss, "Measuring nominal scale agreement among many raters," Psychol. Bull., vol. 76, no. 5, pp. 378-382, 1971.

Paper X

In-vivo Validation of Fast Spectral Velocity Estimation Techniques – Preliminary Results

K. L. Hansen, F. Gran, M. M. Pedersen, I. K. Holfort, J. A. Jensen and M. B. Nielsen

Proceedings of the IEEE International Ultrasonics Symposium

Presented in Beijing, China, Nov. 2008

Digital Object Identifier: 10.1109/ULTSYM.2008.0394

In-vivo validation of fast spectral velocity estimation techniques – preliminary results

Hansen K.L.[1,3], Gran F.[2,3], Pedersen M.M.[1,3], Holfort I.K.[3], Jensen J.A.[3], Nielsen M.B.[1]

1) Department of Radiology, Section of Ultrasound, Rigshospitalet, Blegdamsvej 9, 2100 Kbh. Ø, Denmark
2) GN Resound, Lautrupsbjerg 9, 2750 Ballerup, Denmark
3) Center for Fast Ultrasound Imaging, DTU Elektro, Bldg. 349, Technical University of Denmark, 2800 Lyngby, Denmark

Abstract – **Spectral Doppler is a common way to estimate blood velocities in medical ultrasound (US). The standard way of estimating spectrograms is by using Welch's method (WM). WM is dependent on a long observation window (OW) (about 100 transmissions) to produce spectrograms with sufficient spectral resolution and contrast. Two adaptive filterbank methods have been suggested to circumvent this problem: the Blood spectral Power Capon method (BPC) and the Blood Amplitude and Phase Estimation method (BAPES). Previously, simulations and flow rig experiments have indicated that the two adaptive methods can display sufficient spectral resolution for much shorter OWs than WM. The purpose of this paper is to investigate the methods on a larger population and letting a clinical expert evaluate the spectrograms. Ten volunteers were scanned over the right common carotid artery and four different approaches were used to estimate the spectrograms: WM with a Hanning window (WMhw), WM with a boxcar window (WMbw), BPC and BAPES. For each approach the window length was varied: 128, 64, 32, 16, 8, 4 and 2 emissions/estimate. Thus, from the same data set of each volunteer 28 spectrograms were produced. The artery was scanned using the experimental ultrasound scanner RASMUS and a B-K Medical 5 MHz linear array transducer with an angle of insonation not exceeding 60°. All 280 spectrograms were then randomised and presented to a radiologist blinded for method and OW for visual evaluation: useful or not useful. WMbw and WMhw estimated less useful spectrograms compared to the adaptive methods at OW below 64. The BAPES method performed better than BPC at OW of 16 and 8. Furthermore, BAPES was the only method that estimated spectrograms equally well for OW of 16 compared to OW of 128. All four approaches failed at OW of 4 and 2. The preliminary results indicate that the OW can be reduced to 32 when using the BPC method and to 16 when using the BAPES method for spectral blood estimation. This will liberate processing time in spectral US examination and could be used to increase the frame rate of the interleaved B-mode image.**

I. Introduction

The spectral Doppler (SD) method is a quantitative technique providing estimates of blood flow within a range gate on a single image line. The SD is displayed with a B-mode image in duplex mode in which the B-mode image is used for navigation for correct placement of the range gate. Alternatively SD is displayed in triplex mode with a B-mode image and color flow map.

A typical B-mode image consists of about 100 image lines. The blood flow estimated by SD is found by emitting focused pulses repeatedly along one of these image lines. The pulses reflected by blood scatterers, are received as echoes by the transducer, focused along the line by the scanner and compared to determine the axial blood scatterer movement. Knowing the movement of the scatterer and the time between lines yields the axial velocity [1].

The result of the SD estimation is angle corrected by the operator and presented as blood velocities plotted against time denoted as the power spectrum density (PSD). In most commercial scanners Welch's method (WM) is used for estimation of the PSD [2]. To obtain an acceptable spectral resolution with WM, a window of about 100 consecutive pulses is used for each velocity estimate. Clearly this affects the temporal resolution of the conventional PSD but more importantly it also affects the frame rate of the interleaved B-mode image. Due to the necessary emissions for the different modalities in use, whether the mode is duplex or triplex, the resulting frame rate is low and often decreased to the point where the information of the SD examination is impaired [3;4]. In practice the operator can experience difficulties in placing the range gate in the vessel of interest as the B-mode image used for navigation is not updated adequately.

Adaptive spectral techniques can potentially offer great improvement in spectral resolution and contrast compared to WM.

The Blood spectral Power Capon method (BPC) based on a minimum variance estimator has been proposed by Stoica et al [2;5] and the Blood Amplitude and Phase Estimation method (BAPES) method has been proposed by Gran et al. [6].

The algorithm used in BPC has previously been compared to the averaged periodogram used in WM [7;8]. Furthermore, BPC and BAPES have been evaluated in simulations using Field II [9], in a flow rig with steady laminar flow and in a single *in-vivo* experiment [10].

In this paper the two alternative methods BAPES and BPC are validated *in-vivo* against the conventional WM in a prospective, randomized, blinded trial. Ten volunteers were scanned on the common carotid artery. From each data set, spectrograms were found by using the different methods on a series of different observation windows (OW). The resulting spectrograms were randomized and presented to a radiologist blinded for method and OW for evaluation.

II. Materials and methods

A. Patients

This prospective study was performed after approval by The Danish National Committee on Biomedical Research Ethics. Ten healthy volunteers (nine males and one female, mean age: 29.1 years, range: 24-36 years) entered the study after informed consent. The right common carotid artery was examined in all volunteers using US. All scans were carried out by an experienced radiologist.

The conventional WM along with the two alternative spectral methods are presented in this section. WM is applied on data using two different weighting schemes: WM with a Hanning window (WMhw) and WM with a boxcar window (WMbw).

B. Spectral estimators

WMhw is the preferred conventional spectral estimator. It is well known in digital signal processing [11] that due to Hanning weighting of data the resulting spectrogram has a good contrast at the expense of spectral resolution. On the contrary spectrograms generated with the WMbw approach have a better spectral resolution but a decreased contrast.

The BPC method is an alternative method using adaptive filtration on data. Unique filters are designed to every velocity component in the data set. Hence, a unique matched filterbank is generated for each specific data set where the total power of the filters for each velocity of interest is minimized while not distorting the signal of interest. Thereby a highly improved PSD in terms of contrast and spectral resolution can be achieved compared to WM.

The BAPES method is based on a matched filterbank framework as BPC [2;12]. However, in the BAPES method the filtered noise power is minimized fulfilling the constraint that the signal of interest is not distorted. PSD acquired with the BAPES method has both increased contrast and spectral resolution compared to PSD acquired with the BPC method.

C. Spectrograms and spectra

Spectrograms for one volunteer with three systoles recorded are presented in Fig. 1 and Fig. 2 where estimated blood velocities were plotted against time. In Fig. 1, PSDs generated with an OW of 128 emissions/estimate are presented while an OW of 16 emissions/estimate was used to generate the PSDs presented in Fig. 2. The gaps in the PSDs represent the necessary pulse emissions used for generating the interleaved B-mode images.

The spectra from the PSDs to OW of 128 (Fig.1) and 16 (Fig. 2) taken to identical time are presented in Fig. 3. The spectra are plotted with amplitude given for each velocity component.

In Fig.1 and particular in Fig. 2 it is clear that the width of the white curve representing the estimated blood velocities is narrower e.g. more precise for WMbw than WMhw in terms of spectral resolution. It is seen when generating PSD using an OW of 16 (Fig. 2) that the adaptive methods estimates have a higher spectral resolution than WM and that estimates obtained with BAPES have a higher spectral resolution than estimates found with BPC.

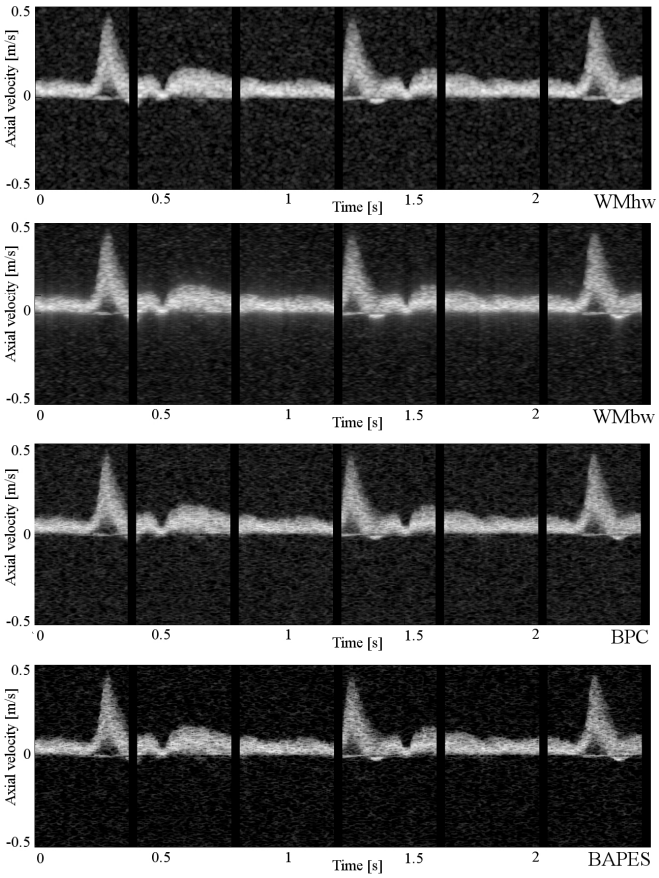

Figure 1: From the same volunteer PSDs are found using the four methods on an OW of 128. All methods display similar performance and it is easy to track the changes in the blood flow during the three systoles. However, WMbw estimates show slightly more spectral leakage as compared to WMhw, BPC and BAPES.

The decrease in contrast from BAPES to BPC and WM is seen in the PSDs as a more smeared appearance around the white curves. WMbw performs poorest among the four methods. The boxcar window results in a ringing phenomenon illustrated in Fig. 2.

The spectra for the methods at OW 128 and OW 16 are shown in Fig. 3. The side lobes representing leakage from the true velocity are suppressed, while the main lobe representing the true velocity is broadened for WMhw compared to WMbw. The pronounced side lobes for WMbw particular seen at OW 16 correspond to the ringing phenomenon shown in Fig. 2. Estimates obtained with BAPES display better side lobe levels and a narrower main lobe as compared to both BPC and WM.

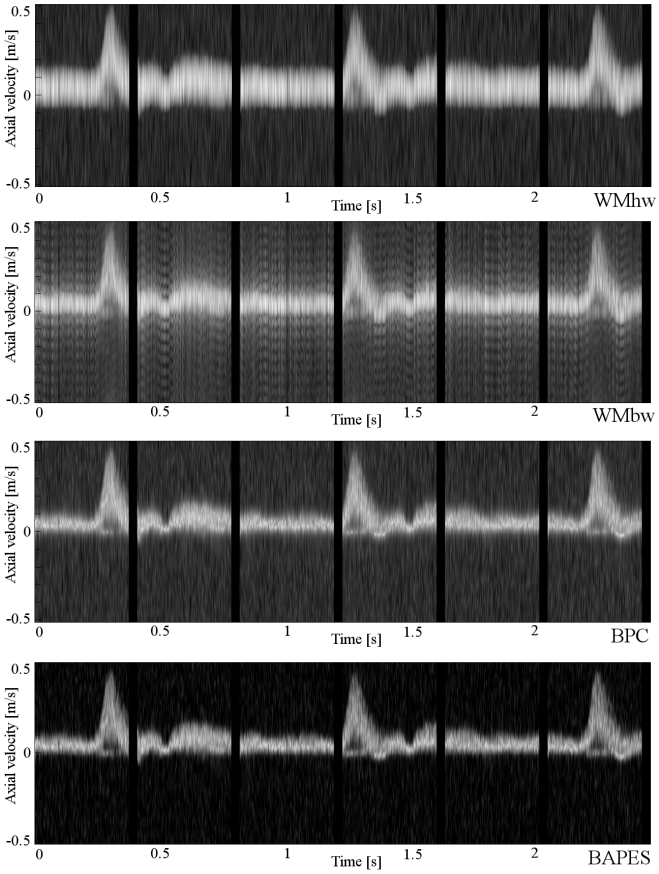

Figure 2: From the same volunteer are PSD found using the four methods with an OW of 16. It is no longer possible to rely on WM estimates due to significant spectral leakage. However, the BPC and BAPES still manage to represent the blood velocity.

D. Setup

Ten healthy volunteers were scanned on the right common carotid artery using the experimental scanner RASMUS [13] and a B-K Medical 8804, 7 MHz linear array transducer. Setup is given in Table 1.

One data set was recorded for each volunteer and post processed using the four different methods; WMhw, WMbw, BPC and BAPES. The post processing was done offline with MATLAB 6.5 (Mathworks, Natick, MA, USA) on a 100 CPU Linux cluster.

TABLE I
SCANNER AND TRANSDUCER SETUP

Parameter	Value
f_s	40 MHz
f_c	7 MHz
f_{prf}	1890 kHz
No. xmt.	64 elements
Apod. xmt.	Uniform
No. rcv.	64 elements
Apod. rcv.	Hanning

BPC and BAPES are both methods based on experimentally obtained data. However, the data was obtained in the same way as in conventional spectral Doppler systems. Thus, the adaptive methods for estimating blood velocities are within the limits of Food and Drug Administration (FDA).

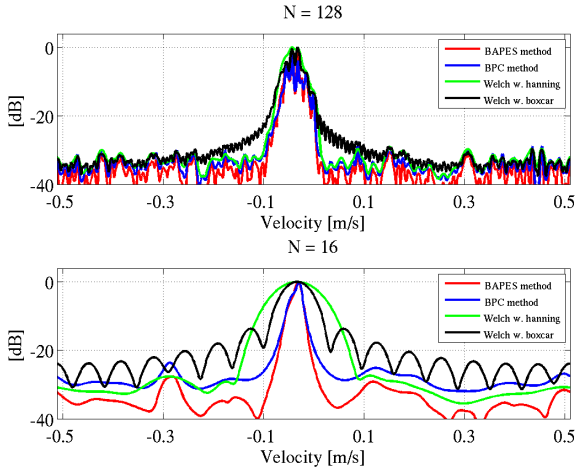

Figure 3: From the same volunteer to identical time a spectrum for each method at OW 128 and OW 16 is shown.

III. RESULTS

The results of the 280 evaluations are depicted in Fig. 4 where the usefulness of the four methods given in percentage is plotted against OW. It is seen that the four approaches perform almost equally good with OW of 128 and 64 while the WM approaches fail to produce useful spectrograms at OW of 32. BAPES is superior to BPC at OW 16 and all the methods fails at OW shorter than of 16.

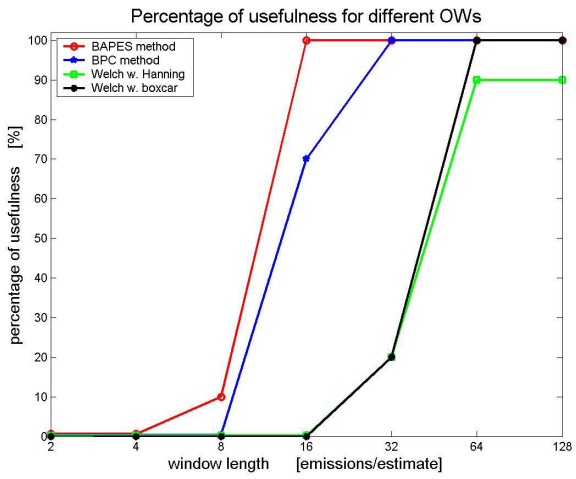

Figure 4: Evaluation of the generated PSDs given by a radiologist is shown as percentage of usefulness for different OWs.

IV. Discussion

The overall result shows that BAPES performed best among the four methods. At OW of 128 and 64, the methods performed equally well except WMhw that scored 90%. When reducing the OW to 32 the alternative methods BAPES and BPC performed better than WMhw and WMbw. However, BAPES was superior to BPC at OW of 16 and 8. At these OWs the conventional methods were useless. When the OW was decreased to 4 and 2 all four methods failed.

Only the BAPES method performed as well for OW of 16 compared to OW of 128.

The US examination of today can potentially be improved if the conventional WM for blood velocity estimation used in commercial scanners was to be replaced with one of adaptive spectral estimators BPC or BAPES. Consequently, either the temporal resolution of the spectrogram will be increased and give the US operator more information of the blood velocity profile. Or the improvement could be an increase in frame rate for the interleaved B-mode image in i.e. triplex scan mode. This will facilitate the navigation under examination so the placement of the range gate can be adjusted according to respiratory movements and be correctly placed in the vessel of interest.

According to Gran et al. (2008), the BAPES method is more computationally demanding compared to BPC which is heavier than the conventional WM. However, when reducing the OW, the computationally costs decrease as well. Therefore the BAPES method implemented with an OW of 16 or the BPC method with an OW of 32 may be as tractable as WM with a much longer OW. It should therefore be possible to implement the methods into commercial scanners and convert the methods to an actual real-time modality.

V. Conclusion

In this paper the performances of two adaptive spectral estimators BPC and BAPES were investigated *in-vivo*. The preliminary results indicated that the adaptive methods were superior to the conventional WM and that BAPES was superior to BPC.

According to the given judgements OW can be reduced to 32 when using BPC, and 16 when using BAPES method for estimating PSD without loosing performance.

Adaptive spectral estimation could potentially bring major improvements to duplex and triplex scan mode as an increase of the temporal resolution of the spectrogram or probably more interesting as an increase of the frame rate for the interleaved B-mode image.

Further studies are needed. An on-going study investigates the performance of adaptive spectral estimation in which spectrograms are evaluated by a number of radiologists to achieve results with statistical relevance. Other studies will concern the estimation of blood velocity estimation in different vessel geometries and scan depths.

Acknowledgement

This work was supported by grant 26-04-0024 from the Danish Science Foundation and by B-K Medical A/S, Herlev, Denmark.

References

[1] J.A. Jensen, Estimation of Blood velocities using ultrasound: A signal processing approach. New York: Cambridge University Press, 1996.

[2] P. Stoica and R. Moses, Spectral analysis of signals Prentice Hall, Upper Saddle River N.J., 2005.

[3] J.B. Kruskal, P.A. Newman, L.G. Sammons, and R.A. Kane, "Optimizing Doppler and color flow US: Application to hepatic sonography," Radiographics, vol. 24, pp. 657-675, 2004.

[4] K. Ferrara and G. DeAngelis, "Color flow mapping," Ultrasound Med Biol, vol. 23, pp. 321-345, 1997.

[5] P. Stoica and R. Moses, Introduction to spectral analysis Prentice Hall, Upper Saddle River N.J, 1997.

[6] F. Gran, A. Jakobsson, and J.A. Jensen, "Adaptive blood velocity estimation in medical ultrasound," Proc IEEE ICASSP, vol. 1, pp. 293-296, 2007.

[7] P.J. Vaikus, R.S.C. Cobbold and K.W. Johnston, "A comparative study and assesment of Doppler ultrasound spectral estimation techniques, Part 2: Methods and results," Ultrasound Med Biol, vol. 14, pp. 673-688, 1988.

[8] P.J. Vaikus and R.S.C. Cobbold, "A comparative study and assesment of Doppler ultrasound spectral estimation techniques, Part 1: Estimation methods," Ultrasound Med Biol, vol. 14, pp. 661-672, 1988.

[9] J.A. Jensen and N.B. Svendsen, "Calculation of pressure fields from arbitrarily shaped, apodized, and excited ultrasound transducers," IEEE Trans Ultrason Ferroelec Freq Contr, vol. 39, pp. 262-267, 1992.

[10] F. Gran, A. Jakobsson, and J.A. Jensen, "Adaptive spectral Doppler estimation," IEEE Trans Ultrason Ferroelec Freq Contr, vol. submitted 2008.

[11] J.G. Proakis and D.G. Manolakis, Digital signal processing: Principles, algorithms and applications, 4. ed. Upper Saddle River, New Jersey, USA: Pearson Prentice Hall, 2007.

[12] P. Stoica, A. Jakobsson and J. Li, "Matched-filterbank interpretation of some spectral estimators," Signal Processing, vol. 66, pp. 45-59, 1998.

[13] J.A. Jensen, O. Holm, L.J. Jensen, H. Bendsen, S. Nikolov, B. G. Tomov, P. Munk, M. Hansen, K. Salomonsen, J. Hansen, K. Gormsen, H. M. Pedersen, and K.L. Gammelmark, "Ultrasound research scanner for realtime synthetic aperture image acquisition," IEEE Trans Ultrason Ferroelec Freq Contr, vol. 52, pp. 881-891, 2005.

Paper XI

Pulse Wave Velocity in the Carotid Artery

G. L. Sørensen, J. B. Jensen, J. Udesen, I. K. Holfort and J. A. Jensen

Proceedings of the IEEE International Ultrasonics Symposium

Presented in Beijing, China, Nov. 2008

Digital Object Identifier: 10.1109/ULTSYM.2008.0336

Pulse Wave Velocity in the Carotid Artery

Gertrud Laura Sørensen[1], Julie Brinck Jensen[1], Jesper Udesen[2], Iben Kraglund Holfort[1] and Jørgen Arendt Jensen[1]

(1) Center for Fast Ultrasound Imaging, Dept. of Electrical Engineering, DTU, Bldg. 349, Technical University of Denmark, DK-2800 Kgs. Lyngby, Denmark
(2) GN ReSound A/S, Lautrupbjerg 9, DK-2750 Ballerup, Denmark

***Abstract*— The pulse wave velocity (PWV) in the carotid artery (CA) has been estimated based on ultrasound data collected by the experimental scanner RASMUS at DTU. Data is collected from one test subject using a frame rate (FR) of 4000 Hz. The influence of FRs is also investigated.**
The PWV is calculated from distension wave forms (DWF) estimated using cross-correlation. The obtained velocities give results in the area between 3 - 4 m/s, and the deviations between estimated PWV from two beats of a pulse are around 10%.
The results indicate that the method presented is applicable for detecting the local PWV. Additional studies with data collections from several test subjects are required to determine the accuracy of the approach. Based on a spectrum analysis it appears that there is no gain from using FRs above 1000 Hz, but it is shown that FRs below 1000 Hz do not give accurate PWVs.

I. Introduction

Arteriosclerosis is a very common cause of death in industrialized countries. It's a disease where deposits of lipids makes a plaque in the inner layer of the arterial wall. Advanced arteriosclerosis can occlude the arteries and involve changes of the vessel wall that reduce its elasticity and flexibility. The disease may not give symptoms before 2/3 of the vessel is occluded. A measure of the degree of arteriosclerosis is therefore valuable, since the disease thereby can be discovered at an earlier stage before it has fatal consequences.
When the heart contracts a pressure pulse wave will propagate through the arteries. The pulse wave velocity (PWV) can be used as a measure of the degree of arteriosclerosis, due to the relation between PWV and the stiffening of the arteries. This relation is described by the Moens-Korteweg equation [1]:

$$\text{PWV} = \sqrt{\frac{E \cdot h}{\rho \cdot d}}, \tag{1}$$

where E is the wall elastic modulus, h the wall thickness, ρ the blood density, and d the lumen diameter. When a vessel is occluded the lumen radius will be reduced and the wall elastic modulus will increase. As a result the PWV will also increase. Therefore it is desirable to find methods for estimating the PWV locally. The PWV is 3-4 m/s in the aorta and even faster in smaller arteries, so a fast data acquisition is needed to properly estimate the velocity.

Previous studies have proved the connection between the stiffening of the arteries and the PWV. As early as 1878 Moens [2] derived the mathematical equation for the PWV described in 1. In 1954 Edler and Hertz [2] used ultrasound to detect the movement of tissue structures by one-dimensional M-mode recordings. The real technical breakthrough, however, came with the development of the Time-Distance-recorder [3], a device for measuring, as a function of time, the relative movements of two echoes visualized by a two-dimensional, real-time ultrasound scanner.
In 1991 Benthin et al. [2] recorded ultrasound measurements at two sites along an artery to detect the diameter change and produce a distension wave form (DWF). By means of cross-correlation of two DWFs, the PWV was estimated. They concluded that in order to reduce the influence of reflections from arterial bifurcations, only the foot of the DWF should be used.
In 2003 Rabben et al. [5] investigated an area-flow method for estimating local PWV from ultrasound measurements. With the area-flow method, the PWV is estimated as the ratio between change in flow and change in cross-sectional area. The ultrasound recordings were performed on the CA of 21 human subjects. They estimated PWVs in the area between 4-9 m/s and found that the velocity is increasing with age. However, improvements in the basic measurements seem necessary to increase the precision of the method.
In 2006 Hermeling et al. [1] investigated the precision of an ultrasound method to measure the PWV. A phantom scaled according to realistic *in vivo* conditions was used. Three approaches were used to identify the systolic foot of the DWF, and the PWV was estimated. The method still needs additional investigation to be applicable to *in vivo* measurements.
In 2007 Williams et al. [4] used two methods to measure the PWV in mice. One of the methods was a regional transit-time method, where the time difference between the rise of a pulse wave at two sites was measured, while the distance between the sites was known. The other method was a local flow-area method, where the cross sectional area and the volume flow through a vessel were measured by means of color flow imaging. The PWV was estimated as the relationship between the change in the flow volume and the cross sectional area. They concluded that the two methods were appropriate to give an understanding of the arterial properties among mice, but they did not conclude on whether the method can be transferred to humans.

Common to the previous studies that measured the PWV by means of ultrasound data, is that they have used conventional ultrasound, which uses a FR of 20-50 Hz. The PWV in smaller arteries than the aorta is expected not to exceed 10 m/s. If

the distance between two measuring sites is 1 cm, the time between the rise of the pulse wave at the first site to the next site can be calculated to:

$$t = \frac{0.01 \text{ m}}{10 \text{ m/s}} = 0.001 \text{ s}. \quad (2)$$

The highest frequency of the received signal should thus be 1000 Hz, and the FR must at least be the double of this.
This paper investigates whether it is possible to find a local measure of the PWV using plane wave ultrasound (PWU) which uses a FR of 4 kHz. Furthermore the influence of the FR is investigated.

This work is a preliminary study. Data is collected from the carotid artery (CA) of one test subject using the experimental scanner RASMUS at DTU [8]. The PWV is calculated by measuring the time difference between two velocity profiles while knowing the distance between the measuring sites. The results are validated by comparing with results from previous studies and by comparing velocities from two different heartbeats.

II. Method

In PWU all transducer elements are excited at the same time thereby creating a pressure wave with a nearly plane wave front. The acquisition time for each frame is thereby lowered significantly, but the contrast and focusing of the image is compromised compared to conventional imaging.
The transmitted pulse consists of a 13 bit Barker code on each transducer element. The code is used to increase SNR. The image is focused using traditional delay-and-sum receive beamforming. Using the RASMUS experimental ultrasound scanner, data from the CA of a 36 year old healthy male is obtained. Data is acquired during a period of 2.2 seconds using a 5.5 MHz linear array transducer, which yields data showing two heartbeats. The transducer set-up is shown in table I [6].

Parameter	Value
Transducer	Linear array
Number of elements	128
Pitch	0,208 mm
Pitch	0,75 $\cdot\lambda$
Kerf	0,035 mm
Height	4,5 mm
Center frequency, f_0	5,5 MHz
Bandwidth (2-way, -6 dB)	60 % af f_0
Elevation focus	25 mm
Sampling frequency	40 MHz
Apodization in transmit	Tukey
Apodization in receive	None

TABLE I

TRANSDUCER SET-UP. λ IS THE WAVELENGTH AT THE CENTER FRECUENCY.

The difference between the relative movement of the upper and the lower arterial wall gives the DWF. By cross-correlating adjacent ultrasound images, the relative movement of the arterial wall is estimated.

Two ways of calculating the DWF have been used to investigate how the influence of noise in the signals effects the results. The 1'st method cross-correlates a signal sequence from the i'th transmission with a signal sequence from the $(i+1)$'th transmission. In the 2'nd method a signal sequence from the i'th transmission is cross-correlated with a signal sequence from the $(i+4)$'th transmission. This cross-correlation function is given by:

$$R_{i,i+K}(\kappa) = \int_{-\infty}^{\infty} s_i(z) s_{i+K}(z-\kappa) dz, \quad (3)$$

where κ is the spatial displacement, s is the signal sequence, i the transmission and K is either 1 or 4 and indicates the gap between the cross-correlated transmissions. When $K = 4$ it does not corresponds to a FR which is 4 times less the one which is used, because all the data is still used, but the detected relative movement of the vessel wall is bigger, which gives rise to a DWF less influenced by noise.

The PWV is estimated as the distance, Δx between two measuring sites divided by the time difference, Δt, between the arise of a pulse wave at these two sites:

$$PWV = \frac{\Delta x}{\Delta t}. \quad (4)$$

The time difference, Δt, is found from the delay between two DWFs at two different spatial positions along the artery. The delay is obtained from the sum-of-squared difference estimator [7]:

$$S_{xy}(l) = \sum_{n=1}^{N} \big(x(n) - y(n-l)\big)^2, \qquad l = 0, \pm 1, \pm 2, ... \quad (5)$$

where l is the spatial displacement and y and x are the two DWFs.
To reduce the influence of reflections from arterial bifurcations, only a part of the DWF is used in the calculation. These parts are the systolic part of one of the DWFs and the foot of the systolic part of the other DWF. In previous studies it is shown that exactly these parts of the DWFs will reduce the influence from reflections [2].

To obtain the most correct DWF, a spatial averaging has been performed, by calculating the average DWF of 3 DWFs from adjacent signal sequences:

$$DWF = \frac{DWF_{x-1} + DWF_x + DWF_{x+1}}{3}. \quad (6)$$

Furthermore the mean of this new DWF is found and this mean value is subtracted from the very same DWF:

$$DWF = DWF - \frac{1}{N} \sum_{n=1}^{N} DWF(n), \quad (7)$$

where z indicates the elements in the DWF and N is the number of elements in the DWF.
The last modification is to avoid difference in the amplitude values at the beginning of the systolic foot of two DWFs used to calculate the PWV. This modification corresponds to removing the 0 Hz component of the spectrum of the DWF.
To compare the different methods used to estimate the PWVs, the relative deviation between two estimated PWVs of two different heartbeats from the same pair of estimated DWFs, is calculated. In this calculation the PWV from the first heartbeat is subtracted from the PWV from the second

heartbeat, and the subtraction is divided by the PWV from the first heartbeat. This calculation is performed for all pairs of DWFs and the mean of each pair is calculated to evaluate which method is the most accurate.

To investigate whether the high FR improves the estimation of the PWV, the measured signals have been resampled to obtain lower FRs. This is done by using only a subset of the image frames, calculate new DWFs and estimate the PWV. From this investigation a graph is produced with the estimated PWV's as a function of FR.

III. Results

When cross-correlating the signal sequence from the i'th transmission with a signal sequence from the (i+1)'th transmission and signal sequence from the i'th transmission with the signal sequence from the (i+4)'th transmission different DWFs are obtained. This is illustrated in Figs. 1 and 2. It can be seen that the DWF calculated from the second cross-correlation method is more smooth, which is consistent with the fact that the detected relative movement of the vessel wall in this method is bigger.

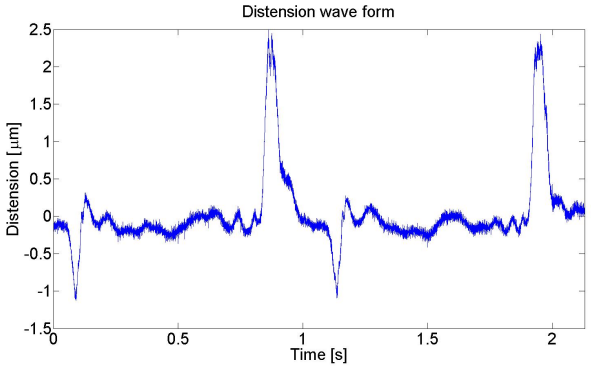

Fig. 1. DWF calculated by cross-correlating the signal sequence from the i'th transmission with a signal sequence from the (i+1)'th transmission

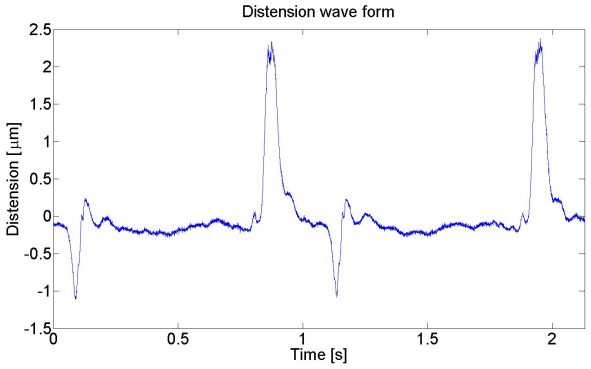

Fig. 2. DWF calculated by cross-correlating the signal sequence from the i'th transmission with a signal sequence from the (i+4)'th transmission

The DWFs that appear when modifications has been performed according to the methods mentioned in section II also look slightly different than the ones shown in Figs. 1 and 2. Therefore different values of PWVs are obtained, when the velocities are calculated from DWFs with different modifications and different cross-correlation methods. The values of the PWVs are shown in Table II.

Method	1'st cross-correlation method		2'nd cross-correlation method	
	1'st heart-beat [m/s]	2'nd heart-beat [m/s]	1'st heart-beat [m/s]	2'nd heart-beat [m/s]
Without modification	2.50	2.18	3.57	3.36
Spatial averaging	2.66	2.49	3.57	3.33
Spatial averaging, subtraction of μ	3.27	3.07	3.77	3.54

TABLE II

PWVs calculated from DWFs with different modifications. For each method the PWV has been calculated from 10 different pairs of DWFs. This table shows the mean value of these calculations. In the table μ represents the mean value of the spatial averaged DWFs.

The results of the PWVs given in Table II are low compared the velocities obtained in previous studies around 4 - 9 m/s [5]. The method that gives velocities closest to the ones given in the literature is when using the second cross-correlation method, spatially averaging the DWFs and then subtracting the mean value of the spatial averaged DWF.

In Table III the relative deviations of the PWVs of two successive heartbeats are shown. PWVs in the table are estimated by using DWFs which have been cross-correlated and modified in different ways. Hereby it is possible to see which method yields the smallest deviation.

Method	1'st cross-correlation method	2'nd cross-correlation method
	Deviation in %	Deviation in %
Without modification	34.9	13.6
Spatial averaging	33.2	11.4
Spatial averaging, subtraction of μ	28.9	9.65

TABLE III

Mean value of the relative deviation between the PWV calculated from two heartbeats. In the table μ represents the mean value of the spatial averaged DWFs.

From (1) it is known that E, h, ρ and d determines the PWV. These variables remain the same for two successive heartbeats measured at the same site in the artery. Therefore the most correct PWVs must be those calculated from the method that gives the smallest deviation between the two heartbeats. From Table III it can be seen that the method that gives the smallest deviation is when the DWFs are spatially averaged and the mean value of the DWF that hereby is obtained is subtracted from the very same DWF. Furthermore the second cross-correlation method where a signal sequence from i'th transmission has been cross-correlated with the signal sequence from the (i+4)'th transmission gives

significantly smaller deviations than the first cross-correlation method. It should be noted that the method giving the smallest deviation is also the method giving the values of PWVs closest to the ones from the literature (as shown in table II). Therefore it seems that this method produces the most correct estimates of the PWV.

In Fig. 3 a graph displaying the estimated PWVs as a function of FR is shown. When investigating the graph it is clear that when the FR becomes lower than 1 kHz the precision of the estimated velocities drop. Thus it would not be possible to measure the PWV with conventional ultrasound. It appears, however, that the estimated PWVs does not change significantly from 1 kHz to 4 kHz. Therefore it seems that nothing is gained by using a FR above 1 kHz.

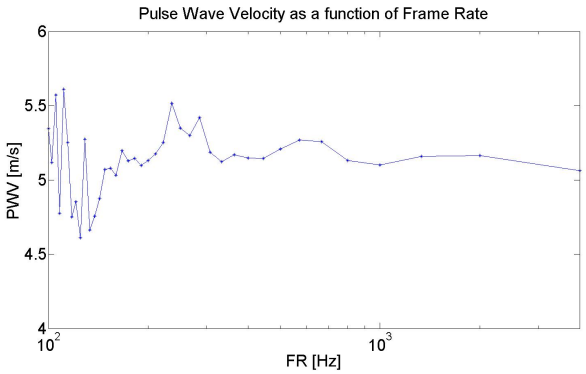

Fig. 3. PWV as a function of FR. The graph is calculated from a set of DWFs which have been spatial averaged where the mean has also been subtracted. Furthermore the cross-correlation method where a signal sequence from i'th transmission has been cross-correlated with the signal sequence from the (i+4)'th transmission has been used. A logarithmic (base 10) scale is used for the X-axis.

IV. Conclusions

It has been investigated whether it is possible to find local measures of the PWV in the CA using PWU. The PWU uses a FR of 4 kHz and therefore it has also been examined whether this high FR gives rise to more correct estimates of the PWV. It is possible to find the PWV in the Carotid Artery. It has been investigated how the cross-correlation of signal sequences should be done in order to obtain the most correct PWVs. This investigation has shown that the most correct PWVs are obtained when DWFs have been calculated by cross-correlating a signal sequence from the i'th transmission with a signal sequence from the (i+4)'th transmission instead of the signal sequence from the i'th transmission with a signal sequence from the (i+1)'th transmission. This is consistent with the fact that the detected relative movement of the vessel wall is bigger when cross-correlating with the (i+4)'th transmission, which gives rise to DWFs less influenced by noise. This paper has, however, not examined if even better estimates of the PWV could be achieved by using a value of K in (3) higher than 4. Therefore it might be an idea to examine this in future studies.

When calculating the PWV it has furthermore been found that certain modifications of the DWFs gives even better results. These modifications includes calculating spatial averaged DWFs, finding the mean-value of the obtained DWF and subtracting it from the DWF. The PWVs that has been calculated from this procedure are in the interval of 3 - 4 m/s. These estimates are low compared to the ones given in previous studies and also compared fact that the PWV is 3 - 4 m/s in the aorta and should be higher in smaller arteries like the CA. An error in the calculations of PWV in this paper might be caused by reflections of the blood in the artery from arterial bifurcations or plaque on the inside of the vessel. Even though it has been tried to avoid the reflections by using only the systolic part of one of the DWFs and the foot of the systolic part of the other DWF when calculating the PWV, it can not be concluded that reflections of the blood have not contributed to an error in the calculations.

When investigating the influence of the value of the FR it has been shown that it is not suitable to use a FR below 1 kHz. The PWV calculated from a FR under 1 kHz will not be accurate. Furthermore it appears that no additional information is obtained by using a FR of 4 kHz instead of 1 kHz, since the estimated PWV does not change significantly in this interval. Finally it should be mentioned that this study is limited, since data has only been collected from one test subject. To make sure that the procedure used in this paper is valid, it has to be tested on more test subjects.

References

[1] Hermeling, E., Reesink, K.D., Reneman, R.S., and Hoeks, A.P.G., *Measurement of local pulse wave velocity: Effects of signal processing on precision*, Ultrasound Med. Biol., Vol. 33, no. 5, pp. 774-781, 2007.

[2] Benthin, M., Dahl, P., Ruzicka, R., and Lindström, K., *Calculation of pulse-wave velocity using cross correlation - effects og reflexes in the arterial tree*, Ultrasound Med. Biol., Vol. 17, No. 5, pp. 461-469, 1991.

[3] Lindström, K., Marsal, K., Gennser, G., Bengtsson, L., Benthin, M., and Dahl, P., *Device for measurement for of fetal breathing movements-I: The TD-recorder. A new system for recording the distance between two echogenerating structures as a function of time*, Ultrasound Med. Biol., No. 3, pp. 143-151, 1977.

[4] Williams, R., Needles, A., Cherin, E., Zhou, Y., Henkelman, R.M., Adamson, S.L., and Foster, F.S., *Noninvasive ultrasonic measurement of regional and local pulse-wave velocity in mice*, Ultrasound Med. Biol., Vol. 33, No. 9, pp. 1368-1375, 2007.

[5] Rabben, S.I., Stergiopulos, N., Hellevik, L.R., Smiseth, O.A., Slrdahl, S., Urheim, S., and Angelsen, B., *An ultrasound-based method for determining pulse wave velocity in superficial arteries*, Journal of Biomechanics, Vol. 37 , No. 10 , pp. 1615 - 1622, 2004.

[6] Udesen, J., Gran, F., Hansen, K.L., Jensen, J.A., Thomsen, C., and Nielsen, M.B., *High frame-rate blood vector velocity imaging using plane waves: Simulations and preliminary experiments*, Accepted for publication IEEE Trans. Ultrason., Ferroelec. and Freq. Contr., 2008.

[7] Viola, F., and Walker, W.F., *A comparison of the performance of time-delay estimators in medical ultrasound*, IEEE Trans. Ultrason., Ferroelec. and Freq. Contr., Vol. 50, No. 4, pp. 392-401, 2003.

[8] Jensen, J.A., Holm, O., Jensen, L.J., Bendsen, H., Nikolov, S.I., Tomov, B.G., Munk, P., Hansen, M., Salomonsen, K., Hansen, J., Gormsen, K., Pedersen, H.M., and Gammelmark, K.L, *Ultrasound Research Scanner for Real-time Synthetic Aperture Data Acquisition*, IEEE Trans. Ultrason., Ferroelec. and Freq. Contr., Vol. 52, No. 5, pp. 881-891, 2005.

Paper XII

Transverse Correlation: An Efficient Transverse Flow Estimator – Initial Results

L. Henze, I. K. Holfort, J. Kortbek and J. A. Jensen

Proceedings of the IEEE International Ultrasonics Symposium

Presented in Beijing, China, Nov. 2008

Digital Object Identifier: 10.1109/ULTSYM.2008.0395

Transverse Correlation: an Efficient Transverse Flow Estimator - Initial Results

Lasse Henze[1], Iben Kraglund Holfort [1], Jacob Kortbek [12] and Jørgen Arendt Jensen[1]

1) Center for Fast Ultrasound Imaging, DTU Electrical Engineering, Bldg. 348,
Technical University of Denmark, DK-2800 Kgs. Lyngby, Denmark
2) B-K Medical, Mileparken 34, 2730 Herlev, Denmark

Abstract— **Color flow mapping has become an important clinical tool, for diagnosing a wide range of vascular diseases. Only the velocity component along the ultrasonic beam is estimated, so to find the actual blood velocity, the beam to flow angle has to be known. Because of the unpredictable nature of vascular hemodynamics, the flow angle cannot easily be found as the angle is temporally and spatially variant. Additionally the precision of traditional methods is severely lowered for high flow angles, and they breakdown for a purely transverse flow. To overcome these problems we propose a new method for estimating the transverse velocity component. The method measures the transverse velocity component by estimating the transit time of the blood between two parallel lines beamformed in receive. The method has been investigated using simulations performed with Field II. Using 15 emissions per estimate, a standard deviation of 1.64% and a bias of 1.13% are obtained for a beam to flow angle of 90 degrees. Using the same setup a standard deviation of 2.21% and a bias of 1.07% are obtained for a beam to flow angle of 75 degrees. Using 20 emissions a standard deviation of 3.4% and a bias of 2.06% are obtained at 45 degrees. The method performs stable down to a signal-to-noise ratio of 0 dB, where a standard deviation of 5.5% and a bias of 1.2% is achieved.**

I. Introduction

Color flow mapping has become an important clinical tool for diagnosing a wide range of vascular diseases. Traditional color flow mapping works by sending out a number of ultrasound pulses in a given direction and then estimating the time shift between the received signals, caused by the movement of the blood scatterers [1]. Only the velocity component along the ultrasonic beam is estimated, so to find the actual blood velocity, the beam to flow angle has to be known. Because of the unpredictable nature of vascular hemodynamics, the flow angle cannot easily be found. The precision of traditional methods is also lowered severely for high flow angles, and they break down for a purely transverse flow. A number of authors have proposed several solutions to this problem. Fox [2] suggested using two active apertures to get two independent beam to flow angles, making it possible to calculate the true velocity. For this to work, a large aperture has to be used, which in a clinical environment is unpractical. The precision of the method is also strongly dependent on the difference in beam to flow angle. This causes problems when imaging at large depths. Trahey [3] used a speckle tracking approach, where a 2D cross correlation between two consecutive images is used to estimate the velocity vector. This approach sets high demands on the beamformer of the imaging system, since a whole image has to be formed for every emission. Jensen and Munk [4] used a dual Hanning weighting on the aperture to introduce a transverse oscillation. The method has shown promising in-vivo result [5], however a substantial number of emissions are needed to get an acceptable standard deviation. Anderson proposed a similar approach [6]. Jensen [7] suggested to find the velocity by beamforming lines along the direction of flow. To find the flow angle Kortbek and Jensen [8] suggested to beamform lines in a range of directions from 0 to 180 degrees and then search for the angle with the largest correlation over emissions. A low standard deviation is obtained, but the approach is very computational demanding. Hein [9] suggested using a time domain correlation technique to estimate the vector velocity. This approach is similar to the one proposed in this article, but sincea fixed geometric focus was used, the method was not able of imaging, and suffers from a poor SNR.

The method presented in this paper measures the transverse velocity component by estimating the transit time of the blood scatteres between two parallel lines beamformed in receive. Using the same data the axial velocity is also obtained, thus yielding the vector velocity. This approach enables imaging with a low number of computations making the method suitable for real time implementation.

II. Theory

In the following section, it is assumed that the flow is moving from left to right and is spatially and temporally invariant. These assumptions are of course invalid for the flow encountered in the human vascular system, but as it will be obvious later in the paper, they are only introduced to ease the theoretical explanation.

The setup of the method can be seen in Fig. 1. The transducer is placed on top of the vessel, and a weakly focused beam is emitted by focusing below the estimation area. A total of N pulses are used to create an estimate, where $N/2$ are used to search for the transit time, and $N/2$ are used to perform averaging. To estimate the velocity at a position given by $\vec{r}$, three lines with the length l are beamformed. The center line L_Z is used for estimating the axial velocity component. The center of L_Z is positioned at $\vec{r}$. The two lines to the left and right from the center, L_A and L_B, are used for estimating the transverse velocity. They are each beamformed a distance d_x in the x direction away from

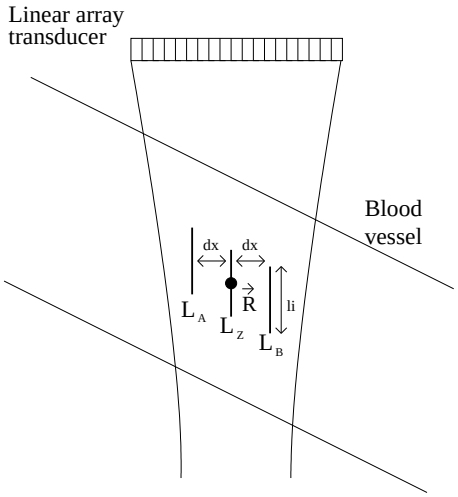

Fig. 1. Setup of the transverse velocity estimator. A linear array sends out a weakly focused beam in transmit. Three lines are beamformed in receive. The center line L_z is used for estimating the axial velocity, the two lines to the side, L_A and L_B are used for estimating the transverse velocity. L_A and L_B are moved d_x away from the center. All three lines have a length of l.

the center, as shown in the figure. The method estimates the axial velocity by using a cross-correlation technique [10].

Since the scatterers move from left to right with a spatially and temporally invariant velocity, the scatterers originally positioned in L_A will eventually move into L_B. L_A is therefore related to L_B by a shift in time and axial position. To find the shift in time, a transit correlation function is created by calculating the normalized correlation coefficient between L_A taken from emission n with L_B taken from emission n to $n + N/2 - 1$. The normalized correlation coefficient is given by

$$C(a,b) = \max\{\frac{R_{ab}(\tau) - \mu_a\mu_b}{\sqrt{[R_{aa}(0) - \mu_a^2][R_{bb}(0) - \mu_b^2]}}\} \qquad (1)$$

where R_{ab} is the cross-corelation between signal a and b, μ_a is the mean of a and μ_b is mean of b. When the time span between L_A and L_B corresponds to the transit time of the blood between the two lines, the scatteres originally positioned in L_A will now be positioned in L_B resulting in a high correlation. The transit time can therefore be found by finding the peak of the transit correlation function. Since the distance between the lines is known, the transverse velocity component is given by

$$V_{x\vec{r}} = \frac{2d_x}{T_t} \qquad (2)$$

where T_t is the estimated transit time. To further increase the performance of the method, a compensation for the axial velocity is applied by moving the two lines up and down according to the estimated axial velocity.

Fig. 2 shows a typical set of beamformed lines used for estimating the transverse velocity. The dotted line is the left line L_A, and the solid line is the right line L_B. The beam to flow angle is 75 degrees, the transverse velocity is 0.6 m/s, L_A and L_B are moved 0.2 mm away from the center, and a f_{prf} of 3 kHz is used. The lines are created by beamforming simulated data. The simulation is described in detail in section III-A. The 6 L_A lines are taken from emission 1, and the 6 L_B lines are taken from emission 1 to 6. The axial shift caused by the axial velocity compensation can be observed on L_A as an upward movement over emissions. It can be visually seen that the scatterers use 2 emissions to travel the distance from L_A to L_B, since L_A and L_B are most similar when L_A is taken from emission 1, and L_B is taken from emission 3. Using (2) this corresponds to a transverse velocity of 0.6 m/s. This estimate matches the velocity used in the simulation.

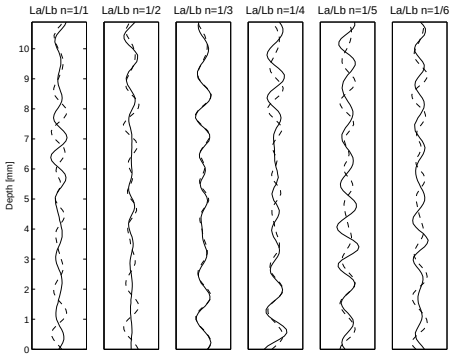

Fig. 2. Shows a set of lines used by the transverse velocity estimator. The dotted line is the left line L_A, and the solid line is the right line L_B as seen in Fig. 1. The L_A lines are taken from emission 1, and the L_B lines are taken from emission 1 to 6. The transit time for the scatterres are found as the instance when the two lines are most similar.

III. Methods

A. Simulations

To evaluate the method, a series of simulations have been carried out under different situations. All the simulations have been made using the Field II program [11] [12]. The flow phantom has a laminar, parabolic velocity distribution given by

$$v(r) = v_0\left(1 - \left(\frac{r}{R}\right)^2\right), \qquad (3)$$

where v_0 is the peak velocity, r is the radial position in the vessel, and R is the radius of the vessel.

The flow phantom is created by placing point scatterers randomly over the region of interest. All the point scatterers are assigned a Gaussian distributed amplitude. The point scatters laying outside the vessel are given a amplitude that is 40 dB higher than the amplitude of the scatterers inside the vessel to mimic the situation encountered in a real scanning situation. The scatterers inside the vessel are moved between each pulse emission according to the spatial velocity field. The propagation of the scatters is given by

$$\vec{r}(t + T_{prf}) = \vec{r}(t) + \vec{v}(\vec{r}(t))T_{prf} \quad (4)$$

where $\vec{r}(t)$ is a vector defining the position of the scatterer at time t, T_{prf} is the time between pulse emissions, and $\vec{v}(\vec{r})$ is the velocity vector at position $\vec{r}$.

The basic parameters for the simulation are given in Table I.

TABLE I
STANDARD PARAMETERS FOR PARABOLIC FLOW SIMULATION AND VELOCITY ESTIMATION

Transducer center frequency	f_0	7 MHz
Speed of sound	c	1540 m/s
Wavelength	λ	0.22 mm
Pitch of transducer elements	w	0.208 mm
Height of transducer elements	h_e	4.5 mm
Kerf	ke	0.035 mm
Number of active elements(receive/transmit)	N_e	128/128
(Elevation focus)	R_e	25 mm
RF lines for estimation	N	15
Sampling frequency	f_s	40 MHz
Pulse repetition frequency	f_{prf}	3000 Hz
Number of oscillations	N_o	1
Length of La and Lb	l	0.55 mm
Distance between La and Lb	$2d_x$	0.4 mm
Correlation interval	C_i	$\pm\frac{\lambda}{4}$
Sampling interval for beamforming	d_{bf}	$\lambda/20$
Radius of vessel	R	8 mm
Distance to vessel center	Z_{ves}	28 mm
Peak velocity	v_0	0.6 m/s
Beam to flow angle	B_a	75 degrees

B. Results statistics

To evaluate the performance of the method, the standard deviation and bias are calculated for all simulations. The bias is given by

$$B_{est}(z_k) = v_\mu(z_k) - v_{true}(z_k), \quad (5)$$

where z_k is a discrete depth, v_μ is the mean of the estimates for the discrete depth, and v_{true} is the true velocity. The standard deviation is given by

$$\sigma_{est}(zk) = \sqrt{\frac{1}{N_{est}-1}\sum_{i=1}^{i=N_{est}}(v_i(z_k) - v_\mu(z_k))^2}, \quad (6)$$

where N_{est} is the number of estimates used for calculating the standard deviation, and v_i is an estimate. To get out a single number representing the performance of a simulation, the mean and standard deviation is averaged over a range $\pm$ 4 mm from the vessel center, and normalized with respect to the peak velocity v_0, as

$$B_{rel} = \frac{1}{v_0 \cdot N_{zk}}\sum_{z_k=1}^{N_{zk}} B_{est}(z_k) \quad (7)$$

$$\sigma_{rel} = \frac{1}{v_0 \cdot N_{zk}}\sum_{z_k=1}^{N_{zk}} \sigma_{est}(z_k) \quad (8)$$

where N_{zk} is the number of estimates in the interval. The outer most parts of the vessels are not included in the calculations of the statistical parameters to avoid wall effects.

Because the method relies on correlation, two types of errors are present [13]. The first, called a false peak error, is when a high sidelobe is identified by the estimator. This type of error is large, but can be removed by spatial or temporal median filtering [14] . The second type of error, called a jitter error, is a slight shift of the peak of the correlation function due to contamination of noise, finite sampling, etc. Since a few false peak errors will have a dominating effect on the calculation of the statistical parameters and they relative easily can be removed, a rejection scheme is used. Only estimates laying within 30% of the true velocity are included in the calculations of the statistical parameters. The percentage of rejected estimates will also be presented.

IV. RESULTS

The top of Fig. 3 shows a plot of 25 transverse velocity profiles for a purely transverse flow. 15 emissions are used to create every profile, with a transmit focus in 56 mm and a correlation line length l of 1.1 mm. The bottom part of Fig. 3 shows the mean and standard deviation for the profile. The mean normalized standard deviation over the profile is 1.64%, and the mean normalized bias is 1.13%. No estimates have been left out due to the rejection scheme. The results show that the estimator works well for spatially variant velocity fields. The standard deviation is seen to increase at the sides of the simulated vessel. This is due to the steeper gradient of the velocity field, and the fact that the scatterers move to slowly to travel the distance between L_A and L_B.

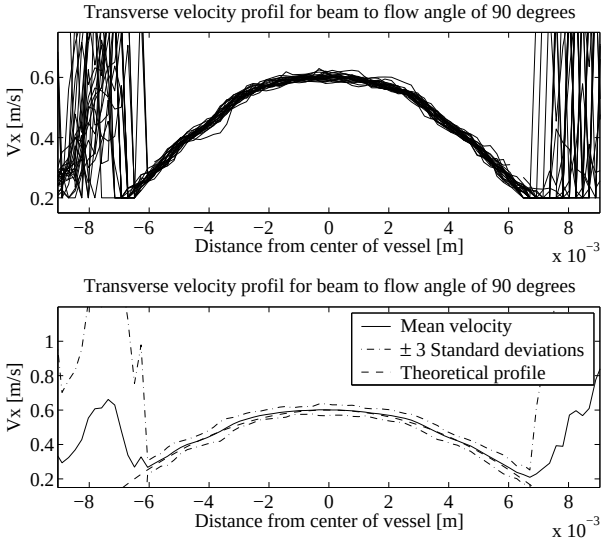

Fig. 3. The top of the figure shows 25 velocity profiles for a beam to flow angle of 90 degrees. The bottom of the figure shows, the mean profile (full) together with $\pm$ 3 standard deviation (dashdot) and the the theoretical profile(dashed).

The top part of Fig. 4 shows a plot of 24 velocity profiles for a beam to flow angle of 45 degrees. 20 emissions are

used to create each profile, with focus in 56 mm and a correlation line length l of 0.55 mm. The bottom part of Fig. 4 shows the mean and standard deviation for the profile. The normalized mean bias over the velocity profile is 2.06%, and the mean normalized standard deviation is 3.40%, 4.6% of the estimates have been left out due to the rejection scheme. The result shows that the method is capable of producing satisfactory results for a low beam to flow angle. Fig. 5 shows

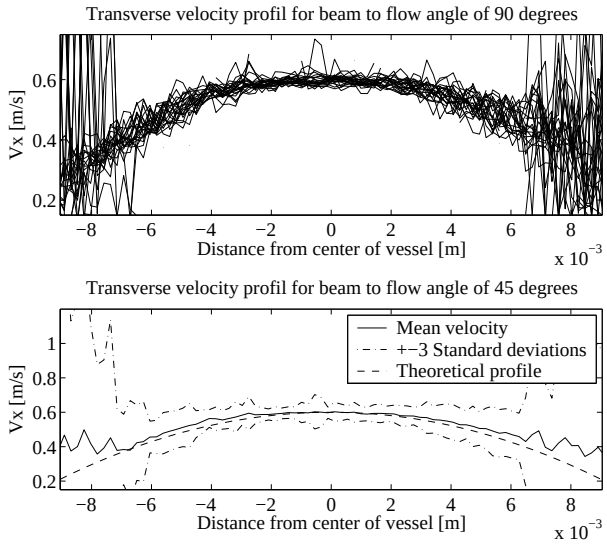

Fig. 4. The top of the figure shows 24 velocity profiles for a beam to flow angle of 45 degrees. The bottom of the figure shows, the mean profile (full) together with $\pm$ 3 standard deviation (dashdot) and the the theoretical profile(dashed).

the performance of the method for different SNR values. The SNR is defined by,

$$SNR_{dB} = 10 \log_{10} \frac{E\{g_b^2(t)\}}{E\{n^2(t)\}}, \tag{9}$$

where $g_b(t)$ is the beamformed signal taken from the middle of the vessel, and $n(t)$ is the noise. The SNR is varied from -10 to 30 dB. The standard deviation falls exponentially until it reaches a plateau of around 3% for a SNR of 10 dB or greater. More than 28% of the estimates are rejected, when the SNR gets below 4.

V. Conclusion

A new transverse velocity estimator has been proposed. Realistic flow simulations have been carried out to test its performance. The estimator is robust and has been able to measure the transverse velocity component with a low standard deviation without any considerable bias.

VI. Acknowledgment

This work was supported by the Faculty of Health Science, University of Copenhagen, by grant 274-05-0327 from the Danish Research Agency, the Radio-parts foundation and by B-K Medical Aps, Denmark.

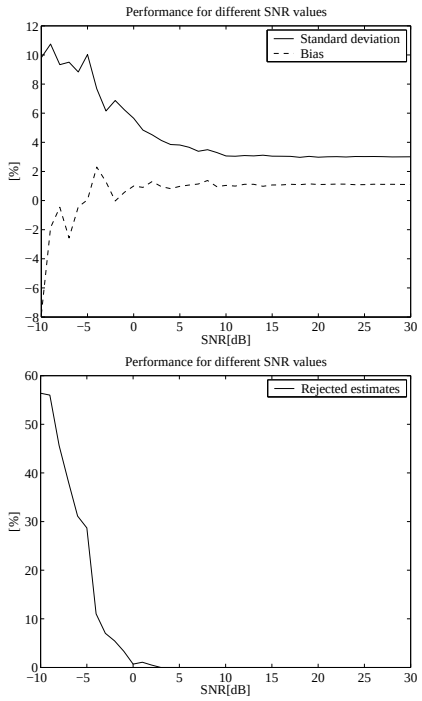

Fig. 5. Variations in SNR

References

[1] J. A. Jensen, *Estimation of Blood Velocities Using Ultrasound: A Signal Processing Approach*, Cambridge University Press, New York, 1996.

[2] M. D. Fox, "Multiple crossed-beam ultrasound Doppler velocimetry," *IEEE Trans. Son. Ultrason.*, vol. SU-25, pp. 281–286, 1978.

[3] G. E. Trahey, J. W. Allison, and O. T. von Ramm, "Angle independent ultrasonic detection of blood flow," *IEEE Trans. Biomed. Eng.*, vol. BME-34, pp. 965–967, 1987.

[4] J. A. Jensen and P. Munk, "A new method for estimation of velocity vectors," *IEEE Trans. Ultrason., Ferroelec., Freq. Contr.*, vol. 45, pp. 837–851, 1998.

[5] J. Udesen, F. Gran, and J. A. Jensen, "A frequency splitting method for CFM imaging," in *Proc. IEEE Ultrason. Symp.*, 2006, p. Accepted for publication.

[6] M. E. Anderson, "Multi-dimensional velocity estimation with ultrasound using spatial quadrature," *IEEE Trans. Ultrason., Ferroelec., Freq. Contr.*, vol. 45, pp. 852–861, 1998.

[7] J. A. Jensen, "Directional velocity estimation using focusing along the flow direction: I: Theory and simulation," *IEEE Trans. Ultrason., Ferroelec., Freq. Contr.*, pp. 857–872, 2003.

[8] J. Kortbek and J. A. Jensen, "Estimation of velocity vector angles using the directional cross-correlation method," *IEEE Trans. Ultrason., Ferroelec., Freq. Contr.*, vol. 53, pp. 2036–2049, 2006.

[9] Ilmar Hein, "3-d flow velocity vector estimation with a triple-beam lens transducer-experimental results," *IEEE Trans. Ultrason., Ferroelec., Freq. Contr.*, vol. 44, pp. 85–95, 1997.

[10] O. Bonnefous and P. Pesqué, "Time domain formulation of pulse-Doppler ultrasound and blood velocity estimation by cross correlation," *Ultrason. Imaging*, vol. 8, pp. 73–85, 1986.

[11] J. A. Jensen, "Field: A program for simulating ultrasound systems," *Med. Biol. Eng. Comp.*, vol. 10th Nordic-Baltic Conference on Biomedical Imaging, Vol. 4, Supplement 1, Part 1, pp. 351–353, 1996b.

[12] J. A. Jensen and N. B. Svendsen, "Calculation of pressure fields from arbitrarily shaped, apodized, and excited ultrasound transducers," *IEEE Trans. Ultrason., Ferroelec., Freq. Contr.*, vol. 39, pp. 262–267, 1992.

[13] W. F. Walker and G. E. Trahey, "A fundamental limit on the performance of correlation based phase correction and flow estimation techniques," *IEEE Trans. Ultrason., Ferroelec., Freq. Contr.*, vol. 41, pp. 644–654, 1994.

[14] J. A. Jensen, "Range/velocity limitations for time-domain blood velocity estimation," *Ultrasound Med. Biol.*, vol. 19, pp. 741–749, 1993c.

Paper XIII

In Vivo Vector Flow Imaging Using Improved Directional Beamforming

L. Henze, I. K. Holfort, J. Kortbek and J. A. Jensen

Proceedings of the IEEE International Ultrasonics Symposium

Presented in New York, USA, Oct. 2007

In Vivo Vector Flow Imaging Using Improved Directional Beamforming

Lasse Henze[1], Iben Kraglund Holfort[1], Jacob Kortbek[1,2], Kristoffer Lindskov Hansen[3] and Jørgen Arendt Jensen[1]

1) Center for Fast Ultrasound Imaging, Ørsted•DTU, Bldg. 348,
Technical University of Denmark, DK-2800 Kgs. Lyngby, Denmark
2) B-K Medical, Mileparken 34, DK-2730 Herlev, Denmark
3) University hospital of Copenhagen, Rigshospitalet Blegdamsvej 9, DK-2100 Copenhagen

***Abstract*— Directional beamforming has shown promising results for creating vector flow images. The method measures both the flow angle and the magnitude of the velocity. The flow angle is estimated by focusing lines in a range of angles from 0 to 180 degrees. The true angle is identified as the angle that produces the largest correlation coefficient across emissions. The magnitude of the velocity is found by cross-correlating consecutive lines focused along the direction of flow, to find the spatial shift corresponding to the velocity. In initial in vivo experiments, the method has however shown weaknesses by yielding outliers when a substantial clutter signal is present after clutter filtering. This is especially a problem when the flow angle is close to 90 degrees as the slow time frequencies from the flow signal is similar to that of the clutter, making clutter filtration difficult. When the angle determination fails, the correct velocity can no longer be found. The purpose of this work is to improve the robustness of the directional beamforming method, making precise in vivo measurement possible. A more robust angle estimator is proposed. Spatial averaging in the axial direction is applied over a depth of 2 wavelengths. Instead of traditionally beamforming a single line, three lines are beamformed with an interline distance of a wavelength. To improve clutter filtering a post correlation clutter filter is applied, by removing peaks in the correlation functions corresponding to low velocities, since these peaks are believed not to be a result of the measured flow. The method has been tested on a flow phantom, using the RASMUS experimental scanner. The flow had a parabolic velocity distribution with a peak velocity of 0.1 m/s, and a flow angle of 90 degrees. The measurement were made with a 6.2 MHz linear array transducer, using 30 emissions and 128 transducer elements for each estimate. Using the same measurement setup, an initial in vivo study has been carried out. The measurements have been performed on the carotid artery of 11 human volunteers. To validate the method MR angiography has been performed on all human volunteers as a gold standard. For the phantom measurement 76.30% of the angle estimates are within ±5 degrees of the actual angle, when using the traditional setup. Using our new approach 98.32% of the angle estimates are within ±5 degrees from the true angle. The comparison between the stroke volume measurements in the carotid artery calculated using directional beamforming and MR angiography, gives a correlation coeficient of 0.84. Phantom and in vivo measurements has been carried out with a more robust implementation of the directional beamforming method. With the applied changes, the method has shown improved results for in vivo measurements.**

I. Introduction

In traditional ultrasonic velocity estimation systems, only the axial velocity component is estimated. So to find the absolute velocity, the beam to flow angle must be found. The absolute velocity is an important clinical parameter, so the ability to measure it accurately is of great value. Jensen [1] suggested to cross-correlate lines beamformed in the flow direction, to directly measure the magnitude of the velocity vector. The method performs well, even for pure transverse flow, but needs a priori knowledge of the flow angle.

To find the flow angle Kortbek and Jensen [2] suggested to beamform lines in a range of directions, from 0 to 180 degrees, and then search for the direction with the largest correlation over time. It was shown in simulations and phantom measurements that the method was capable of finding both the correct flow angle and velocity magnitude using few emissions. However when Holfort et al. [3] performed initial in vivo experiment is was shown that the angle estimator breaks down when a substantial amount of clutter is present after clutter filtering. When the angle determination fails, the correct velocity can no longer be found.

The purpose of this work is to improve the robustness of the angle estimator to enable accurate velocity vector estimation. This is performed by applying spatial averaging, and improving clutter filtering.

II. Methods and materials

A. Angle Estimation

To find the flow angle, directional signals are beamformed in a range from 0 to 180 degrees as shown in Fig 1. The directional signal is given by $S_i(x'_\phi)$, where i is the emission number, ϕ is the beam angle, as seen on the figure, and x' is the spatial location on the line.

The directional signal, corresponding to the true flow angle, for emission i, contains the same blood scatterers, as for emission $i+1$, excepts for the few scatterers that has left the signal in the end or entered at the start. This will make the correlation between consecutive signals high. For the remaining angles, a different distribution of scatters will be examined for each emission, due to the misalignment between the signals and the direction of flow. As a result the correlation will be low. The directional signal corresponding to the true flow angle, can therefore be identified as the signal that produces the largest normalized correlation coefficient over emissions. The correlation coefficient for different angles is calculated using

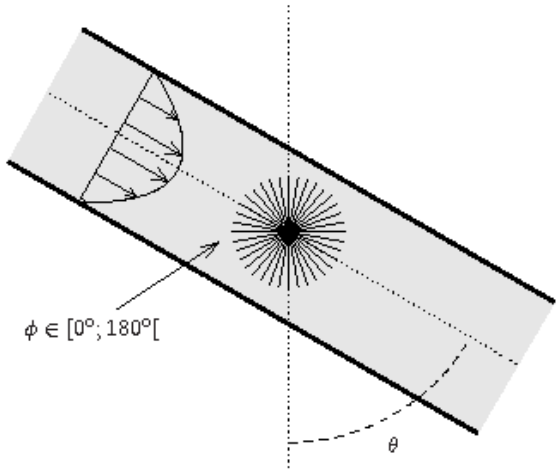

Fig. 1. Setup for the method. Directional signals are beamformed from 0 to 180 degrees at the estimation point. The directional signals are correlated over emissions. The signal with the largest correlation is identified as the direction of flow. When the direction of flow is found, the magnitude of the velocity is found by cross-correlating consecutive signals to find the spatial shift corresponding to the blood velocity.

$$P(\phi) = \max\{\sum_{i=1}^{N-1} C(S_i(x'_\phi), S_{i+1}(x'_\phi))\}, \tag{1}$$

where N is the total number of emissions, and C is the normalized correlation coefficient defined by

$$C(a,b) = \frac{R_{ab}(k) - \mu_a\mu_b}{\sqrt{[R_{aa}(0) - \mu_a^2][R_{bb}(0) - \mu_b^2]}}, \tag{2}$$

where R_{ab} is the cross-correlation between signal a and b, μ_a is the mean of a and μ_b is mean of b. The sum in (1) is introduced to perform averaging.

The angle can now be estimated by searching for the largest correlation coefficient,

$$\theta_e = (\arg\max_\phi\{P(\phi)\}) \tag{3}$$

B. Velocity Estimation

When the direction of flow is known, the magnitude of the velocity can be found. Two signals taken from consecutive emissions, beamformed along the direction of flow, is related to each other by a spatial shift x'_s given by

$$S_i(x'_\phi) = S_{i+1}(x'_\phi - 2VT_{prf}) \tag{4}$$

where V is magnitude of the velocity and T_{prf} is the time between emission. The spatial shift is found be locating the peak of the cross-correlation function taken between two consecutive signals.

$$x'_s = \arg\max_k \sum_{i=1}^{N-1} R_{S_iS_{i+1}}(k), \tag{5}$$

The velocity is now given by

$$V = \frac{x'_s}{T_{prf}} \tag{6}$$

For a more in depth description of the basic method see [2].

C. Spatial Averaging

To improve the robustness, spatial averaging is applied on the angle estimator in the axial dimension. The spatial averaging is applied by beamforming three lines for every angle. The three lines are beamformed with in a range of 2λ. The new angle estimator is given by

$$P(\theta) = \max\{\sum_{j_z=1}^{3}\sum_{i=1}^{N-1} C(S_{i,\theta,(j_z-2)\lambda}(t), S_{i+1,\theta,(j_z-2)\lambda}(t))\}, \tag{7}$$

The length of the directional signals, in the used setup, is 20λ, so the applied spatial averaging will only marginally reduce the spatial resolution of the estimator.

D. Post Correlation Clutter Filtering

To improve clutter filtering, peaks in the correlation function taken in (2) identified to be a product of the clutter is removed. The directional signals are composed of two major components, one flow component, coming from the blood scatterers and one clutter component, coming from the stationary tissue,

$$S_i(x') = F_i(x') + N(x'), \tag{8}$$

where $F_i(x')$ is the flow component and $N(x')$ is the clutter component. It is assumed that the clutter and blood component is uncorrelated and that the clutter component is stationary over emissions. When the cross-correlation is taken in (2) between two consecutive emissions, it corresponds to the cross-correlation of the flow signal, added with the auto-correlation of the clutter signal

$$R_{S_i(x'),S_{i+1}(x')} = R_{F_i(x'),F_{i+1}(x')} + R_{N(x'),N(x')}\,. \tag{9}$$

It is known from basic signal processing, that the auto-correlation function peaks at lag zero and from (4) it is known that the cross-correlation of the flow signal, for the true angle, peaks at lag $2V\frac{T_{prf}}{c}$. So the post correlation clutter filtering is done by ignoring peaks laying around lag zero in (2).

By doing this, peaks emerging as a result of the clutter is removed, without affecting the true peak coming as a result of the measured flow.

E. Measurements

To test the performance of the method, phantom and in-vivo measurements have been carried out on the experimental ultrasound scanner RASMUS [4]. The parameters used for all measurements can be seen in Table I.

Phantom measurements have been performed on a circulating flow rig as seen on Fig 2. A long tube is connected to a flow pump. The transducer is placed in a fixture, with a known beam to flow angle. An electromagnetic flow meter is placed around the tube to read the flow, as a reference. Measurements has been carried out for a beam to flow angle of 90 degrees.

A transmit focus is placed in the double depth of the tube, to get a wide transmit beam. The vector flow images have been created by measuring 16 flow lines per image with an axial spacing of λ between each estimate. 64 elements are used in transmit and 128 elements are used in receive. The used scanner has access to 128 channels, so a sliding aperture can only be achieved in transmit. To avoid tilting of the point spread function, a boxcar apodization is applied in receive to force a symmetric receive aperture.

The in-vivo measurements have been carried out on the carotid artery of 11 healthy human volunteers. To validate the method MR angiography has been performed on all 11 volunteers as an gold standard. To enable a comparison, the volume flow over a heart cycle has been calculated. The volume flow has been calculated using the assumption of rotational symmetry. All in-vivo measurements have been performed by an experienced medical doctor.

Prior to the in-vivo measurements, the intensities of the transmit setup have been measured using a hydrophone. All measured intensities were below the limits set by the U.S Food and Drug Administration [5].

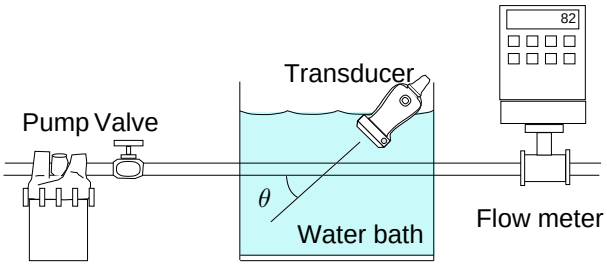

Fig. 2. Setup of the used flowrig. A pump secures a steady parabolic flow in the tube. A fixture holds the transducer at a known beam to flow angle. An electro magnetic flow meter measures the volume flow as a reference.

III. Experimental Results

A. Phantom Measurements

The top graph in Fig. 3 shows the angle estimates, for the phantom measurement, calculated using the traditional setup. Angle estimates from 10 images each containing 16 flow lines are plotted. 76.3% of the estimates are within $\pm 5\%$ from the correct angle. The angle estimates, at the side of the tube, are slightly worse than the estimates in the middle. The method performs best on the central flow lines. This is because they have the largest recieve aperture.

The bottom of Fig.3 shows angle estimates, calculated with the improvements. 98.32% of the estimates are with in $\pm 5\%$ from the correct angle. A slight worsenning of the estimates can again be observed at the side of the tube, but not to the same extend as in the top figure. A fairly even performance is observed over the individual flow lines. Using the improvements a satisfactory result is optained for the phantom measurements.

TABLE I
Standard parameters For Phantom and In-vivo measurements

Type		Linear array
Transducer center frequency	f_0	7 MHz
Wavelength	λ	0.22 mm
Pitch of transducer elements	w	0.208 mm
Height of transducer elements	h_e	4.5 mm
Kerf	ke	0.035 mm
Number of active elements(receive/transmit)	N_e	128/64
Apodization(receive/transmit)		Boxcar/Hanning
Number of excitation periods		2
Elevation focus	R_e	25 mm
Radius of tube	R	6 mm
Peak velocity in flow profile	v_0	0.15 m/s
Beam to flow angles	θ	90°
RF lines for estimation	N	32
Length of directional signals		20λ
Sampling frequency	f_s	40 MHz
Number of oscillations	N_o	2
Speed of sound	c	1480/1540 m/s

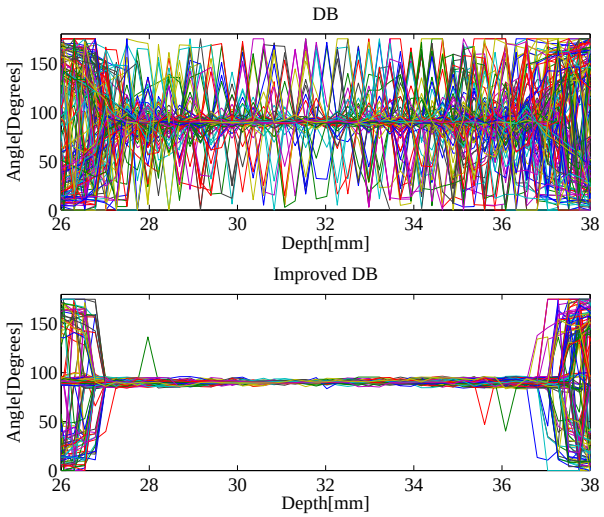

Fig. 3. Angle estimates from the phantom measurements, for a beam to flow angle of 90 degrees. The top figure shows the estimates calculated with a direct implementation of Directional beamforming. The bottom figure shows the estimates calculated with the improved version of Directional beamforming.

B. In-vivo Measurements

The top of Fig 4 shows a velocity vector image of the common carotid artery and jugular vein, calculated using the traditional setup. The brightness of the color and the length of the arrows, shows the magnitude of the velocity and the direction of the arrows shows the flow angle. The main direction of flow in the artery and vein can be observed, but the image is dominated by errors.

The bottom of Fig 4 shows, for the same frame as the top of the figure, a velocity vector image, calculated using the new method. A more believable result is obtained and only few estimates can visually be determined to be errors.

Fig 5 shows the regression line for stroke volume, estimated using Directional beamforming and MR angiography. The MR measurements directly measures the volume flow, where as the ultrasound measurements is based on the assumption of a rotational symmetric velocity field. The vertical line on each of the data points, show the possible distribution of volume flow estimates, if the MR measurements where based on the same assumptions as the ultrasound measurements. The correlation coefficient is calculated to be 0.84, with a 95% confidence interval from 0.49 to 0.96.

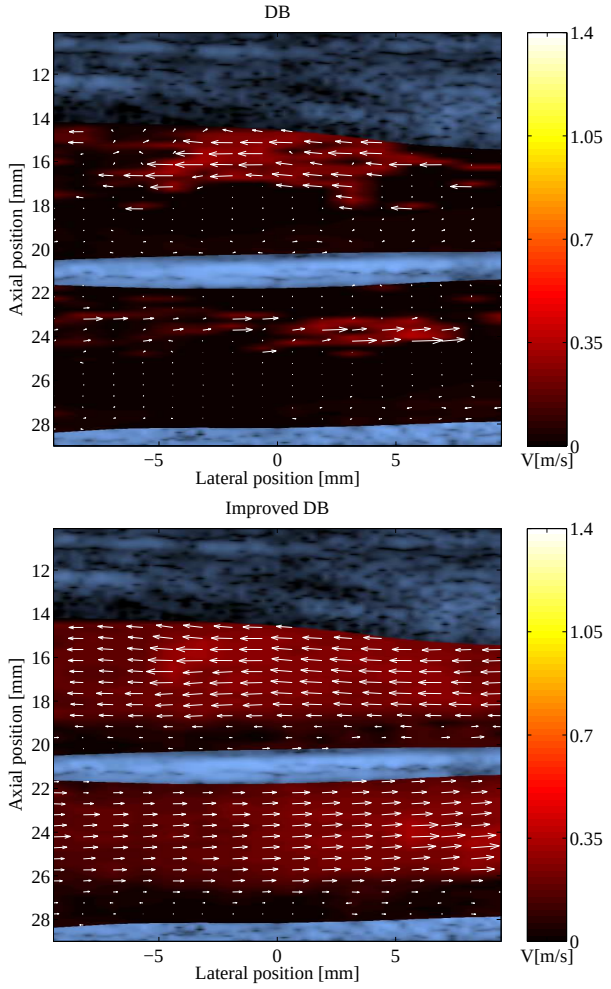

Fig. 4. In-vivo scan of the carotid artery and jugular vein. The top figure shows the estimates calculated with a direct implementation of Directional beamforming. The bottom figure shows the estimates calculated with the improved version of Directional beamforming.

IV. Conclusion

A more robust version of Directional beamforming has been implemented. The method has been tested in circulating flowrig. 11 successful in vivo measurements have been carried out. MR angiography has been performed as a reference. A correlation coefficient of 0.84 has been achieved for stroke volume estimated using MR and ultrasound. The preliminary results look encouraging for further research.

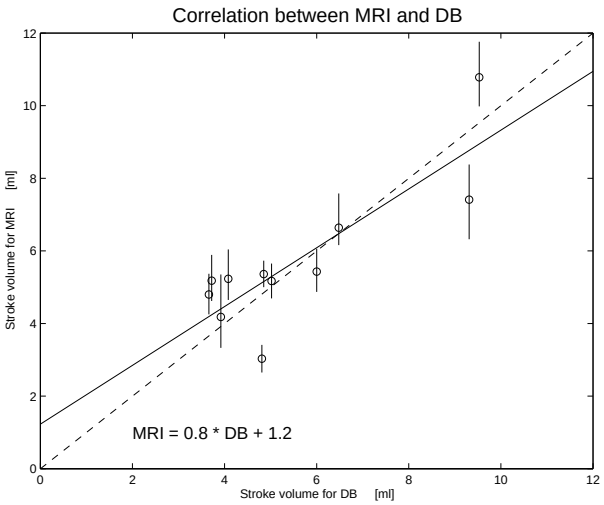

Fig. 5. Regression line for volume flow estimated with MR and ultrasound. The vertical line on each of the data points shows the uncertainty of the ultrasound estimates, due to the assumption of rotational symmetry.

V. Acknowledgment

This work was supported by the Faculty of Health Science, University of Copenhagen, by grant 274-05-0327 from the Danish Research Agency, the Radio-parts foundation and by B-K Medical A/S, Denmark.

References

[1] J. A. Jensen, "Directional velocity estimation using focusing along the flow direction: I: Theory and simulation," *IEEE Trans. Ultrason., Ferroelec., Freq. Contr.*, pp. 857–872, 2003.

[2] J. Kortbek and J. A. Jensen, "Estimation of velocity vector angles using the directional cross-correlation method," *IEEE Trans. Ultrason., Ferroelec., Freq. Contr.*, vol. 53, pp. 2036–2049, 2006.

[3] I. K. Holfort, J. Kortbek, and J. A. Jensen, "Vector velocity imaging using cross-correlation and virtual sources," in *Proc. IEEE Ultrason. Symp.*, 2006, pp. 2023–2026.

[4] J. A. Jensen, O. Holm, L. J. Jensen, H. Bendsen, S. I. Nikolov, B. G. Tomov, P. Munk, M. Hansen, K. Salomonsen, J. Hansen, K. Gormsen, H. M. Pedersen, and K. L. Gammelmark, "Ultrasound research scanner for real-time synthetic aperture image acquisition," *IEEE Trans. Ultrason., Ferroelec., Freq. Contr.*, vol. 52 (5), pp. 881–891, May 2005.

[5] FDA, "Information for manufacturers seeking marketing clearance of diagnostic ultrasound systems and transducers," Tech. Rep., Center for Devices and Radiological Health, United States Food and Drug Administration, 1997.

Paper XIV

In-vivo Vector Velocity Imaging Using Directional Cross-Correlation

I. K. Holfort, J. Kortbek and J. A. Jensen

Proceedings of the IEEE International Ultrasonics Symposium

Presented in Vancouver, BC, Canada, Oct. 2006

In-vivo Vector Velocity Imaging Using Directional Cross-Correlation

Iben Kraglund Holfort[1], Jacob Kortbek[1,2] and Jørgen Arendt Jensen[1]

1) Center for Fast Ultrasound Imaging, Ørsted•DTU,
Build. 349, Technical University of Denmark, DK-2800 Lyngby, Denmark.
2) B-K Medical, Mileparken 34, DK-2730 Herlev, Denmark.

***Abstract*— Previous investigations have shown promising results in using the directional cross-correlation method to estimate velocity vectors. The velocity vector estimate provides information on both velocity direction and magnitude. The direction is estimated by beamforming signals along directions in the range $[0^\circ; 180^\circ[$ and identifying the direction that produces the largest correlation across emissions. An estimate of the velocity magnitude is obtained from the spatial shift between signals beamformed along the estimated direction.**

This paper expands these investigations to include estimations of the vector velocities of a larger region by combining the estimations along several scan lines. In combination with a B-mode image, the vector velocities are displayed as an image of the investigated region with a color indicating the magnitude, and arrows showing the direction of the flow.

Using the RASMUS experimental ultrasound scanner, measurements have been carried out in a water tank using a 7 MHz transducer. A 6 mm tube contained the flow and a Danfoss, MAG 3000, magnetic flow meter measured the volume flow. The tube has a parabolic flow profile with a peak velocity of 0.29 m/s. During the experiments fixed beam-to-flow angles at $\{60^\circ, 75^\circ, 90^\circ\}$ have been applied. The images are obtained using a pulse repetition frequency of 15 kHz, and the images contain 33 lines with 60 emissions for each line.

Corresponding to the three fixed beam-to-flow angles, the angle estimates along the center scan line have a bias of $\{-3.9^\circ, -12.8^\circ, -18.1^\circ\}$ and standard deviation of $\{10.0^\circ, 18.2^\circ, 32.2^\circ\}$. The estimates of the velocity magnitude have bias of $\{4.4\%, 8.1\%, -5.4\%\}$ and standard deviation of $\{9.7\%, 14.3\%, 13.4\%\}$ relative to the peak velocity. The amount of in-tube angle estimates in the range of $\pm 10^\circ$ from the true angle are $\{74\%, 77\%, 66\%\}$.

In-vivo measurements are carried out on a human volunteer. These measurements include the common carotid artery and the femoral bifurcation.

I. Introduction

In conventional blood flow estimation, the velocities are dependent on the direction of the emitted beam, as only the axial component of the velocity vector is estimated. The directional cross-correlation method suggested by Jensen in [1]-[2] is capable of estimating the two-dimensional velocity vector. The two-dimensional velocity vector is independent on the beam direction and provides information on the magnitude as well as the direction of the flow.

In this paper, the directional cross-correlation method is investigated. Based on the theory in [1]-[2], a fully automatic velocity vector estimation algorithm is developed and implemented. Experimental investigations are carried out; these include an experimental setup using a water tank with three different fixed beam-to-flow angles and in-vivo. The in-vivo measurements include the common carotid artery and the femoral bifurcation

II. Velocity Vector Estimation

The two-dimensional velocity vector is obtained by estimating flow direction and velocity magnitude separately as described below.

A. Velocity Estimation

The magnitude of the velocity vector is estimated by identifying the spatial shift of a directional signal over time. Beamforming along the estimated flow direction, two directional signals, $g_1(x')$ and $g_2(x')$, are obtained. Assuming laminar flow, the two directional signals are identical, except for a displacement, due to the movement of the blood scatterers.

The spatial shift between the two signals is found by cross-correlating the two signals

$$\begin{aligned} R_{12}(\tau) &= \frac{1}{L}\int_L g_1(x')\, g_2(x'+\tau)\, dx' \quad (1)\\ &= \frac{1}{L}\int_L g_1(x')\, g_1(x' - |\vec{v}|\, T_{prf} + \tau)\, dx' \\ &= R_{11}(\tau - |\vec{v}|\, T_{prf}), \quad (2)\end{aligned}$$

where L is the length of the directional signal, $R_{11}(\tau)$ and $R_{12}(\tau)$ denote the auto-correlation and the cross-correlation functions, respectively. $R_{12}(\tau)$ is a shifted version of the auto-correlation of the signal $g_1(x')$. The auto-correlation function normally peaks at $\tau = 0$, but due to the subtraction of the term $|\vec{v}|\, T_{prf}$, R_{11} reaches its maximum at $\tau_{peak} = |\vec{v}|\, T_{prf}$. Thus, the magnitude of the velocity vector is found by identifying the lag corresponding to the maximum peak

$$\tau_{peak} = \arg\max_{\tau}\{R_{12}(\tau)\}. \quad (3)$$

The magnitude of the velocity along the flow direction is then

$$|\vec{v}| = \frac{\tau_{peak}}{T_{prf}}, \quad (4)$$

where T_{prf} is the pulse repetition interval.

B. Angle Estimation

The direction of the flow is obtained by estimating the beam-to-flow angle, θ. Based on an assumption of laminar flow, the flow direction provides the largest amount of correlation between the two directional signals. The amount of correlation can be quantified by the correlation coefficient. Let $g_1(x')$ and $g_2(x')$ denote the two directional signals beamformed along the direction, ϕ. By denoting the mean values of each of the signals, μ_1 and μ_2, the correlation coefficient can be estimated by [3]

$$\rho = \max \left\{ \frac{R_{12}(\tau) - \mu_1\mu_2}{\sqrt{[R_{11}(0) - \mu_1^2][R_{22}(0) - \mu_2^2]}} \right\}, \qquad (5)$$

where $R_{11}(0)$ and $R_{22}(0)$ denote the auto-correlation functions at lag 0, and $R_{12}(\tau)$ is the cross-correlation function given by (1). The auto- and cross-correlation functions in (5) are obtained along the direction ϕ.

By beamforming directional signals at angles $\phi \in [0°; 180°[$, the angle estimate can be found from the largest correlation

$$\hat{\theta}_d = \arg\max_{\phi}\{\rho(\phi)\}, \qquad (6)$$

where $\hat{\theta}_d$ is the discrete estimated beam-to-flow angle.

To improve the accuracy of the discrete estimate, $\hat{\theta}_d$, is interpolated using the following expression

$$\hat{\theta} = \hat{\theta}_d - \frac{\rho(\hat{\theta} + \Delta\phi) - \rho(\hat{\theta} - \Delta\phi)}{2(\rho(\hat{\theta} + \Delta\phi) - 2\rho(\hat{\theta}) + \rho(\hat{\theta} - \Delta\phi))}\Delta\phi \qquad (7)$$

where $\Delta\phi$ is the angular distance between two consecutive beamform angles.

III. Measurements

To validate the implemented velocity vector algorithm, a set of measurements have been carried out using the experimental ultrasound scanner, RASMUS [4]. The standard parameters for all measurements are stated in Table I.

A. Experimental Setup

An experimental setup uses a water tank with a tube as illustrated in Fig. 1. The transducer is placed at a fixed beam-to-flow angle, θ, within the water tank. The tube is connected to a pump, and the volume flow rate of the fluid is controlled by a valve and registered by a Danfoss MAG 1100 flow meter. The flow is assumed to be laminar and have a parabolic flow profile, which is characterized by [5]

$$v(z') = v_0 \left(1 - \left(\frac{z'}{R}\right)^2\right), \quad z' \in [-R; R] \qquad (8)$$

where z' denotes the direction perpendicular to the flow direction, R is the radius of the vessel and v_0 is the peak velocity in the center of the vessel. v_0 is determined by the chosen volume flow rate of the pump.

Measurements are carried out using the three beam-to-flow angles, $\theta = \{60°, 75°, 90°\}$, where $\theta = 90°$ is transverse flow.

Type	Linear array
Center frequency, f_0	7 MHz
Pitch of transducer element	208 μm
Height of transducer element	4.5 mm
Kerf	35 μm
Elevation focus	25 mm
Number of transducer elements	128
Apodization, Transmit/Receive	Hamming/None
Number of elements, Transmit/Receive	64 / 64
Excitation pulse, $e(t)$	$\sin(2\pi f_0 t)$
Number of excitation periods	2
Sampling frequency, f_s	40 MHz
Pulse repetition frequency, f_{prf}	15 kHz
Speed of sound, c (in water tank/in-vivo)	1485 m/s / 1540 m/s
Wavelength, $\lambda = c/f_0$ (in water tank/in-vivo)	212 μm / 220 μm
Radius of tube, R	6.0 mm
Peak velocity in flow profile, v_0	0.29 m/s
Volume flow rate, Q	60 l/h
Beam-to-flow angles, θ	$\{60°, 75°, 90°\}$
Depth of focus point, z_f	$\{56, 44, 36\}$ mm
f-number, $f_\#$	$\{4.2, 3.3, 2.7\}$

TABLE I

STANDARD PARAMETERS USED IN THE CONDUCTED MEASUREMENTS.

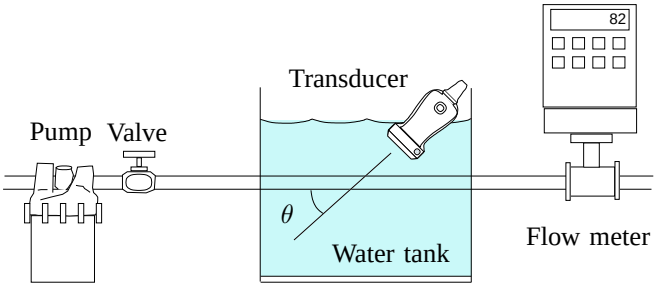

Fig. 1. Illustration of the experimental setup. From [6].

B. Measurement Sequence

The measurements have been carried out using 64 active elements, which are both transmitting and receiving. These 64 elements obtain data, which provides information for one scan line. To obtain data for a full image, the active part of the aperture is displaced along the lateral direction. A total of 33 scan lines with 60 emissions for each line have been acquired resulting in a frame rate of $\simeq 7.5$ Hz.

C. Experimental Validation

The performance of the implemented velocity vector estimation algorithm has been investigated along the center scan line. The performance measures, bias and standard deviation, are stated in Table II. The velocity estimates have been estimated using two different approaches; along the fixed direction, θ, and along the estimated direction, $\hat{\theta}$.

Along the fixed direction, the velocity estimation demonstrates a very satisfying performance for all three test angles, including transverse flow. A decrease in performance, especially for the transverse flow, is identified, when estimating the velocities along the estimated directions. This decrease is a direct consequence of the performance of the angle estimates. Thus, the fully automatic velocity vector estimation algorithm

is limited by the performance of the angle estimation.

Vector flow images have been produced. The velocity vector estimates are visualized using a color to display the magnitude, and an arrow pointing in the direction of the flow. The arrows are scaled by the magnitude of the velocity.

In Fig. 2, the vector flow image of the $\theta = 75°$ measurement is shown. The intensity of the colors and the scaling of the arrows indicate a parabolic flow profile. The general direction of the flow is easily recognized. The distribution of the estimated angles have been investigated. The percentages within $\theta \pm 10°$ are stated in Table III. For all three test angles, the majority of the angle estimates fall within this interval.

θ	$60°$	$75°$	$90°$
Velocity estimates along fixed angles			
B_v	4.39%	8.09%	-5.41%
σ_v	9.66%	14.27%	13.40%
Velocity estimates along estimated angles			
B_v	-3.70%	-11.29%	-25.55%
σ_v	15.12%	18.46%	33.21%
Angle estimates			
B_θ	$-3.91°$	$-12.82°$	$-18.11°$
σ_θ	$10.03°$	$18.24°$	$32.24°$

TABLE II

BIAS AND STANDARD DEVIATION FOR THE VECTOR VELOCITY ESTIMATION ALGORITHMS ALONG THE CENTER SCAN LINE. UNITS ARE IN % RELATIVE TO THE PEAK VELOCITY, v_0, OR IN DEGREES.

θ	$60°$	$75°$	$90°$
$P(\hat{\theta} \in \theta \pm 10°)$	74.33%	77.35%	66.03%

TABLE III

PERCENTAGE OF IN-TUBE ANGLE ESTIMATES WITHIN $\theta \pm 10°$.

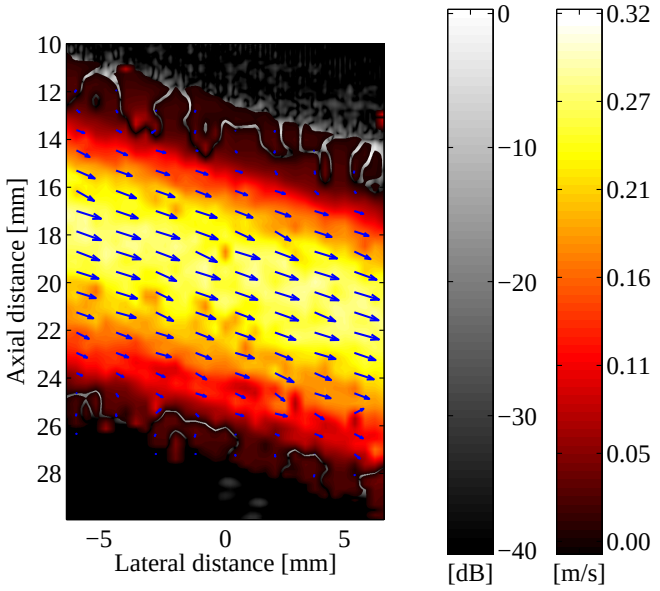

Fig. 2. Vector flow image of the $\theta = 75°$ measurement.

IV. IN-VIVO MEASUREMENTS

Measurements have been carried out on a human volunteer. All measurements are from a healthy 25-year-old female volunteer. The measurements have investigated the blood flow in the common carotid artery and the femoral bifurcation.

Prior to the in-vivo blood flow measurements, the intensities of the actual measurement sequence have been measured. This is a requirement to accommodate the restriction [7] set by the U.S. Food and Drug Administration (FDA). The measured intensities are $I_{spta.3} = 39$ mW/cm^2, $I_{sppa.3} = 9$ W/cm^2 and $MI = 0.14$, which all are well within FDA limits.

For each of the measurements, a sequence of 28 vector flow images have been acquired. These have been combined into movies visualizing the pulsating blood flow in the two arteries. In the following, two single frames from the two movies are shown.

A. Common Carotid Artery

The two vector flow images, Fig. 3, visualize the blood flow in the common carotid artery. In both vector flow images, the general direction of the flow is easily recognized, and the velocities fall in the range of $[0; 0.5]$ m/s.

To estimate the cardiac cycle, the variation of the mean velocity as shown in Fig. 4 is investigated. Each point represents a frame in the acquired sequence. The peak systoles are easily recognized. However, due to the sparse representation, the peak systoles cannot be regarded as more than indications. As a consequence, the first peak has not been acquired. This peak is indicated by the dashed curve.

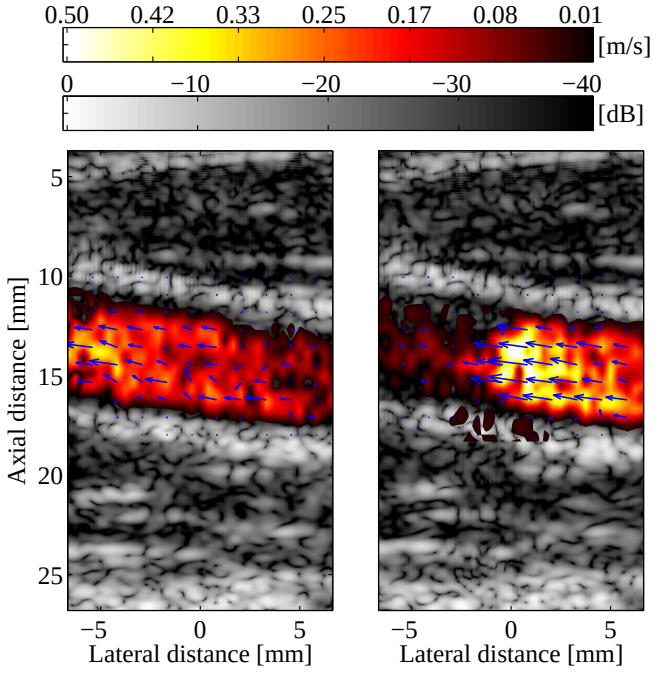

Fig. 3. Vector flow images of the blood flow in the common carotid artery. The two images correspond to peak systoles in the cardiac cycle, and they are acquired at $t = 0.54$ s (left) and $t = 1.74$ (right).

Based on the estimated cardiac cycle, a heart rate of 89.5 bpm is estimated from the time difference between two peaks. Again, due to the sparse representation, the heart rate is merely a rough estimate. The resting normal heart rate is 60-80 bpm [8]. The measured rate is somewhat high, which could be due to stress during the measurement sequence.

The mean blood flow velocity during the systole and diastole in the greater arteries is in the range of 5-18 cm/s [8]. The temporal mean velocity during the entire cardiac cycle is 9.7 cm/s and indicated by the horizontal dashed line in Fig. 4.

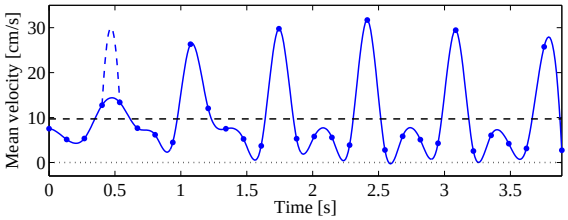

Fig. 4. Variation of the mean velocity in the common carotid artery.

B. Femoral Bifurcation

The estimated blood flow in the femoral bifurcation is visualized by the two vector flow images in Fig. 5. In general, the estimated mean velocities in the femoral arteries are somewhat lower than in the common carotid artery. There are several explanations for this phenomenon, e.g., the reduction of the hydrostatic pressure in the vessels due to a supine position of the test subject.

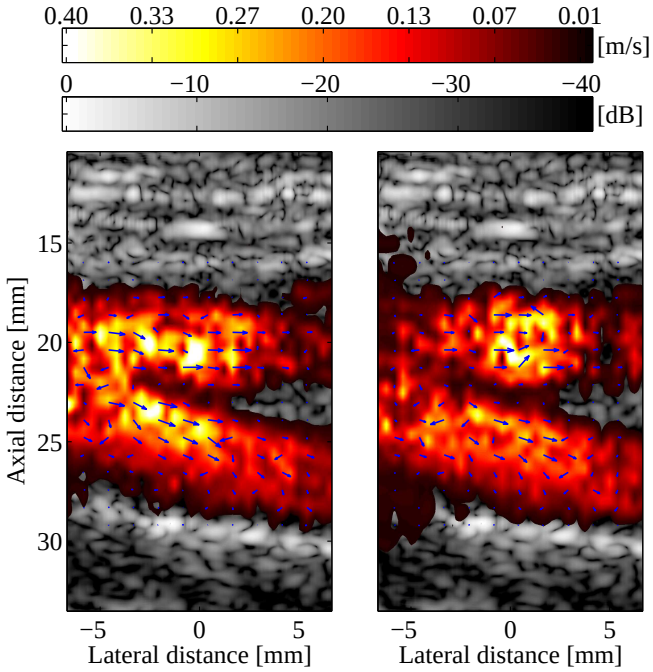

Fig. 5. Vector flow images of the blood flow in the femoral bifurcation. The two images correspond to peak systoles in the cardiac cycle.

The estimated direction of the flow is not as distinct as in the previous measurement. The majority of the angle estimates indicate the direction of the flow from the bifurcation point into the two branches. However, several angle estimates are not consistent with the assumed flow direction. Especially in the deep branch, the angle estimates appear underestimated.

In [9], investigations of the blood flow in the carotid bifurcation using the Transverse Oscillation method have shown a turbulent flow pattern at the bifurcation point and in the internal carotid artery. The turbulent behavior is not evident in Fig. 5. However, this could explain the less distinct flow direction.

V. Conclusions

Based on the theory of the directional cross-correlation method, a fully automatic velocity vector estimation algorithm has been developed and implemented in Matlab. The algorithm has been validated against measurements using an experimental setup. The validation has provided satisfying performance measures. In-vivo measurements have been carried out on a human volunteer for the common carotid artery and the femoral bifurcation. Based on these measurements, vector flow images and movies have been produced.

Acknowledgment

This work was supported by grant 9700883, 9700563 and 26-04-0024 from the Danish Science Foundation and by B-K Medical A/S.

References

[1] J. A. Jensen. Directional velocity estimation using focusing along the flow direction: I: Theory and simulation. *IEEE Trans. Ultrason., Ferroelec., Freq. Contr.*, pages 857–872, 2003.

[2] J. A. Jensen. Velocity vector estimation in synthetic aperture flow and B-mode imaging. In *IEEE International Symposium on Biomedical imaging from nano to macro*, pages 32–35, 2004.

[3] J. S. Bendat and A. G. Piersol. *Engineering Applications of Correlation and Spectral Analysis*. John Wiley & Sons, New York, 2nd edition, 1993.

[4] J. A. Jensen, O. Holm, L. J. Jensen, H. Bendsen, S. I. Nikolov, B. G. Tomov, P. Munk, M. Hansen, K. Salomonsen, J. Hansen, K. Gormsen, H. M. Pedersen, and K. L. Gammelmark. Ultrasound research scanner for real-time synthetic aperture image acquisition. *IEEE Trans. Ultrason., Ferroelec., Freq. Contr.*, 52 (5):881–891, May 2005.

[5] J. A. Jensen. *Estimation of Blood Velocities Using Ultrasound: A Signal Processing Approach*. Cambridge University Press, New York, 1996.

[6] J. A. Jensen and R. Bjerngaard. Directional velocity estimation using focusing along the flow direction: II: Experimental investigation. *IEEE Trans. Ultrason., Ferroelec., Freq. Contr.*, pages 873–880, 2003.

[7] FDA. Information for manufacturers seeking marketing clearance of diagnostic ultrasound systems and transducers. Technical report, Center for Devices and Radiological Health, United States Food and Drug Administration, 1997.

[8] A. Despopoulos and S. Silbernagl. *Color Atlas of Physiology*. Thieme, 1986.

[9] J. Udesen. *2-D blood vector velocity estimation using a phase shift estimator.* PhD thesis, Ørsted•DTU, Technical University of Denmark, 2800, Lyngby, Denmark, 2005.